Strategies to Reduce Rate of Charge Recombination: Long-Lived Charge Separated States Through Self-Assembly

A thesis submitted for the degree of

Doctor of Philosophy

in the

School of Chemistry

by

Ajith R. Mallia

Indian Institute of Science Education and Research Thiruvananthapuram
Thiruvananthapuram – 695016
Kerala, India

August 2016

Declaration

I hereby declare that the work reported in this thesis is original and was carried out by me during my tenure as a PhD student at the School of Chemistry, Indian Institute of Science Education and Research Thiruvananthapuram. Such material as has been obtained from other sources has been duly acknowledged in the thesis.

Place: IISER-Thiruvananthapuram   **Ajith R. Mallia**
 Date: 30-09-2016

Certified that the work incorporated in this thesis "**Strategies to Reduce Rate of Charge Recombination: Long-Lived Charge Separated States Through Self-Assembly**" submitted by **Ajith R. Mallia** was carried out by the candidate under my supervision. This thesis has not formed the basis for the award of any degree, of any university or institution.

Place: IISER Thiruvananthapuram   **Dr. Mahesh Hariharan**
 Date: 30-09-2016   (Thesis supervisor)

Dedicated To...

    My Beloved Parents, Anuradha,

    Jerly Sir and Maya for

    their Unconditional Love

    and Constant Support

ACKNOWLEDGEMENTS

Finally, I thank God almighty for having given me everything what I deserve.

Ajith R. Mallia

Preface

Emergence-upon-assembly approach is a bottom-up strategy unrivalled in nature wherein diverse properties are embedded in hierarchical superstructures by bringing simple modular components together, to engineer nano/micro scale organization. The order and periodicity across the molecular-macroscopic continuum is dictated by various non-covalent interactions programmed into individual molecular components. The supramolecular ordering prevailing in such architectures can emulate remarkable changes in orbital interactions which would find potential applications in electronic devices such as solar cells, field effect transistors and light emitting diodes. Molecular ordering at nano/micro dimensions can aid tuning of the optoelectronic properties for controlling the energy and electron transfer processes in artificial light harvesting assemblies. The increasing energy crisis demands a renewable resource of energy which can replenish at a rate much faster than the rate at which non-renewable resources are being consumed. As solar energy serves as nature's rechargeable battery we set out to explore various strategies which can efficiently perform photon-to-energy conversion by efficiently capturing sunlight through self-assembly.

The present thesis aims at designing and constructing ordered and oriented supramolecular architectures from simple organic frameworks for efficient capture, transfer and storage of solar light employing self-assembly approach. A brief illustration of various strategies adopted incorporating electronically complementary donor and acceptor (D-A) chromophores to modulate the behavior of photogenerated excitons in the aggregated state relative to the monomeric state is provided in Chapter 1. Electronic interaction between D-A pairs, possessing suitable redox counterparts, can lead to photoinduced electron/hole transfer a key process in generating the excitons in photovoltaic and opto-electronic devices for efficient light capture.

The second chapter demonstrates a significant (10,000-fold) enhancement in the charge recombination lifetime of photogenerated excitons in the aggregated state relative to the monomeric state of D-A bichromophores comprised of naphthalene and naphthalimide (NIN). The observed enhancement in the survival time of the charge transfer intermediates (CTIs) in the aggregated state could be attributed to the non-parallel arrangement of the D and A stacks and/or delocalization of the excitons across the segregated bi-continuous D-A stacks. The molecule being amphiphilic undergo self-assembly in $CHCl_3$ to form spherical aggregates that transform into thick torroidal

architectures by virtue of non-covalent interactions. The CTIs survive for > 1.2 ns in the aggregated state (τ_{cr}^{a}) when compared to the monomeric state (CH$_3$CN; $\tau_{cr}^{m} = 110\ fs$) as probed by femtosecond transient absorption spectroscopic investigations.

Multi-chromophoric arrays of organic molecules that self-assemble into ordered segregated D-A frameworks can ensure unrestricted charge transport across the symmetrical domains. The third chapter deals with C$_3$-symmetric D-A multicomponent redox gradient trefoils constituted from triphenylamine and naphthalimide. The trefoils undergo self-assembly in THF forming spherical/vesicular aggregates in contrast to monomer in ACN aided by weak non-covalent interactions. Long-lived CTIs surviving for 2.52 ns are probed in the aggregated state in comparison to ≤ 110 fs, in the monomeric state. Enhancement in the lifetime of CTIs by four orders in the aggregated state when compared to the monomeric state could be due to the delocalization of photogenerated excitons along non-planar twisted D-A domains.

Fourth chapter describes a colossal enhancement in the lifetime of the charge separated states in the self-assembled non-symmetric D-D-A triad composed of triphenylamine, anthracene and naphthalimide (TAN). Steric inhibition imposed by diisopropyl units of naphthalimide and propeller shaped triphenylamine enforces the D-D-A triad to possess antiparallel dimeric arrangement, via C-O••O-C and C-H••π interactions. Nanosecond and femtosecond transient absorption spectroscopic investigations in the monomeric and aggregated state validate persistence of CTIs by 10^8-fold in the aggregated state relative to the monomeric state. The observed long-lived charge separated lifetime of photogenerated excitons n the aggregated state could be a direct consequence of hoping of photogenerated excitons through naphthalimide domains and/or structural heterogeneity.

The organic photonic nanostructures capable of efficient light harvesting and storage detailed in the present thesis can provide new avenues for the design and construction of solution processable organic solar cells, photovoltaic devices and photofunctional materials.

Contents

List of Figures

List of Tables

List of Schemes

Chapter 1

Approaches to Reduce Rate of Charge Recombination Through Self-Assembly

1.1. Photosynthesis

Life on earth is preserved by means of "photosynthesis," a fundamental process involving the conversion of solar energy, the most abundant resource of energy we have at our disposal, into chemical energy by green plants and photosynthetic bacteria [1-4]. Natural photosynthesis involves a series of highly efficient electron/energy transfer cascades wherein the light energy trapped by the chromophore bound light harvesting complexes (LHCs) is funneled to the photosynthetic reaction center (RC) [5]. The unrivalled creation and designs of nature, which never ceases to amaze chemists by its complex and elegant supramolecular architectures inspired researchers to understand and mimic the structural and functional aspects of such superstructures. The pursuit to translate the rudimentary principles governing the organization of modular components in natural photosynthetic reaction center paved the pathway in constructing novel organic materials with specific functions (Figure 1.1.a).

Klaus Schulten *et. al.* through theoretical calculations [6] demonstrated that chromatophoric units (Figure 1.1.b) identified at the surface of RC, through their

curvature properties funnels the light energy towards center on a 10-100 ps timescale, enhancing photon-to-energy conversion. A series of electron transfer events associated with RC and therein converts water and carbon dioxide to oxygen and carbohydrates which serve as food and fuel for mankind. Capturing of sunlight by LHC and the subsequent electron transfer processes occurring in RC are governed by electronic coupling between the molecules. Electronic excited states thus produced in the RC are converted into separated charges via an array of sequential electron transfer processes and 'gear down' the ultrafast dynamics of light harvesting to relatively slow timescales [5, 7]. Organic materials which could be transformed into higher order superstructures via supramolecular organization can find potential application in mimicking natural photosynthesis, solution processable organic solar cells and photovoltaic devices [1-3].
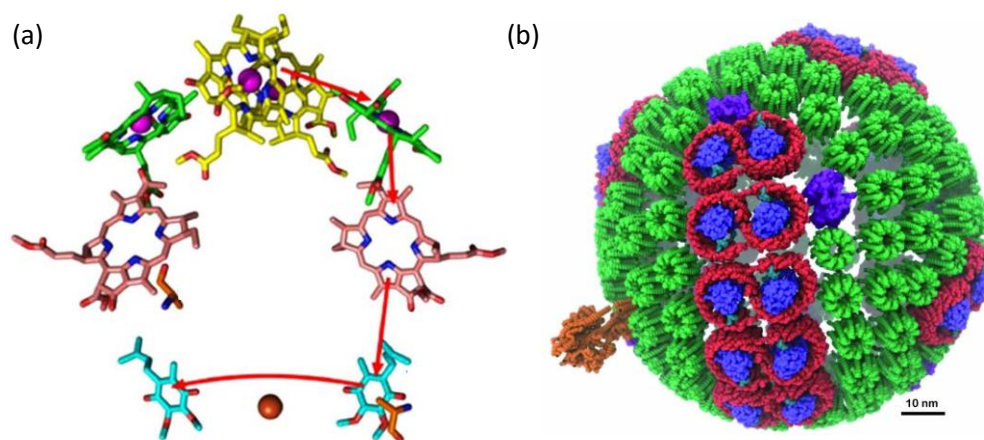
Figure 1.1. *Schematic representation of (a) modular components of natural photosynthetic reaction center and (b) chromatophoric unit found at the reaction center (adapted from the references 3 and 6 respectively).*

1.2. Energy source

Existing energy resources have been placed on a huge strain by economic acceleration, demographic explosion and technical evolution [8]. Complementing the scenario, modern lifestyles, industrialization and future technological revolution demand at least a 56% enhancement in the world energy consumption to in the next 30 years. However, the fossil fuels which are predominantly consumed to meet our current energy demands, apart from belonging to limited reserves is also a major contributor to global warming and climate issues [8]. One of the most comprehensive insurances for ensuring the quality of life in future could be to discover a novel, renewable, cheap and clean energy source [9]. In lieu of non-renewable energy resources, solar energy represents a renewable, economic and green alternative in the future energy market which can replenish at a rate much faster than the non-renewable resources are getting consumed. The solar power received on earth's surface is approximately 6.12×10^{20} J/h, which could cover the world's total energy consumption in a whole year (5.6×10^{20} J in the year of 2010). Solar cells with an efficiency of 10% covering 0.16% of land area could produce 20 TW energy with extremely low economic and environmental cost, which is approximately twice the energy produced by fossil fuel.

The implementation of solar fuel as energy source [9] is still not widespread, mainly due to the high costs and the low power conversion efficiency (PCE) [10]. The

commercially available silicon based photovoltaic cells are relatively expensive because of their calumniatory manufacturing and processing conditions. Consequently, the scientists and engineers are relentlessly in search of an efficient and inexpensive technology for the conversion of sunlight to electricity [10]. Organic photovoltaics (OPV), a young technology has encouraged scientists to continue their efforts toward new classes of solar cells due to their outstanding potentials in the cost-effective production along with unique properties such as prevalent material availability, low-temperature solution-processability, and roll-to-roll refinement. Ready availability of numerous carbon feedstocks [11] with flexible synthetic pathways, are attractive materials for solar applications. As global warming continues to be the most serious issue of the century, undoubtedly we have to find an alternative non-CO_2-releasing way to produce, transport, and store electricity [11]. However, critical requirements such as efficiency, lifetime, cost, clean and prospect (how far OPVs will go into the market) need to be addressed for the commercialization of OPVs.

1.3. Fundamental aspects of conventional organic photovoltaic devices

Solution processable organic heterojunction solar cells [12-14] have gained a lot of attention in recent years due to the higher values of efficiency being reported for OSCs [15]. Over the past 20 years after the first report on bilayer heterojunction cell from Tang and co-workers [16], PCE of heterojunction devices crept from an uncertified

value of 1% to slightly less than 5%. Following the pioneering report by Heeger, Brabec and co-workers in 1996 [17, 18], forecasting the significance of bulk heterojunction solar cells, wherein 10% enhancement in energy conversion efficiency is achieved [10], efficiency values have surged with Solarmer and Heliatek demonstrating organic photovoltaic cells with efficiencies exceeding the 8% barrier [19, 20].

A solar cell device converts solar photons into electrons followed by electrical energy (Figure 1.2.). The light to energy conversion [10] process involves the following sub-processes [20], (i) solar photon absorption and exciton generation, (ii) exciton diffusion and subsequent separation at the donor-acceptor interface, (iii) mobile electron and hole transport and (iv) mobile charge collection and (v) electrical power output. An organic heterojunction solar cell (OSCs) [21] typically consists of a thin photoactive organic layer sandwiched between a high work function anode, typically a transparent indium tin oxide (ITO) layer or fluorine doped tin oxide (FTO), and a relatively low work function metal cathode such as Aluminium (Al)/Calcium (Ca)/ Barium (Ba).The thin photoactive layer in OSCs is composed of two light-absorbing organic semiconductors, one with an electron-donating character (donor) and the other with an electron-accepting character (acceptor). These semiconductors could either be deposited as two distinct layers where the donor–acceptor interface resides only between the two layers (bilayer), or be blended as an almost homogeneous mix where

interfacial interaction between donor and acceptor exists throughout the blended bulk layer, otherwise termed as bulk heterojunctions).

When incident photons are absorbed by the photoactive layer [20, 21], electrons belonging to the donor and acceptor entities get excited. Electrons from HOMO (highest occupied molecular orbital) of the donor (D) jump to the LUMO (lowest unoccupied molecular orbital) of the acceptor (A), forming geminate pairs (excitons) in which the electron–hole pairs are bound together through electrostatic attraction [21]. The excitons diffuse within the active layer, and may recombine back to their ground state through destructive geminate charge recombination beyond the lifetime of the exciton. Alternatively, if the exciton reaches a D–A interface within the exciton's lifetime, electrons can transfer from the LUMO of D to that of the A and holes can transfer from the HOMO of the A to that of the D. In this state, the electron and hole on the A and D
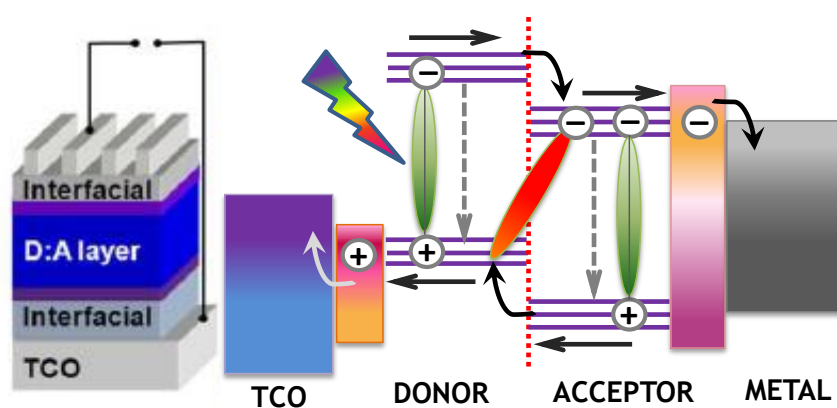
Figure 1.2. *Schematic representation of conventional organic photovoltaic device architecture (adapted from the reference 21).*

respectively, remain Coulombically bound, forming a germinate D^{+}/A^{-} pair [21]. The electron–hole pair can naturally undergo germinate recombination to return to the ground state, but with the assistance of the built-in electric field that exists between the two electrodes of differing work functions, the electron–hole pair can also dissociate into free hole/ electron charges which then move in opposite directions and gets collected at the respective electrodes to drive the external circuit [21].

Solar photons are captured by the photoactive layer and subsequently separated at the donor-acceptor interface due to the differences in the D and A LUMO ($E_{LUMO,D-A}$ = $E_{LUMO,D}$ − $E_{LUMO,A}$) and HOMO energies ($E_{HOMO,D-A}$ = $E_{HOMO,D}$ − $E_{HOMO,A}$). In general, the difference between $E_{LUMO,D-A}$ and $E_{HOMO,D-A}$ should be greater than 0.3 eV for efficient exciton separation [21]. The energy difference (E_{D-A}) between the acceptor LUMO ($E_{LUMO,A}$) and donor HOMO ($E_{HOMO,D}$) is related to the open-circuit voltage (V_{oc}) via the following empirical relationship: V_{oc} = (E_{D-A} − E_0)/q, where E_0 is an empirical factor with a typical value of 0.3–0.4 eV, and q is the electron charge (-1.602×10^{-19} C). Furthermore, recent studies found that experimental V_{oc} values can be linearly correlated to the energy level of the charge transfer state (CT state) generated at the D-A interface [21]. As observed for many donor-acceptor systems, a higher acceptor LUMO energy (acceptors having high electron affinity) and lower donor HOMO energy (donors having low ionization energy) generally lead to a higher V_{oc} [21].

The hetero-junctions (HJs) [22, 23] in the active layer of organic photovoltaics are termed as "transport highways" [24] which drives the charge carriers to the respective electrodes. Wise design and organization at the molecular level is vital in accomplishing nanoscopic dimensions of the HJs in OSCs dictating the fate of photo-generated excitons[25]. An elegant approach to address this thorny issue is to design interpenetrating donor (D) - acceptor (A) networks at the HJs which could self-assemble/self-sort into various novel architectures. Alternatively, taking cue from nature emergence-on-self-assembly approach has been adapted to mimic natural photosynthetic reaction center wherein molecules act in concert. Nevertheless, molecular ordering relies on interplay between various inter/intra molecular interactions such as multi-pole electrostatic interactions, dispersion and inductive effects, $\pi-\pi$ interactions, hydrogen bonding etc. thermodynamically and kinetically control the aggregation and donor-to-acceptor phase segregation behaviors of organic semiconducting molecules [25]. It is observed that increasing the solid-state order of the donor and acceptor domains can significantly reduce the geminate charge recombination. The reduction in the geminate losses might result from the fact that the local crystallinity of the electron acceptor domains can promote the delocalization of the geminate electron-hole pair states, thereby facilitating charge dissociation at the D-A interface [21, 25].

Moreover, it is found that normal and inverted cell structures have different solar cell performances, partially due to the vertical phase separation of the blended D-A materials. Studies on such device architectures concluded that breaking the co-planarity of the conjugated backbone can improve the solution processability of organic molecules with a large π system [21]. Also, the twisted conformation can reduce aggregation, thereby reducing excimer formation leading to nanoscale domain formation, facilitating exciton dissociation. Orthogonal arrangement of D and A scaffolds through a single covalent bond can attenuate orbital overlap of the D-A atomic orbitals assisting photo-generated excitons to sustain for longer times [21]. However, organic molecules with twisted conformations are less likely to form compact, long-range π-π stacks than planar organic molecules. Therefore, newly designed molecules with twisted π systems can create charge transport pathways possessing favorable π-π stacks for efficient charge-dissociation, transport and trapping [21]. Top-down approaches [26] to improve the molecular organization, and thus the conductivity exploit the use of differential solubilizers [15], dendritic polymers, covalent dyad systems and mixed crystals [23].

In biological photosystems, excitation of the "special pair" of chlorophylls is followed by directional, ultrafast electron transfer cascade along sophisticated redox gradients to the remote ubiquinone acceptor [24, 27-29]. The hole left behind is transferred in the other direction along orthogonal redox gradient ultimately oxidizing

water [30]. These cascade electron/hole transfer pathways are essential for the efficiency of photosynthesis, and are held together in antiparallel manner by a large protein bilayer membrane [24]. Increasing organization of BHJs ultimately leads to a situation wherein hole (h^+) and electron (e^-) transporting channels are separated and aligned at the molecular level otherwise termed as supramolecular n/p-heterojunctions (SHJs) [24]. The bottom-up nature of this approach allows the rational design of ordered and oriented nanostructures to achieve high conductivity and to impart structural complexity in the system.

The funneling of electronically complementary holes and electrons through antiparallel hole and electron transporting π-columnar conduits is termed as oriented multicolored antiparallel redox gradients (OMARG-SHJ), as coined by Prof. Stefan Matile [24]. The discussion of oriented SHJs on surfaces began with selected examples like the ''fuzzy'' architectures obtained from layer-by-layer (LBL) assembly. Oriented SHJs on solid grounds could also be installed through interdigitating inter- and intra-layer recognition motifs in LBL architectures [24]. Modulating photo-generated excitons in crowded environments is crucial in the development of photo-functional materials such as organic light emitting diodes and photovoltaic devices [31].

1.4. Charge transfer (CT) interactions

Benesi and Hildebrand [32] seven decades ago published their seminal investigations describing the unique UV-Vis spectral changes accompanying the spontaneous complexation of various aromatic hydrocarbons (ArH) with iodine in nonpolar solvents such as CCl_4, C_6H_{14}, etc. Later, Keefer and Andrews [33] while extending such spectroscopic studies predicted the formation of 1:1 inter-molecular complexes from the values of the thermodynamic equilibrium constants K_{CT}. Immediately following the Benesi–Hildebrand report, Mulliken published another landmark paper in 1950 [34, 35], in which he assigned the observed new spectral features to the unusual electronic transition from the ground-state complex [D, A] to the dative excited state $[D^{.+}, A^{.-}]$ where D is the generic representation of electron donors and A represents the electron acceptors [35]. The most important characteristic of the ground state charge transfer (CT) interaction is the retention of covalent character of the system along with presence of ionic character as a result of partial charge separation in the system owing to electronic complementarity between the constituents [35]. One of
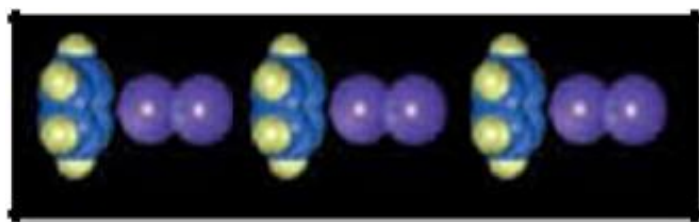
Figure 1.3. *π– σ^* charge transfer complex formed between benzene and iodine in the ground state (adapted from the reference 34).*

the elegant examples of the ground state CT is observed in benzene-iodine charge transfer complex, where benzene donates its electron to the σ^* orbital of iodine thereby forming π– σ^* CT complex as shown in Figure 1.3. [34].

The design of the donor acceptor molecules with complementary electronic distribution is also important in the operation of the CT interactions. Usually, aromatic cores functionalized with electron donating groups serve as better donors, whilst incorporation of the electron withdrawing groups reduce the electron density considerably, enhancing the acceptor character [34, 35]. These molecules can stack one over the other to form CT complexes having alternating, inter-digitating arrangement [25]. A schematic representation of D-A interaction existing in such arrangement is depicted in Figure 1.4.

When a donor (D) having very low ionization potential is in close proximity with an acceptor (A) possessing high electron affinity, due to complementary nature of electron density distributions between the two entities, there will be a re-distribution of electronic cloud or transfer of charge from the former (D) to the latter (A) giving rise to charge transfer (CT) complex [21, 25]. The CT interactions existing in such D-A pair can operate either in the ground state or in the excited state of the CT complex. As electronically complementary D and A are involved in CT interactions, such interactions are otherwise designated as electron donor-acceptor (EDA) interactions. According to Valence bond theory proposed by Mulliken et al., the CT interactions in
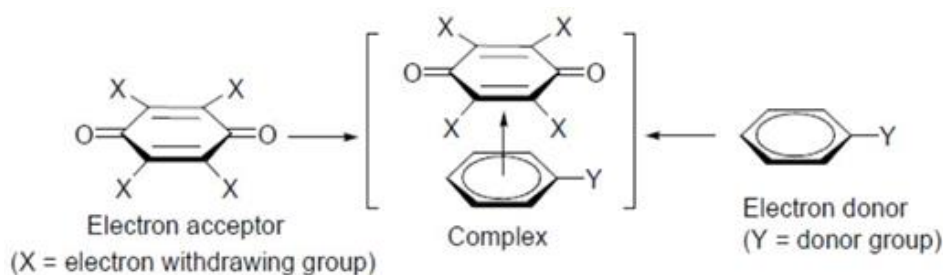
Figure 1.4. *Schematic representation of D-A interaction existing in aromatic cores*

functionalized with complementary electronic distribution (adapted from the reference 25).

the ground/excited state occur as a result of orbital mixing of the respective orbitals [35,

36]. The HOMO of D mixes with the HOMO of the A to generate bonding and

antibonding HOMO of the D-A pair and the electrons present in the parent HOMO's of

D and A gets evenly distributed in orbitals of D-A and the latter (antibonding HOMO of

D-A) acts as the HOMO of the D-A pair. Similarly, lowest unoccupied molecular

orbitals (LUMO) of D and A mixes to form bonding and antibonding LUMO's of D-A

pair, wherein former (bonding LUMO of D-A) features as the LUMO of the D-A pair.

The energy difference between LUMO and HOMO of D-A pair is termed as the energy

gap of D-A pair. Thus in general one can emphasize that HOMO of D and LUMO of A

units are largely responsible for the location of Frontier orbitals in the D-A system [34].

Tuning of energy gap in D-A system is achieved by altering the HOMO and

LUMO levels of D and A respectively which in turn dictate the light absorbing

characteristics of the material. Appearance of an additional band in the absorption

spectrum distinct from the constituents signifies EDA interactions operating in the ground state [34]. Generally absorption spectra of CT complexes are broad and devoid of vibrational structure due to the small binding energies of the interactions. Many structural configurations possible for the complex can cause them to exist in equilibrium with each other resulting in the broadening of CT band [37]. An important characteristic of an EDA absorption band is the sensitivity towards solvent polarity. Due to the stabilization of the D-A pair through the CT interactions in highly polar solvents such as methanol, DMSO etc. a bathochromic shift in the absorption and emission maxima are observed [37, 38] which could be attributed to the solvent
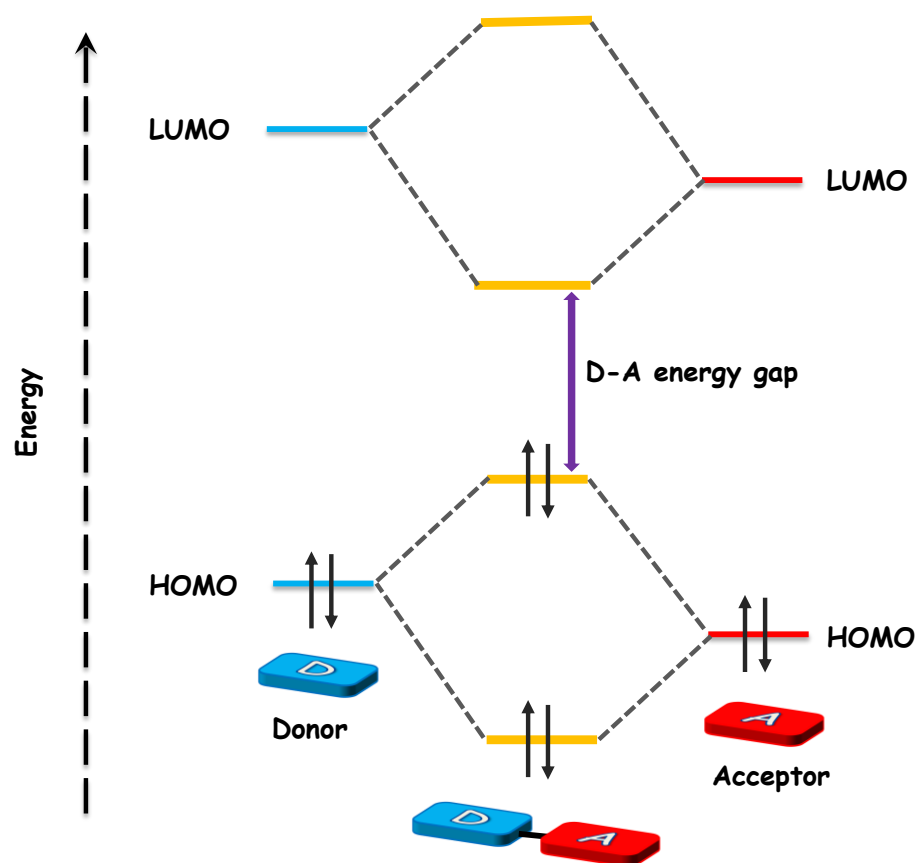
Figure 1.5. *Molecular energy level diagram describing CT interactions observed in D-A pair.*

assisted mixing of the wave-functions for the states involved in the EDA interactions [38]. An energy level diagram depicting EDA interaction in a D-A pair is illustrated in Figure 1.5.

1.5. Photoinduced electron and hole transfer

The photoinduced electron transfer (PET) process plays vital role in natural and artificial photosynthesis, bio-molecular sensing and photo-voltaic devices [7, 39]. Photoexcitation enhances the electron or hole transfer properties of the molecules, which are other ways not possible through ground state electron transfer processes. Electron transfer processes can operate through two possible mechanisms namely photoinduced electron and hole transfer both of which require a compatible A in close proximity to the D moiety. In photoinduced electron transfer an electron is transferred from the D excited state (LUMO) to the empty, lower energetic LUMO of the nearby A
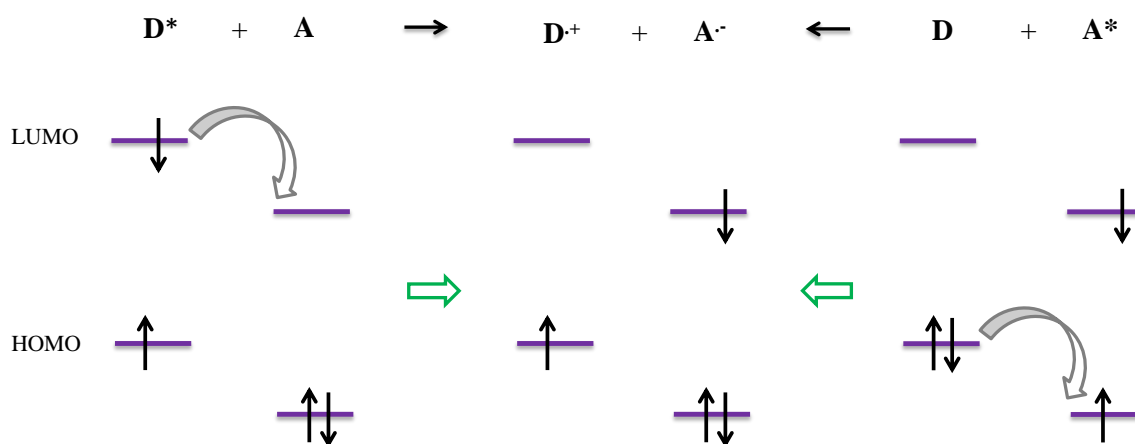
Figure 1.6. *Scheme representing photo-induced electron (left side) and hole (right side) electron transfer (adapted from the reference 39).*

unit creating a charge separated state with a positively charged D and negatively charged A. In the photoinduced hole transfer, HOMO of the A in the excited state abstract an electron from the HOMO of the D thereby creating similar charge separated state as in the case of photoinduced electron transfer. Both the electron transfer mechanisms can be followed by back electron transfer, after which both D and A will be returned to the ground state. The high energy charge separated state lead to various types of photochemistry, which can be useful for various photochemical reactions and long-lived charge separated intermediates for n- and p-type semiconducting solar cells. The electron transfer across the interface can happen through a static binding process by the formation of an encounter complex or by collisional pathways (Figure 1.6.).

The energy change for a PET is given by the Rehm Weller equation [40, 41]

$$\Delta G^0 = E_{ox}(D) - E_{red}(A) - E_{00} + e^2 \big/ \varepsilon_s d_{cc}$$

where, $E_{ox}(D)$ represents the oxidation potential of the donor, $E_{red}(A)$ is the reduction potential of the acceptor, E_{00} is the zero–zero excitation energy (smallest bandgap in the system), e is the electronic charge, ε_σ is the dielectric constant of the solvent under consideration and d_{cc} is the center to center distance between the donor and acceptor. Factors affecting the energetics of electron transfer and theories governing the thermodynamics and kinetics of these processes (Marcus theory) are well documented and hence not elaborated.

The discovery of metallic electrical conductivity in molecular-based materials has led to the development of new fields of research such as room temperature conductivity, high temperature superconductivity etc [42]. Well-known examples include iodine doping of polyacetylene [43] which paved path for the emergence of polymer electronics [44, 45], alkali intercalation of the fullerenes [46, 47] and the development of charge-transfer salts [48]. All these properties has been confined to bulk compounds while the realization of metallic conductivity [49] at the surface of molecular-based materials received less success and attention The electronic properties of interfaces [50] between two different solids [51] can differ strikingly from those of the parent constituent materials [50]. Highly conducting interfaces [42] with resistivity ranging from 1 to 30 kΩ per square. The observed electrical conduction originates from a large transfer of charge between the two crystals that takes place at the interface, on a molecular scale [42].

As the interface assembly process is simple and can be applied to crystals of virtually any conjugated molecule, the conducting interfaces described by tetrathiafulvalene (TTF) and 7,7,8,8-tetracyanoquinodimethane (TCNQ) represent the first examples of a new class of electronic systems [52]. TTF and TCNQ forms the first charge transfer complex discovered in 1973 wherein the constituent units are arranged in quasi one-dimensional linear chains [42], in contrast to the herringbone arrangement observed in the constituents (Figure 1.7.). Electrons in the HOMO of TTF are transferred
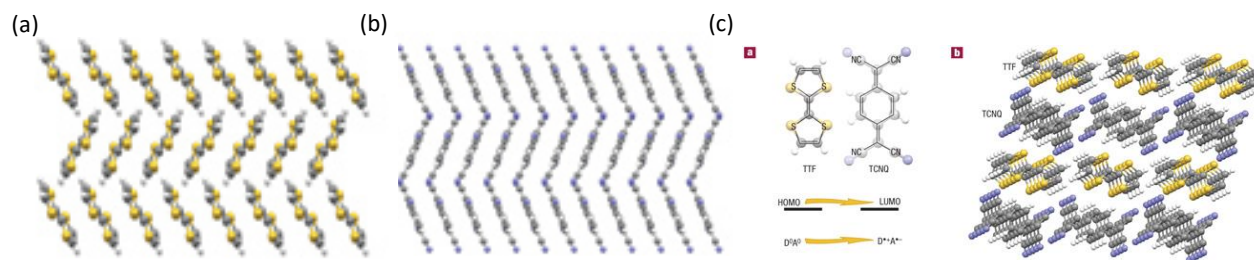
Figure 1.7. S*olid state herringbone arrangement observed in (a), tetrathiafulvalene [TTF], (b)*

7,7,8,8-tetracyanoquinodimethane (TCNQ) and (c) a quasi-one dimensional chain like

arrangement of the TTF and TCNQ charge transfer complex (adapted from the reference 42).

to the LUMO of TCNQ, with virtually no hybridization between the molecular levels.

As a result, the TTF and TCNQ chains behave as decoupled one dimensional electronic

system, and at room temperature the material is highly conducting [42].

Material properties of D-A CT complexes are dictated by many factors such as

crystal structure, precise spatial organization and relative orientation of the D and A

subunits (Figure 1.8.) [25]. Governed by the complementary electrostatic and aromatic

π-π interactions between the redox gradients, D-A complexes can adopt segregated

(Figures 1.8.a,b,d) and/or interdigitating, mixed (Figures 1.8.c,e,f) stacking

arrangements [25]. Examples of interdigitating stacking arrangement (-A–D–A–D-)

include CT complexes of anthracene–pyromellitic dianhydride,

dibenzotetrathiafulvalene-TCNQ, pyrene–TCNQ, and perylene–TCNQ [25]. The

segregated-stacking arrangement arising as a result of π-stacking of D and A subunits

separately as represented by A–A–A–A and D–D–D–D and/or D-on-D and A-on-A

arrangement is observed in CT salt of TTF–TCNQ and HBC appended with PMI or PDI [25]. Random organization of D and A moieties results in mixed D-A arrangement as illustrated in P3HT polymer films blended with fullerenes usually observed in the heterojunctions of BHJ-OSCs. Surprisingly, the CT complexes formed from tetramethyltetraselenafulvalene (TMTSF) and TCNQ, crystallizes both in segregated-stacked and mixed-stack arrangements displaying metallic and semiconducting properties respectively [25].

Though each type of stacking geometry shows some general trends in properties segregated stacking is necessity for room temperature metallic conductivity. Further studies need to be devoted to elucidate specific relationships between the structure of the crystal and the electronic function. The degree of tilt between the donor–acceptor
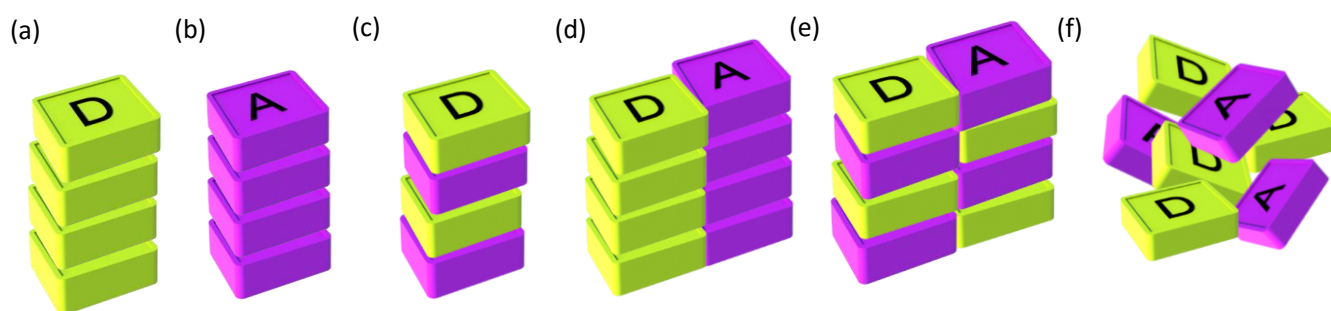
Figure 1.8. *Packing arrangement observed in segregated (a) donor, (b) acceptor stacks. (c) interdigitating arrangement of D and A units. (d) segregated D-on-D and A-on-A, (e) alternate D-on-A and A-on-D and (f) random/dispersed D-A arrangement observed in various motifs (adapted from the reference 25).*

pairs with respect to the stacking axis can be correlated to both the degree of charge transfer and the conductivity of the sample [25]. The overlap between the molecular orbitals of the charge-donating and charge accepting moieties of the parent compounds can be associated with the degree of charge transfer between donor and acceptor pairs as suggested by Herbstein [25]. CT complexes with complex D:A ratios, such as 2 : 1, 3 : 1, and 3 : 2, are less prominent to promote charge transport. In these cases, extra donor or acceptor molecules have been shown to exist either within the stack thereby participating in the charge transfer process, or lie within the interstitial space between the stacks. For example, perylene–TCNQ D-A CT complex, which exhibit 2:1 ratio show that an additional perylene molecule located perpendicular and between the stacks; does not participate in the charge transfer [25]. Hence a detailed understanding of aromatic stacking interactions is necessary to examine the nature and various intermolecular interactions responsible for precise spatial organization of modular components.

1.6. Models proposed for describing aromatic stacking interactions

1.6.1. Polar/π model

In 1990s, Hunter and Sanders proposed a model to predict the aromatic stacking geometry that emphasizes on the overall polarization of the aromatic π-electron cloud [53]. The model partitions electron-rich π-cloud of aromatic molecules from the σ-

framework. According to this model, the partially positively-charged σ-framework around the periphery of the molecule is "sandwiched" between two partially negatively-charged π-electron clouds, envisaging the existence of a quadrupole moment in the system, when visualized from a side-on perspective. The term "polar/π" model was coined by Cozzi and Siegel [54]. Conducting a series of experiments on 1,8-diarylnaphthalene system, they established that interaction of aromatic molecules can be predicted in terms of the polarization of π-electron density (Figure 1.9.). The approaches put forth by (i) Cozzi and Siegel [54] and (ii) Hunter– Sanders could offer [53] an explanation for the general tendency of neutral, non-substituted polyaromatic
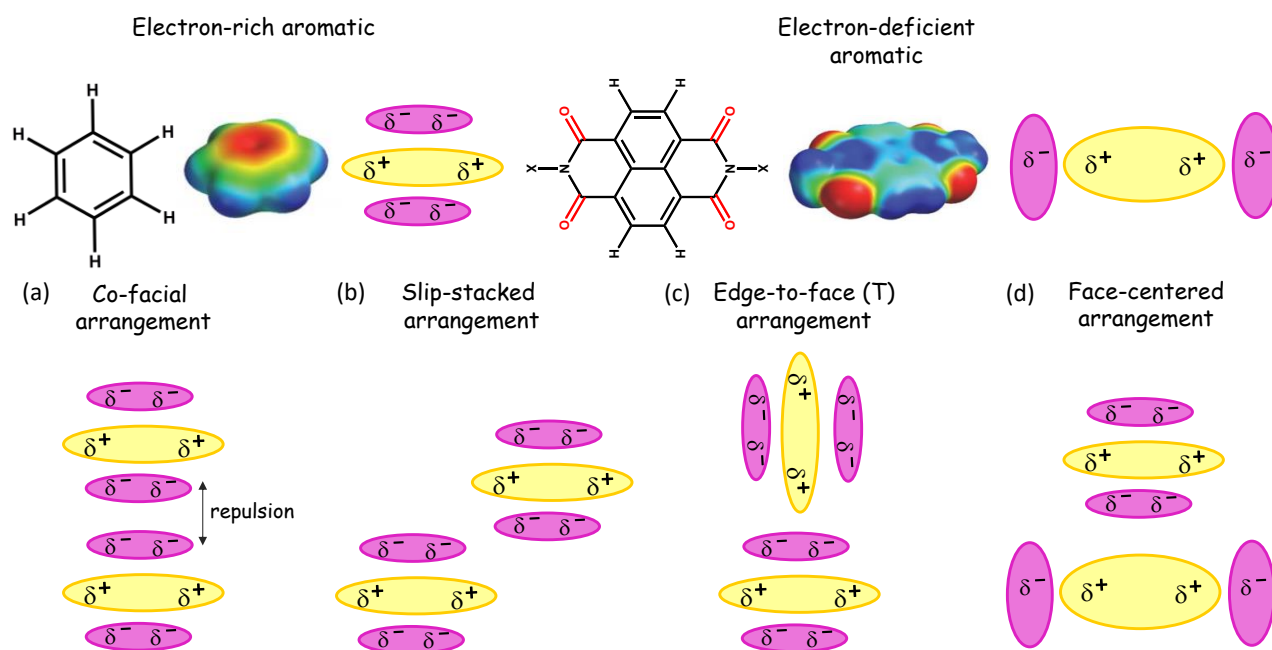
Figure 1.9. *Plausible interactions observed between electron-rich and electron-deficient aromatics (adapted from the reference 58).*

hydrocarbons to interact with each other in a T-shaped, or ''herringbone'' geometry or possibly an off-set (slip) stacked geometry rather than a face-centered (co-facial) stacked geometry. The partially negatively-charged π-electron clouds are presumed to repel each other, resulting in disruption of face-centered (co-facial) arrangement in most of the aromatic units [55].

The polar/π model also predicts that when strongly electron-withdrawing functional groups are placed on the periphery of an aromatic molecule, the π-electron cloud can be polarized such that the quadrupole moment is reversed, generating an electron-deficient aromatic core surrounded by a partially negatively-charged periphery [55]. Reversal in polarization of the aromatic core is often used to explain why aromatics with strongly electron-withdrawing substituents at the core prefer to stack in an alternating face-centered arrangement when associated with relatively electron-rich units, as exemplified in solid-state complex of benzene with hexafluorobenzene [55].

1.6.2. Local, direct interaction model

An alternative model to demonstrate the aromatic stacking interactions existing in substituted aromatic molecules was proposed by Rashkin and Waters from their seminal experimental work [56]. Rashkin and Waters [56] predicted that orientation of stacks constituted from substituted aromatic molecules plays pivotal role in the magnitude of observed interactions between aromatic units (Figure 1.9.). Direct

through-space electrostatic interactions of polarized substituents around the periphery of the aromatic core provide a stabilizing effect. Wheeler and Houk [57] from the calculated interaction energies between substituted benzene dimers, examined the direct complementary interactions between the substituents of aromatic units and concluded that the interaction energy provide a driving force for stacking interactions. The resulting trends in interaction energies indicated that no significant additional stabilizing energy was afforded by the aromatic core of the substituted benzene relative to the H–X analogue, even when the substituents (X) demonstrated similar trends in interaction energies. This led to the conclusion that ''substituent effects in the sandwich configuration of the benzene dimer do not involve the π-system of the substituted benzene''. This observation was in agreement with experimental work by Houk et al. [57] and computational work by Wheeler to develop a refined model for predicting the interaction of substituted aromatic units. Besides, ''local, direct interaction'' model, administers that the local, direct through-space electrostatic attraction/repulsion between highly polarized substituents around the periphery of aromatic units is the dominant factor in determining the stacking geometry of aromatics.

Iverson and co-workers [58] ascertained the existence of aromatic interactions in naphthyl units functionalized with electronically complementary subunits (DAN- 1, 5-dialkoxynaphthalene and NDI- 1,4,5,8-naphthalenetetracarboxylic acid diimide). Specific non-covalent interactions existing between aromatic core of DAN and NDI

assist the construction of foldameric assemblies in aqueous environments (Figure 1.10.) [58]. The electrostatic potential surface maps of these two molecules reveal that the polarization of aromatic core and substituents is derived from the electron-donating alkoxy groups in DAN and electron withdrawing imide carbonyl groups in NDI, respectively. Replacement of dialkoxy substituent with flexible hydrophilic amino acid residues resulted in pleated structures leading to the formation of alternating face-centered (co- facial) stacks of D and A entities termed as aedamers. Face-centered stacking is predicted by either the ''polar/π'' or ''local, direct interaction'' models [59]. π-orbital mixing introduced by the face centered geometry results in a bathochromic charge-transfer absorption band, characteristic of red-purple color once the colorless solutions of DAN and NDI are mixed. According to Martinez and Iverson [59], for
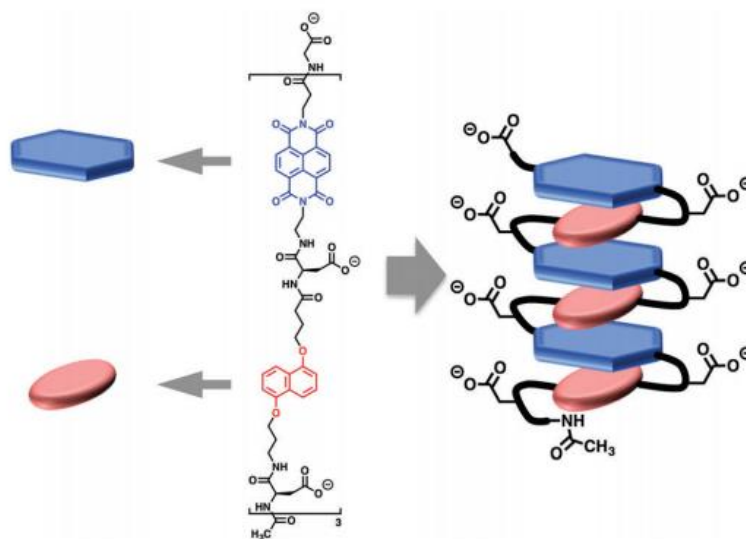
Figure 1.10. *Schematic illustration of alternating D-A stack observed in aedamers (adapted from the reference 58).*

aromatic units, stacking is a geometry, not a particular interaction and these terms do not have meaning while discussing energetically important interactions despite their common use in the literature. Dispersion interactions does contribute to the stability of stacked aromatic molecules, moreover, is the dominant stabilizing contribution to the interaction energy for the benzene dimer in certain configurations suggesting that aromaticity in monomeric units is not a requirement for the stacked geometry [59].

1.7. Non-covalent interactions
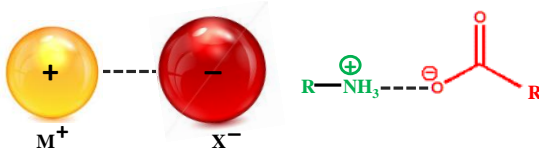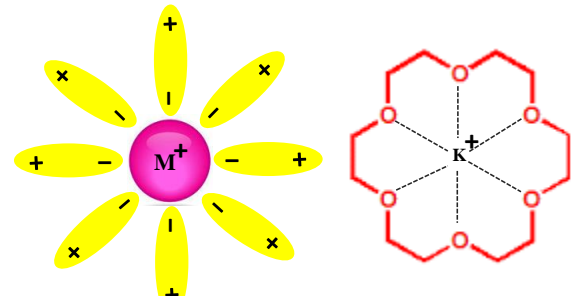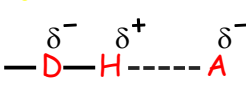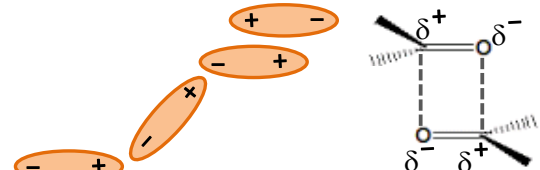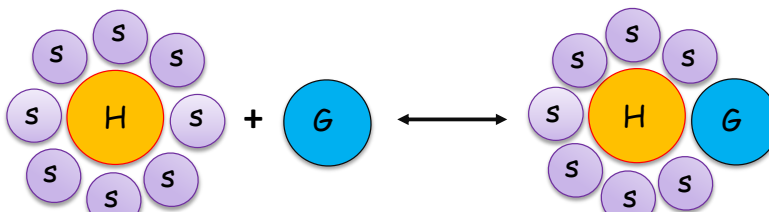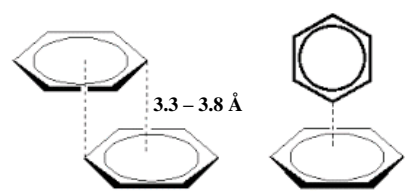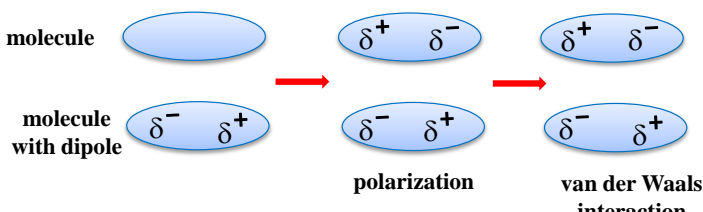
Molecular interactions [60] individually seem weaker with enthalpy change of 1-10 kcal/mol, lower limit of the order of RT and an upper limit significantly lesser than that of a covalent bond. Even though they are weak individually, cumulatively the energies of molecular interactions are significant. Covalent interaction holds atoms together within molecules. Covalent bonds are strong, with enthalpies of the order of 100 kcal/mole (400 kJ/mol) [60]. Covalent bonds break during chemical reactions and remain intact when ice melts, water boils, proteins unfold, RNA unfolds, DNA strands separate and when membranes disassemble. Whereas when two aromatic molecules interact with each other in close proximity they do so non-covalently resulting in slip-stacked, T-shaped or face-centered (co-facial) stacking arrangement [60]. Usually, non-covalent interactions originating as a result of intricate array of mutually competing and interacting hydrogen bonding, ionic, electrostatic, van der Waals, solvophobicity and

charge transfer interactions constitutes more thermodynamically favorable association, resulting in folding and assembly of biochemically useful structures [60].

Non-covalent interactions are strongly dependent on the electron density distributions of the counterparts [60]. Non-covalent inter- and intra-molecular interactions arising from different combinations of monomeric units along an oligomer or polymer chain form complex and sophisticated higher order molecular architectures such as the DNA double-helix, secondary, tertiary and quaternary protein structures. How these non-covalent interactions work together to form such complex and highly ordered architectures is of particular interest for organic chemists and biochemists who desire to improve, mimic, or manipulate natural biological systems.

One of the finest aspects of supramolecular chemistry [61] is the ability to employ noncovalent interactions acting in concert, for modulating self-assembly of functional building blocks to impart emergent properties. Noncovalent interactions can be constituted by attractive or repulsive intermolecular forces, with interaction energies ranging from 4-400 kJ/mol as stated in Table 1.1 [61]. The decreasing strength of non-covalent interactions follow the order (a) electrostatic interactions (ion-ion, ion-dipole and dipole-dipole interactions) (b) hydrogen bonding (c) π-π stacking (d) solvent effects and (e) van der Waals interactions [62]. Ion-ion, ion-dipole and dipole-dipole interactions are basically electrostatic (Coulombic) interactions, arising due to the

Table 1.1. Schematic representation of various non-covalent interactions.

Entry	Interaction	Energy (kJ/mol)	Illustration
1	Ion-ion	50-400	
2	Ion-dipole	50-200	
3	Hydrogen bond	4-120	
4	Dipole-dipole	4-40	
5	Solvent effects	4-40	
6	π-π stacking	4-20	
7	van der Waal forces	< 5	

delocalization of charges [63]. Ion-ion interactions are the strongest non-covalent interaction, having strength comparable to the covalent bonds and result from the attraction between opposite charges. The binding of an ion, such as Na^+, with a polar molecule, such as water, due to the attraction of oxygen lone pairs to the cation is a well-known example of ion-dipole interactions. Another typical example is the binding of cations to crown ethers [62].

Alignment of adjacent dipoles in the opposite direction leads to the electrostatic attraction between the opposite poles [62]. A hydrogen bond (H-bond), D-H…A, is formed between a hydrogen atom attached to an electronegative donor atom (D and a neighboring acceptor atom with lone pair of electrons (A). The directionality, specificity and tunability of the H-bonds make them favorite glue to stick molecules. Weak electrostatic interactions operating between aromatic rings are termed as π-π stacking interactions. There are two general types of π-π stacking interactions (i) face-to-face (co-facial, slip-stacked) and edge-to-face (T-shaped). Stacking of nucleobases to stabilize the DNA double helical arrangement is an example of one such interaction co-facial interactions [63].

Hydrophilic and hydrophobic interactions [62] between solute and solvent molecules constitute solvent effects in supramolecular chemistry. Hydrophobic interactions tend to exclude large solvent molecules from the proximity of the weakly

solvated solutes in polar solvents, particularly from water [63]. This in turn leads to an attraction between organic molecules and play a crucial role in the binding of organic guest molecules to cyclodextrin or cyclophane host systems in water. Hydrophilic interactions are the attractive interactions between water and organic molecules. van der Waals interactions arise from the temporary polarization of an electron cloud by the proximity of an adjacent nucleus, resulting in a weak electrostatic interaction [63]. They are usually non-directional and can be of attractive or repulsive in nature. Despite the fragile nature of non-covalent interactions, the cooperative action of several such interactions may lead to thermodynamically and kinetically stable supramolecular assemblies under various conditions [63]. The reversibility of such non-covalent interactions will allow self-sorting, self-correction and self-healing during the organization process leading to well-defined supramolecular architectures. The term 'non-covalent synthesis' refers to the use of non-covalent interactions to design reversible and complex macromolecular structures [63].

1.8. Approaches to reduce rate of charge recombination

1.8.1. Self-assembled D-A dyad conjugates

Investigation of charge-separation mechanism in OPVs is necessary for developing strategies to design devices with high efficiency. Photo-generated hole and electrons are still subject to their mutual Coulomb interaction and can self-trap at the heterojunction, giving rise to charge transfer (CT) excitons. By tracking the modulation

of the optical absorption arising from the electric field generated between the charges, R.H. Friend and coworkers [64] evaluated electrostatic energy arising from electron-hole separation in disordered OPVs, composed of [(poly[N-11"–henicosanyl-2,7-carbazolealt-5,5-(40,70-di-2-thienyl-20,10,30-benzothiadiazole)] as donor with $PC_{61}BM$ (phenyl-C_{61}-butyricacid methyl ester), as acceptor (Figure 1.11.). It was estimated that within 40 fs of excitation, corresponding to a charge separation (CS) distance of 4 nm, electrostatic energy arising from electron-hole separation is of the order of ~200 meV. At this separation (4 nm), the residual Coulomb attraction between charges is at or below thermal energies, so that electron and hole separate freely. Coulomb barrier for CS is surmounted at 40 fs, suggesting that rapid charge motion away from the interface
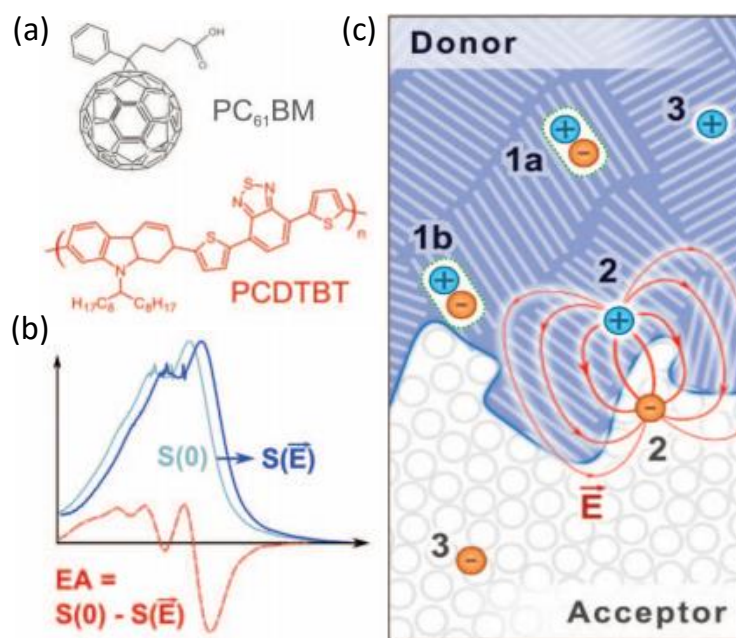
Figure 1.11. *Disordered D-A arrangement of PCDTBT and PC₆₁BM in PMMA matrix (adapted from the reference 64).*

through delocalized band states is necessary for long-range charge seperation.

Aida and coworkers [65] perceived that heterojunctions constituted by electron D and A entities at a macroscopic level allows the conversion of light energy into electrical energy. If one can elaborate a nanoobject composed of molecularly conjugated domains of such a redox couple, the resultant material is expected to serve as a nanoscopic energy converter. With this intention, Aida and coworkers demonstrated the formation of nanotubes or microfibers possessing distinct photochemical properties via controlled self-assembly of a trinitrofluorenone-appended gemini-shaped amphiphilic hexabenzocoronene (HBC). Gemini-shaped amphiphilic HBCs can self-assemble to form well-defined nanotubular objects, whose walls consist of a graphitic layer of π-stacked HBC with their inner and outer surfaces covered by hydrophilic triethylene glycol (TEG) chains (Figure 1.12.). Doping of HBC with oxidants, HBC graphitic nanotubes become electrically conductive. Aida and his coworkers prepared HBC-TNF conjugates, which bear an electron accepting 4, 5, 7-trinitro-9-fluorenone (TNF) functionality at the terminus of TEG chains.

HBC-TNF was synthesized by oxidative cyclization of hexaphenylbenzene precursors with $FeCl_3$ in CH_2Cl_2/ $MeNO_2$ [65]. Investigation of HOMO and LUMO energy levels of HBC and TNF respectively by means of square wave voltammetry established that, photoinduced electron transfer (PET) is energetically feasible between
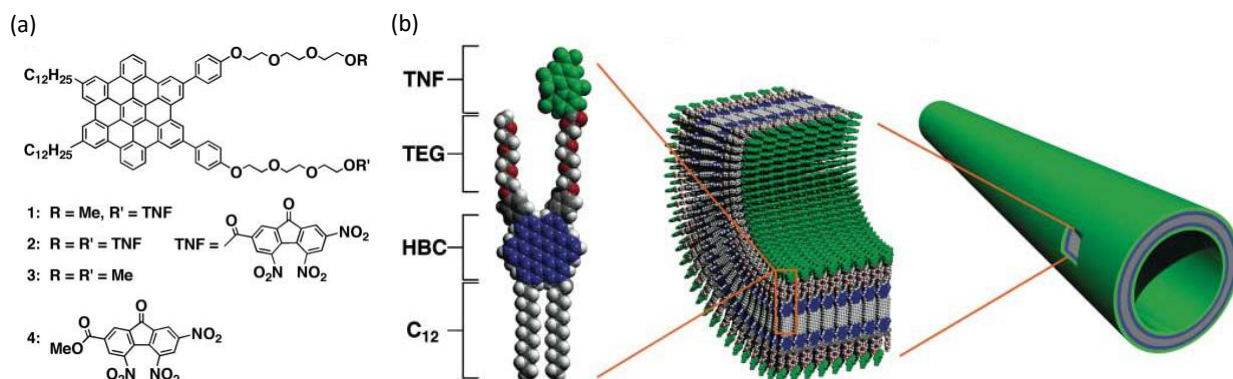
Figure 1.12. *Co-axial D-A nanotubular arrangement of HBC and TNF (adapted from the reference 65).*

HBC and TNF functionalities. A molecular layer of electron-accepting TNF laminates an electron-donating graphitic layer of π-stacked HBC generating nanotubes, which are of 16 nm in diameter and several micrometers long. HBC-TNF in tetrahydrofuran (THF) was colored brown, indicating a CT interaction between HBC and TNF. Coaxial nanotubular architecture thus generated allows photochemical generation of spatially separated charge carriers and a quick photoconductive response with a large on/off ratio greater than 10^4 that is difficult to attain with other carbon-based materials. Molecularly engineered photoconductive materials with tubular morphology are unusual and join the few examples of photoconductive nanostructured assemblies that have electrical conduction. Meanwhile, the microfibers formed as a result of CT interaction between the HBC and TNF parts exhibiting almost no photocurrent generation [65].

Widely studied D-A molecular architectures which find uses in OSCs so-called bulk heterojunctions are formed coincidentally from D/A mixtures upon phase separation. One of the fundamental challenge existing would be to tailor a linear organic heterojunction at the nanoscale joining dissimilar semiconducting one-dimensional molecular objects by overcoming the dynamic nature of molecular assembly. Organic nanostructures connected one-dimensionally possessing dissimilar semiconducting properties are expected to provide reliable platform in understanding the behaviors of photo-carriers, which are essential for the construction of efficient photon-to-electrical energy conversion systems. Bottom-up supramolecular approaches are considered to be promising for the realization of nanoscale heterojunctions. Aida and coworkers [66] developed semiconducting nanoscale organic heterojunctions, by stepwise nanotubular co-assembly of two strategically designed molecular graphenes. The dissimilar nanotubular segments, even though connected non-covalently, were able to communicate electronically with one another over the heterojunction interface. Unlike respective homotropically assembled nanotubes these hetero-nanotubes displayed characteristic charge transport.

Gemini-shaped hexa-perihexabenzocoronene (HBC) derivative [66], bearing two triethylene glycol-appended phenyl groups on one side of the HBC core and dodecyl side chains on the other, self-assembles into a semiconducting nanotube (HBCi) with inner and outer diameters of 14 and 20 nm, respectively was realized by Aida and co-

workers (Figure 1.13.). Structural analysis of HBCi employing synchrotron x-ray diffraction technique revealed that the nanotube is composed of a graphite-like bilayer wall consisting of helically twisted columnar arrays of π-stacked HBC units. For the realization of a nanotubular heterojunction using this self-assembling motif, essential pre-requisites are (i) formation of morphologically stabilized seed nanotube and (ii) design of a second graphene monomer capable of tubularly assembling from the extremely thin facets of the seed nanotube termini. To address these features Aida and coworkers synthesized respective seed (HBC1) and second monomeric (HBC2) nanotubular fragments. HBC 1 carries two bipyridine (bpy) subunits that enable
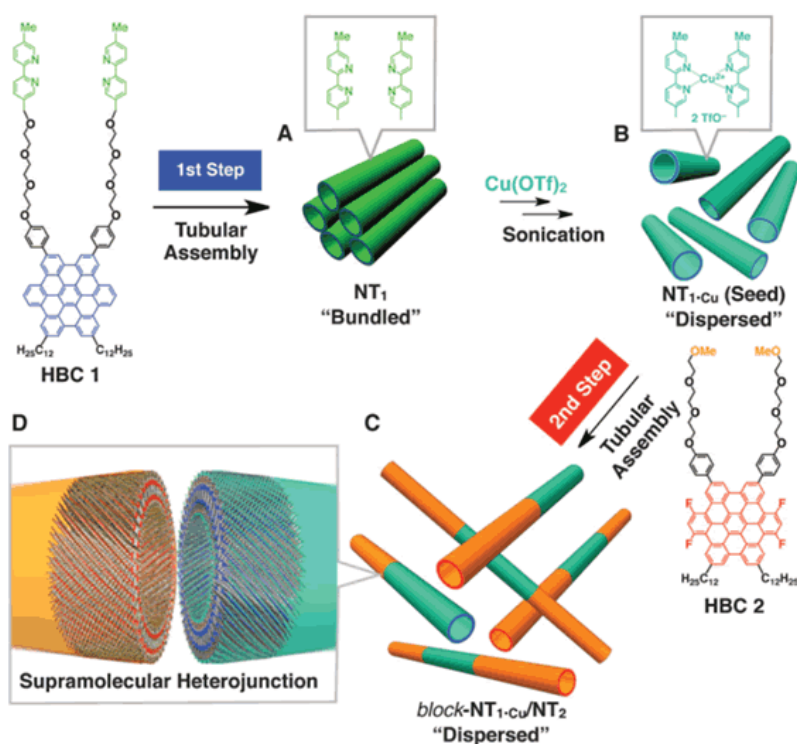
Figure 1.13. *Contiguous D-A nanotubular arrangement of HBC1 and HBC2 (adapted from the reference 66).*

resulting seed nanotube to be morphologically stabilized by forming a metal-coordination network [66]. The charged surface of the resultant seed also merits its homogeneous dispersion to electrostatic repulsion. On the other hand, HBC 2 bears four electron-withdrawing fluorine substituents, so it can adhere electronically to the seed termini and self-assemble selectively from their nanotubular facets. When these HBC molecules co-assemble stepwise, the resultant connecting segments are electronically dissimilar to one another.

Positioning D and A chromophores in well-defined distance is indispensable in ameliorating energy and electron-transfer cascades in OPVs as recognized in natural photosynthetic systems (PS) for efficient light-harvesting and long-lived charge separation (CS) [67]. The development of easily tailorable scaffolds for multi-chromophore organization and photophysical studies of the energy- and charge-transfer dynamics in such systems can provide insight into how factors such as geometry, energetics, and environment modulate these photo-conversion processes. Inspired by elegant supramolecular organization in natural PS architecture, Wasielewski and coworkers [67] attempted (Figure 1.14.) to spatially organize guanine (G, D) and PDI (A) chromophores in such a way as to facilitate antithetical conduction for the traversal of photo-generated excitons, resulting in long lived CS states. In presence of cations such as potassium the highly symmetrical guanine-PDI D-A motifs, transforms into guanine quadruplex (GPDI), possessing core–shell columnar
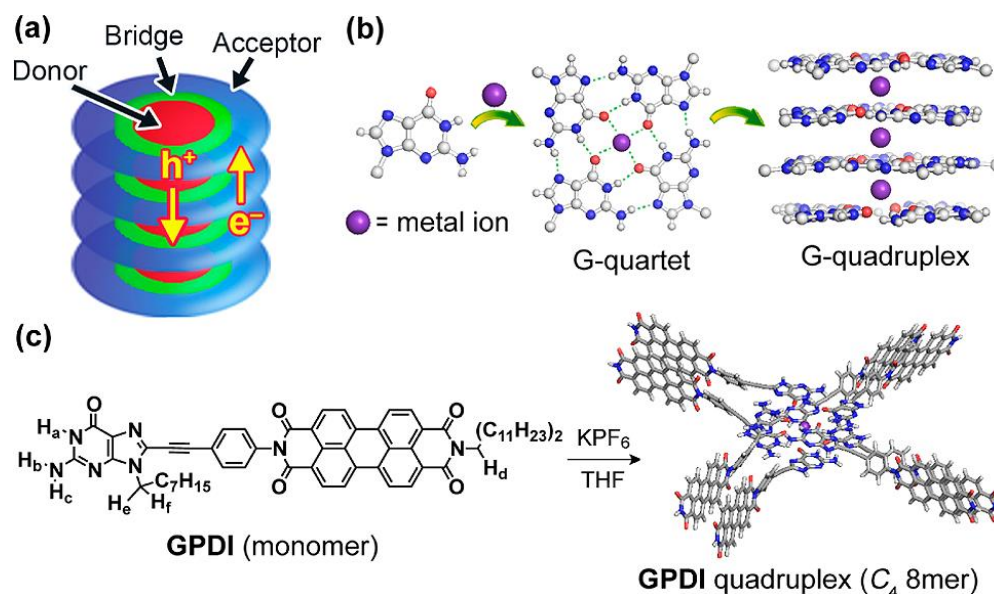
Figure 1.14. *Core-shell D-A columnar arrangement of guanine and PDI (adapted from the reference 67).*

arrangement. Guided by synergistic cation–dipole, π–π, and Coulombic interactions, G-PDI derivatives undergo cation induced G-quadruplex formation forming H-bonded cyclic tetramers (G-quartet) which stack into octamers, hexadecamers and higher analogues. Estimation of lifetimes of transient intermediates formed as a result of photo-induced electron transfer from G to PDI, reveals that the charge transfer intermediates survives > 100-fold in the aggregated state relative to the monomeric state.

1.8.2. Self-assembled D-A trefoils

Trefoil (from Latin trifolium, "three-leaved plant") is a graphic form composed of the outline of three overlapping rings and three-fold shape used in architecture and Christian symbolism. Unrestricted ambipolar charge transport of photogenerated

excitons could be ensured in multi-chromophoric arrays of organic molecules that self-assemble into ordered phase-segregated D-A frameworks. Realization of isotropic photoinduced charge transport in symmetrical D-A molecular scaffolds encouraged construction of easily tailorable superstructures at nanoscopic dimensions. Well-ordered multi-chromophore structures are inevitable for optimized energy transfer in artificial photosynthetic systems for solar energy conversion.

Chlorophyll (Chl)-based derivatives [68-70] (Figure 1.15.) have been widely exploited in energy transfer systems because they exhibit wide spectral coverage, and the presence of reduced pyrrole moiety in Chls greatly enhances the transition dipole moment of their lowest energy Qy optical transitions. To mimic the versatile precise spatial organization observed in artificial photosynthetic systems, Wasielewski and coworkers prepared Chl trefoil arrays which displayed both energy and charge transfer controlled by the structure of the rigid linker between three identical Chls. The Chl trefoils exhibited laser energy dependent singlet-singlet annihilation. Assuming that annihilation is the result of random exciton energy transfer between the adjacent chromophores exciton hopping lifetime constant have been calculated as 6.0 ps from annihilation time constant of 1.8 ps. Charge transport within the Chl trefoils was studied by generating their radical cations, by the addition of I_2 and $AgClO_4$ dissolved in acetonitrile and characterized employing electron nuclear double resonance (ENDOR) spectroscopy [69].

(a)

(b)
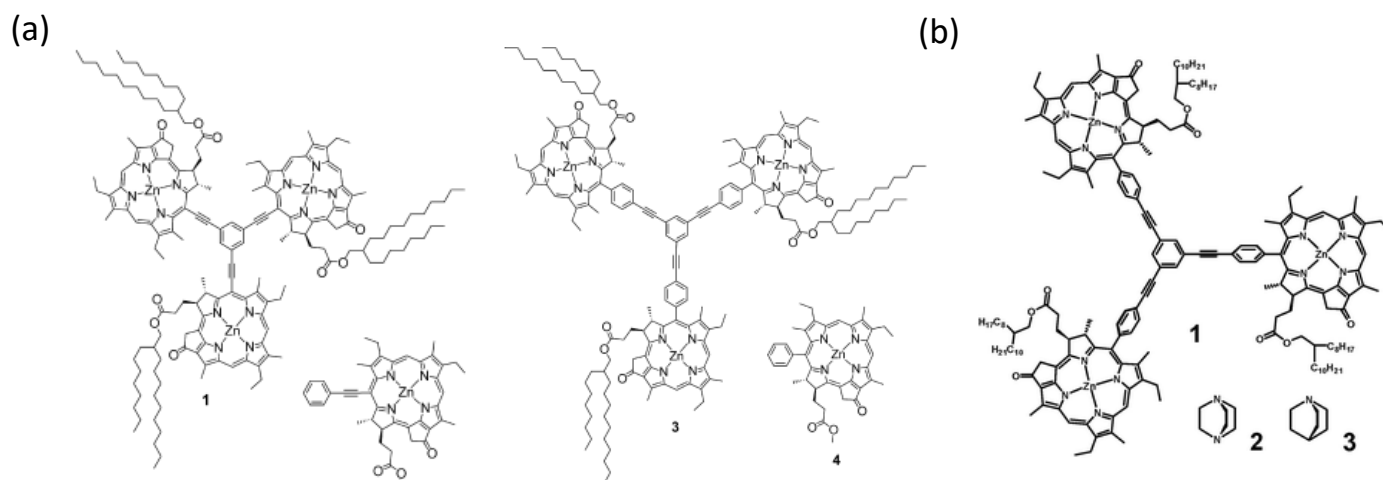
Figure 1.15. *(a), (b) chlorophylls explored to investigate linker controlled energy and charge transfer (adapted from the references 68-70).*

Chemically identical chlorophylls (Chls) operating through symmetry breaking charge separation serve as donors and acceptors for transporting energy and charge in natural photosynthetic organisms [69]. The specific role that these Chls perform is differentiated by their specific interactions with other Chls, nearby redox cofactors, and the surrounding protein. In light-harvesting proteins, the interactions of the Qy transition dipole moments of neighboring Chls induce significant spectral shifts as a result of exciton coupling. In addition, metal–ligand binding using bridging ligands has successfully been implemented to self-assemble supramolecular structures from covalent, multi-Chl(and multi-porphyrin) building blocks [70]. The bifunctional ligand 1,4-diazabicyclo[2.2.2]octane(DABCO), has been used to assemble a wide variety of supramolecular porphyrin systems, exploiting metal–ligand binding between two porphyrin metal centers and the two nitrogens of one DABCO molecule thereby

generating a dimeric sandwich complex from two covalent multi-porphyrin arrays. Femtosecond transient absorption spectroscopic investigation implied laser pulse energy dependent singlet–singlet annihilation resulting from energy transfer between [1]Chl* molecules. The unique hexagonal supramolecular light-harvesting arrays of Chls offer interesting insights into the self-assembly of Chls that could be explored in artificial photosynthetic systems and photofunctional devices.

Imitation of the economic design seen in photosynthetic proteins is a key strategy for solar energy conversion; where well-ordered chromophore assemblies carry out the initial steps of photosynthesis, including efficient light harvesting as well as energy and charge transfer over large distances (Figure 1.16.). The trefoil is synthesized substituting 1, 3 and 5 positions of 1,3,5-triphenylbenzene by perylenemonoimide through Suzuki-Miyaura cross coupling reaction [71]. The trefoils undergo self-assembly in MCH to form cofacial trimeric and larger tridecameric assemblies as evidenced by synchrotron-based small- and wide-angle X-ray scattering measurements in contrast to the
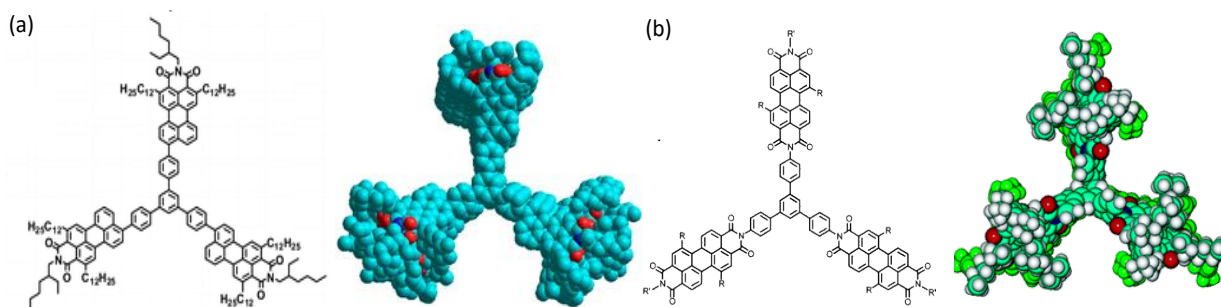
Figure 1.16. *Self-assembled 1,3,5-triphenylbenzene (a), PMI and (b) PDI light harvesting trefoils (adapted from the references 71 and 72).*

monomeric assembly in THF. Time-resolved spectroscopy reveals that the trefoils initially form excitonically coupled excited states that subsequently relax to excimer states having 20 - 8.4 ns lifetimes. Long-lived excimer states thus produced in the aggregated state will help in exploring charge transport phenomenon through various types of π-stacked PMI assemblies.

The delocalization or rapid hopping of charge transfer intermediates among neighboring molecules is a prerequisite to achieve long-lived charge separated states and larger exciton diffusion lengths in organic electronic and photovoltaic devices [68]. Pioneering studies of charge delocalization in both photosynthetic proteins and aromatic molecules in solution have employed electron paramagnetic resonance (EPR) and electron-nuclear double resonance (ENDOR) spectroscopy to reveal charge sharing in dimers [68]. Imidization of perylene-3,4:9,10-bisanhydride (PDA) with 1,3,5-tri(4-aminophenyl)benzene afforded the trefoil (b). The significant blue shift of the trefoils in CH_2Cl_2 relative to the monomers validates characteristic exciton coupling in H-aggregates formed through π- π interactions in CH_2Cl_2.Photoexcitation of the trefoil with an Ar+ laser at 457 - 488 nm indicated the presence of radical ion pair intermediates, could be due to the electron transfer from TEA to $^1PDI^*$ in dry CH_2Cl_2 occurring within the timescale of the experiment [68].

Organic semiconductors have become indispensable building blocks for the production of next-generation cost-effective flexible electronic devices such as OPVs

and OLEDs. The performance of hole-transporting (p-type) organic semiconductors has steadily been improved demonstrating charge carrier mobilities similar to that of amorphous silicon. On the other hand, n-type semiconductor materials with multiple imide substituents may increase the electron affinity of the parent material, facilitating electron injection and charge transport. However, the incorporation of multiple imide substituents is synthetically challenging, and only a few examples of tri- and tetraimides have been reported through lengthy and/or low-yielding synthetic routes such as oxidative Diels–Alder reactions on rylenes/equatorial fusion of rylene diimides. Fred Wudl and coworkers [26, 72, 73] (Figure 1.17.) reported a novel 10-ring fused polycyclic hydrocarbon decacyclene with three fold symmetry that can be functionalized using various imides resulting in a promising class of n-type organic semiconductors called decacyclenetriimides (DTIs). DTIs undergo self-assembly in THF
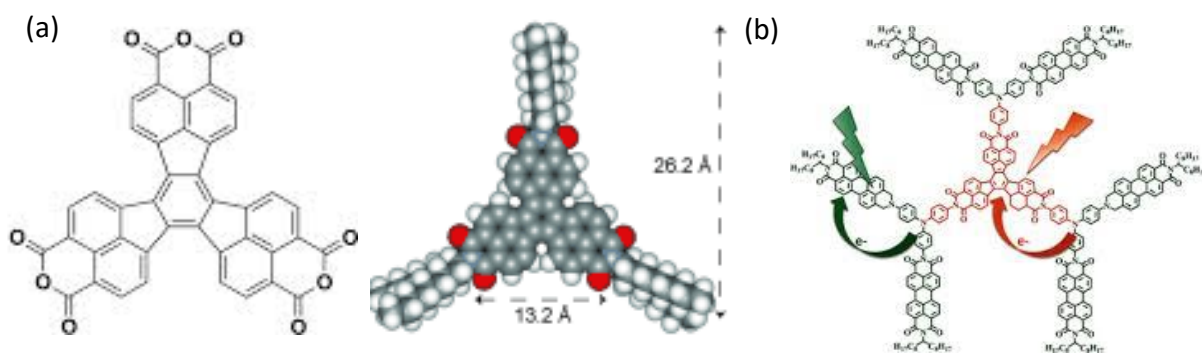
Figure 1.17. *Molecular structure of (a) decacyclenetrianhydride. (b) polyimide dendrimers containing multiple donor-acceptor chromophores for light harvesting (adapted from the references 72 and 73).*

to form well-defined hexagonal pillars approximately 1 μm wide and 3 μm long as validated by scanning tunneling microscopy.

Fascinated by the self-assembling properties of decacyclenetriimides obtained through regioselective hextuple Friedel Crafts carbamylation, polyimide dendrimers decorated with multiple electron donor–acceptor units were explored by Wudl and co-workers [72]. The photo-physical properties of the dendrimers were investigated by steady-state a8bsorption, time-resolved emission and pump–probe transient absorption spectroscopic techniques. Photoinduced charge-separated (CS) states were formed on the femtosecond timescale (230 fs) upon visible excitation of the polyimide dendrimers that deactivate with a lifetime ofca.10–100 ps. To be precise, interchromophoric coupling among dye subunits was negligible in the ground state but upon excitation very fast photoinduced CS states were formed, via PET from TPA units to DTIs or PDIs. Indeed, these macromolecular D–A dendrimeric architectures with well-defined structures possess film forming capabilities similar to polymers exhibiting high charge-carrier mobilities.

1.8.3. Self-assembled D-A triad conjugates

Control of supramolecular organization in the active layer of OPVs and OSCs has been found to be beneficial in dictating properties and performance of OSCs. Especially when blends of self-organizing D and A moieties are utilized at the HJs, their precise organization, mutual orientation and degree of supramolecular ordering are decisive in

controlling the fundamental charge transport characteristics. Discotic organic chromophores such as HBC and perylenetetracarboxydiimide (PDI) were found to be promising candidates for OPVs, as they can be functionalized and self-assembled into discrete columnar superstructures. The emergent properties emulated in the bulk state with specific phase separation on the nanometer scale can provide efficient transport channels for charge carriers. The remarkable performance achieved is mainly attributed to the excellent horizontal phase separation within the active layer, providing a large interfacial area and close packing between D and A domains. Driven by non-covalent intermolecular interactions, Mullen and coworkers [74] successfully synthesized the HBC-PDI D-A dyads that self-assemble into well-ordered two-dimensional nanostructures (2.1 nm, Figure 1.18.) with controllable mutual orientations and distances between D and A in the solution and in the solid state. Nano-segregated stacks of HBC and PDI provide charge transport channels for efficient intermolecular electron transfer preserving potential percolation pathways for holes and electrons facilitating ambipolar charge transport.
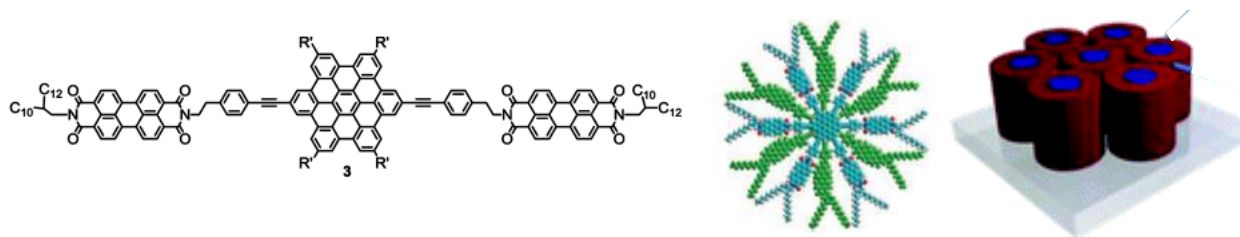
Figure 1.18. *Parallel D-A columnar arrangement of HBC and PDI (adapted from the reference 74).*

Molecular recognition in organized chromophoric assemblies in crowded environment plays key role in the structural design of functional motifs for mimicking and constructing natural PS, OPVs and OSCs. Wurthner and coworkers [75] exploiting complementary H-bonding interactions present in [oligo(p-phenylenevinylene), OPPV] and PDIs constructed hierarchical D-A chiral helical nanofibers exhibiting photo-induced electron transfer (Figure 1.19.). Existence of intermolecular triple H-binding interactions between OPPV and PDI in 2:1 co-assembled superstructures was confirmed by assembling and dissembling the superstructures performing temperature dependent absorption, emission and circular dichroism spectroscopic investigations. Charge transfer intermediates (CTIs) generated as a result of photoexcitation of OPPV-PDI is examined employing femtosecond transient absorption spectroscopic measurements. fTA measurements of OPPV-PDI in methylcyclohexane at room temperature showed CTIs that live for 60 ps in the self-assembled state whereas in the monomeric state at 80°C the CTIs survive for 300 ps [75]. Ratio of CTI lifetime in the aggregated to
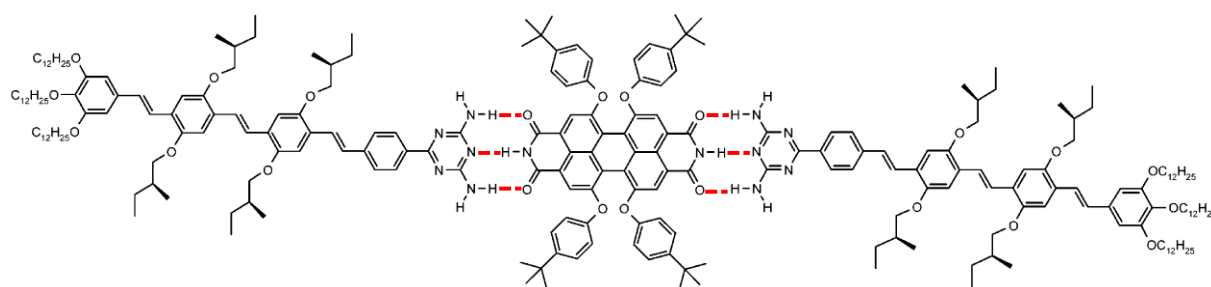
Figure 1.19. *2:1 co-assembled superstructures of OPPV and PDI formed through complementary intermolecular H-bonding (adapted from the reference 75).*

monomeric state is estimated to be 0.2 which shows that CTIs live longer in monomeric state compared to aggregated state.

Rapidly increasing performance of OPVs and the impetus to understand the physics underlying CT interactions between the D and A brought out various strategical designs, wherein electron transfer rates can be easily modulated. Wasielewski and coworkers [76] succeeded in attaining long-lived charge carrier generation in ordered and oriented films of covalently linked PDI-diketopyrrolopyrrole (DPP)-PDI (Figure 1.20.). Ultrafast photodriven charge separation is envisaged in PDI-DPP dyad and PDI-DPP-PDI triad constituted by end capping PDI with PDI-DPP dyad. Solvent vapor annealing (SVA) of PDI-DPP-PDI thin films in saturated dichloromethane revealed presence of self-assembled co-facial PDI chromophoric stacks possessing higher degree of intermolecular coupling. More precisely, PDI forms H-aggregates to stipulate efficient transport of mobile electrons. Grazing incidence X-ray scattering measurements of PDI-DPP-PDI affirmed that DPP and PDI are oriented perpendicular to each other, quintessential for enhanced OPV efficiencies. Photoexcitation of PDI-DPP-PDI in toluene results in charge separated states that recombine within 340 ps (monomeric state, solution state), while unannealed/disordered films of the same displays recombination lifetime of 6 ns [76]. Counterintuitive to this, photoexcitation of vapor annealed thin films of PDI-DPP-PDI exhibited spin-correlated radical ion pairs that survive for ~4 μs [76]. The absence of
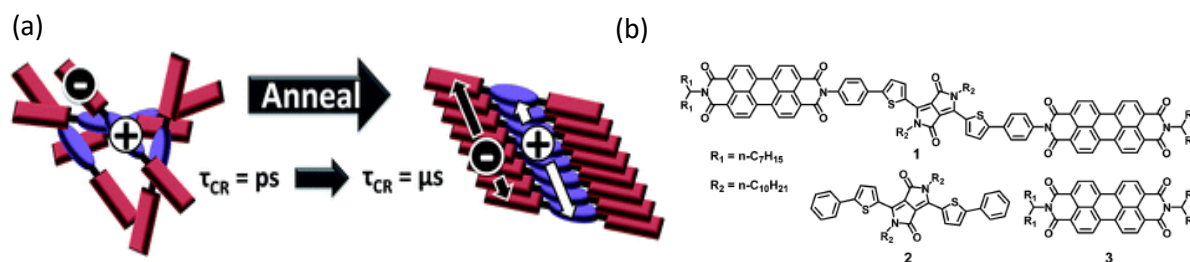
Figure 1.20. *Slip-stacked D-A arrangement in vapor annealed thin films of DPP and PDI (adapted from the reference 76).*

long-lived charge transfer intermediates in the disordered/unannealed film suggests that few charge carriers are generated. Persistence of charge carriers for longer time in ordered/vapor annealed films of PDI-DPP-PDI could be corroborated to the slip-stacked arrangement of PDI-DPP-PDI in the self-assembled state [76]. Significant enhancement ($\sim 1.1 \times 10^4$-fold) in the lifetime of charge transfer intermediates engendered in the vapor annealed thin films of PDI-DPP-PDI with respect to the unannealed films suggest that charge carriers are stabilized by dissociation into free charge carriers through well-ordered slip-stacks of PDI-DPP-PDI [76].

Complex optical and electronic properties in natural systems are achieved by employing an "emergence upon assembly" approach [77], wherein new properties that are absent in the individual components emerges upon formation of hierarchical superstructures [78]. Desire to mimic natural PS reaction center and its attractive aspects, motivated Braunschweig and coworkers (Figure 1.21.) to design D-A supramolecular system composed of electron rich DPP donor and PDI acceptor that
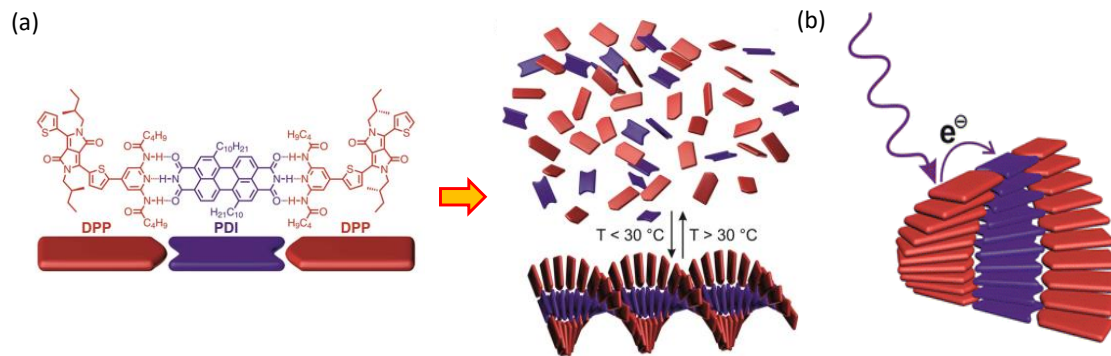
Figure 1.21. *Double helical columnar arrangement in 2:1 co-assembled DPP and PDI (adapted from the reference 77).*

forms 2:1 co-assembled helical architectures as a result of triple H-bonding between PDI and DPP and π-π stacking orthogonal to the H-bonding axis [78]. Braunschweig and coworkers demonstrated that electronic and optical properties of these assemblies are directed by reversible supramolecular interactions. DPP and PDI are selected as D and A subunits in such a way that the two chromophores are electronically complementary and the FMO levels are positioned such that photoexcitation of either DPP or PDI, generate charge separated states by photo-induced electron transfer either from PDI or DPP [77].

Disaggregated individual components did not exhibit charge transfer intermediates upon photo-exciting either DPP or PDI [77]. This approach demonstrates that hierarchical superstructures generated conjoining favorable cooperative interactions operating in concert with desirable thermodynamically favored charge separation between D and A entities can impart emergent charge transfer properties.

Variable temperature fluorescence measurements displayed that the co-assembled superstructures undergo dissembly at higher temperatures as intermolecular H-bonding between DPP and PDI get destroyed collapsing the superstructure. Femtosecond transient absorption spectroscopic measurements in the disassembled and co-assembled state revealed that ~150-fold enhancement in the survival time of charge transfer intermediates is achieved in the co-assembled state compared to the disaggregated state.

Construction of sophisticated multicomponent supramolecular functional architectures on transparent conducting oxide solid film surfaces, through self-organizing surface-initiated polymerization (SOSIP) [79-81] was accomplished by
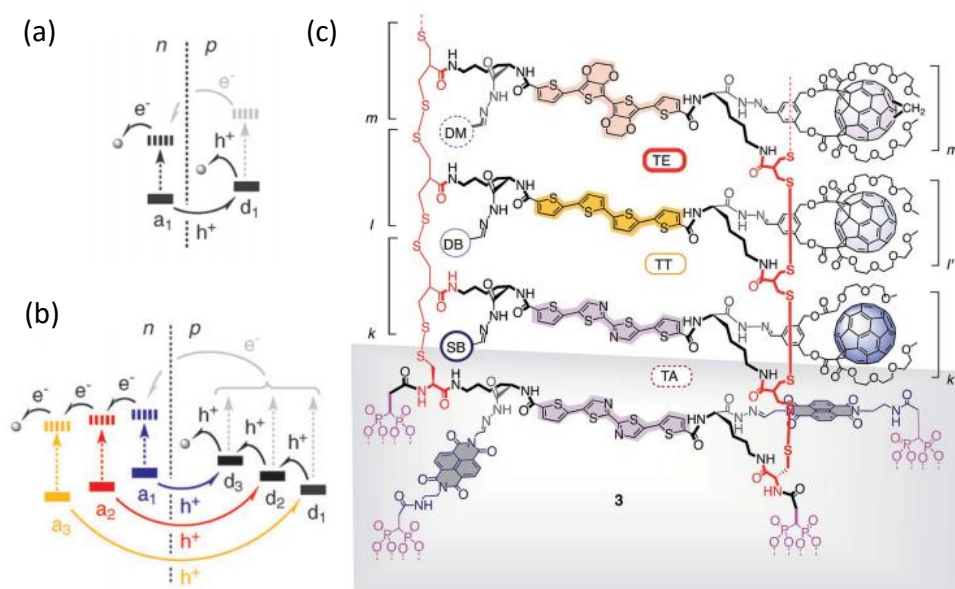
Figure 1.22. *Schematic representation illustrating photo-induced electron transfer upon photoexcitation of 'a₁'in (a) SHJ, (b) OMARG-SHJ and (c) SOSIP operating in self-assembled stacks of oligothiophene and fullerene (adapted from the references 79-81).*

Matile and coworkers (Figure 1.22.). SOSIP employs pertinent lessons from nature to elaborate directional growth of oriented and ordered superstructures to mimic natural PS through dynamic covalent bonds. The unique SOSIP approach could yield covalently linked, ordered and oriented D-A oligomers, which can perform stack exchanging with fullerenes, lateral and templated self- sorting on surfaces, self-repair, surface reactivation and charge transport in napthalenedimide, perylenediimde and oligothiophene stacks through symmetry breaking charge separation. SOSIP technique was further exploited to construct complex multifunctional frameworks such as three co-axial charge transporting conduits and antiparallel three-component gradients [24] in double channel pathways. Artificial photosystems thus generated validated that oriented multi-component antiparallel redox gradients are crucial in driving the charges apart after their generation. With increase in each level of sophistication charge recombination rates were found to decrease from 29% to 2% [30, 82].

Water soluble conjugated organic polymers constituted from small organic molecules have been studied widely as photoactive materials for OPVs [83]. Unlike most inorganic materials, organic materials allow easy solution processing and inexpensive device fabrication. Lack of solid-state order in conjugated polymers, results in charge traps which attenuates charge-carrier mobilities relative to those of crystalline aromatic small molecules. Improved degree of order in the solid state could be translated to enhanced charge carrier mobilities, employing various self-assembly
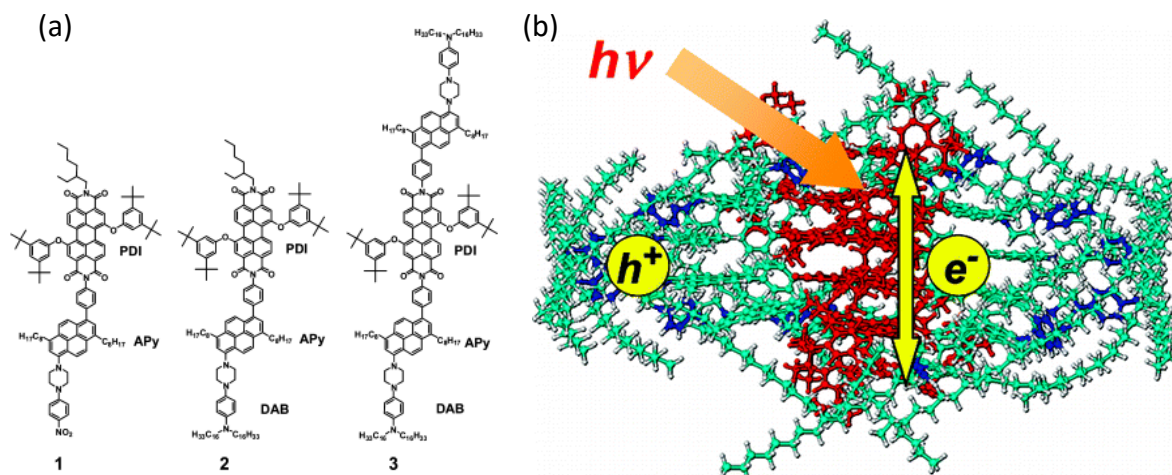
Figure 1.23. *Schematic representation of (a) Apy-PDI, DAB-APy-PDI and DAB-APy-PDI-APy-DAB triads under investigation and (b) model representing the photoinduced electron transfer through heptameric columnar stacks (adapted from the reference 83).*

approaches listed above. Efficient charge transport of the separated charges over tens of nanometers to the respective electrodes require sufficiently long pathways for radical ion pairs to permit rapid charge hopping even though the modular components are weakly interacting. Wasielewski and co-workers [83] designed D-D-A triad comprising of aminopyrene primary donor (APy) and a p-diaminobenzene secondary donor (DAB) attached to either one or both imide nitrogen atoms of PDI, generating DAB-APy-PDI and DABAPy-PDI-APy-DAB triads (Figure 1.23.). In toluene, both the triads exist as monomers, while in methylcyclohexane, ordered helical heptameric and hexameric self-assembly is observed. Wide-angle X-ray scattering measurements of such triads concluded that the PDI molecules are π-stacked in a columnar fashion. This work demonstrated that electron hopping through the π-stacked PDI molecules is fast

enough to compete effectively with charge recombination (40 ns) in these systems, making these materials suitable for artificial photosynthesis and organic photovoltaics [83].

Stephane Mery and Irene Burghardt [84] along with their coworkers demonstrated self-assembly of covalently bound DA block copolymers or co-oligomers which forms smectic liquid crystalline (LC) films at ambient temperatures emphasizing the importance of molecular ordering in dictating charge transport characteristics (Figure 1.24.). Siloxane functionalized novel class of covalently bound bisthiophene−PDI-bisthiophene; D-A-D co-oligomer aggregates were prepared which transforms into smectic films. To investigate ultrafast charge transfer dynamics, time-resolved optical spectroscopy in solution and smectic films were employed. The studies concluded that DA system in solution exhibits ultrafast resonant energy transfer ($\sim$ 130 fs) followed by slower ($\sim$ 2.7 ps) charge separation, while the film exhibits sub picosecond ($\sim$ 60 fs) CT formation. Recombination to the ground state occurs within $\sim$ 50 ps in the film, and triplet states appear on longer time scale >1 ns [85].

Despite the efficient CT formation in the LC phase, recombination as well as triplet formation seems to severely limit the transient photocurrent [85]. A striking feature of the smectic LC phase is the large tilt angle ($\sim$ 70°), between the molecular planes of D and A with the normal plane of the crystal. A very similar situation was observed to be existent in the slip-stacked donor−acceptor assemblies composed of
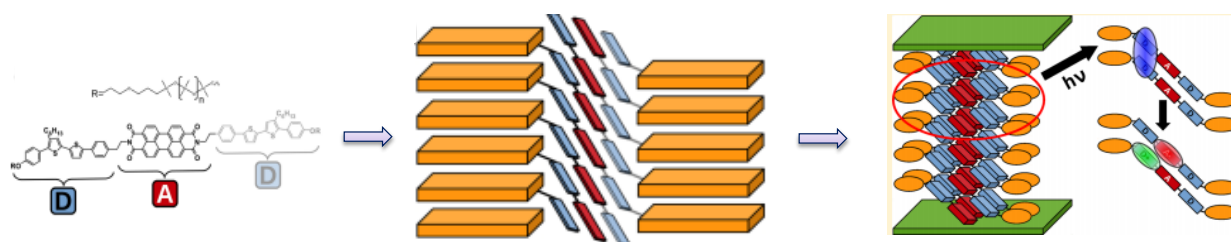
Figure 1.24. *Schematic representation of modular components in bisthiophene-PDI-bisthiophene D-A-D triad self-assembly appended with siloxane functionality (adapted from the reference 84).*

oligo(p-phenylenevinylene) (OPV) and PDI units [86]. In such system, intermolecular charge transfer was found to be predominant, in contrast to H-aggregate assembly of the same donor−acceptor units possessing slower intramolecular charge transfer. More generally, the combined effects of excitonic and charge-transfer interactions may lead to the intriguing photophysical and charge transport properties that necessitate a detailed understanding of intermolecular packing [86].

Supramolecular polymerization of π-conjugated monomers could be exploited to make them more relevant in miniaturized organic device applications [87]. In fact, such strategy can offer precise organization of structural motifs, without altering features of polymers such as phase segregation, film formation etc. Fernandez, Laquai and Ghosh [87] with their coworkers (Figure 1.25.) revealed for the first time H-bonding-initiated supramolecular polymerization of a melamine (M-1)-diaminonaphthalenediimide(NDI-H) conjugates. The supramolecular polymerization of NDI-H was examined in a few organic solvents and gelation was observed in n-decane. The lack of gelation in the presence of M-1, possessing a complementary H-bonding motif of DAD type, suggests
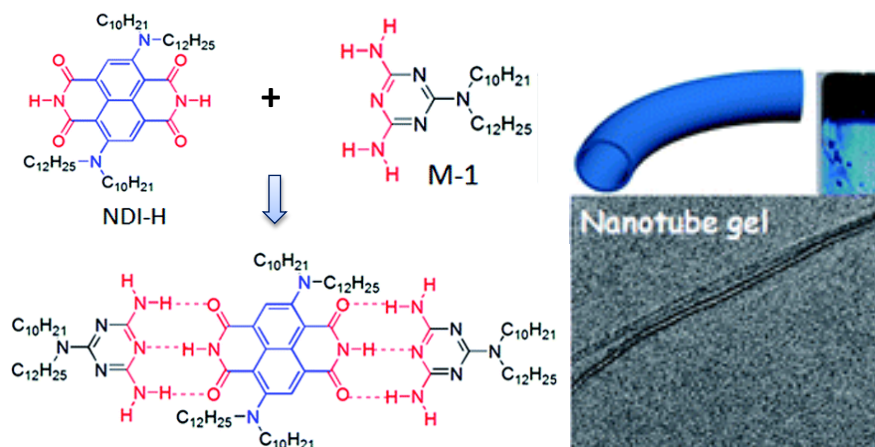
Figure 1.25. *Self-assembled 1,3,5-triphenylbenzene (a), PMI and (b) PDI light harvesting trefoils (adapted from the reference 87).*

that supramolecular polymerization by extended H-bonded chain formation among the imide groups of the NDI-H is crucial for the observed gelation to occur. The transient signal measured in THF at 600 and 652 nm decays with a lifetime of 200 ps and a bi-exponential decay which has a lifetime of 8.3 ps and 34 ps respectively. On the other hand, aggregated NDI-H in n-decane showed a kinetic profile that decays with a lifetime of 26 ps with an additional offset accounting for >10% signal intensity remaining even beyond 3 ns. Nanosecond transient absorption spectroscopic measurements revealed that the decay proceeds on the ns–ms timescale around 800 nm and is very slow extending beyond 100 ms which is ascribed to the delocalized charged states. The origin of the long lived signal is attributed to the delocalization of the excited state across several NDI-H J-aggregates.

Supramolecular polymers are a promising class of materials that could potentially be used for preparing organized films which can undergo photoinduced charge separation. Braunschweig and coworkers [78] developed a supramolecular polymer composed of a monodiamidopyridine diketopyrrolopyrrole (mDPP) electron donor and a perylenebisimide (PDI) electron acceptor that assembles into 2:1 mDPP:PDI helical supramolecular polymers (Figure 1.26.). mDPP:PDI forms a hierarchical self-assembly governed by cooperative interactions involving $\pi\cdots\pi$ stacking and H-bonding. In solution, this mDPP:PDI supramolecular polymer undergoes ultrafast photoinduced charge separation into $mDPP^{.+}:PDI^{.-}$ followed by a recombination $\tau_{CR} = 33$ ps [78].

In order to translate the emergent photoinduced charge separation observed in the solution state to solid state, the group have fabricated mDPP:PDI supramolecular
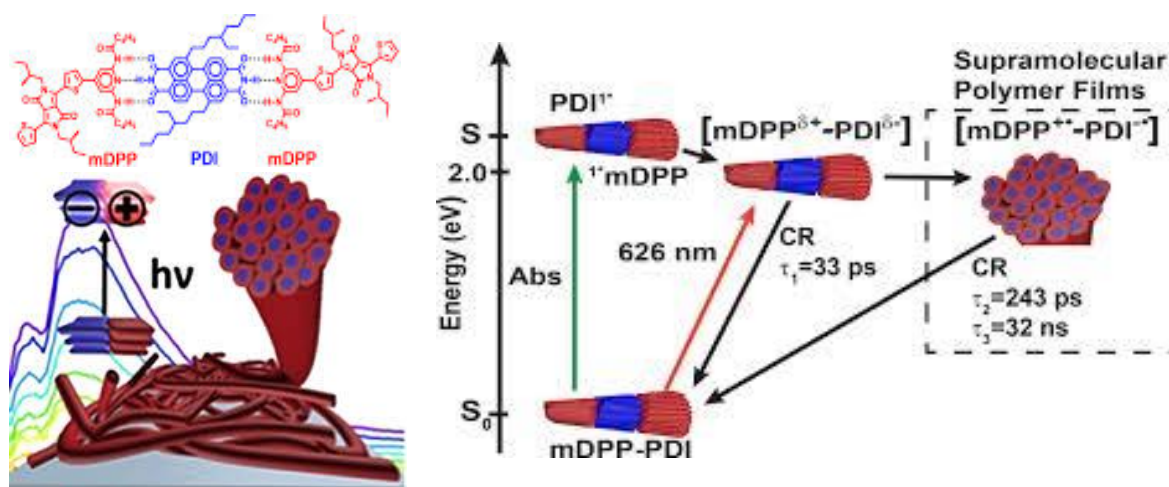
Figure 1.26. *Supramolecular polymer films composed of a 2:1 mixture of monodiamidopyridine diketopyrrolopyrrole (DPP) electron donors and perylenebisdiimide (PDI) electron acceptors (adapted from reference 78).*

polymer thin films. Braunschweig and coworkers successfully demonstrated that supramolecular polymer structure is maintained in the solid state with molecular and micrometer length scales. The photoinduced charge separated states persist 1000-fold longer in the H-aggregates generated in the solid-state than in solution.

1.9. Objective of the thesis

Self-assembled organic multicomponent supramolecular architectures have attained widespread attention owing to their unique charge transport properties. Precise spatial organization of electronically complementary donor and acceptor entities play pivotal role in dictating the fate of photogenerated excitons in isolated and/or crowded environments. To install ordered and oriented 'transport highways' for efficient exciton migration at the supramolecular heterojunctions at the active layer of optoelectronic devices various strategies have been adopted.

The thesis outlines novel approaches to achieve long-lived charge separated states in the aggregated state exploiting simpler structural designs. Chapter 1 illustrates modulation in geminate charge recombination of photogenerated excitons in non-parallel segregated D-A stacks. Chapter 2 describes enhancement in the radical ion pair intermediate lifetime in the aggregated state relative to the monomeric state as a result of lower probability of charge annihilation across non-parallel trefoil stacks. Chapter 4 deals with remarkable augmentation in the CTI lifetimes by eight orders of magnitude in the self-assembled state by virtue of delocalization of excitons through antiparallel dimeric stacks and/or structural heterogeneity arising as a result of non-symmetrical D-D-A triad architecture.

Chapter 2

Nonparallel Stacks of Donor and Acceptor Chromophores Evade Geminate Charge Recombination

Abstract

We report a nonparallel stacked arrangement of donor–acceptor (D–A) pairs for prolonging the lifetime of photoinduced charge-separated states. Hydrogen–hydrogen steric repulsion in naphthalimide-naphthalene (NIN) dyad destabilizes the planar geometry between the constituent units in solution/ground state. Sterically imposed nonplanar geometry of the dyad allows the access of nonparallel arrangement of the donor and acceptor stacks having triclinic space group in the crystalline state. Antiparallel trajectory of excitons in nonparallel D–A stacks can result in lower probability of geminate charge recombination, upon photoexcitation, thereby resulting in a long-lived charge-separated state. Upon photoexcitation of the NIN dyad, electron transfer from naphthalene to the singlet excited state of naphthalimide moiety results in radical ion pair intermediates that survive >10,000-fold longer in the aggregated state (τ_{cr}^{a} > 1.2 ns) as compared to that of monomeric dyad (τ_{cr}^{m} < 110 fs), monitored using femtosecond transient absorption spectroscopy.
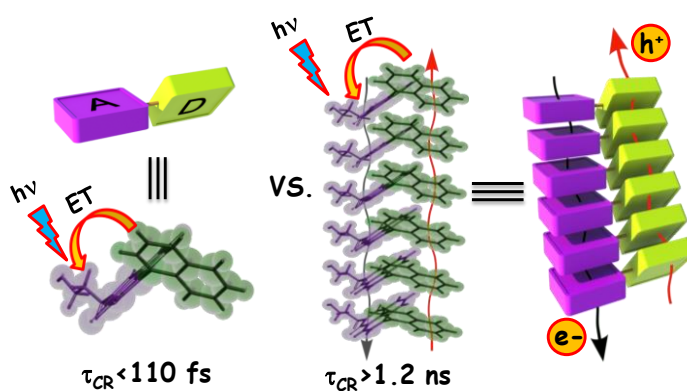
2.1. Introduction

Modulating the behavior of photogenerated excitons [64, 88, 89] is crucial in the development of materials for artificial photosynthesis and photovoltaic device applications [90]. Precise spatial organization [25] of electronically complementary chromophores [58] is a prerequisite to afford long-lived photoinduced charge separation [59]. Generation of photoinduced long-lived charge separated states in isolated donor–acceptor (D–A) systems continues to possess enormous interest [91-102]. State-of-the-art theoretical [90, 103-105] and experimental [2, 106-109] investigations suggest that D–A systems that assemble to form extended architectures can effectively prolong the lifetimes of photogenerated excitons. Electron donors and acceptors tend to stack on one another by virtue of their electronic complementarity [25, 65, 110, 111], thereby trapping and instantaneously annihilating the photogenerated charge carriers through geminate charge recombination [65]. Attempts to circumvent the interdigitating arrangement of donor and acceptor include utilization of π–π stacking [112], hydrogen-bonded [77, 78, 113], cooperative [7, 71, 77, 114], metal–ligand interactions [114, 115], chiral auxiliaries [66, 116], and self-organizing surface-initiated polymerization [24, 27, 30, 80-82]. Such approaches have provided defined oligomers to large aggregates possessing parallel [112, 117], coaxial [65], contiguous [66], cylindrical [118], slipped [76], slipped-sandwich [119], double-helical [77, 120], or helix wrapped [121] columnar stacks [122] of D–A chromophores (Scheme 2.1.).
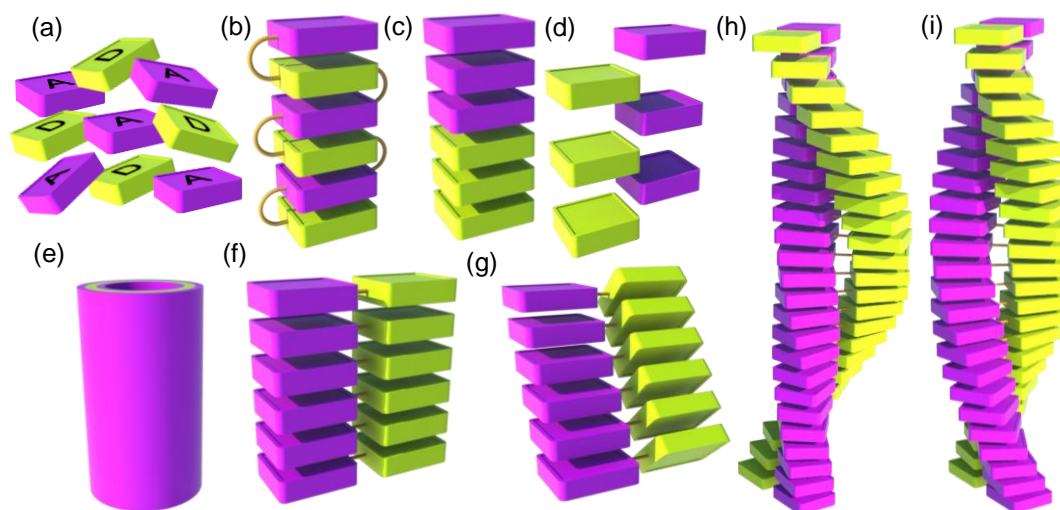
Scheme 2.1. *Representative strategies adopted to spatially organize electron donors and acceptors for emergent properties.*

Our continued interest toward the design of near-orthogonally arranged D−A systems, for exploiting favorable photoprocesses in isolated [123, 124] and organized environment [31, 125], enabled us to restrict the co-facial arrangement [58, 59] of electronically complementary aromatic chromophores [25]. A significant energy barrier (~100 kJ/ mol) [123] to rotation between naphthalene and naphthalimide units connected across single covalent bond enforces a nonplanar arrangement of the dyad in ACN solution. Spherical/ring-like architectures of the dyad formed in CHCl$_3$, upon addition of hexane, crystallize as nonparallel stacks (Scheme 1g) of naphthalene and naphthalimide, in contrast to the disordered aggregates proposed for similar architectures [64, 76, 126, 127]. We herein report the first example of the formation of

long-lived charge-separated states ($\tau_a^{cr} > 1.2$ ns) from the molecular aggregates of nonparallel arrangement of segregated D–A stacks upon photoexcitation.

2.2. Syntheses and Characterization of naphthalimide derivatives NI, NIPh and NIN

Synthesis of NI: To a solution of 1,8-naphthalic anhydride (5.05 mmol) in 100 ml of water, 3-amino-1-propanol (50.5 mmol) was added and heated at 70 °C for 5 h. The reaction mixture was then cooled, filtered, washed with water and dried. Purification by column chromatography (silica gel, EtOAc: petroleum ether 1:1) afforded NI (85%) as a white solid. m. p. - 123 °C ; ^{1}H NMR (500 MHz, CDCl$_3$): δ = 8.54 - 8.52 (d, J = 8 Hz, 2H), 8.16 - 8.14 (d, J = 9 Hz, 2H), 7.70 - 7.67 (m, 2H), 4.29 - 4.26 (t, J = 6.5 Hz, 2H), 3.54 - 3.51 (t, J = 5.5 Hz, 2H), 1.93 - 1.91 (m, 2H); ^{13}C NMR (125 MHz, CDCl$_3$): δ = 164.89, 134.28, 131.59, 128.18, 127.04, 122.32, 58.93, 36.83, 31.01; IR (KBr): 3477.66, 3059.10, 2966.52, 2862.36, 1695.43, 1651.07, 1583.56, 1440.83, 1363.67, 1327.03, 1232.51, 1146.72, 1076.28, 949.98, 842.89, 781.17, 542.00 cm^{-1}; HR-MS (EI)-(m/z): 255.0682. Calcd. for C$_{15}$H$_{13}$NO$_3$: 255.0895; Anal. Calcd. for C$_{15}$H$_{13}$NO$_3$: C, 70.58; H, 5.13; N, 5.49. Found: C, 70.60; H, 5.38; N, 5.32.

Synthesis of NIPh and NIN: To a solution of 4-bromo-N-(3-hydroxypropyl)-naphthalene-1,8-dicarboximide (1.1 mmol) in 40 ml THF, 20 ml of 2 M aqueous K$_2$CO$_3$ solution was added under nitrogen atmosphere. To this solution, 1.1 mmol of corresponding aryl boronic acid was added followed by Pd(PPh$_3$)$_4$ (14.7 μmol). This

reaction mixture was heated at 70 °C for 12 h, after which it was extracted using dichloromethane. The solvent was removed under reduced pressure and the residue purified by column chromatography (silica gel, EtOAc: petroleum ether) to yield the products NIPh and NIN in 70 and 65% yield respectively.

NIPh- m. p. 152 ^{0}C ; ^{1}H NMR (500 MHz, CDCl$_3$): δ = 8.61 - 8.58 (m, 2H), 8.24 - 8.22 (m, 1H), 7.67 - 7.64 (m, 2H), 7.50 - 7.43 (m, 5H), 4.33 - 4.31 (t, J = 6.15 Hz, 2H), 3.55 - 3.53 (t, J = 5.6 Hz, 2H), 1.97 - 1.93 (m, 2H); ^{13}C NMR (125 MHz, CDCl$_3$): δ = 165.01, 164.82, 147.36, 138.68, 133.07, 131.56, 131.21, 129.87, 128.72, 128.60, 127.95, 126.93, 122.50, 121.35, 58.91, 36.83, 31.04; IR (KBr): 3547.09, 3057.17, 2958.80, 1695.43, 1651.07, 1585.49, 1440.83, 1388.75, 1359.82, 1230.58, 1062.78, 785.03, 702.09, 542.00 cm^{-1}; HR-MS (EI)-(m/z): 331.3242. Calcd. for C$_{21}$H$_{17}$NO$_3$: 331.1208; Anal. Calcd. for C$_{21}$H$_{17}$NO$_3$: C, 76.12; H, 5.17; N, 4.23. Found: C, 76.30; H, 5.08; N, 4.32.

NIN- m. p. 165 ^{0}C ; ^{1}H NMR (500 MHz, CDCl$_3$): δ = 8.67- 8.66 (d, J = 5 Hz, 1H), 8.57- 8.56 (d, J = 5 Hz, 1H), 7.96 - 7.91 (m, 2H), 7.75 - 7.73 (m, 2H), 7.58 - 7.41 (m, 4H), 7.28 - 7.21 (m, 2H), 4.36 - 4.33 (t, J = 5 Hz, 2H), 3.58 - 3.56 (t, J = 5 Hz, 2H), 2.00 - 1.95 (m, 2H); ^{13}C NMR (125 MHz, CDCl$_3$): δ= 165.03, 164.90, 146.01, 136.16, 133.58, 133.38, 132.22, 131.70, 131.36, 131.15, 129.07, 129.03, 128.46, 127.85, 126.98, 126.67, 126.28, 125.81, 125.29, 122.50, 121.86, 58.91, 36.84, 31.07; IR (KBr): 3549.02, 3055.24, 2958.80, 1693.50, 1653.00, 1587.42, 1442.75, 1381.03, 1352.10, 1230.58, 1174.65, 1049.28, 804.32, 781.17 cm^{-1}; HR-MS (EI)-(m/z):

381.2326. Calcd. for $C_{25}H_{19}NO_3$: 381.1365; Anal. Calcd. for $C_{25}H_{19}NO_3$: C, 78.72; H, 5.02;

N, 3.67. Found: C, 78.80; H, 5.09; N, 3.52.

2.3. Crystal structure analyses of NIPh and NIN

Suzuki−Miyaura cross-coupling of 4-bromonaphthalimide with the corresponding arylboronic acids offered naphthalimide-naphthalene (NIN) and naphthalimide-phenyl (NIPh) dyads (Figure 2.1.a). NIN and NIPh crystallize in triclinic (*P*1) and orthorhombic (*P*bcn) space groups, from DCM:hexane (1:3) mixture, whereas

Table 2.1. Crystal data and structure refinement of NI derivatives.

Unit cell parameters	NI	NIN	NIPh
Empirical formula	$C_{15}H_{13}NO_3$	$C_{25}H_{19}NO_3$	$C_{21}H_{17}NO_3$
Formula weight	255.26	381.41	331.36
a (Å) :	4.8045(2)	4.8152(5)	23.723
b (Å) :	25.7786(10)	13.5941(15)	9.233
c (Å) :	9.8034(4)	14.9103(15)	15.182
α(alpha):	90°	106.190(6)°	90°
β(beta):	95.380(2)°	95.651(6)°	90°
γ(gamma):	90°	94.036(6)°	90°
Volume (Å³) :	1208.83(8)	927.84(17)	3325.4
Crystal system	Monoclinic	Triclinic	Orthorhombic
Space group:	$P2_1/c$	P1	Pbcn
Calculate density (mg/m³):	1.403	1.365	1.324
Z:	4	2	8
Temperature (K) :	296(2)	296(2)	296(2)
R(F, %):	4.04	8.25	7.53
$R_w(F^2)$:	1.124	1.089	1.053
CCDC number	1422139	1422140	1422141
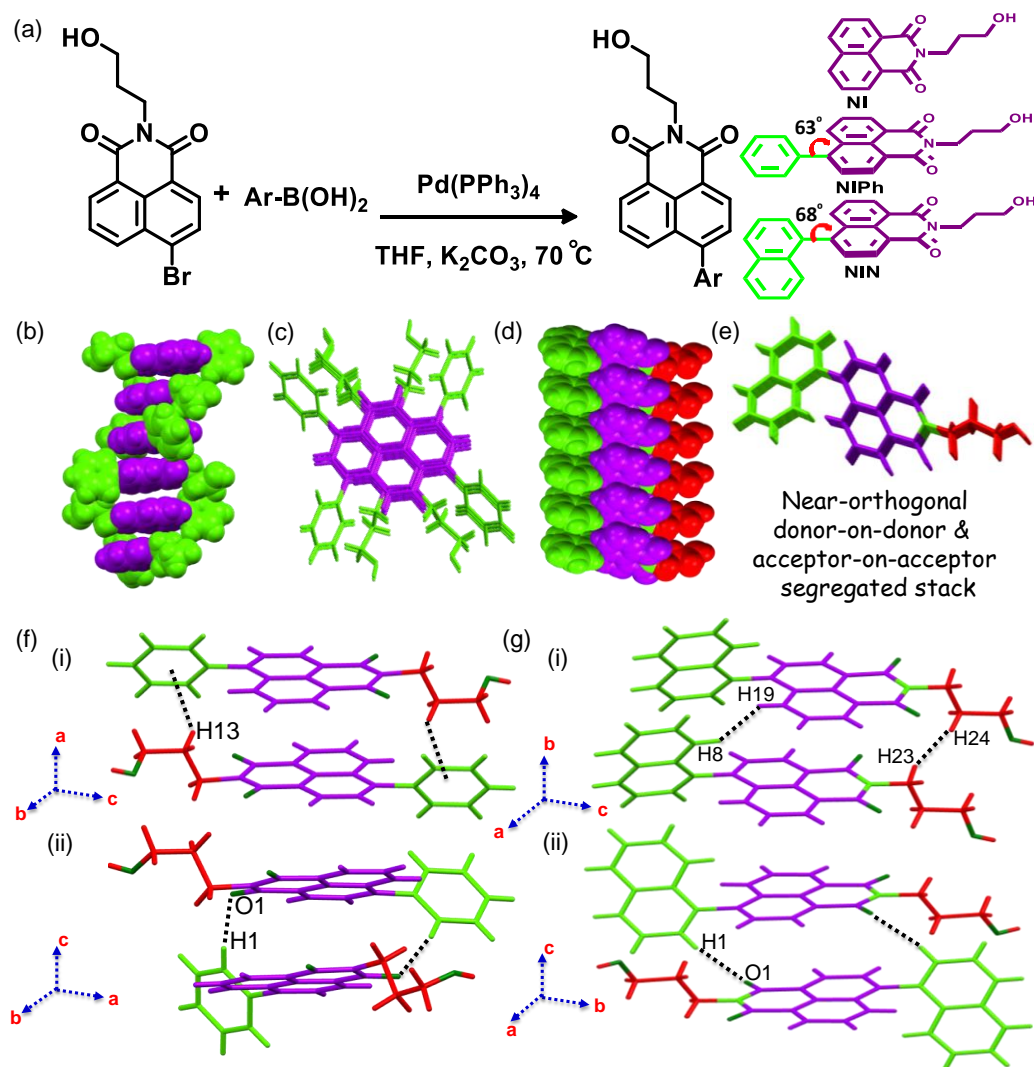
Figure 2.1. *(a) Syntheses scheme for dyads NIPh and NIN with respective chemical structures. Packing arrangements of (b) NIPh (along c-axis) and (d) NIN (along b-axis). Perspective views of (c) NIPh and (e) NIN along c and a-axis, respectively. Self-assembled structures of (f) NIPh and (g) NIN, respectively along c-axis.*

NI crystallizes in monoclinic ($P2_1$/c) space group (Table 2.1). The phenyl (Ph) and naphthyl (N) groups are tilted by 63° and 68° with respect to the NI plane in NIPh and

NIN, respectively, suggesting non-parallel arrangement of constituents in the dyads (Figure 2.1.a). In addition, synergistic C−H•••π, π−π, and C−H•••O interactions along *b*-axis further propagate nonparallel stacks resulting in donor-on-donor and acceptor-on-acceptor arrangement in crystalline NIN (Figure 2.1.d-f). Nearest donor-to-donor and acceptor-to-acceptor π−π separations in NIN are found to be 3.76 and 3.55 Å respectively (Figure 2.1.gi). The intermolecular C−H•••O and C−H•••π interactions along *a*- axis constitute self-assembled structures in NIN (Figures 2.1.gii) that do not have nonparallel donor and acceptor stacks. In NIPh, C−H•••π interaction between methylene C−H of one molecule and the phenylic π-cloud of the adjacent one at a distance of 2.80 Å promotes the formation of an antiparallel stacked (3.60−3.89 Å; Figure 2.1.fi) NIPh dimer. C−H•••O interaction between phenylic C−H and imidic oxygen at a distance of 2.62 Å and an angle of 170° connects two successive self-assembled dimers (Figure 2.1.fii). The successive self-assembled dimers are rotated relative to each other by an angle of 65° resulting in a double helical organization with a pitch of 15.18 Å incorporating eight molecules per turn (Figures 2.1.b-c, 2.2.d).

Quantum theory of atoms in molecules [128-130] analysis (Figure 2.2.a) indicates strong dihydrogen interactions between (i) C−H moiety of NI and N units of adjacent dyad at a distance of 2.28 Å (Figure 2.2.b) and (ii) the methylene protons of hydroxypropyl side chains of neighboring dyads at a distance of 2.27 Å (Figure 2.2.c).
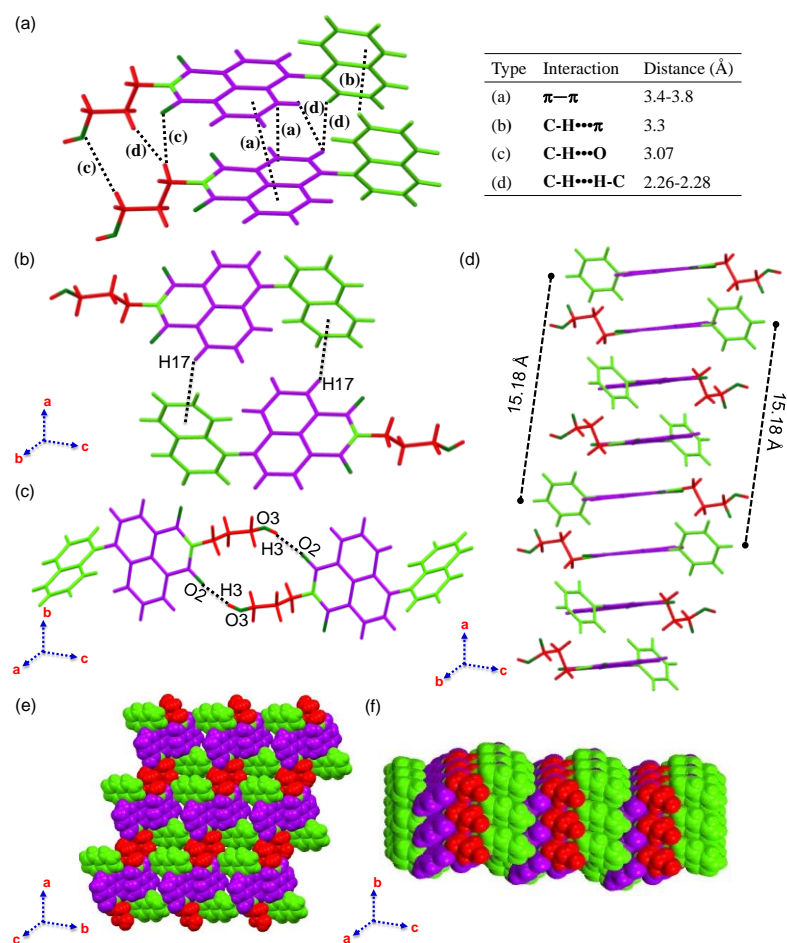
Figure 2.2. *(a) QTAIM topological analysis of NIN. Self-assembled dimers of NIN formed by (b) C17-H17•••π interaction with the distance of 2.82 Å, (c) O2-H3•••O3 hydrogen bonding interaction with the distance and angle of 2.30 Å and 132.8⁰ respectively and (d) double helical columnar arrangement of NIPh generated as a result of C-H•••π and C-H•••O bonding interactions. (e-f) three dimensional packing arrangement of NIN.*

However, the interactions discussed in Figure 2.2.b and 2.2.c do not contribute to the segregated stacking arrangement in NIN. The intermolecular hydrogen bonding interactions found in NIN between O3-H3•••O2 hydrogen bonding interaction with

the distance and angle of 2.30 Å and 132.8^0 respectively drives the formation of parallel segregated NIN non-parallel stacks which can conduit the charge transfer intermediates more efficiently in comparison to the interdigitating/alternating arrangements.

2.4. Morphological analyses

Dynamic light scattering (DLS) experiments were performed to explore the existence and nature of NIN aggregates in solution (Figure 2.3.a). DLS measurements of 0.01 mM NIN in CHCl$_3$ indicate the existence of aggregates with an average hydrodynamic diameter (D_H) of 350 nm. Successive increments (up to 1 mM) in concentration of NIN in CHCl$_3$ exhibit a bimodal distribution with D_H of 300 nm and 4.5 μm (Figure 2.3.a). Non-equilibrated spherical aggregates that possess smaller D_H transform to larger aggregates with an increase in the concentration of NIN. Morphological analyses of 0.1 mM NIN in CHCl$_3$ using tapping mode AFM, SEM, TEM, and confocal microscopic techniques confirm the existence of spherical particles having an average size of 370–400 nm, which is in good agreement with the DLS measurement (Figures 2.3.b-i). At higher concentration (2 mM) of NIN in CHCl$_3$, spherical particles having an average diameter of 1.45, 1.67, and 1.86 μm are observed from AFM, SEM, and confocal microscopic techniques (Figures 2.4.a-d).

Co-existence of ring-like structures having an average diameter of 3.1 μm along with the larger spherical particles is observed. Ring-like architectures further transform

into discrete thick torroidal nanostructures (Figures 2.3.e-h, 2.4.e-s). Selected area electron diffraction (SAED) of NIN aggregates in $CHCl_3$ indicates single-crystalline nature having hexagonal/cubic crystal system (Figure 2.2.j) [131]. The amphiphilic
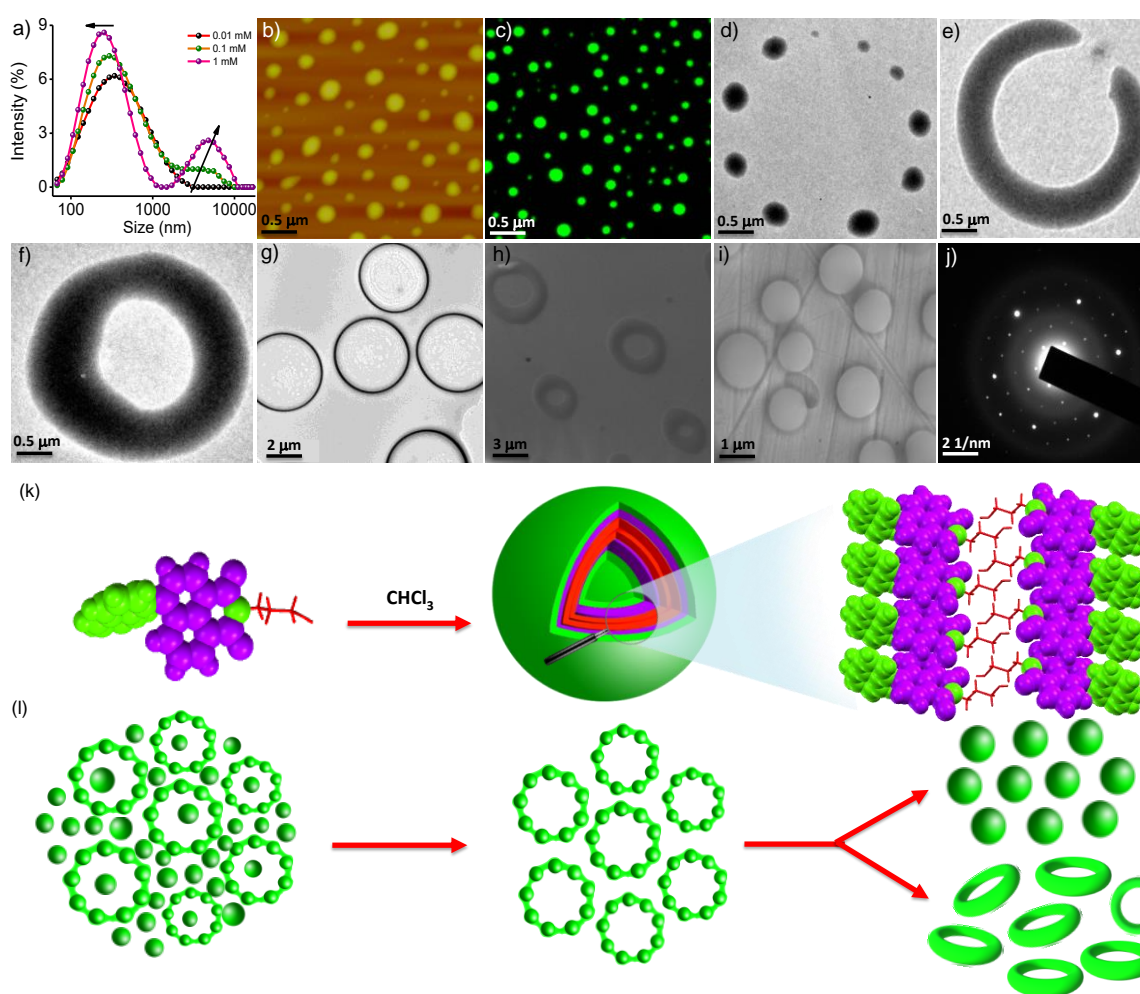
Figure 2.3. *(a) Concentration-dependent particle size distribution of NIN from DLS; (b) tapping-mode AFM, (c) confocal microscopic image of 0.1 mM NIN excited at 405 nm; TEM images of (d) 0.1 and (e-g) 1 mM NIN; (h-i) SEM image of NIN in $CHCl_3$ drop casted on carbon coated Cu substrate; (j) SAED pattern of NIN. (k-l) scheme representing time-dependent transformation of spherical aggregates into torroidal nanostructures.*

nature of NIN enables the molecule to form bilayers in $CHCl_3$ at higher concentrations resulting in small spherical architectures that transform to larger spherical/ring-like architectures, consistent with similar amphiphilic molecules [132-134]. Such bilayer assembly could maintain the donor-on-donor and acceptor-on-acceptor arrangement even in the aggregated state similar to that in the crystalline state (Figure 2.2.k-l).
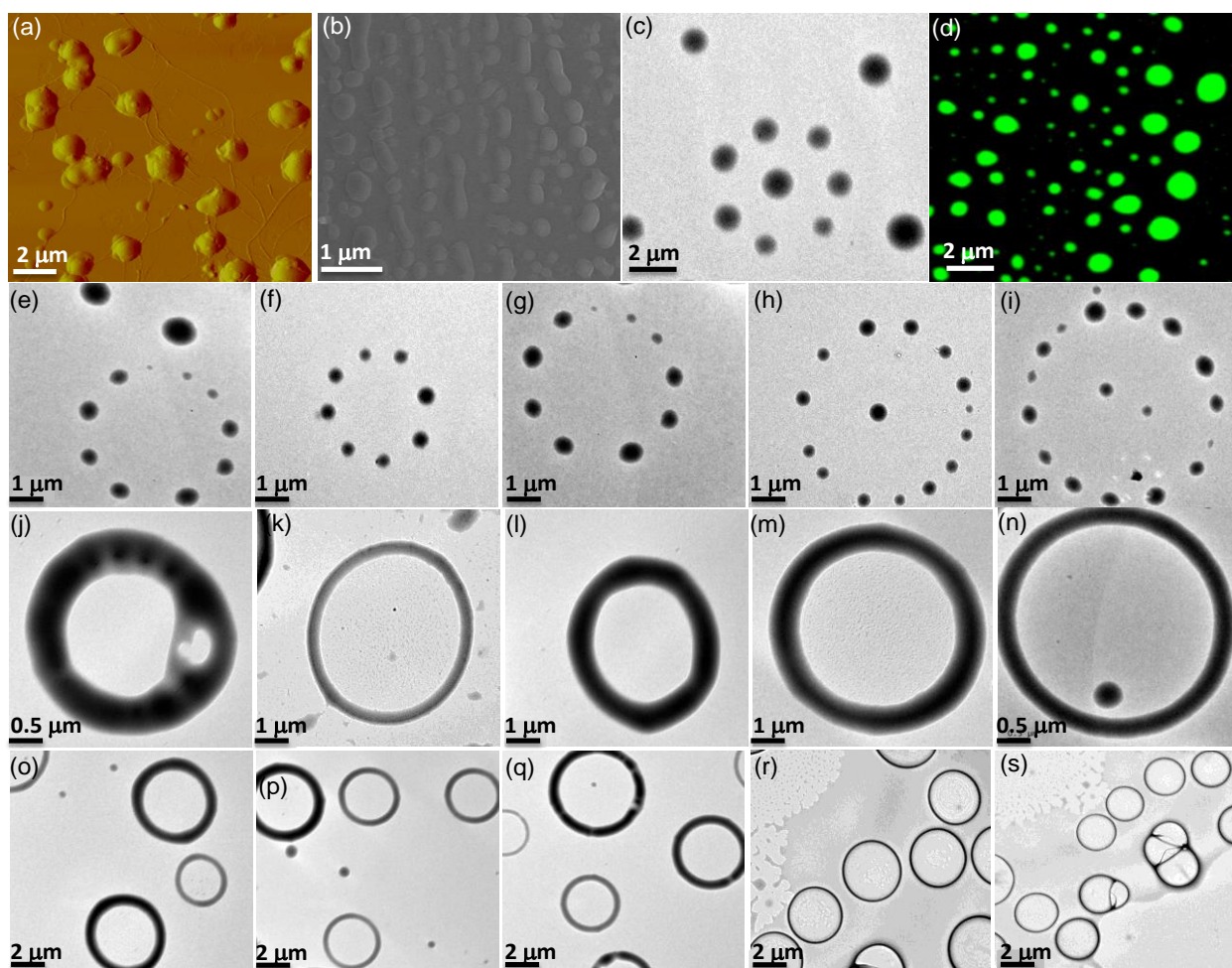
Figure 2.4. *(a), (b), (c) and (d) represent AFM, SEM, TEM, and confocal fluorescence images of 2 mM NIN drop casted from $CHCl_3$ representing larger aggregates. (e-s) TEM images of 1 mM NIN drop casted from $CHCl_3$ showing transformation of spherical aggregates to ring-like architectures.*

2.5. Frontier molecular orbital analysis

Having established the formation of nonparallel donor-on-donor and acceptor-on-acceptor stacks in the aggregated state, we have evaluated the ability of the system to prolong the long lived charge-separated states. Frontier molecular orbital (FMO), UV−Vis, fluorescence, and cyclic voltammetric measurements are employed to investigate the extent of perturbations in electronic interactions between donors (N/Ph) and acceptor (NI) in the aggregated vs monomeric state of the dyads. FMO analyses
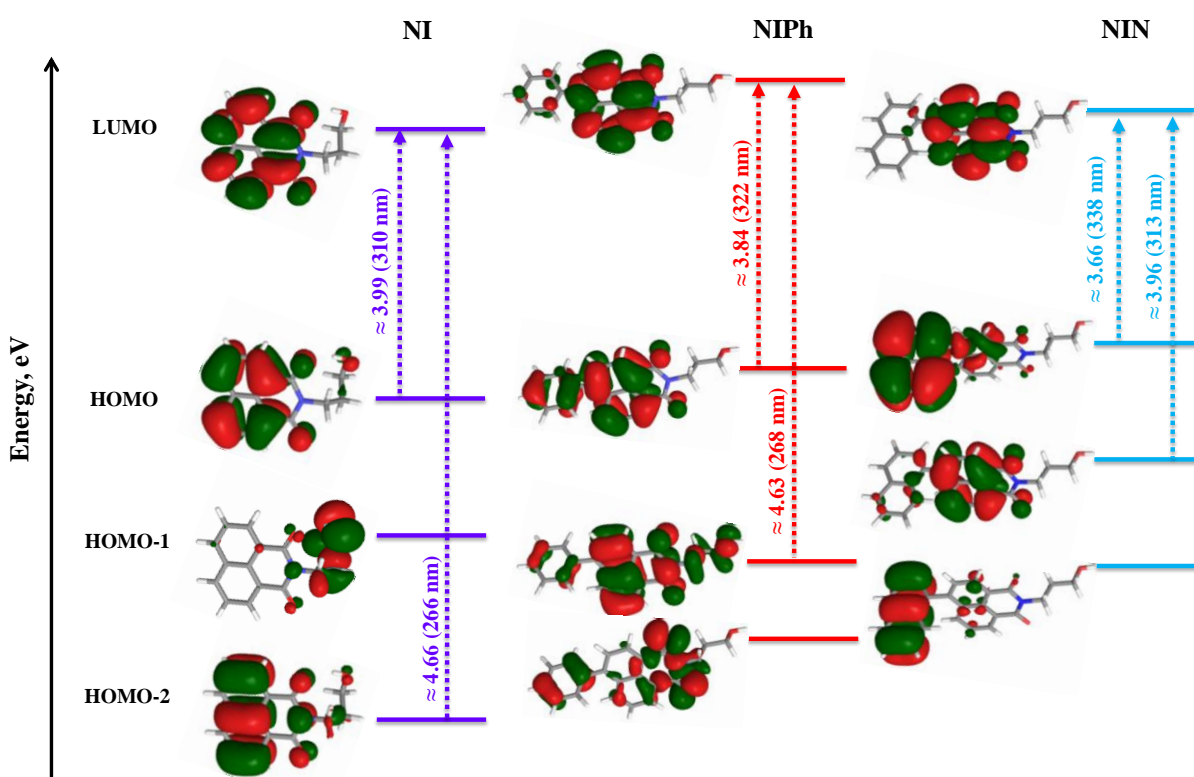
Figure 2.5. *Energy level diagram of NI derivatives calculated from B3LYP/6-311G**+ level of theory in Schrödinger Materials Science Suite using Jaguar DFT engine.*

(Figure 2.5.) of NIN and NIPh show that the electron density of HOMO is distributed in NI and N/Ph units, while electron density of LUMO is completely localized on NI unit. This is clearly suggestive of the presence of charge-transfer (CT) interaction between the constituents in the ground state consistent with 4-substituted naphthalimide derivatives reported earlier [135-137]. Similar theoretical examinations for the HOMO–LUMO energy gap (Eg, Figure 2.6.) for the di/tetrameric vs monomeric NIN indicated a
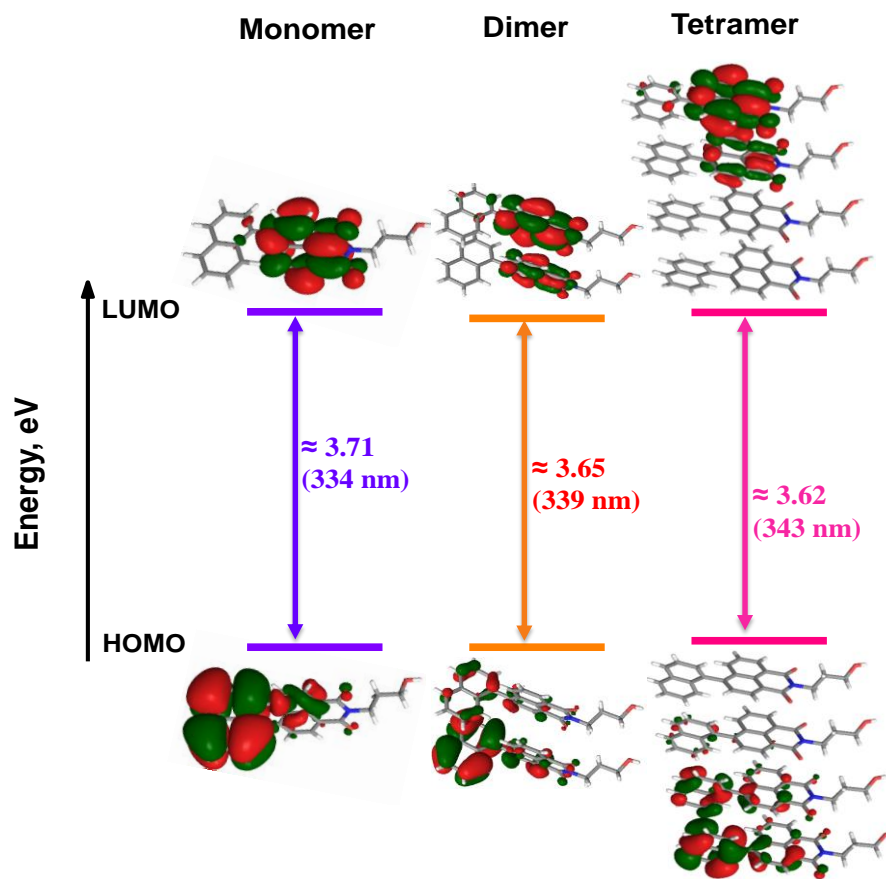
Figure 2.6. *Frontier molecular orbital (FMO) analysis of NIN (mono, di and tetramer) calculated from B3LYP-D3/6-311G**+ level of theory from crystal structure in Schrödinger Materials Science Suite using Jaguar DFT engine.*

decrease in the E*g* suggestive of the possibility of more favorable photoinduced charge separation in the aggregate when compared to the monomer [138, 139].

2.6. Steady-state absorption and emission measurements

UV−Vis absorption spectra of NIN and NIPh in ACN exhibit bands centered around 270−280 and 350−353 nm, respectively (Figure 2.7.a). Both the short and long wavelength transitions are red-shifted (∼ 8 − 11 nm) compared to that of NI. The longer wavelength band in NIN and NIPh arises from a $\pi-\pi^*$ (HOMO→LUMO) transition that has CT character [137], while the shorter wavelength band corresponds to a n−π^* (HOMO-1→LUMO) transition. Upon excitation at 340 nm, NIN and NIPh in ACN exhibit broad emission centered at 570 and 430 nm respectively (Figure 2.7.b). Time-correlated single photon counting measurements performed for NIN and NIPh in ACN exciting the samples at 375 nm displayed fluorescence lifetime of 4.15 ns and 3.55 ns respectively (Figure 2.7.c). A significant red-shift (∼ 185 nm) in the emission maximum of NIN in ACN, compared to NI, further confirms a very strong CT character in NIN (Figure 2.7.d-f).

Solvent polarity dependent spectral investigations established negligible changes in the absorption maxima and a substantial bathochromic shift of 125 and 27 nm, respectively, in the emission maxima (Figures 2.7.g-h) of NIN and NIPh respectively. With an increase in solvent polarity, a 49% enhancement in fluorescence quantum yield
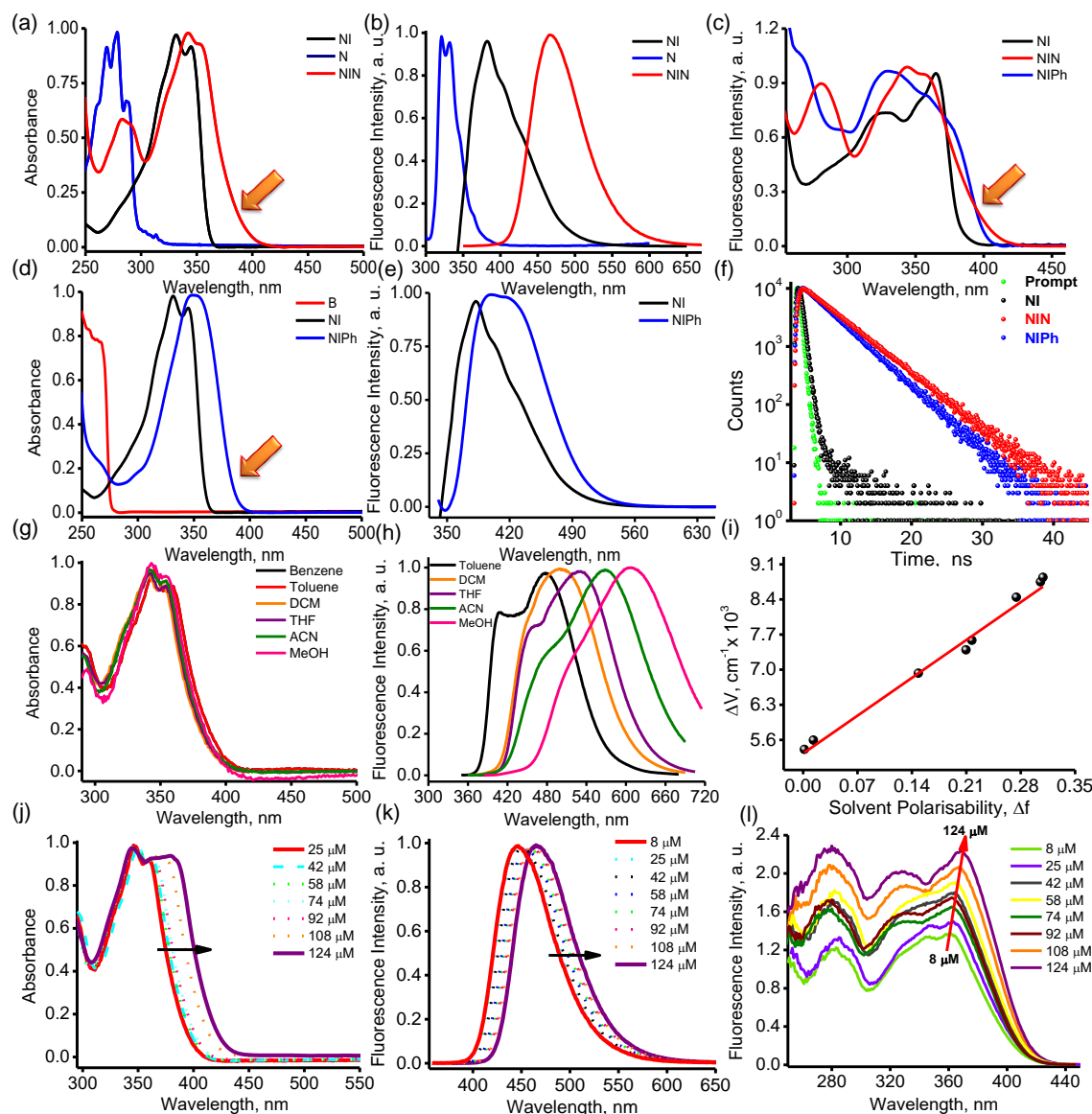
Figure 2.7. *Normalized (a) absorption spectra, (b) emission spectra (λ_{exc} = 340 nm) of N, NI and NIN in ACN, (c) excitation spectra for NI, NIN and NIPh recorded in ACN and collected at respective emission maxima, (d) absorption spectra of benzene (B), NI and NIPh, (e) emission spectra of NI and NIPh (λ_{exc} = 340 nm) and (f) fluorescence lifetime decay profiles of NI, NIN and NIPh (λ_{exc} = 340 nm). Arrow indicates the characteristic feature corresponding to aggregate. Solvent polarity dependent normalized (g) absorption spectra, (h) emission spectra, (i) Lippert-Mataga plot of NIN, concentration dependent normalized (j) absorption spectra, (k) emission spectra (λ_{exc} = 340 nm) and (l) excitation spectra collected at 470 nm of NIN in CHCl$_3$.*

Table 2.2. Photophysical properties of NI derivatives.

	Solvent	λ_{abs}, nm	λ_{ems}, nm	Φ_f	Lifetime τ, ns ($\chi2$)	k_r (ns)$^{-1}$	k_{nr} (ns)$^{-1}$
NIPh	Toluene	357	417	0.005	3.302 (1.03)	0.001	0.301
	CHCl$_3$	359	426	0.433	3.321 (1.03)	0.131	0.171
	ACN	354	430	0.303	3.551 (1.17)	0.085	0.196
	MeOH	356	440	0.403	4.710 (1.11)	0.086	0.127
NIN	Toluene	355	443	0.165	1.721 (1.02)	0.096	0.485
	CHCl$_3$	359	469	0.113	1.473 (1.01)	0.768	0.602
	ACN	355	570	0.124	4.154 (1.11)	0.029	0.211
	MeOH	357	610	0.158	4.350 (1.18)	0.036	0.193

of NIPh is observed, which could be due to the decrease in the non- radiative rate constant (Table 2.2). The difference between excited- and ground-state dipole moments in NIN and NIPh is estimated to be 8.02 and 4.17 D, respectively, employing Lippert–Mataga (LM) equation (Figure 2.7.i, see appendix). The degree of charge separation in NIN and NIPh is determined to be 38.61% and 21.10%, respectively, from the centers of the spin density distributions [140] and L-M plots (see appendix) [141]. At higher concentrations (0.125 mM) of NIN in CHCl₃, a bathochromic shift of ∼ 20 nm in UV−Vis, emission, and excitation measurements suggests the possibility of aggregation in NIN (Figure 2.7.j–l). Solvent polarity dependent absorption and emission spectral investigations corresponding to NIPh are illustrated in Figure 2.8.a-b. Under similar conditions, NIPh in CHCl₃ exhibits no characteristic features corresponding to self-aggregation (Figure 2.8.c-d) in comparison to NIN.
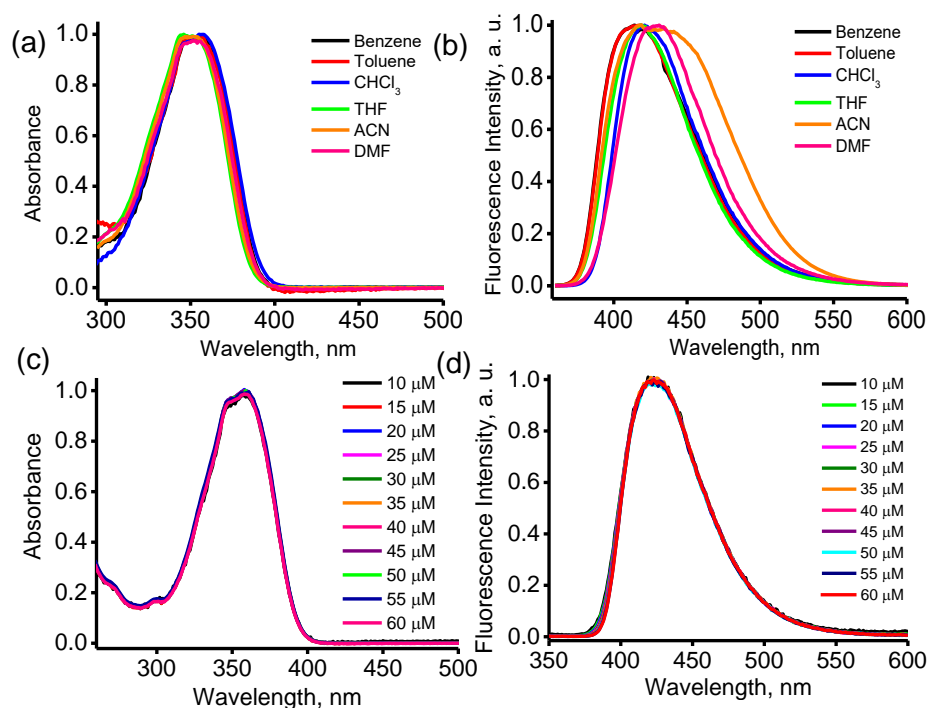
Figure 2.8. *Solvent polarity dependent normalized (a) absorption spectra, (b) emission spectra (λ_{exc} = 340 nm), concentration dependent (c) absorption spectra, and (d) emission spectra (λ_{exc} = 340 nm) of NIPh in CHCl$_3$.*

2.7. Transient absorption spectroscopic measurements

A favorable ΔG_{ET} of −0.78 eV (see appendix for Rehm−Weller analysis) [40] for photoinduced electron transfer from N to singlet excited state of NI (^{1}NI*) in NIN prompted us to employ femtosecond and nanosecond transient absorption (fTA and nTA) techniques [31, 96] to investigate the existence of charge-transfer intermediates (CTIs) in the monomeric vs aggregated state of NIN. Upon excitation at 355 nm, nTA spectra of NIN in ACN/CHCl$_3$ exhibit absorption bands centered at 400 and 480 nm
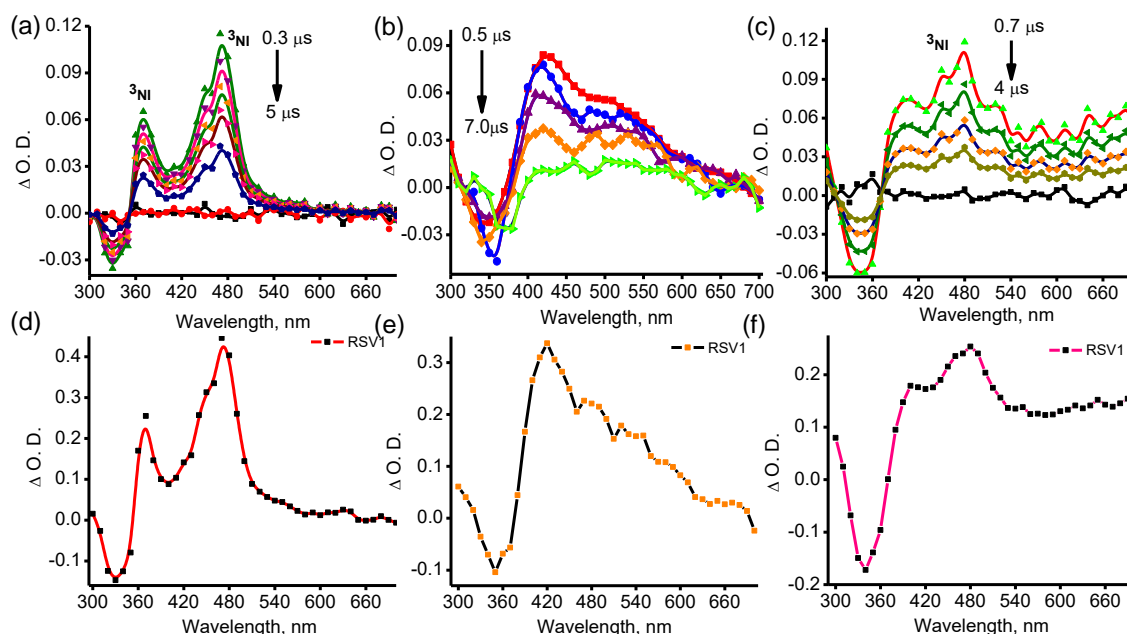
Figure 2.9. *Nanosecond transient absorption spectra of (a) NI, (b) NIPh, (c) NIN (λ_{exc} = 355 nm) in ACN and (d), (e), (f) represent corresponding right singular vectors obtained from singular value decomposition analysis.*

having a lifetime of 3.36 μs (Figure 2.9. and Table 2.3) that is characteristic of triplet absorption of NI (^{3}NI*) chromophore [142, 143]. Lack of observation of CTIs from nTA experiments of NIPh and NIN states that even if CTIs do exist in either ACN or CHCl$_3$ they recombine within the pulse width of the instrument (≥ 8-10 ns). The fTA measurement of NIN in ACN has positive absorption centered at 440 and 600 nm. NIN in ACN yielded single principal component having a lifetime of 1.99 ns, which could be attributed to the naphthalene $T_1(\pi-\pi^*)$ transition (Figures 2.10.a,c) [144, 145]. Absence of

Table 2.3. Lifetimes obtained from SVD analysis of nanosecond laser flash photolysis of NI derivatives in ACN (λ_{exc} = 355 nm).

	Lifetime (μs)	
	under N_2	under O_2
NI	5.64	1.00
NIPh	2.69	0.54
NIN	3.36	0.75

CTIs in nTA/fTA measurements with significant population of triplet excited state of N/NI substantiates ultrafast charge separation [76, 77] followed by geminate charge recombination resulting in the formation of ^{3}N*/^{3}NI* [123, 140], upon photoexcitation of NI, consistent with earlier reported similar D−A systems.
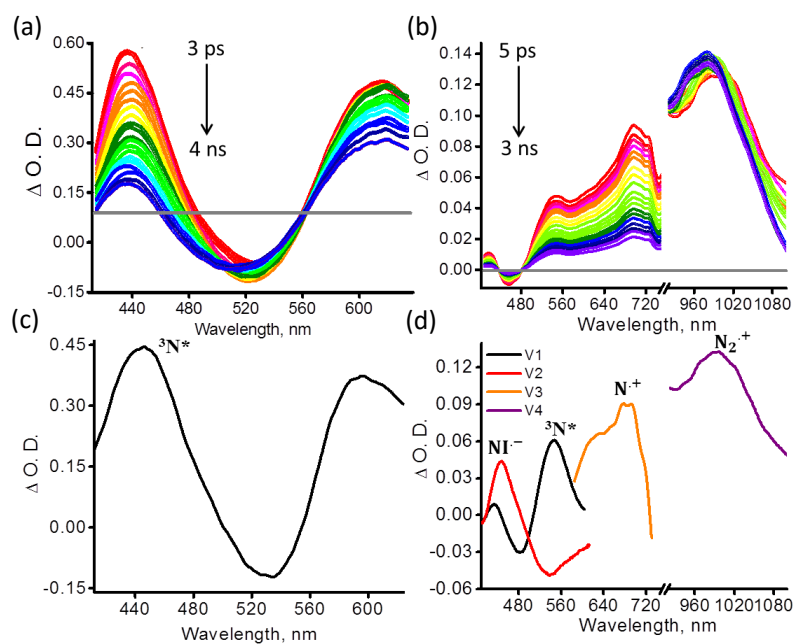
Figure 2.10. *Femtosecond transient absorption spectra of 5 mM NIN in (a) ACN and (b) CHCl₃. (c and d) Right singular vectors obtained from singular value decomposition.*

Upon excitation at 400 nm, fTA spectra of aggregated NIN in CHCl$_3$ exhibit positive absorption bands at 420, 550, 710, and 1020 nm (Figure 2.10.b,d) that consist of four principal components obtained by singular value decomposition (SVD) followed by global analyses (Table 2.4). Right singular vector at 420 nm possessing a lifetime of 1.52 ns corresponds to the naphthalimide radical anion (NI$^{\bullet-}$) [143], a twin absorption centered at 430 and 560 nm corresponds to naphthalene T$_1$($\pi-\pi^*$) transition [144, 145] that decays with a lifetime of 2.02 ns (see appendix), while the third right singular vector at 710 nm, having a lifetime of 2.53 ns, corresponds to naphthalene radical cation (N$^{\bullet+}$) [146]. We also observed a positive band centered at 1020 nm, a feature that is not
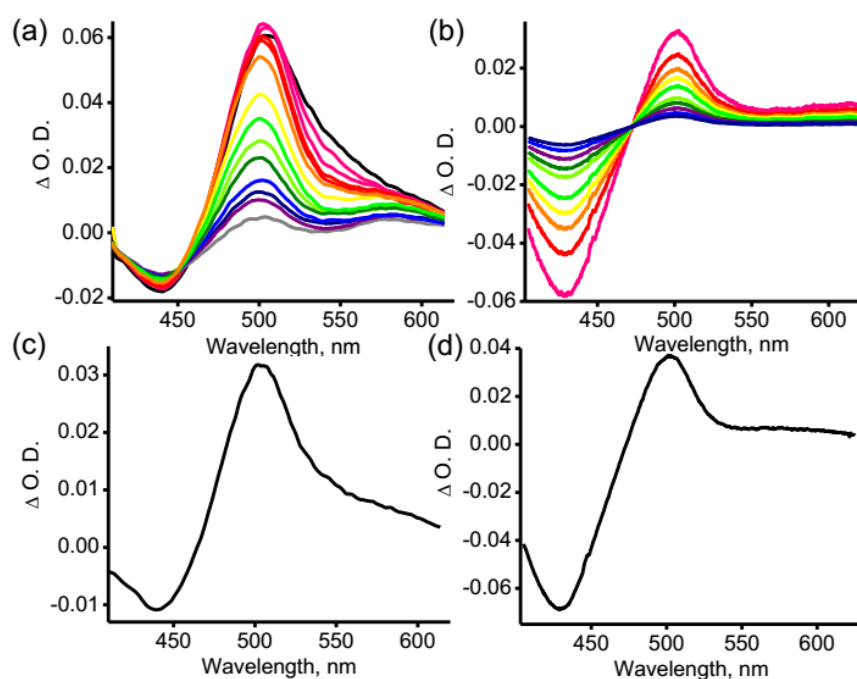
Figure 2.11. *fTA spectra of NIPh in (a) ACN, (b) CHCl$_3$ and (c), (d) represent corresponding right singular vectors obtained from global analyses.*

found in monomeric NIN, which undergoes time-dependent shift of ~ 60 nm. Positive

band centered at 1020 nm having a lifetime >1.2 ns [147] corresponds to naphthalene

dimer radical cation ($N_2^{\bullet+}$) as reported earlier [146].

Observed time-dependent shift in the peak corresponding to $N_2^{\bullet+}$ could be

attributed to the evolution of a radical cation with discrete $\pi-\pi$ stacks of naphthalene,

as observed in $\pi-\pi$ stacks of perylenimide [123]. In contrast, fTA measurements of NIPh

in ACN and CHCl$_3$ exhibit a positive absorption band centered around 550 nm which

could be attributed to the single excited state of NI (^{1}NI*). SVD analysis followed by
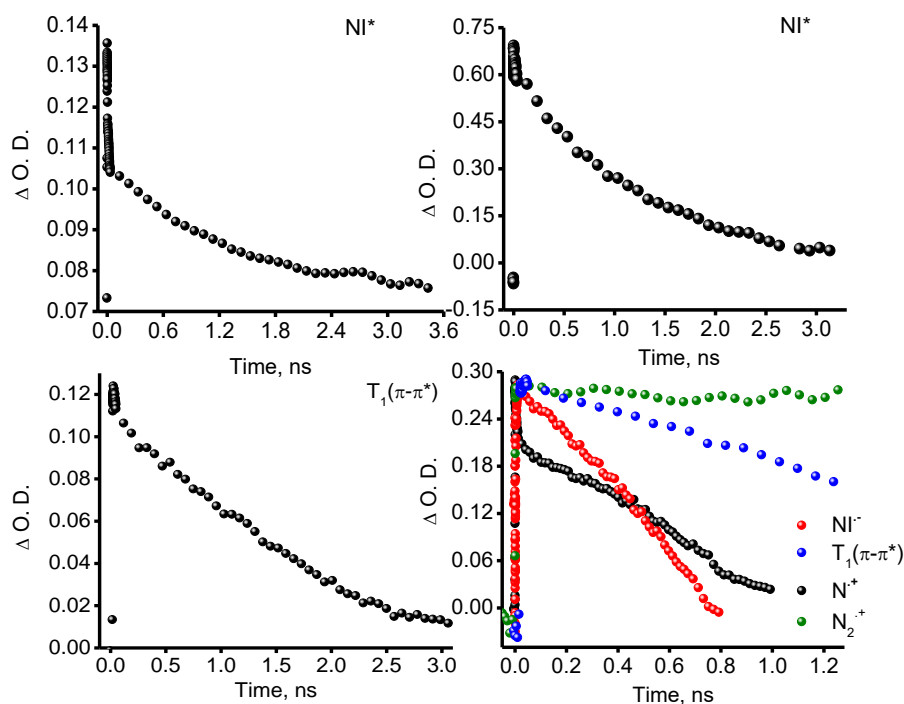
Figure 2.12. *Right singular vectors obtained from global analyses for NIPh in (a) ACN and (b)*

CHCl$_3$ respectively and NIN in (c) ACN (d) CHCl$_3$ respectively.

Table 2.4. *Lifetime obtained from global analyses of fTA spectra of NIN and NIPh (λ_{exc} = 400 nm).*

	Solvent	Lifetime (ns)				
		$NI^{\cdot-}$	$T_1(\pi-\pi^*)$	$N^{\cdot+}$	$N_2^{\cdot+}$	$^1NI^*$
NIN	ACN	-	1.99	-	-	-
	CHCl$_3$	1.52	2.02	2.53	> 1.2	-
NIPh	ACN	-	-	-	-	1.17
	CHCl$_3$	-	-	-	-	1.98

global analysis of NIPh in monomeric and aggregated state afforded one principal component centered at 500 nm having a lifetime of 1.17 and 1.98 ns respectively, corresponding to ^{1}NI* (Figure 2.11-12, Table 2.4) [148, 149].

2.8. Electrochemical measurements

Cyclic voltammetric (CV) measurements of (0.1 M *n*-Bu$_4$NPF$_6$ in ACN) NI in ACN exhibited reversible reduction potential around -1.33 V. CV of NIN and NIPh (Figure 13a and Table 2.5) displayed oxidation peaks at 1.54 and 2.48 V, while reduction peaks appeared at −1.33 and −1.30 V respectively. Ph/N substitution at fourth position of NI induced significant perturbations in the oxidation potentials as compared to unsubstituted NI, while reduction potentials (E$_{red}$ = −1.33 V vs SCE) exhibited negligible change as observed earlier [137]. At higher concentrations (15 mM, Figure 2.13.b-c), reduction of NIN in CHCl$_3$ occurs 133 mV more positive compared to that at lower
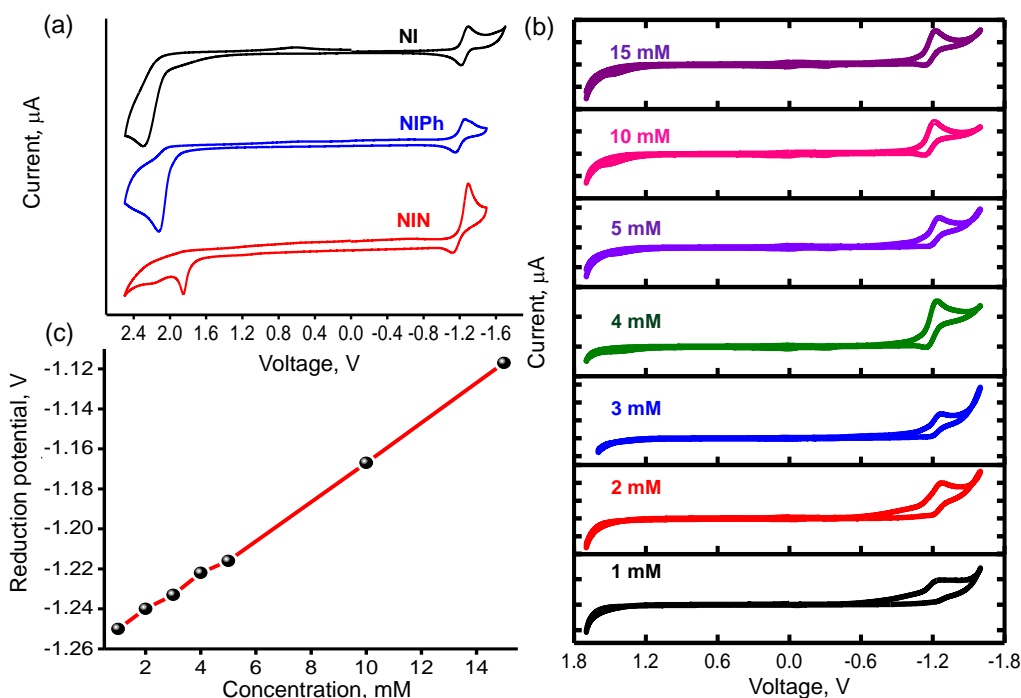
Figure 2.13. (*a*) *Cyclic voltammograms of NI, NIPh and NIN in ACN, (b) concentration dependent (1-15 mM) cyclic voltammetric measurements of NIN in CHCl₃ and (c) a plot showing variation of reduction potential of NIN with concentration.*

concentrations (1 mM). In contrast, NIPh under similar conditions (data not shown) exhibited concentration-independent redox behavior. Facile electrochemical reduction of aggregated NIN relative to monomer suggests alteration in thermodynamic feasibility for photoinduced charge separation/recombination in the monomeric vs. aggregated NIN. Such perturbations in the redox properties are a direct consequence of delocalization of hole and electron in the NIN assembly consistent with the observation of $N_2^{\bullet+}$ using fTA spectroscopy [146].

Table 2.5. Geometry optimized (B3LYP/6-311G**+ level of theory) calculations and redox properties of NIPh and NIN using in Schrödinger Materials Science Suite using Jaguar DFT engine.

| | Energy (eV) | | | | E_g (eV) | Redox Potential (V) | |
	HOMO-1	HOMO	LUMO	LUMO+1	(E_{LUMO}-E_{HOMO})	E_{ox}	E_{red}
NIPh	-7.31	-6.38	-3.28	-1.27	3.10	2.48	-1.30
NIN	-6.64	-6.14	-3.29	-1.54	2.85	1.54	-1.33

A Jablonski diagram (Figure 2.14.) depicting these excited state photoprocesses are illustrated below [41, 150]. Photoexcitation of NIN using laser pulse of 355 nm (nTA) and 400 nm (fTA) causes selective excitation of NI which promotes instantaneous
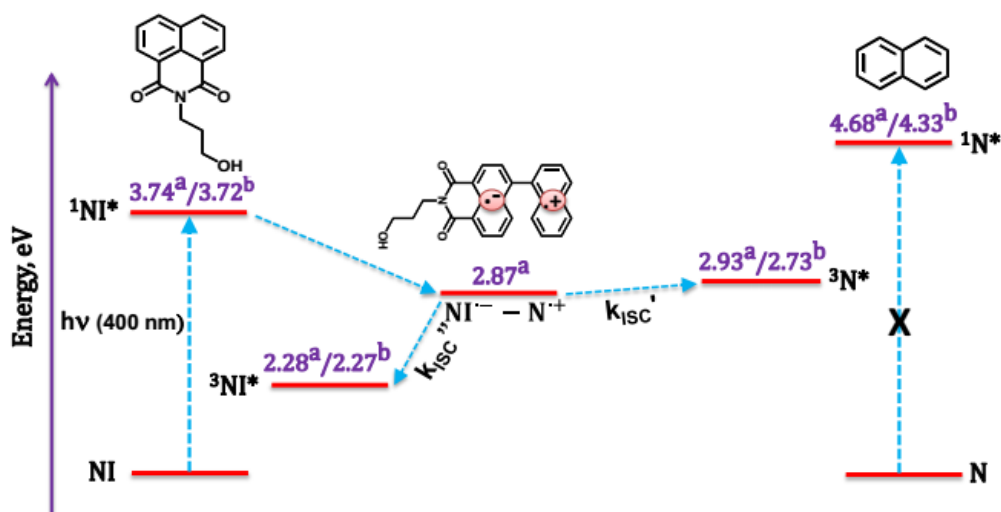
Figure 2.14. *Jablonski diagram depicting excited state energy levels of naphthalene (N), naphthalimide (NI) and the charge separated state of NIN. [a]Experimental (in eV) and [b]theoretical (in eV) energies corresponding to each levels are provided; theoretical calculations were performed at B3LYP/6-311G**+ level of theory using Gaussian-09 program suite.*

electron transfer from N to NI generating charge transfer intermediates namely $N^{\cdot+}$ and

$NI^{\cdot-}$ (E = 2.87 eV) [150].The geminate pairs thus generated undergo geminate charge

recombination, a deleterious process populating the triplet excited state of either NI

($^3NI^*$) or N ($^3N^*$). The operation of this mechanism is confirmed from the evidence that

triplet state of N is populated albeit the excitation of NI (indirect excitation) [123, 140].

Triplet excited state of naphthalene ($k_{ISC}' > 9 \times 10^{12}$ s^{-1}, $^3N^*$) and naphthalimide (k_{ISC}'',

$^3NI^*$) was probed using femtosecond and nanosecond transient absorption

spectroscopic measurements strongly suggesting the possibility of charge

separation→geminate charge recombination→triplet formation before relaxing to the

ground state in monomeric NIN ($k_{ISC}' >>> k_{ISC}''$).

2.9. Conclusion

In summary, a nonparallel segregated D−A stacked arrangement of a dyad

formed by naphthalimide and naphthalene that undergo self-assembly in $CHCl_3$ by

virtue of co-operative weak interactions is reported. The self-assembled D−A

architecture thus generated can enhance the survival time of CTIs, upon

photoexcitation, by >10^4 fold ($\tau_{cr}^{a}/\tau_{cr}^{m}$) in comparison to the monomeric NIN. Observed

long-lived CTIs in the aggregated vs monomeric state of NIN possessing simple

components could be corroborated to the synergistic effects induced by (i) nonplanar

arrangement of the D−A pair and (ii) the delocalization of excitons across the nonparallel D−A stacks.

Significant smaller increases (Table 2.6) in the survival time of CTIs, ∼1.5, 3, >100 and >150-fold are observed in the aggregated state for cylindrical melamine-perylenediimide (PDI) [83], chlorophyll-pyromellitimide-naphthalenediimide [151], guanine-PDI G-quartet [114], and diketopyrrolopyrrole (DPP)-PDI [77], respectively, in

Table 2.6. *A comparative account of the charge recombination lifetimes of photo-generated radical ion pair intermediates in the monomeric (τ_{cr}^m) and aggregated state (τ_{cr}^a) reported in various literatures.*

	Contributed by	Supramolecular D-A Structure (Reference)	τ_{cr}^m	τ_{cr}^a	$\dfrac{\tau_{cr}^a}{\tau_{cr}^m}$
1	Würthner, Meijer and coworkers	**Chiral OPV-PDI** (*JACS* **2002**, *124*, 10252)	300 ps	60 ps	0.2
2	Wasielewski and coworkers	**Cylindrical Melamine-PDI** (*Chem. Mater.* **2005**, *17*, 6295)	110 ps	164 ps	1.5
3	Wasielewski and coworkers	**Foldameric Melamine-PMI** (*JPC Lett.* **2012**, *3*, 3798)	<110 fs	261 ps	>2300
4	Wasielewski and coworkers	**Tetrameric Chlorophyll-PI-NDI** (*JACS* **2012**, *134*, 4363)	10 ns	30 ns	3
5	Wasielewski and coworkers	**Guanine-PDI G-Quadruplex** (*JACS* **2013**, *135*, 13322)	13 ps	1.2 ns	∼100
6	Braunshweig and coworkers	**Helical Diketopyrrolopyrole-PDI** (*JACS* **2014**, *136*, 7809)	<200 fs	30 ps	>150
7	Wasielewski and coworkers	**PDI-Diketopyrrolopyrole-PDI** (*Chem. Sci.*, **2015**, *6*, 402)	340 ps[m]	6 ns[b]/ 4 μs[c]	∼18[b]/ 11765[c]
8	Braunshweig and coworkers	**Diketopyrrolopyrole-PDI** (*J. Phys. Chem. C* **2015**, *119*, 19584)	33 ps	32 ns	∼1000
9	Our data	**Non-Parallel Naphthalene-Naphthalimide**	<110 fs	>1.2 ns[d]	>10000

[m]monomeric state; [a]aggregated state; [b]unannealed aggregated state in thin film; [c]CH_2Cl_2 annealed aggregated state in thin film; [d]lifetime of the naphthalene dimer radical cation could not be measured due to due to the lack of NIR detector coupled to our nTA spectrometer

solution, relative to the respective monomeric dyads. In thin films, a 1000-fold enhancement in the survival time of CTIs was observed for DPP-PDI when compared to the monomer [76, 78]. Solvent vapor annealed thin films of PDI-DPP-PDI reported by Wasielewski et al. [76] yielded CTI lifetime of 4 μs. Simple design and ease of processing exploiting synergistic effects offered by various non-bonded interactions make our strategy superior in moderating the behavior of CTIs in the aggregated state compared to the earlier "emergence-upon-assembly" approaches [77, 152]. Self-assembled nonparallel D−A architectures that possess a potential barrier for charge recombination with enhanced survival time of CTIs (τ_{cr}^{a} > 1.2 ns) could serve as promising scaffold for light harvesting, molecular electronics, and novel photofunctional applications.

Chapter 3

Self-Assembled Harvesting Donor-Acceptor Trefoils: Long-Lived Charge Separated State Through Aggregation

---

Abstract

Organic photonic nanostructures, capable of efficient light harvesting and storage, provide new avenues in constructing solution processable solar cells and photovoltaic devices. Here, we demonstrate a 10^4-fold enhancement in the photoinduced charge recombination lifetime in the aggregated state of donor-acceptor (D-A) dyads and trefoils comprised of triphenylamine-naphthalimide (TN). The D-A dyads and trefoils undergo self-assembly in THF forming spherical/vesicular architectures dictated by weak co-operative intermolecular interactions in contrast to monomer in CH₃CN. Observed long-lived charge transfer intermediates in the aggregated state of TN conjugates could be attributed to the delocalization of photogenerated excitons through non-parallel D-A stacks. D-A molecular aggregates thus evolved could serve as promising scaffolds for light harvesting, molecular electronics and photofunctional applications.

or

Spherical/vesicular aggregates

$\tau_{cr} \leq 110$ fs
(ACN)

$\tau_{cr} = 2.52$ ns
(THF)
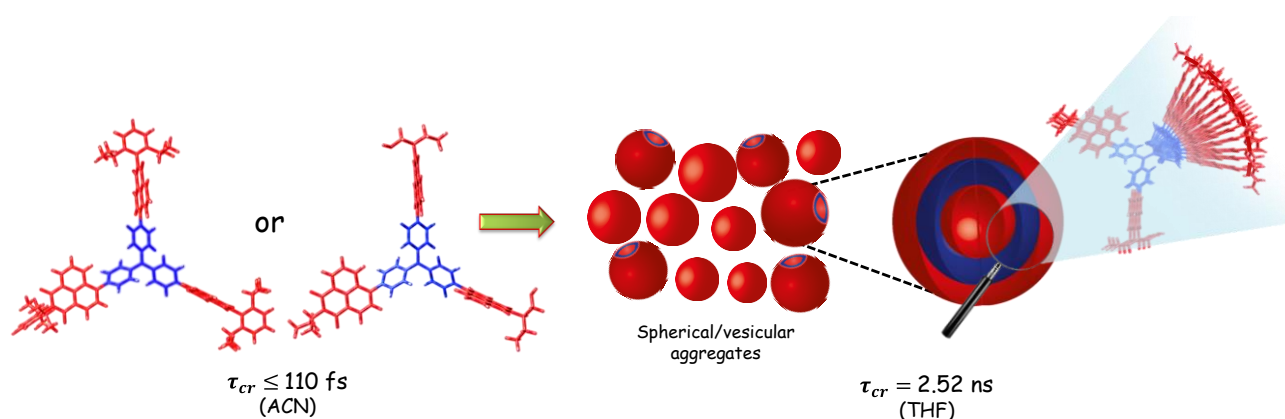
3.1. Introduction

Molecular engineering of photoconductive organic frameworks are indispensable for the development of photon-to-energy converters and organic photovoltaics (OPVs) [88, 153]. Taking cue from natural photosynthetic reaction center, [3] plethora of approaches aims at precise spatial organization of donor (D) and acceptor (A) modular fragments into hierarchical superstructures [26]. Non-covalent interactions such as electrostatic [66], dipole-dipole [65], ion-dipole [67], H-bonding [77, 113], π-π interactions [65, 74] etc. act in concert in stitching molecules together. Multi-chromophoric arrays of organic molecules that self-assemble into ordered phase-segregated D-A frameworks [2] can ensure unrestricted ambipolar charge transport of photogenerated excitons [154]. Realization of isotropic photoinduced charge transport [42] in symmetrical D-A molecular scaffolds instigated construction of easily tailorable superstructures at nanoscopic dimensions. Self-assembled C_3-symmetrical triphenylamine(T)-perylenediimide(PDI) [155], decacyclene triimides (DTI) [72, 73], 1,3,5-triphenylbenzene(P)-perylenemonoimide(PMI)/PDI [71], Melamine(M)-PDI, hexaazatriphenylene-porphyrrins, triphenylborane mesogens [156], tetrahedral tetraphenylmethane-PDI [155], ethynyl-P-linked chlorophylls [69, 70, 157] and adamentyl-naphthalenediimide(NDI) conjugates have been introduced as porous organic materials and/or for excitation energy and/or electron transfer. C_3-symmetrical D-A conjugates for enhancing the survival time of charge transfer intermediates (CTIs)

with emergent photoinduced electron transfer properties in the aggregated state relative to the monomeric state remain less explored till date.

Triphenylamine (T) is a well-identified hole transporting material with exquisite hole transporting properties exploited in OPVs. Naphthalimide (N), a less explored rylene monoimide possessing versatile electron accepting properties could serve as an electron acceptor in constructing triphenylamine-naphthalimide (TN) D-A conjugates. Our ongoing interests [129, 158, 159] towards the design of twisted D-A architectures [31, 158], for delaying the rate of charge recombination encouraged us in exploring C_3-symmetric TN conjugates for extended charge separation (Figure 3.1.). To examine the self-assembly properties of TN conjugates, hydrophyllic 1-hydroxy-2-amino-butyl (OH) and hydrophobic diisopropylaniline (DI) end groups are introduced as the side chains on N. The TN conjugates undergo self-assembly in THF forming spherical/vesicular aggregates, in contrast to monomer in acetonitrile (ACN). We herein report the first example of the formation of long-lived charge-separated states ($\tau_{cr}^a > 2.52$ ns) from the molecular aggregates of C_3-symmetrical trefoils of TN conjugates upon photoexcitation.

3.2. Syntheses and Characterization of TN Conjugates

Synthesis of NOH: 4-Bromo-1,8-naphthalic anhydride (0.50 g, 1.8 mmol, 1 eq.) was dissolved in 10 ml DMF and added 10 ml of dioxane. To this R(-)-2-amino-1-butanol (0.34 ml, 3.6 mmol, 2 eq.) was added. The reaction was refluxed with constant stirring for 24 hrs followed by bringing the reaction temperature to the room temperature. Product was precipitated from the reaction

mixture by the addition of water (50 ml) followed by filtration and the product was thoroughly washed with methanol/water (1:1) solution. The crude product thus obtained was subjected to column chromatography (SiO$_2$, acetone:DCM, 1:9) to afford a white solid (69%, m. p. = 173 °C). ^{1}H NMR (500MHz, CDCl$_3$): δ=8.59 (m, 1H), 8.52 (m, 1H), 8.35 (d, J = 10 Hz, 1H), 7.98 (d, J = 5 Hz, 1H), 7.80 (m, 1H), 5.23 (m, 1H), 4.16 (m, 1H), 3.91 (m, 1H), 2.01 (m, 2H), 0.91 (t, J = 15 Hz, 3H); ^{13}C NMR (125 MHz, CDCl$_3$): δ=164.82, 133.35, 132.37, 131.56, 131.17, 130.55, 129.10, 128.15, 123.13, 122.24, 77.27, 63.59, 57.32, 21.30, 11.00; IR (KBr): 3512.37, 3086.11, 2964.59, 2875.86, 1695.43, 1654.92, 1581.63, 1363.67, 1240.23, 1047.35, 975.98, 779.24 cm^{-1}. HR-MS (EI)-(m/z): 347.01. Calcd for C$_{16}$H$_{14}$BrNO$_3$: 346.50; Anal. Calcd for C$_{16}$H$_{14}$BrNO$_3$: C, 55.19; H, 4.05; N, 4.02. Found: C, 55.30; H, 3.89; N, 3.95.

Synthesis of NDI: To a solution of 1,8-naphthalic anhydride (5.05 mmol) in 100 ml of acetic acid, 2,6-diisopropylaniline (50.5 mmol) was added and heated at 110 °C for 5 h. The reaction mixture was then cooled, filtered, washed with water and dried. Purification by column chromatography (silica gel, ethylacetate:hexane, 3:7) afforded NBr as a white solid (95%, m. p. 130 °C); ^{1}H NMR (500 MHz, CDCl$_3$): δ = 8.66 (d, J = 10 Hz, 1H), 8.60 (d, J = 10 Hz, 1H), 8.42 (d, J = 10 Hz, 1H), 8.04 (d, J = 10 Hz, 1H), 7.84 (t, J = 15 Hz, 1H), 7.42 (t, J = 15 Hz, 1H), 7.26 (d, J = 10 Hz, 2H), 2.66 (m, 2H), 1.08 (d, J = 5 Hz, 12H); ^{13}C NMR (125 MHz, CDCl$_3$): δ = 133.61, 132.59, 131.75, 131.21, 130.94, 130.66, 130.56, 129.70, 129.63, 128.20, 124.07, 123.19, 122.31, 29.18, 23.96; IR (KBr): 2962.66, 2866.22, 1710.86, 1672.28, 1587.42, 1460.11, 1352.10, 1238.30, 1186.22, 962.48, 900.76, 783.10, 511.14 cm^{-1}; HR-MS (EI)-(m/z): 435.0389. Calcd. for C$_{24}$H$_{22}$BrNO$_2$: 435.0895; Anal. Calcd. for C$_{24}$H$_{22}$BrNO$_2$: C, 66.03; H, 5.11; N, 3.17. Found: C, 66.06; H, 5.08; N, 3.21.

Synthesis of TNOH: To a solution of 4-bromo-N-(-1-(hydroxymethyl)propyl)-naphthalene-1,8-dicarboximide (1.1 mmol) in 40 ml THF, 20 ml of 2 M aqueous K_2CO_3 solution was added under nitrogen atmosphere. To this solution, 1.1 mmol of 4-(diphenylamino)phenylboronic acid was added followed by Pd(PPh$_3$)$_4$ (14.7 μmol). The reaction mixture was heated at 70 °C for 12 h. The reaction mixture was allowed to cool down, and then it was extracted with dichloromethane. The solvent was removed under reduced pressure and the residue purified by column chromatography (silica gel, EtOAc:hexane, 5:5) to afford yellow amorphous TNOH powder (88%). m. p. 370 °C; ^{1}H NMR (500 MHz, CDCl$_3$): δ = 8.67 (d, J = 8.5 Hz, 2H), 8.45 (d, J = 8.5 Hz, 1H), 8.08 (d, J = 8 Hz, 2H), 7.87 (t, J = 10 Hz, 2H), 7.76 (t, J = 10 Hz, 2H), 7.40 (d, J = 10 Hz, 2H), 7.36 (d, J = 10 Hz, 2H), 7.24 (d, J = 8.5 Hz, 4H), 7.14 (d, J = 8.5 Hz, 2H), 5.35 (m, 1H), 4.26 (m, 1H), 4.03 (m, 1H), 2.12 (m, 2H), 1.03 (m, 3H); ^{13}C NMR (125 MHz, CDCl$_3$): δ = 148.44, 147.33, 146.98, 133.41, 133.02, 131.78, 131.21, 130.79, 129.92, 129.50, 128.99, 128.19, 127.76, 126.77, 125.08, 122.88, 122.47, 63.91, 57.03, 21.24, 11.02; IR (KBr): 3518.16, 3059.10, 2962.66, 1695.43, 1647.21, 1585.49, 1490.97, 1396.46, 1355.96, 1319.31, 1278.81, 1238.30, 1182.36, 1058.92, 783.10, 754.17, 696.30 cm^{-1}. HR-MS (EI)-(m/z): 513.2166. Calcd. for C$_{34}$H$_{28}$N$_2$O$_3$: 512.2108; Anal. Calcd. for C$_{34}$H$_{28}$N$_2$O$_3$: C, 79.67; H, 5.51; N, 5.46. Found: C, 79.65; H, 5.08; N, 5.49.

Synthesis of TNDI: To a solution of 4-bromo-N-(2,6-diisopropyl)-naphthalene-1,8-dicarboximide (1.1 mmol) in 30 ml THF, 15 ml of 2 M aqueous K_2CO_3 solution was added under nitrogen atmosphere. To this solution, 1.1 mmol of 4-(diphenylamino)phenylboronic acid was added followed by Pd(PPh$_3$)$_4$. The reaction mixture was heated at 70 °C for 12 h. The reaction mixture is then allowed to cool down, and further extracted with dichloromethane. The solvent

was removed under reduced pressure and the residue is purified by column chromatography (silica gel, DCM:hexane, 4:6) to afford yellow amorphous TNDI in moderate yield (92%). ^{1}H NMR (500 MHz, CDCl$_3$): δ = 8.73 (d, J = 10 Hz, 2H), 8.52 (t, J = 10 Hz, 1H), 7.81 (t, J = 15 Hz, 2H), 7.51 (t, J = 15 Hz, 1H), 7.44 (d, J = 10 Hz, 2H), 7.38 (m, 6H), 7.28 (m, 6H), 7.15 (t, J = 15 Hz, 2H), 2.81 (m, 2H), 1.20 (m, 12H); ^{13}C NMR (125 MHz, CDCl$_3$): δ = 164.40, 148.44, 147.34, 145.70, 133.14, 131.71, 131.45, 130.30, 129.52, 127.77, 126.77, 125.12, 124.02, 123.71, 122.48, 121.32, 29.16, 24.01. IR (KBr): 3030.17, 2960.73, 2866.22, 1703.14, 1664.57, 1585.49, 1489.05, 1357.89, 1278.81, 1236.37, 1188.15, 835.18, 754.17, 696.30 cm^{-1}. HR-MS (EI)-(m/z): 513.2166. Calcd. for C$_{34}$H$_{28}$N$_2$O$_3$: 512.2108; Anal. Calcd. for C$_{34}$H$_{28}$N$_2$O$_3$: C, 79.67; H, 5.51; N, 5.46. Found: C, 79.65; H, 5.08; N, 5.49.
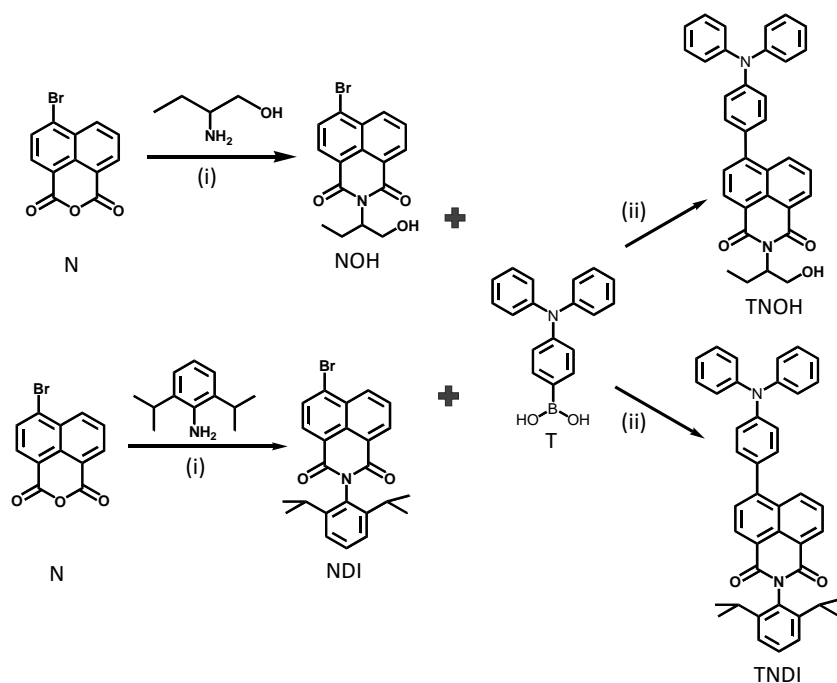
Scheme 2.1. *(i) Acetic acid; 110 °C; 5 h, (ii) Pd(PPh$_3$)$_4$; Anhyd. THF; 2 M K$_2$CO$_3$; 70 °C; 12 h.*

Synthesis of T: Tris-(4-bromophenyl)-amine (0.54 g, 2.9 mmol, 1 eq) was dissolved in 4 ml of THF; followed by cooling it to -78 °C. n-BuLi (5.2 mmol, 1.79 eq, 3.25 ml) was added dropwise

and kept at -78 °C for 1 hour. 2-isopropoxy-4, 4, 5, 5-tetramethyl-1, 3, 2-dioxaborolane (26 mmol, 8.9 eq, 4.86 ml) was added drop wise. After addition, the reaction temperature was elevated to room temperature and stirring was continued overnight. 5 ml of H_2O was added to quench the reaction. The water layer was extracted with methylene chloride for 2-3 times and the combined organic layers were dried over Na_2SO_4. After the volatile solvent was removed under reduced pressure, it was subjected to purification by column chromatography (SiO$_2$, EtOAc:hexane, 2:8) to yield the product T as white crystals. (50%, m. p. > 300 °C). ^{1}H NMR (500MHz, CDCl$_3$): δ = 7.61 (d, J = 8 Hz, 6H), 7.02 (d, J = 8 Hz, 6H), 1.233 (s, 36H), ^{13}C NMR (125 MHz, CDCl$_3$): δ = 149.8, 135.9, 123.5, 83.7, 24.9. IR (KBr): 2980.02, 1597.06, 1359.82, 1321.24, 1284.59, 1143.79, 1091.71, 860.25, 657.73 cm^{-1}. (m/Z): 623.4502. Calcd for $C_{36}H_{48}B_3NO_6$: 623.2165; Anal. Calcd for $C_{36}H_{48}B_3NO_6$: C, 69.38; H, 7.76; N, 2.25. Found: C, 69.01; H, 7.50; N, 2.18.

Synthesis of TN(OH)$_3$: 4-bromo-N-(-1-(hydroxymethyl)propyl)-naphthalene-1,8-dicarboximide (93 mg, 0.256 mmol, 3.2 eq.) was dissolved in 30 ml anhydrous THF and stirred in a N_2 atmosphere for 5 minutes. To this 15 ml of 2 M aqueous K_2CO_3 was added and stirred. T (50 mg, 0.08 mmol, 1 eq.) was added and stirred in N_2 atmosphere again for 5 minutes. Pd(PPh$_3$)$_4$ (0.89 mg, 0.01 mmol) was added and the temperatures was increased to 70 °C, and refluxed for 12 hrs. THF was removed by rotary evaporation and compound was extracted using DCM. The DCM layer was dried and the crude product obtained was subjected to column chromatography (SiO$_2$, acetone:DCM, 1:9) to afford an orange fluorescent solid (90%, m. p. > 300 °C). ^{1}H NMR (500MHz, CDCl$_3$): δ = 8.61 (m, 6H), 8.38 (d, J = 8.25 Hz, 3H), 7.72 (d, J = 9.5 Hz, 6H), 7.48 (d, J = 8.3 Hz, 6H), 7.42(d, J = 8.3 Hz, 6H), 5.27 (d, J = 6 Hz, 3H), 4.19 (t, J = 12 Hz, 3H), 3.94 (t,

J = 12 Hz, 3H), 2.06 (m, 6H), 1.98 (s, 3H), 0.98 (t, J = 9 Hz, 9H). ^{13}C NMR (125 MHz, CDCl$_3$): δ =

165.4, 147.5, 146.9, 133.8, 132.7, 131.6, 131.3, 129.8, 128.9, 127.9, 126.9, 124.4, 123.0, 121.6, 63.8,

57.1, 21.3, 11.0. IR: 3462.22, 2926.01, 2873.94, 1697.36, 1651.07, 1583.56, 1504.48, 1462.04, 1396.46,

1354.03, 1319.31, 1238.30, 1184.29, 1056.99, 837.11, 785.03, 759.95 cm^{-1}. HR-MS (EI)-(m/z):

1047.3961: Calcd. for $C_{66}H_{54}N_4O_9$: 1047.1621; Anal. Calcd. for $C_{66}H_{54}N_4O_9$: C, 75.70; H, 5.20; N,

5.35. Found: C, 75.66; H, 5.18; N, 5.39.

Synthesis of TN(DI)$_3$: The 4-bromo-N-(2,6-diisopropyl)-naphthalene-1,8-dicarboximide (104.4

mg, 0.256 mmol, 3.2 eq.) was dissolved in 30 ml anhydrous THF and stirred in a N$_2$ atmosphere

for 5 minutes. To this 15 ml of 2 M aqueous K$_2$CO$_3$ was added and stirred. T (50 mg, 0.08 mmol,

1 eq.) was added and stirred in N$_2$ atmosphere again for 5 minutes. Pd(PPh$_3$)$_4$ (0.89 mg, 0.01

mmol) was added and the temperatures was increased to 70 ^{o}C, and refluxed for 12 hrs. THF

was removed by rotary evaporation and compound was extracted using DCM. The DCM layer

was dried and the crude product obtained was subjected to column chromatography (SiO$_2$,

DCM: hexane, 6:4) to afford an orange fluorescent solid (82%, m. p. > 300 ^{o}C). ^{1}H NMR (500

MHz, CDCl$_3$): δ = 8.68 (q, J = 13 Hz, 6H), 8.46 (d, J = 8 Hz, 2H), 7.77 (d, J = 8.5 Hz, 4H), 7.72 (d, J =

7 Hz, 2H), 7.53 (d, J = 8.5 Hz, 4H), 7.48 (m, 5H), 7.44 (m, 5H), 7.33 (d, J = 8.5 Hz, 2H), 7.28 (d, J =

8.5 Hz, 6H), 2.71 (m, 6H), 1.42 (s, 36H). ^{13}C NMR (125 MHz, CDCl$_3$): δ = 163.28, 147.5, 146.9,

132.93, 131.81, 130.79, 130.40, 130.24, 130.12, 129.80, 129.24, 128.48, 126.89, 125.93, 123.47, 123.03,

122.82, 122.08, 120.70, 29.17, 22.97. IR: 2923.25, 2861.53, 1708.09, 1667.59, 1586.58, 1503.64,

1463.13, 1358.98, 1316.54, 1237.46, 1187.31, 836.27, 784.19 cm^{-1}. HR-MS (EI)-(m/z): 1311.6026:

Calcd. for $C_{90}H_{78}N_4O_6$: 1311.6125; Anal. Calcd. for $C_{90}H_{78}N_4O_6$: C, 82.42; H, 5.99; N, 4.27. Found: C, 82.38; H, 5.95; N, 5.94.
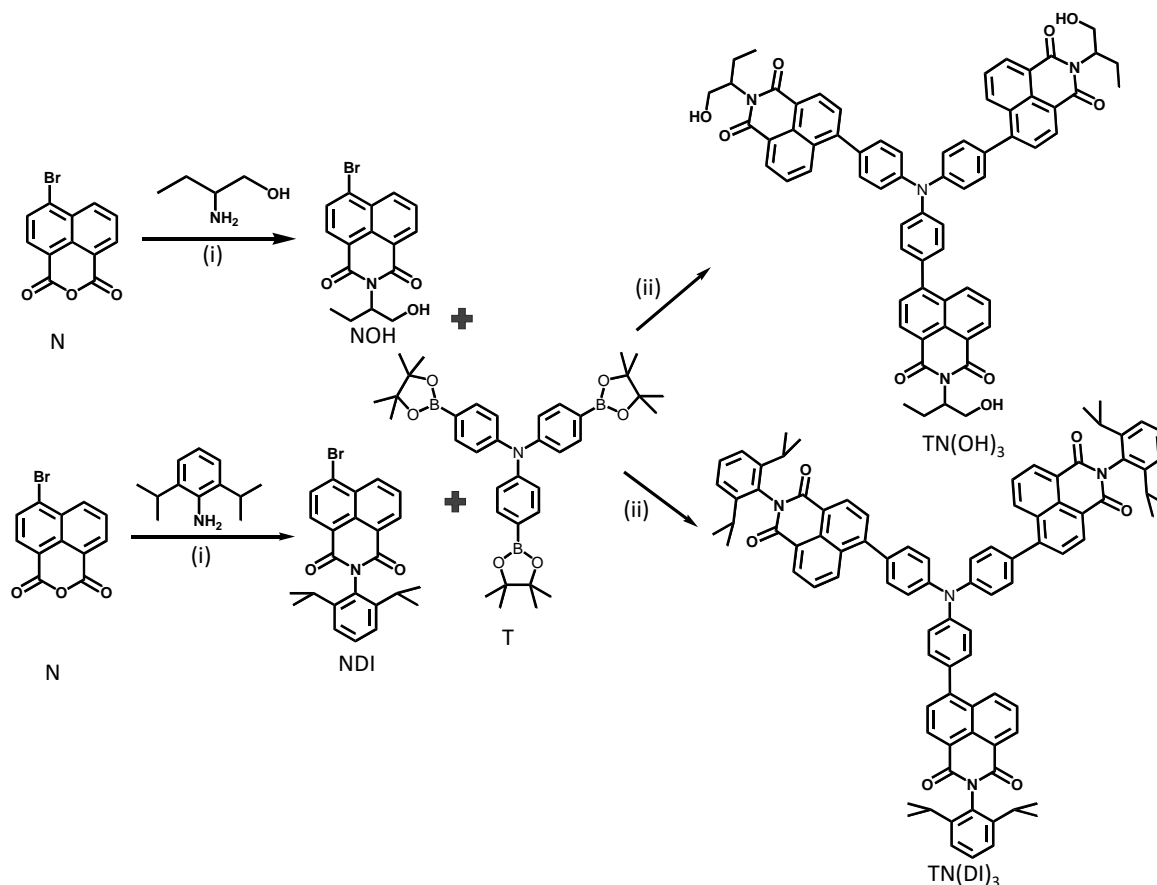
Scheme 3.2. *(i) Acetic acid; 110 °C; 5 h, (ii) Pd(PPh₃)₄; Anhyd. THF; 2 M K₂CO₃; 70 °C; 12 h.*

Palladium (0) catalyzed Suzuki-Miyaura cross-coupling reaction of NOH and NDI with 4-(diphenylamino)phenylboronic acid furnished TNOH and TNDI dyads respectively in moderate yields (Scheme 3.1., Figure 3.1.). Suzuki coupling of NOH and NDI with tris(4-(4,4,5,5-tetramethyl-1,3,2-dioxaborolan-2-yl)phenyl)amine (T) yielded the trefoils TN(OH)₃ and TN(DI)₃ respectively in low to higher yields (Scheme 3.2., Figure 3.1.). Slow evaporation of TNDI from 1:3 dichloromethane: hexane mixture
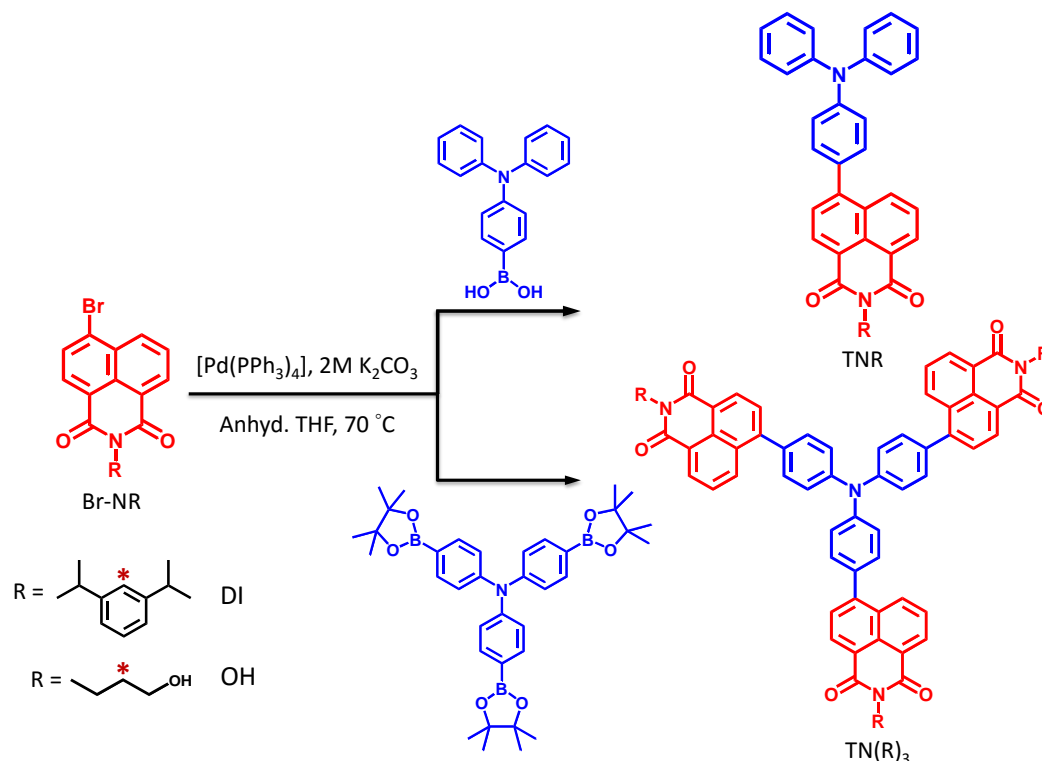
Figure 3.1. *Synthesis scheme of triphenylamine-naphthalimide dyads and trefoils.*

under ambient conditions rendered orange plate like crystals of TNDI. Single-crystal X-ray diffraction analyses of TNDI resulted in solvent free crystals belonging to monoclinic $P4_2/n$ crystal system (Table A3.1., appendix). The dihedral angle and C-C bond length between triphenylamine (T) and naphthalimide (NDI) units in TNDI are 44° and 1.49 Å respectively (Figure 3.1.-2.). π−π interaction between T and NDI units at a distance of 3.39 Å constitutes twisted self-assembled dimers in TNDI (Figure 3.2.a). (i) edge-to-face ($d_{H\cdots\pi}$ = 2.80 Å) and (ii) dihydrogen interactions [129, 130] ($d_{H\cdots H}$ = 2.39 Å) between T units together with C-H•••O interaction ($d_{H\cdots O}$ = 2.63 Å) between T and NDI units along *b*-axis dictate two-dimensional sheet like arrangement in TNDI (Figure
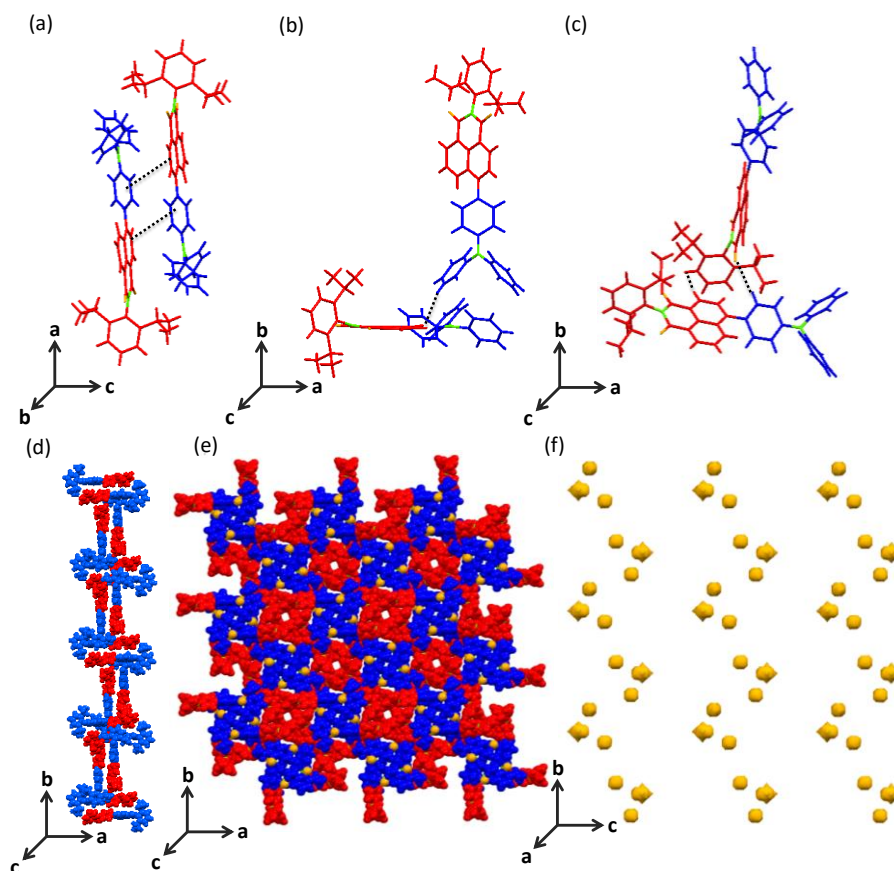
Figure 3.2. *(a) π–π, (b) C-H •••O and (c) C-H•••H-C interactions observed in crystalline TNDI. (d), (e) two dimensional solid state arrangement in TNDI. (f) pore size distribution analyses in two dimensions for TNDI.*

3.2.b-e).Examination of pore size distribution in TNDI indicated the presence of voids occupying 0.9% volume of the unit cell with a void volume of 59.7 $Å^3$. The TN conjugates explored in the current investigation could find potential application in constructing materials for gas adsorption and storage (Figure 3.2.f) consistent with the recent reports.

3.3. Hirshfeld surface and electrostatic surface potential maps

Hirshfeld surface (HS) [160] and electrostatic surface potential (ESP) [161] maps was generated for TNDI derivative (Figures 3.3.a-c). Isodensity (0.0002 e/a. u.) surface was used to construct ESP with color codes varying from red to blue representing increasing electrostatic potential from negative to positive respectively. The intense red region constitutes electron deficient carbonyl oxygen atoms corresponding to negative electrostatic potential localized on oxygen atom. Electron donating nature of T moiety is described by the light blue domains which forms a belt around the aromatic rings and are strong positive potential regions (Figure 3.3.c). Examination of 2D-fingerprint plots
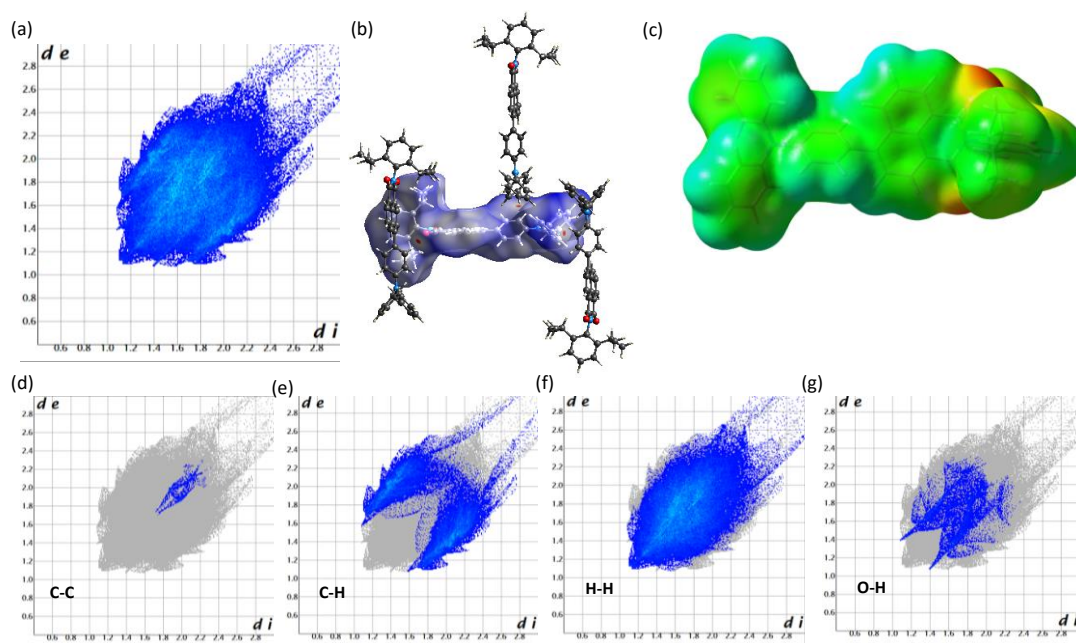
Figure 3.3. (a) *Hirshfeld surface analyses of TNDI. (d), (e), (f), (g) describes two-dimensional fingerprint plots representing π−π, C•••H, H•••H and O•••H interactions. (b) and (c) indicates d_{norm} and electrostatic surface potential maps of TNDI respectively.*

obtained from HS analyses establishes that $\pi-\pi$, C−H•••π, C−H•••H-C and C−H•••O interactions dictate packing arrangement in TNDI (Figures 3.3.d-g). A pair of wings and sharp spikes observed in the 2D-fingerprint plot of TNDI could be attributed to C−H•••O and C−H•••π interactions respectively (Figures 3.3.f-g). A value of $\rho[(\%C•••H)/(\%C•••C)]$ = 30.56 for TNDI, indicates the formation of a herringbone arrangement ($\rho > 4.5$) in the crystalline lattice. The presence of diagnostic intense red and orange hot-spots observed in distinct HS (d_{norm}) maps for TNDI (Figure 3.3.b) represents existence of short intermolecular interactions consistent with the crystal structure.

3.4. Morphological analyses

Dynamic light scattering (DLS) experiments were performed to investigate the nature of aggregation in THF solution of TN conjugates (Figure 3.4., first column). DLS measurements of 0.5 mM TNOH, TNDI, TN(OH)$_3$ and TN(DI)$_3$ in THF exhibit bimodal particle size distribution with an average hydrodynamic diameter (D_H) of 727 nm, 1.22 μm, 467 nm and 700 nm respectively as tabulated in Table 3.1. Morphological analyses of 0.5 mM TN conjugates in THF employing tapping mode atomic force (AFM), confocal, scanning (SEM) and tunneling (TEM) electron microscopy further confirmed the presence of spherical/vesicular aggregates, consistent with the DLS measurements (Table 3.1, Figure 3.4.). Selected area electron diffraction measurements of TN

Table 3.1. Particle size distribution of TNOH, TNDI, TN(OH)$_3$ and TN(DI)$_3$ in THF obtained from DLS, SEM, TEM, AFM and confocal measurements.

	DLS (Size, nm)	SEM (Size, nm)	TEM (Size, nm)	AFM (Size, nm)	Confocal (Size, nm)
TNOH	727, 5500	236	437	370	279
TNDI	1220, 5200	526	672, 1150	845, 1150	660
TN(OH)$_3$	467, 5250	272	500	271	260
TN(DI)$_3$	700	451	322	773	476

conjugates as drop casted from THF solution suggests polycrystalline nature (Figures 3.4., fifth column). The histograms representing particle size distribution of spherical/vesicular aggregates obtained from various morphological analyses are shown in Figure 3.5.a-d. The TN conjugates TNOH and TN(OH)$_3$ are amphiphilic in nature. The amphiphilicity administered by hydrophilic hydroxyl groups and hydrophobic aromatic units in TNOH and TN(OH)$_3$ enforces the formation of bilayers in THF through intermolecular hydrogen bonding interactions. TNOH and TN(OH)$_3$ undergo formation of spherical/vesicular aggregates consistent with similar amphiphilic molecules.

The mechanism of self-assembly can be envisaged by considering the steric bulk offered by the triphenylamine unit to naphthalimide units. The triphenylamine unit in
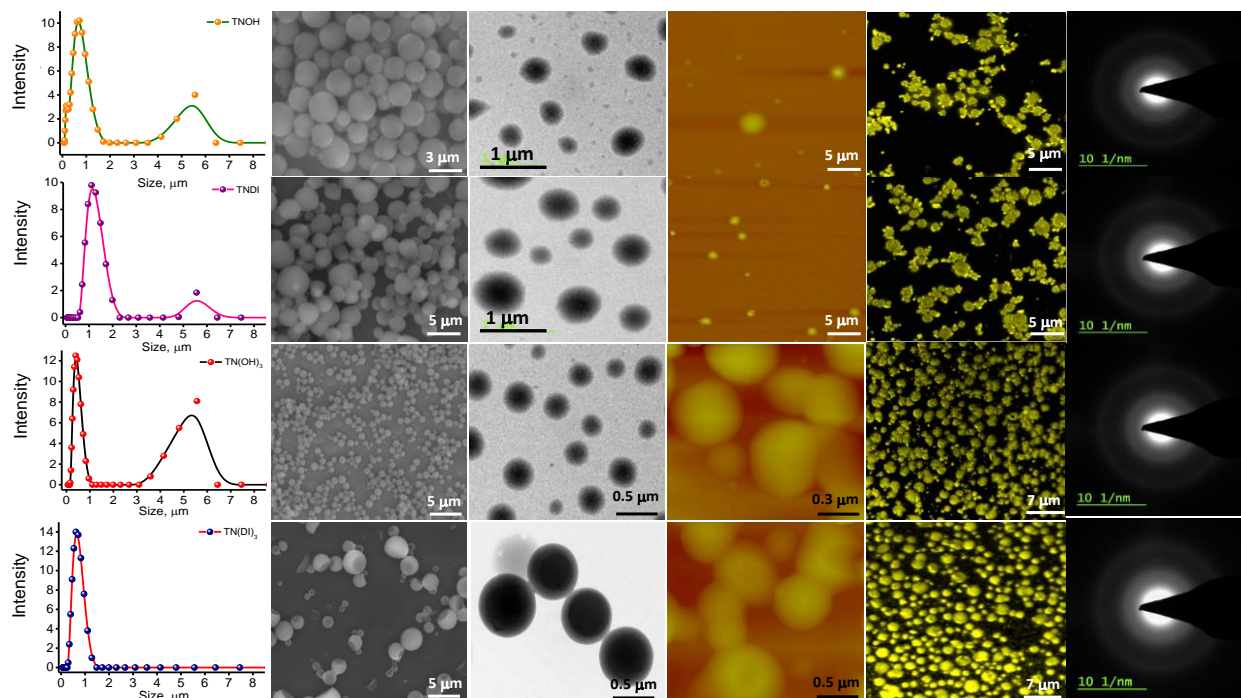
Figure 3.4. *Morphological analyses of TN conjugates. Column 1; dynamic light scattering experiments, column 2; SEM, column 3; TEM, column 4; AFM, column 5; confocal fluorescence microscopic measurements exciting the samples at 405 nm and column 6; selected area electron diffraction experiments of 0.5 mM TN conjugates as drop-casted from THF. Row 1, row 2, row 3 and row 4 correspond to morphological analyses of TNOH, TNDI, TN(OH)₃ and TN(DI)₃ respectively.*

TN conjugates possesses propeller skeleton which enforces N units to be canted out of the plane by an angle of 55° obstructing extended π-columnar arrangement of naphthalimide units. The steric bulk imposed by the T units along with co-operative non-covalent C-H•••O, C-H•••H-C and C-H•••π intermolecular interactions as observed in the crystal structure installs 'pin-wheel' arrangement in TN conjugates which further promotes formation of spherical/vesicular architectures in THF (Figure
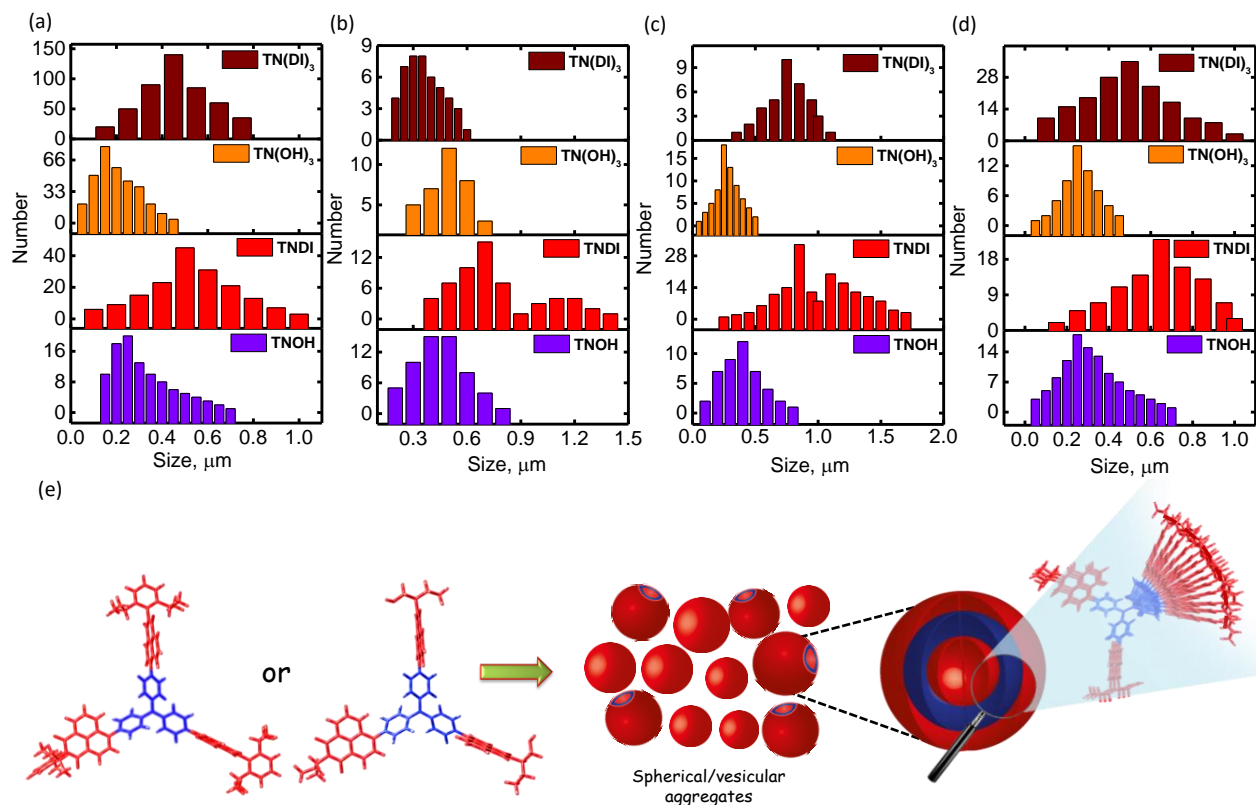
Figure 3.5. *Particle size distribution analyses of TN conjugates obtained from (a) SEM, (b) TEM, (c) AFM and (d) confocal fluorescence microscopic measurements respectively. (e) mechanism of formation of spherical/vesicular aggregates of TN conjugates in THF.*

3.5.e). It is pertinent to note that the amphiphilicity of TN conjugates do not play major role in dictating the morphology, rather the steric bulk imposed by T unit predominates because of which the donor T and the acceptor N units in TN dyads and trefoils are aligned in different planes with a dihedral angle of 44° and 55° respectively.

3.5. Frontier molecular orbital analyses

Having established the presence of spherical/vesicular aggregates in THF solution, we explored the propensity of self-assembled TN conjugates in moderating the
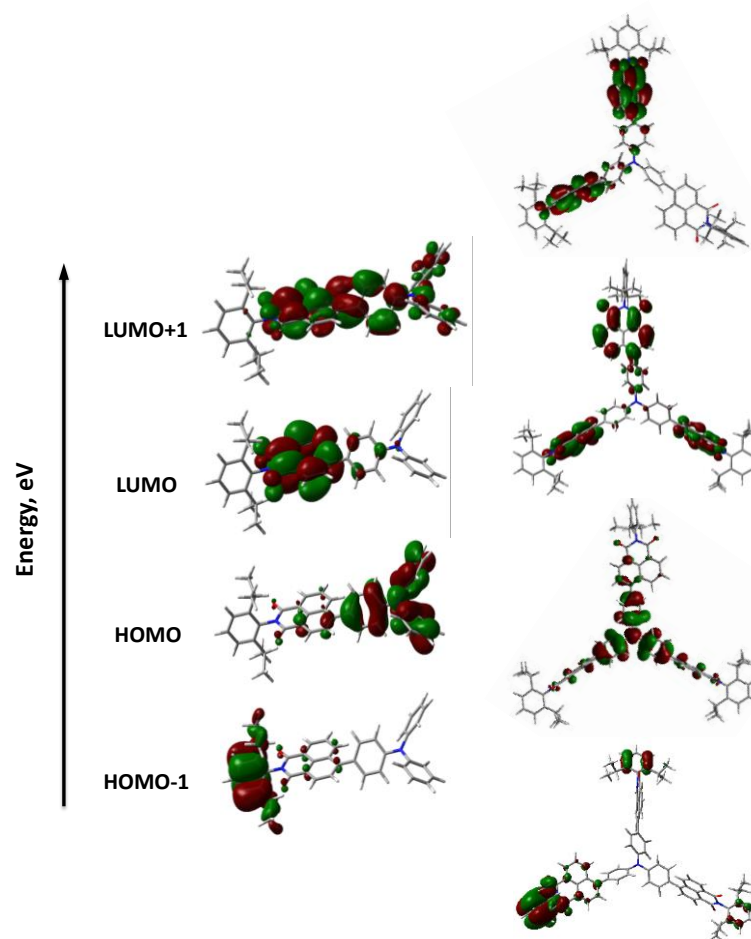
Figure 3.6. *Representative frontier molecular orbital energy diagram of TNDI and TN(DI)₃ constructed employing B3LYP/6-311G+** level of theory.*

rate of charge recombination. Existence of perturbations in the electronic interactions between D and A units in the monomeric vs. aggregated states was examined employing frontier molecular orbital (FMO) analysis, UV-Vis, fluorescence and cyclic voltammetric measurements. A representative FMO analyses of TNDI and TN(DI)₃ (Table 3.2, Figure 3.6.) indicate that the electron density of HOMO is distributed between the donor T and the acceptor NDI units for TNDI and TN(DI)₃, whereas

Table 3.2. Geometry optimized (B3LYP/6-311G**+ level of theory) calculations and redox properties of representative TN conjugates [TNDI and TN(DI)$_3$].

	Energy (eV)				E_g (eV)	Redox Potential (V)	
	HOMO-1	HOMO	LUMO	LUMO+1	(E_{LUMO}-E_{HOMO})	E_{ox}	E_{red}
TNDI	-6.45	-5.57	-2.71	-1.36	2.86	1.17	-1.22
TN(DI)$_3$	-6.32	-5.68	-2.73	-2.73	2.94	0.94	-1.17

electron density of LUMO is solely localized on NDI unit for both TNDI and TN(DI)$_3$. This observation clearly indicates the possibility of charge transfer (CT) interactions [136] existing between electronically complimentary T and NDI units in the ground state. Substitution at fourth position of naphthalimide induces significant perturbations in the ionization potentials relative to the unsubstituted NI, while electron affinity shows negligible changes as observed from the theoretical predictions [137].

3.6. Steady-state absorption and fluorescence measurements

UV-Vis absorption spectrum of T and N in ACN (Figure 3.7.a) exhibit peak centered at 310 nm for T unit and two absorption bands at 340 and 360 nm for N unit. The fluorescence spectrum of T and N in ACN has emission peaks centered at 360 and 390 nm, when excited at 310 and 340 nm respectively. The spectral overlap between emission spectrum of T and absorption spectrum of N demonstrates plausible energy transfer from T to N when T is being excited (Figure 3.7.b). The TN conjugates could

exhibit light harvesting properties wherein T acts as the donor and N the acceptor.

However focus of the present thesis is limited to electron transfer processes in the
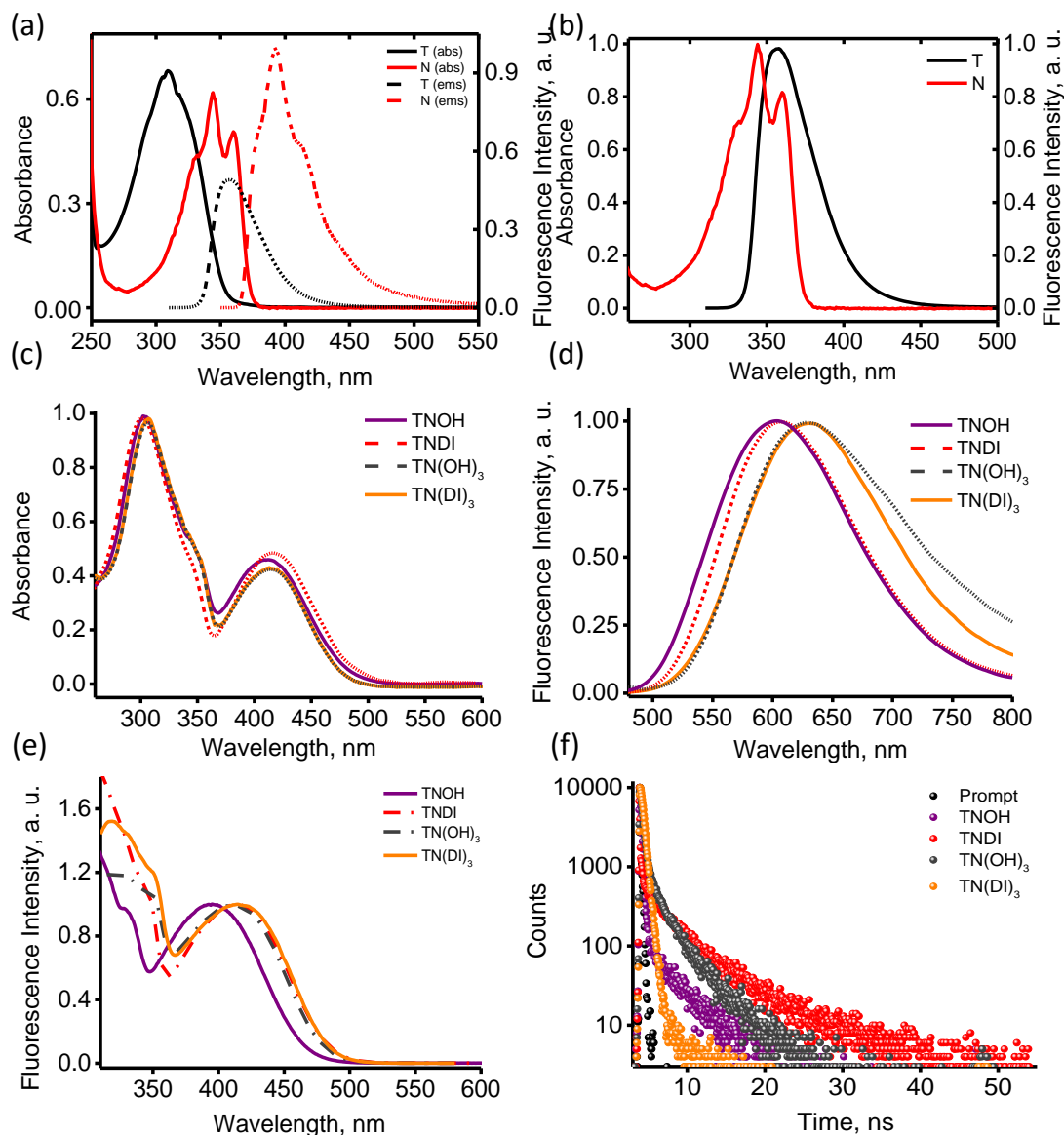
Figure 3.7. *Steady-state (a) UV-Vis and fluorescence measurements of T and N in ACN. (b) spectral overlap of emission spectrum of T with absorption spectrum of N in ACN illustrating light harvesting properties. (c) absorption and (d) emission spectrum of TN conjugates in ACN. (e) excitation spectra of TN conjugates monitored at respective emission maxima and (f) time-resolved fluorescence decay profile of TN conjugates in ACN excited at 440 nm.*

monomeric vs. aggregated state and hence light harvesting properties are not described.

Steady-state UV-Vis absorption spectrum of TN conjugates display absorption bands centered at 310 nm and 410-420 nm with a shoulder around 340 nm. The short wavelength absorption band at 310 nm is attributed to $\pi \rightarrow \pi^*$ transition corresponding to the T unit, whereas significantly red-shifted band around 410 - 420 nm is due to the CT interactions [136, 162] in TN conjugates in the grounds state as evidenced from FMO analyses (Figures 3.7.c). The shoulder band around 340 nm could be due to the HOMO-1$\rightarrow$LUMO transition observed in N unit. The emission spectrum of TN conjugates in ACN (Figure 3.7.d) exhibit emission maxima centered around 605 - 630 nm when excited at 425 nm. Significant bathochromic shift in emission maxima (ca. 200 nm) of TN conjugates when compared to the constituents T and N units suggests possibility of strong CT interaction.

Excitation spectra (Figure 3.7.e) of TN conjugates in ACN resembles corresponding absorption spectra ensuring the emissive nature of charge transfer species formed, when collected at respective emission maxima. This observation further confirms absence of electronic perturbations in the ground state of TN dyads and trefoils. Time correlated single photon counting measurements of TN conjugates when excited at 440 nm in ACN, exhibited a bi-exponential decay profile. The longer component possessing a lifetime of 2.51 - 2.56 ns corresponds to the fluorescence lifetime of the chromophore while shorter component with a lifetime of 0.17 - 0.38 ns

could be attributed to the CT states formed via photoinduced electron transfer (PET)

from T to N units in TN conjugates (Figure 3.7.f) respectively.

3.6. Solvent-polarity and concentration dependent absorption and fluorescence measurements
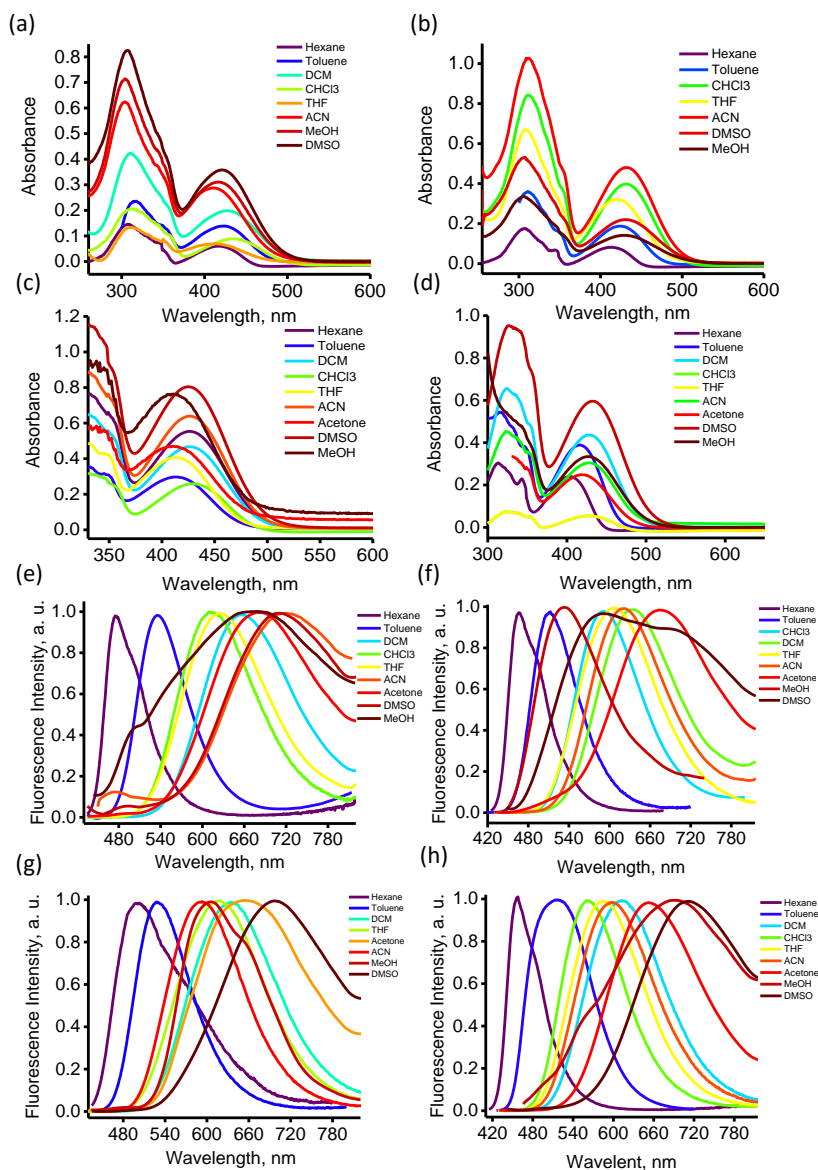
Figure 3.8. *Solvent polarity dependent (a-d) absorption and (e-h) emission spectra of TNOH, TNDI, TN(OH)₃ and TN(DI)₃ respectively.*

Solvent polarity dependent UV-Vis absorption measurements of TN conjugates established negligible changes in the absorption maxima (Table 3.3, Figures 3.8.a-d). In contrast, TNOH, TNDI, TN(OH)$_3$ and TN(DI)$_3$ displayed a substantial bathochromic

Table 3.3. Solvent polarity dependent photophysical measurements of TNOH, TNDI, TN(OH)$_3$ and TN(DI)$_3$.

Solvent	TNOH			TNDI			TN(OH)$_3$			TN(DI)$_3$		
	λ^a (nm)	λ^b (nm)	τ^c (ns)	λ^a (nm)	λ^b (nm)	τ^c (ns)	λ^a (nm)	λ^b (nm)	τ^c (ns)	λ^a (nm)	λ^b (nm)	τ^c (ns)
Hexane	415	477	3.92	413	467	4.05	414	500	4.65	405	456	2.55
Toluene	412	534	5.36	424	511	4.96	426	529	4.85	415	516	3.65
DCM	417	656	2.63	421	591	5.39	415	590	5.52	427	562	6.99
CHCl$_3$	421	611	5.65	431	606	7.43	427	635	6.67	430	585	6.27
THF	417	624	0.68	433	620	1.25	408	618	1.86	427	613	6.47
ACN	423	711	2.56 (17%), 0.17 (83%)	434	636	3.74 (12%), 0.14 (88%)	425	635	2.51 (5%), 0.36 (95%)	428	600	0.38 (87%), 0.62 (13%)
MeOH	421	672	1.26 (37%), 0.29 (63%)	431	675	2.99 (99%), 0.19 (1%)	431	638	1.69 (59%), 0.32 (41%)	428	690	≤ 0.1^d
DMSO	428	722	2.41 (8%), 0.22 (92%)	435	700	2.64 (41%), 9.30 (44%), 0.19 (15%)	431	696	0.43	434	711	0.14 (10%), 0.39 (90%)

[a] - absorption; [b] - emission; [c] - time-resolved fluorescence measurements performed exciting the samples at 440 nm; [d] - within the pulse width of the instrument.
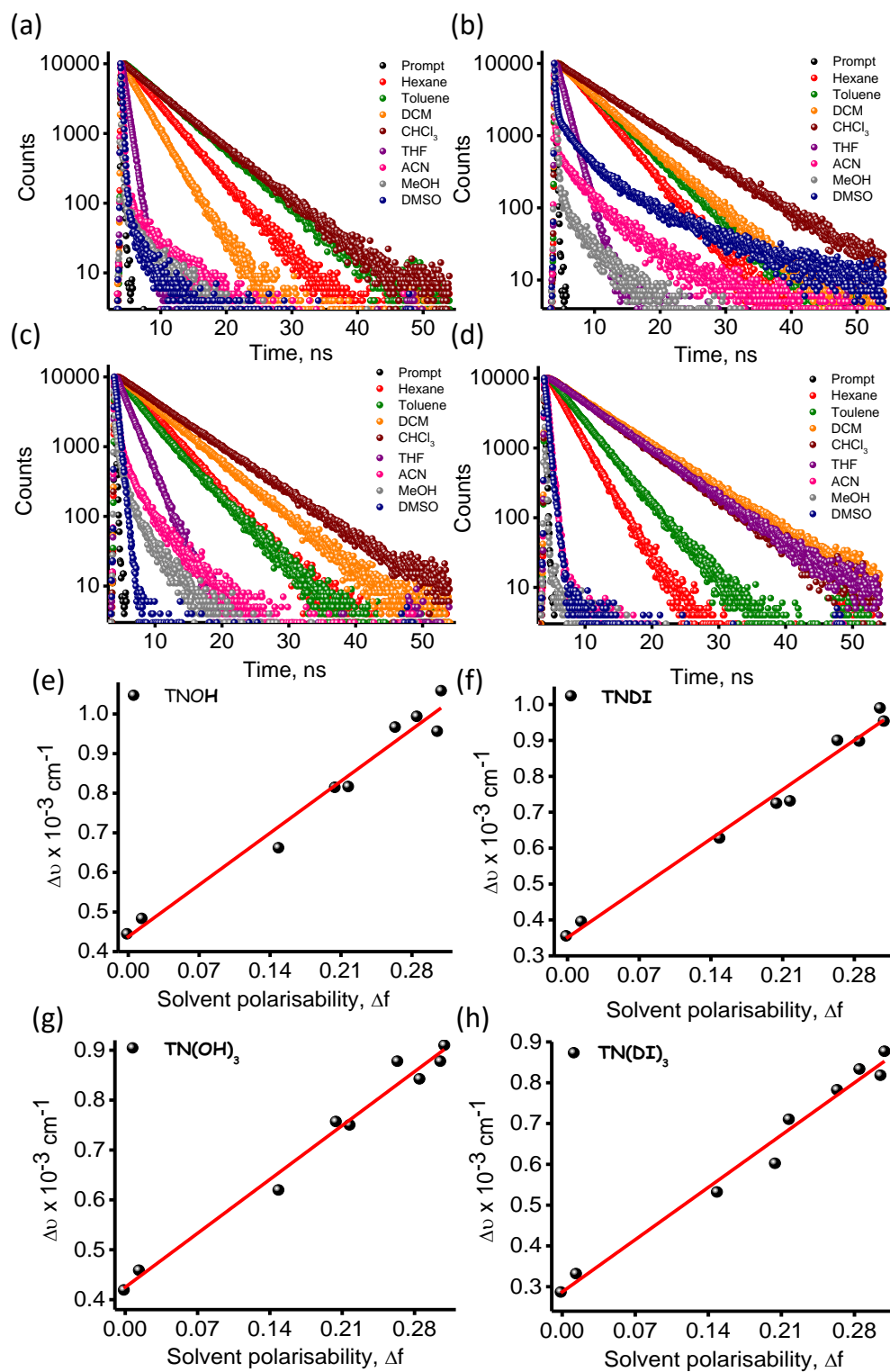
Figure 3.9. *Solvent polarity dependent (a-d) time-resolved fluorescence decay profiles excited at 440 nm and (e-h) Lippert- Mataga plots of TNOH, TNDI, TN(OH)$_3$ and TN(DI)$_3$ respectively.*

shift of 240, 235, 200 and 255 nm respectively, (Table 3.3, Figures 3.8.e-h) in the emission maxima with increasing solvent polarity. Solvent polarity dependent time-resolved fluorescence decay (τ_f) measurements of TN conjugates displayed a mono-exponential decay in non-polar solvents, while in polar solvents a bi-exponential decay profile is observed when excited at 440 nm (Table 3.3, Figure 3.9.). In nonpolar solvents PET is less favored and the decay corresponds to the τ_f of the respective molecule whereas, polar solvents facilitate stabilization of CT interactions. The species corresponding to the longer component is attributed to the τ_f of the respective TN derivatives, whereas the shorter component could be due to the CT states confirming existence of CT states in polar solvents (Table 3.3, Figures 3.9.a-d). Subsequently, with increasing solvent polarity TNOH, TNDI, TN(OH)$_3$ and TN(DI)$_3$ exhibited 70, 83, 44 and 61% reduction in fluorescence quantum yield (Φ_f, Table 3.3) respectively.

The observed decrease in Φ_f for TN conjugates with increase in solvent polarity demonstrates the possibility of photoinduced electron transfer in the dyad and trefoils. The difference between excited and ground-state dipole moment ($\Delta\mu$) in TNOH, TNDI, TN(OH)$_3$ and TN(DI)$_3$ is estimated to be 10.02, 11.59, 11.08 and 9.45 D respectively employing Lippert–Mataga equation (Equation 3.1., Figures 3.9.e-h) [141]. The degree of charge separation in TNOH, TNDI, TN(OH)$_3$ and TN(DI)$_3$ is determined to be 25.05, 26.70, 24.98 and 22.14 % respectively, from the centers of the spin density distributions [140] and Lippert-Mataga plots (see appendix).

$$\overline{\vartheta_A} - \overline{\vartheta_F} = \frac{2}{hc}\left(\frac{\epsilon-1}{2\epsilon+1} - \frac{n^2-1}{2n^2+1}\right)\frac{(\mu_e-\mu_g)^2}{a^3} + \text{constant} \tag{3.1.}$$

wherein, $\overline{\vartheta_A} - \overline{\vartheta_F}$ is the Stokes shift between absorption and emission intensity in
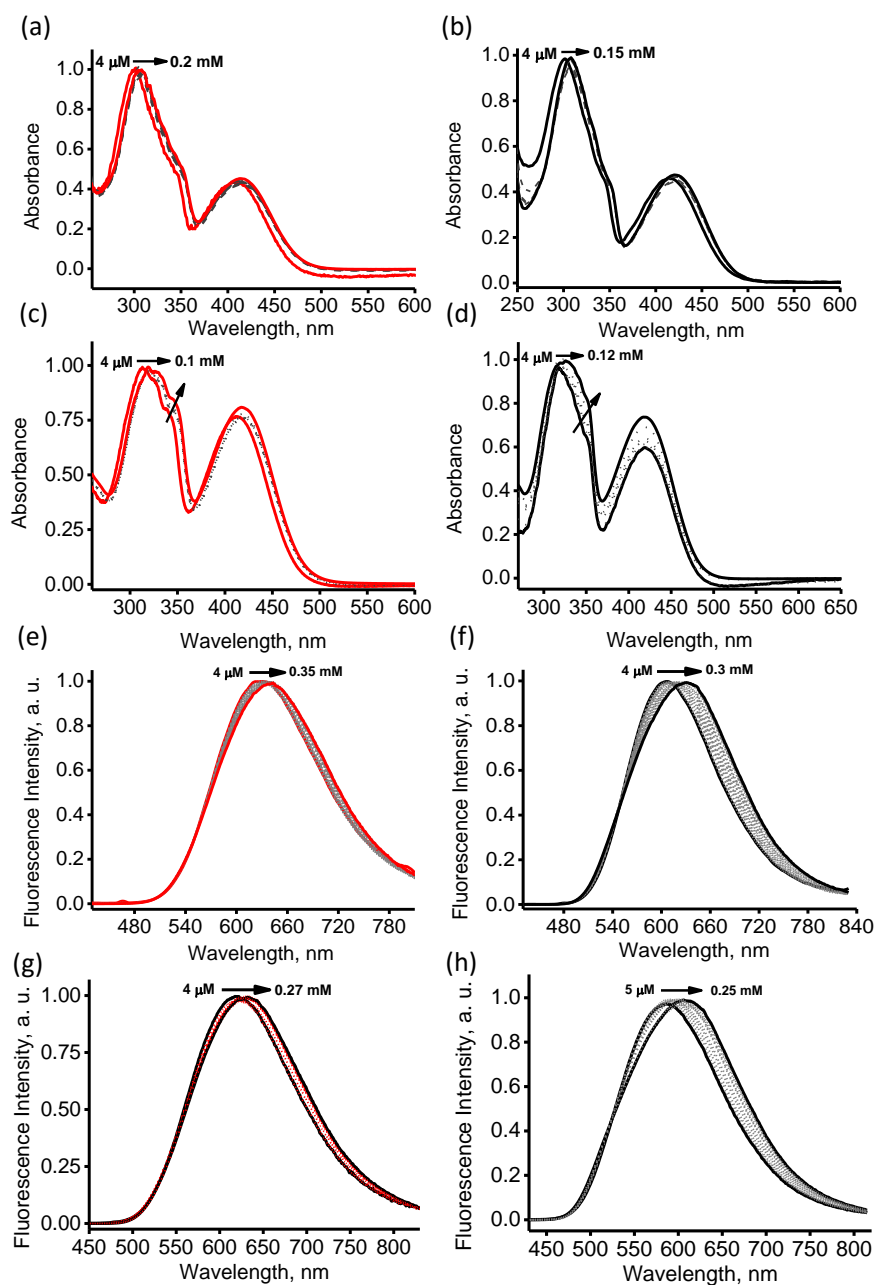
Figure 3.10. *Concentration dependent (a-d) absorption and (e-h) emission measurements (λ_{exc} = 420 nm) of TNOH, TNDI, TN(OH)₃ and TN(DI)₃ respectively in THF.*

respective solvents expressed in wavenumbers (cm^{-1}), '*h*' the Planck's constant in ergs (6.626x10^{-27} ergs), '*c*' the speed of light in cm/s (3x10^{10} cm/s) and '*a*' the Onsager cavity
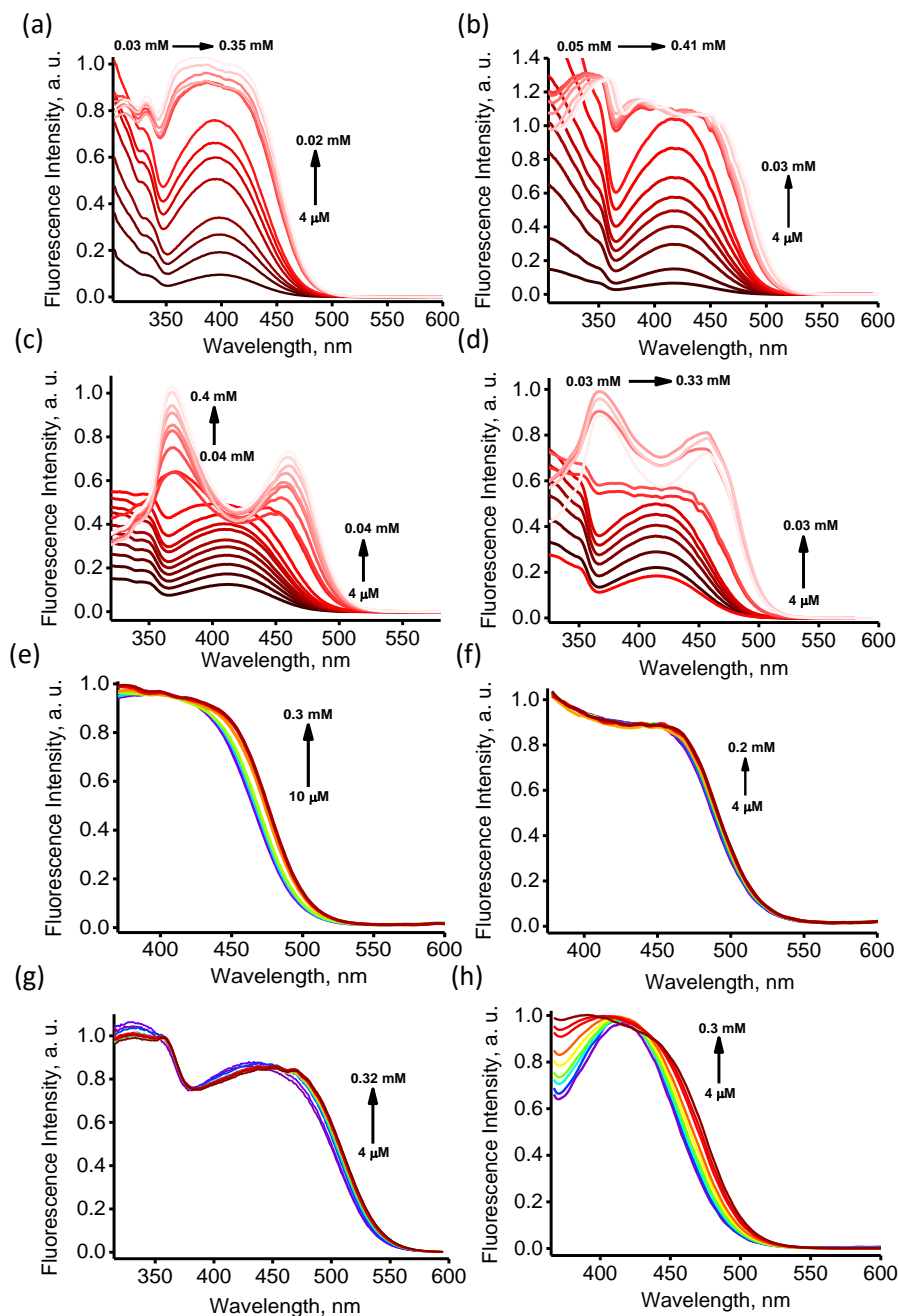
Figure 3.11. *Concentration dependent excitation spectral measurements of TN conjugates in (a-d) THF and (e-h) ACN.*

radius in which the fluorophores resides.

Concentration dependent absorption spectra of TNOH, TNDI, TN(OH)$_3$ and TN(DI)$_3$ in THF exhibited 9, 6, 5 and 7 nm bathochromic shift in the absorption band
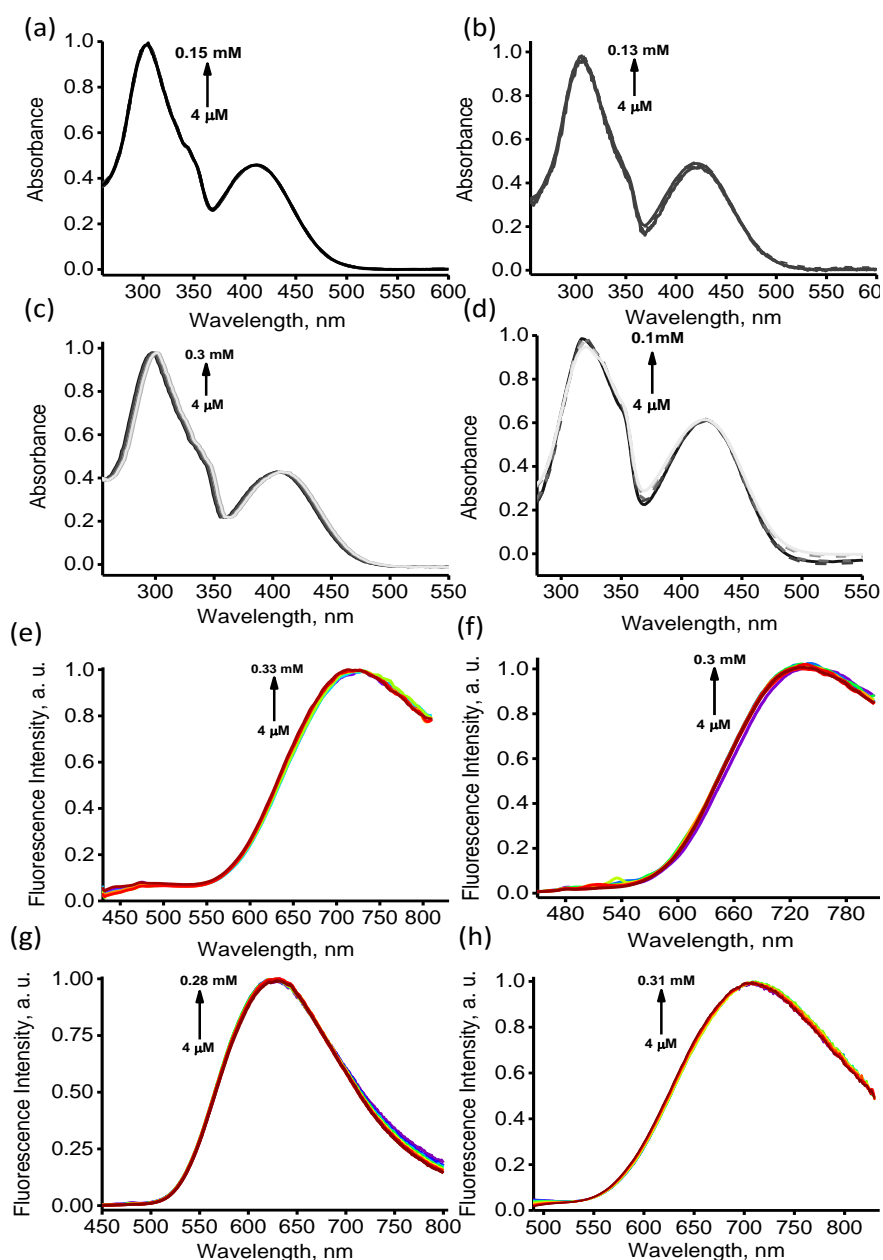
Figure 3.12. *Concentration dependent (a-d) absorption and (e-h) emission measurements (λ_{exc} = 420 nm) of TNOH, TNDI, TN(OH)$_3$ and TN(DI)$_3$ respectively in ACN.*

centered around 300 - 320 nm respectively (Figures 10a-d). Correspondingly, concentration dependent fluorescence measurements of TNOH, TNDI, TN(OH)$_3$ and TN(DI)$_3$ in THF showed 20, 15, 25 and 30 nm red-shift in the emission maxima respectively (Figures 3.1.0e-h) suggesting the probability of aggregation at higher concentrations ($\geq$ 0.3 mM). Concentration dependent excitation spectral measurements (Figures 3.11.a-b) of TNOH and TNDI in THF displayed a broad band around 350 - 450 nm with increasing concentration from 0.03 to 0.35 mM. Similarly, for TN(OH)$_3$ and TN(DI)$_3$ in THF, appearance of two new red-shifted bands at 365 and 455 nm with increasing concentration from 0.04 to 0.4 mM indicates presence of aggregates at higher concentrations (Figures 3.11.c-d). In contrast, concentration-dependent absorption, emission and excitation measurements of TN conjugates in ACN did not show aggregate formation (Figures 3.11.e-h, 3.12.).

3.8. Transient absorption experiments

The thermodynamic feasibility of PET, from T to N, in TN conjugates is evaluated employing Rehm-Weller analysis. A favourable Gibb's free energy (ΔG_{ET}) of -0.96 eV for PET is observed for TN conjugates upon photoexcitation of N. Nanosecond and femtosecond transient absorption (nTA and fTA) spectroscopic measurements were employed to examine the presence of CTIs in the monomeric and aggregated state of the TN conjugates. Upon photoexcitation of TN conjugates at 355 nm, nTA spectra of TNOH and TNDI in ACN
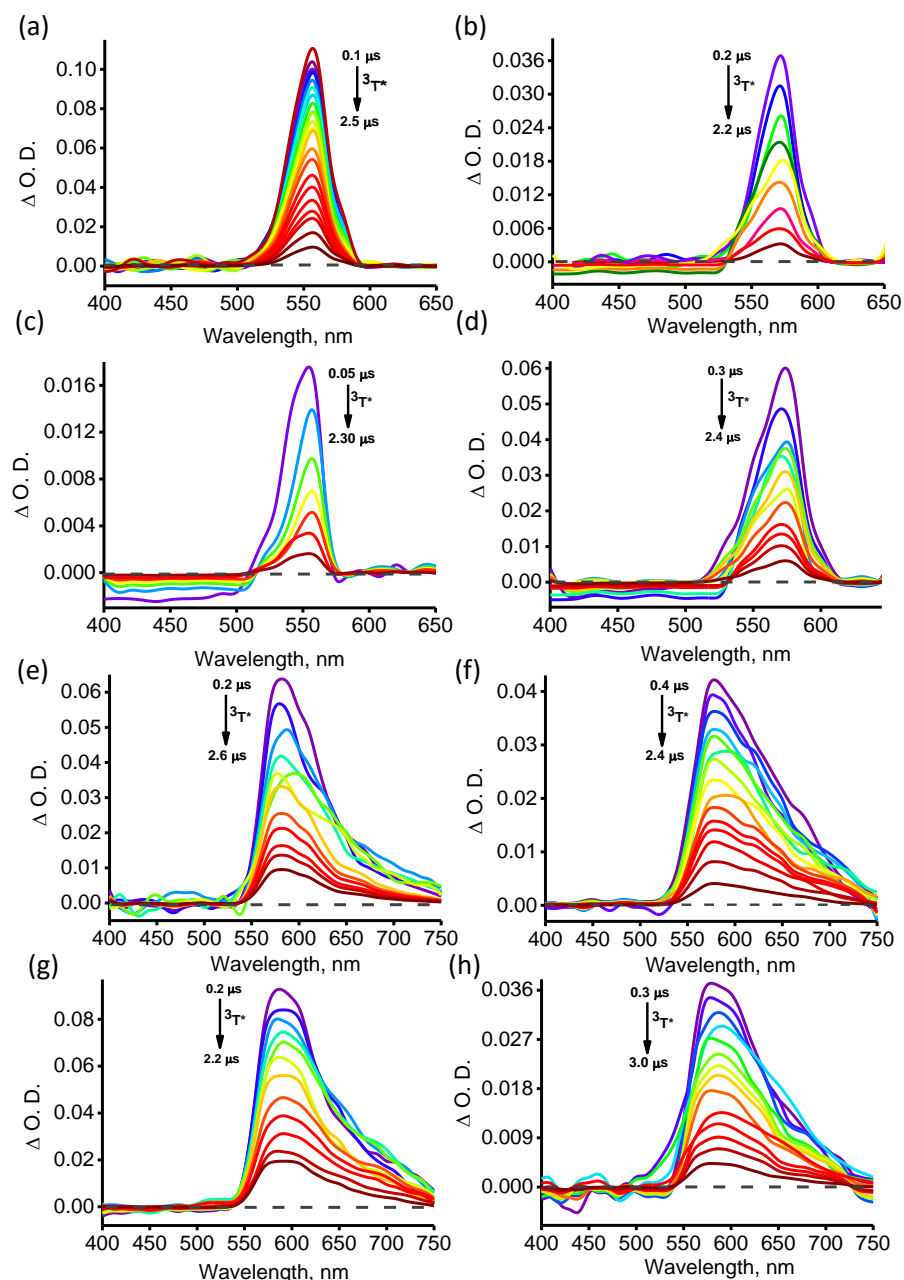
Figure 3.13. *Nanosecond transient absorption (λ_{exc} = 355 nm) spectroscopic measurements of TNOH, TNDI, TN(OH)₃ and TN(DI)₃ in the monomeric (a-d) aggregated state (e-h).*

(monomeric state), exhibited absorption centred at 555 and 570 nm respectively with a lifetime of 0.87 and 0.57 µs (Figures 3.13.a-b, Table 3.4) respectively. nTA spectra of TN(OH)₃ and TN(DI)₃ in ACN displayed positive absorption centered

Table 3.4. Lifetimes of TN derivatives obtained from kinetic analyses of nTA spectra (λ_{exc} = 355 nm).

		TNOH		TNDI		TN(OH)$_3$		TN(DI)$_3$	
		N$_2$ purging (τ, µs)	O$_2$ purging (τ, ns)	N$_2$ purging (τ, µs)	O$_2$ purging (τ, ns)	N$_2$ purging (τ, µs)	O$_2$ purging (τ, ns)	N$_2$ purging (τ, µs)	O$_2$ purging (τ, ns)
nTA	ACN	0.87	96.83	0.57	29.21	1.87	9.20	1.54	16.32
	THF	0.38	35.62	2.89	10.83	3.42	2.38	5.36	40.54

at 555 and 571 nm possessing lifetime of 1.87 and 0.57 µs (Figures 3.13.c-d, Table 3.4, Figures A3.1, appendix) respectively. nTA spectra of TNOH, TNDI, TN(OH)$_3$ and TN(DI)$_3$ in THF (aggregated state) showed a positive absorption peak
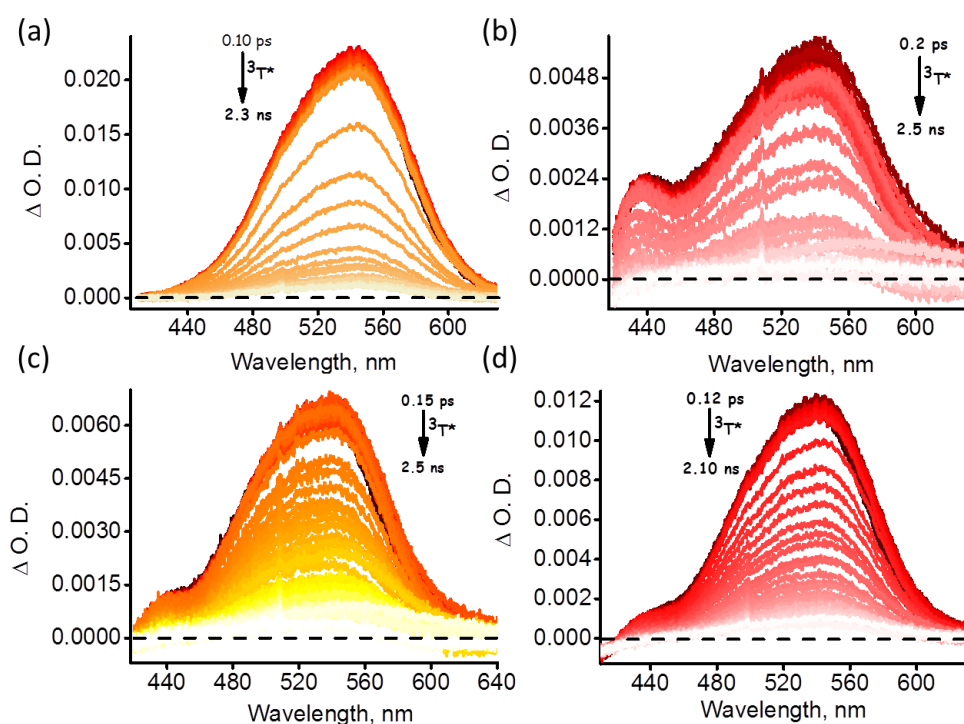
Figure 3.14. *fTA measurements of (a) TNOH, (b) TNDI, (c) TN(OH)$_3$ and (d) TN(DI)$_3$ respectively in ACN (λ_{exc} = 400 nm).*

centred at 580, 578, 585 and 580 nm having a lifetime of 0.38, 2.89, 3.42 and 5.36 µs

(Figures 3.13.e-h, A3.2, Table 3.4, appendix) respectively. The positive absorption

band centered around 555-580 nm observed in the nTA measurements of

monomeric and aggregated state of TN conjugates is attributed to the triplet

absorption of T (^{3}T*) [163]. nTA measurements of TN derivatives in the

monomeric and/or aggregated state failed to detect the presence of CTIs, upon

excitation at 355 nm. Lack of signals corresponding to the CTIs from nTA

measurements of TN conjugates, could be attributed to the ultrafast charge
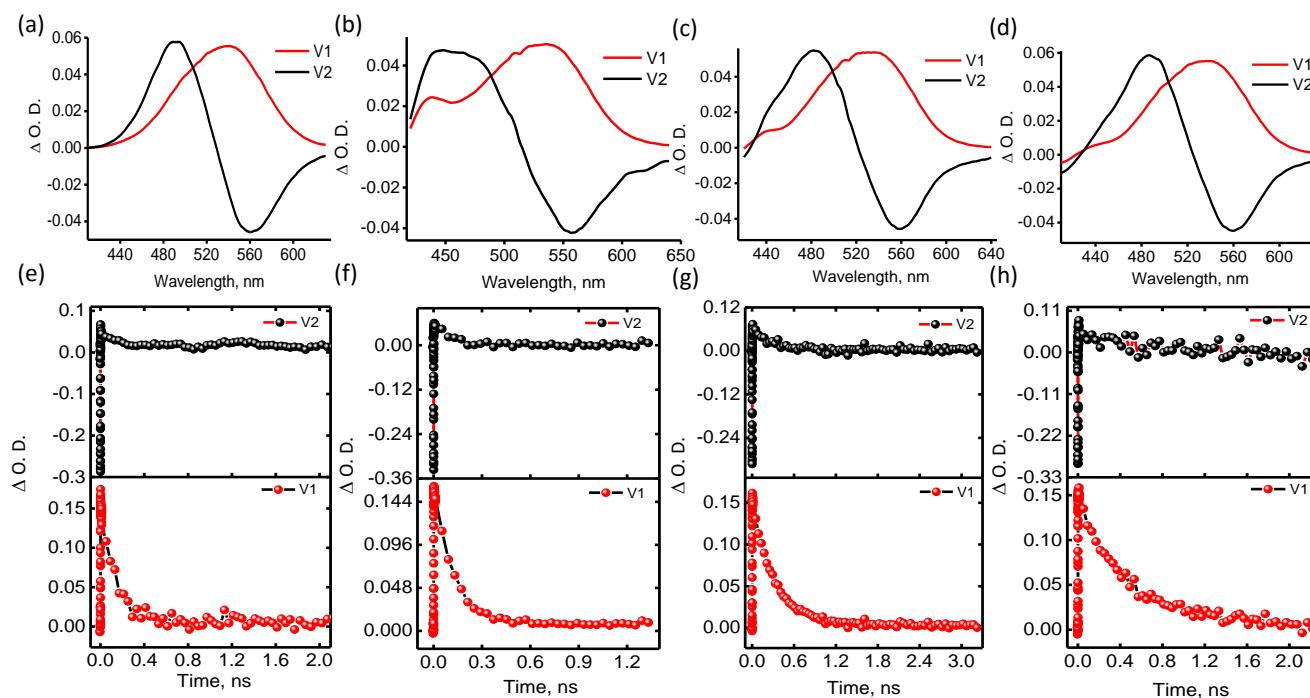
Figure 3.15. *Species associated decay spectra (SADS) obtained for (a,e) TNOH, (b,f) TNDI, (c,g) TN(OH)₃ and (d,h) TN(DI)₃ respectively after singular value decomposition (SVD) and global analysis of fTA spectra in ACN.*

separation/recombination occurring faster than the time resolution of the instrument (10 ns) leading to the population of triplet of T (^{3}T*) [163].

fTA spectra of TN conjugates in ACN display absorption peak centered around 530 - 540 nm (Figure 3.14.). Singular value decomposition (SVD) of ΔA versus time and
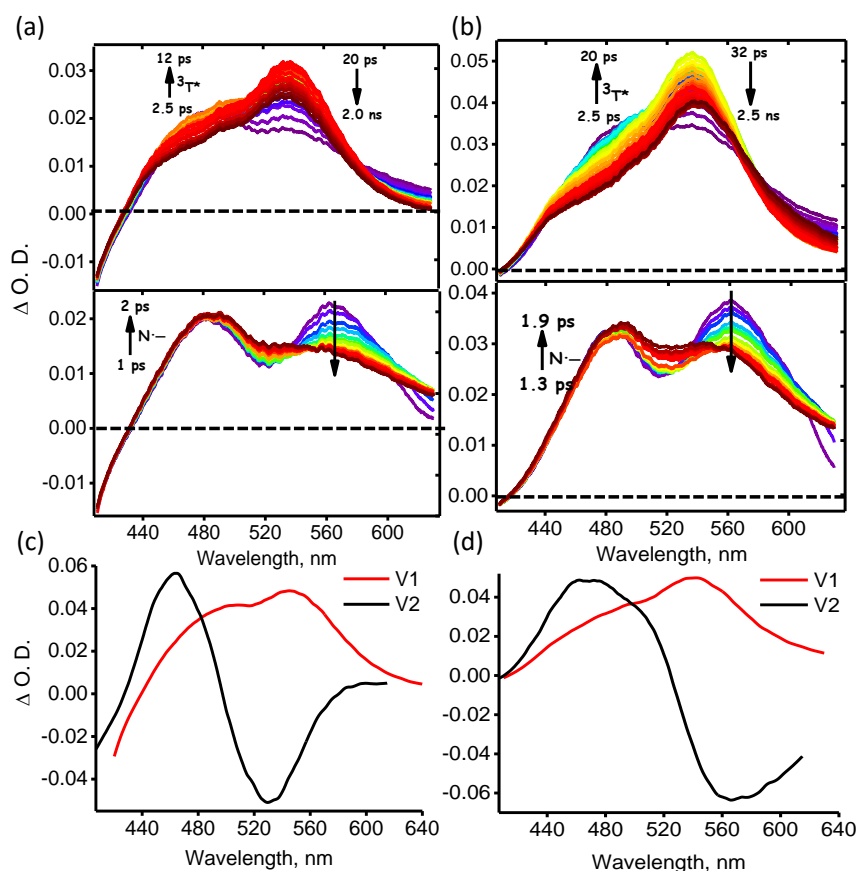
Figure 3.16. fTA *(λ_{exc} = 400 nm) spectroscopic measurements of TN(OH)₃ and TN(DI)₃ in the aggregated state. fTA spectra of (a) TN(OH)₃ and (b) TN(DI)₃; SADS spectra of (c) TN(OH)₃ and (d) TN(DI)₃ in THF obtained after global analyses. Lower panel of (a) and (b) shows photoprocesses occurring in TN(OH)₃ and TN(DI)₃ after 1 - 2 ps of photoexcitation respectively while second panel shows the photoprocesses occurring in TN(OH)₃ and TN(DI)₃ after 2.5 ps - 2.5 ns of photoexcitation respectively.*

wavelength based three-dimensional map of monomeric and aggregated TN conjugates obtained from the fTA measurements is demonstrated in Figures 3.15. The species associated decay spectra (SADS) obtained from SVD and global analyses for TNOH, TNDI, TN(OH)₃ and TN(DI)₃ in the monomeric state has two principal components centered at 490 and 540 nm respectively (Figure 3.15.a-d). The positive absorption bands centered at 490 and 540 nm are ascribed to the triplet absorption of N (^{3}N*) and T (^{3}T*)[163] units respectively. The lifetime of the principal components (Table 3.5, Figure 3.15.e-h) obtained from SVD analyses for TN conjugates in the monomeric state are tabulated in Table 3.5.

The fTA spectra of TN conjugates in the aggregated state consist of positive absorption bands centered at 545 nm and a twin absorption around 470 and 580 nm respectively (Figures 3.16.a-b, A3.3, appendix). Upon photoexcitation of TN

Table 3.5. Lifetimes of TN derivatives obtained from kinetic analyses of fTA spectra (λ_{exc} = 400 nm).

	ACN (τ, ps)		THF (τ)	
	V_1	V_2	V_1 (ns)	V_2 (ps)
TNOH	121.98	10.28	0.83	504.46
TNDI	136.76	175.61	0.10	3.38
TN(OH)₃	421.39	223.45	2.52	2.94
TN(DI)₃	315.22	263.41	1.07	384.90

conjugates at 400 nm, ultrafast charge separation results in the generation of radical anion of N ($N^{\cdot-}$) [158] after 1 - 2 ps of the laser pulse [Figures 3.16.a-b, A3.3a-d (lower panel), appendix]. Subsequently, the photogenerated excitons populates the triplet state of T ($^3T^*$) [163] through geminate charge recombination. The SADS spectra of TN conjugates obtained after SVD and global analyses comprise of two principal components centered at 550 and 460 nm respectively that are attributed to the triplet absorption of T ($^3T^*$) and radical anion of N ($N^{\cdot-}$) [164, 165] respectively (Figure A3.4, appendix). The kinetic profiles associated with the principal components are described in Figure A3.4, appendix and the corresponding lifetime is tabulated in Table 3.5.

3.9. Electrochemical measurements

To examine the redox properties displayed by the TN conjugates, cyclic voltammetric measurements were performed in ACN with n-Bu$_4$NPF$_6$ as the supporting electrolyte (Figure 3.17.). Cyclic voltammograms (CV) of 1 mM TNOH exhibits oxidation peak at 1.24 V and two reduction peaks at -1.81 and -1.19 V (reversible). CV of 1 mM TNDI possesses oxidation peak at 1.17 V, and two reduction peaks at -1.81 and -1.22 V (reversible). CV of 1 mM TN(OH)$_3$ consists of oxidation peak at 0.94 V with reduction peaks at -1.69 and -1.22 V (reversible). CV of 1 mM TN(DI)$_3$ display oxidation peak at 0.89 V and reduction peaks at -1.72 and -1.17 V (reversible). Comparison of cyclic voltammograms of

TN conjugates with the model compounds T and N in ACN established that oxidation peaks around 0.89 - 1.24 V could be due to the oxidation of A unit, while reduction peaks around -1.1 to -1.22 V and -1.69 to -1.81 V are corroborated to the reduction of N unit.

Upon photoexcitation of N (λ_{ex} = 400 nm) in ACN, ultrafast photoinduced electron transfer from T to N unit (ΔG_{ET} = -1.09 eV) results in ultrafast charge separation/recombination (τ_{cs} = τ_{cr} ≤ 110 fs) in the monomeric state. Photoexcitation (λ_{ex} = 400 nm) of TN conjugates in THF (aggregated state)
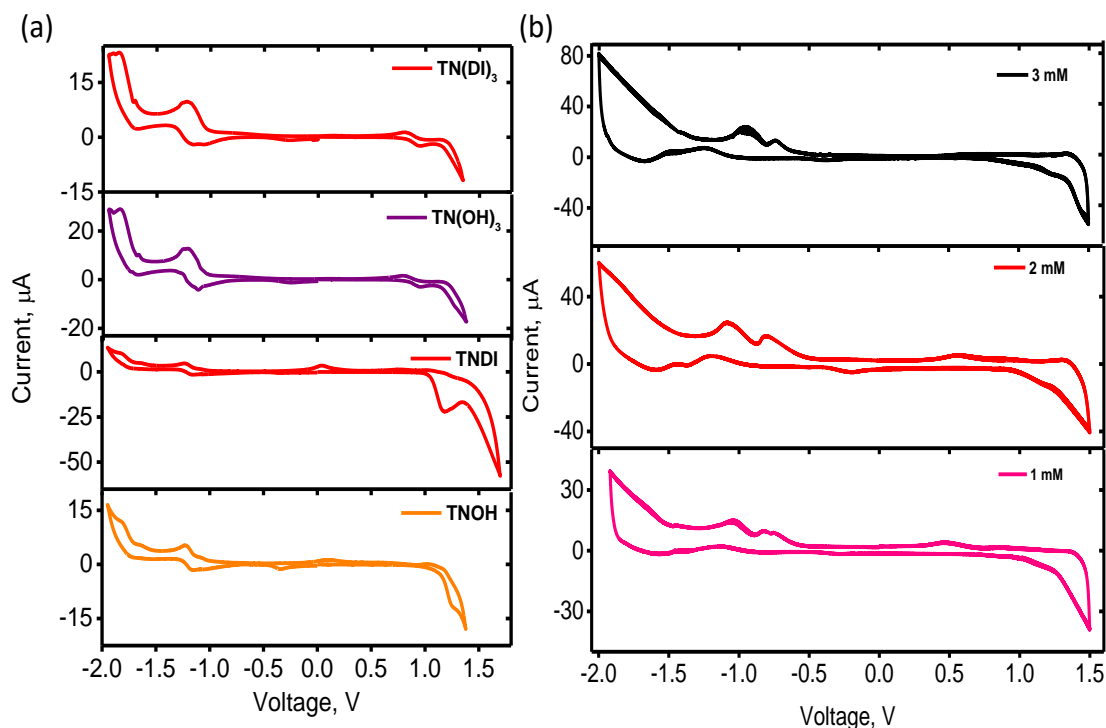
Figure 3.17. *(a) cyclic voltammetric measurements of TN conjugates in ACN and (b) concentration dependent cyclic voltammetric measurements of TN(DI)₃ in THF.*

generates CTIs namely $(T^{·+})$ and $(N^{·-})$ following 1-2 ps of laser pulse. The photogenerated excitons in TNOH and TNDI recombine with a lifetime of τ_{cr} = 0.10 and 0.83 ns respectively in THF, whereas charge recombination lifetime of CTIs in TN(OH)₃ and TN(DI)₃ is enumerated to be τ_{cr} = 1.07 and 2.52 ns respectively. Remarkable increase (ca. 10^4-fold) in the survival time of CTIs in the aggregated state of TN conjugates compared to the monomeric state (Table 3.6) could be attributed to the delocalization of excitons across spherical/vesicular nano-architectures. Following PET from T to N, the CTIs formed undergo geminate charge recombination populating the triplet of T (^{3}T*) [163], ascertaining charge recombination leading to the triplet formation mechanism responsible for the excited state deactivation, consistent with the earlier reports [140, 158].

Persistence of CS states by four orders of magnitude more in the aggregated state of TN conjugates when compared to the monomeric state could be ascribed to the favourable supramolecular arrangement of the donor–acceptor systems for ultrafast charge separation followed by slow charge recombination. A significant decrease in the rate of charge recombination in the aggregated state could be a consequence of the extended charge delocalisation through self-assembled spherical/vesicular scaffolds aided by non-covalent interactions (Figure 3.5.e).

Table 3.6. A comparative account of the C_3-symmterical donor-acceptor molecular architectures reported in various literatures.

Contributed by	C_3-symmetrical architecture	Reference	Purpose
Our data	Triphenylamine-naphthalimide dyads and trefoils		Comparison of photoinduced electron transfer in the aggregated state.
F. Wudl and coworkers	decacyclene triimides (DTI)	(i). Angew. Chem. Int. Ed. **2013**, *52*, 1446-1451. (ii). Angew. Chem. Int. Ed. **2015**, *54*, 6775-6779.	Photoinduced electron transfer in the monomeric state.
M. R. Wasielewski and coworkers	1,3,5-triphenylbenzene(P)-perylenemonoimide(PMI)	J. Phys. Chem. Lett. **2014**, *5*, 1608-1615.	Excitation energy transfer in the aggregated state.
M. R. Wasielewski and coworkers	P-PDI	J. Am. Chem. Soc. **2006**, *128*, 1782-1783.	Photoinduced electron transfer in the aggregated state in presence of TEA.
M. R. Wasielewski and coworkers	tetrahedral tetraphenylmethane-PDI	J. Phys. Chem. C. **2014**, *118*, 16941-16950.	Excitation energy transfer in the aggregated state.
M. R. Wasielewski and coworkers	ethynyl-P-linked chlorophylls	(i). Angew. Chem. Int. Ed. **2006**, *45*, 7979-7982. (ii). Chem. Commun. **2010**, *46*, 401-403.	Excitation energy transfer in the aggregated state.

3.10. Conculsion

In summary, twisted donor-acceptor triphenylamine-naphthalimide (TN) dyads and trefoils for extended charge separated states upon self-assembly is illustrated. TN conjugates undergo self-assembly in THF through synergetic $\pi-\pi$ and H-bonding interactions. Solvent polarity dependent absorption and emission measurements in conjunction with Lippert-Mataga analyses established the presence of ground state CT interactions. Concentration dependent photophysical measurements along with morphological analyses in THF demonstrated existence of spherical/vesicular aggregates. Following photoexcitation of N unit, TN dyads and trefoils in the aggregated state display radical ion pair intermediates with long-lived charge separated

lifetime (τ_{cr}^{a}) of ca. 1.07 and 2.52 ns compared to the $(\tau_{cr}^{m} \leq 110$ fs) monomer in ACN, as observed from nTA and fTA spectroscopic measurements. A 10^4–fold enhancement in the lifetime of CTIs in the aggregated state when compared to the monomeric TN could be due to the favorable arrangement that stabilizes photogenerated excitons in a self-assembled supramolecular architecture, a feature that is not feasible in non-assembled D–A systems.

Chapter 4

Colossal Enhancement in the Lifetime of Charge Separated States in Self-Assembled Twisted Non-Symmetric Donor-Acceptor Triad

Abstract

Organic materials which can self-assemble into higher order superstructures gained extensive applications in artificial light harvesting systems, solution processable bulk-heterojunction solar cells and photo-functional devices owing to their unique charge transport properties. In this report, we demonstrate a self-assembled non-symmetric donor-acceptor triad composed of triphenylamine, anthracene and naphthalimide units, for achieving long-lived charge separation via aggregation. Steric hindrance imposed by diisopropyl groups of naphthalimide and propeller shaped triphenylamine unit obstruct planarization in TAN. Quantum theory of atoms in molecules analyses demonstrated the presence of synergetic C-H•••π, C-H•••H-C, π–π and C–O•••O–C interactions between the constituent units of adjacent TAN molecules in the crystalline state. The nonplanar geometry of TAN triad in the monoclinic space group dictates a unique antiparallel arrangement between the adjacent TAN units along b-axis. Solvent polarity dependent Lippert-Mataga and spin density distribution analyses of TAN established the presence of charge transfer interactions in the ground state. Femtosecond and nanosecond transient absorption measurements of TAN revealed ca. 10^8-fold increase in the lifetime of charge separated state in the aggregated TAN ($\tau_{cr}^a = 20$ μs) in $CHCl_3$ when compared to that in monomeric TAN ($\tau_{cr}^m < 110$ fs) in CH_3CN. Extension in lifetime of charge separated state in the self-assembled state is attributed to the delocalization of excitons across stacked antiparallel dimers of TAN.

$\tau_{cr} \leq 110$ fs $\qquad\qquad$ vs. $\qquad\qquad$ $\tau_{cr} \cong 20$ μs
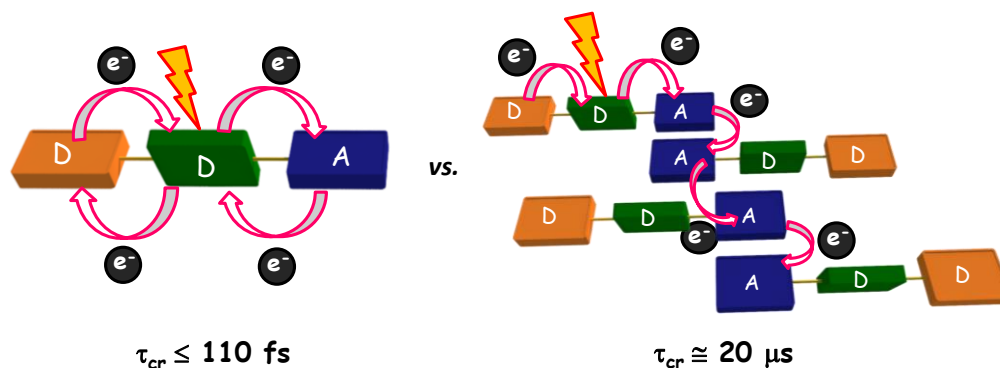
4.1. Introduction

Self-assembled π-conjugated donor-acceptor molecular architectures have gained widespread consideration owing to their distinct charge transport properties [26, 90]. Stimulated by peculiar chromophoric arrangements in natural photosynthetic systems (PS) [1, 2, 106, 111], enormous designs have been demonstrated to generate electron donor-acceptor (D-A) systems [7, 64, 107] for efficient energy conversion [2, 7, 107]. Optimization [28, 104, 106, 166, 167] of stoichiometry and distance between the complementary redox gradients [24, 79, 81] is vital for persistent charge transfer intermediates (CTIs) in monomeric D-A systems [88, 108]. In D-A aggregates, precise organization [4, 7, 24, 89, 168, 169] of modular components is quintessential in regulating the rate of charge recombination. To install oriented "transport highways" for efficient exciton migration, in D-A dyads [86, 170, 171], emergence-upon-assembly approach [77, 112, 113, 172-175] have been employed by several groups [176, 177]. Supramolecular [115] J-aggregates of bisthiophene(BT)-perylenediimide(PDI)-bisthiophene [84-86], melamine(M)-naphthalenediimide(NDI)-melamine [87], double helical arrangement of diketopyrrolopyrrole(DPP)-PDI-diketopyrrolopyrrole [77, 78], hydrogen-bonded oligo(p-phenylenevinylene)[OPV]–PDI–oligo(p-phenylenevinylene) [75, 178], columnar anthracene(An)–PDI–anthracene [179], slip-stacked PDI-DPP-DPP [76] triads and oriented push-pull triple-channel surface architectures [27, 80] have been demonstrated for extending the lifetimes of photogenerated excitons in the aggregated

Chapter 4- Colossal Enhancement in the Lifetime of Charge Separated States in Self-Assembled Twisted Non-Symmetric Donor-Acceptor Triad

141

state. To date, aggregated non-symmetric D-D-A triads for surviving CTIs have not been explored.

In our earlier contributions, we have successfully demonstrated attenuation in the rate of charge recombination in i) vesicular scaffold [31] and ii) nonparallel stacks [158] of D-A bichromophores [123, 159]. Realization of long-lived charge separated (CS) states [87, 95] in a self-assembled naphthalene-naphthalimide (NIN) dyad, compared to the monomeric NIN, could be due to the delocalization of excitons through individual D and A stacks oriented in different spatial planes. In contrast, a homologous dyad containing anthracene and naphthalimide (AN) showed ultrafast charge recombination (< 110 fs) in monomeric/aggregated state. Contrary to NIN, absence of donor-on-donor and/or acceptor-on-acceptor arrangement in the AN dyad could be responsible for short-lived CTIs in the aggregate state. Lack of long-lived CS states in aggregated AN dyad prompted us to design and synthesize a non-symmetrical triphenylamine-anthracene-naphthalimide (TAN) D-D-A triad. We herein report the first example of an aggregated non-symmetric D-D-A triad TAN for prolonging the CS state (ca. 10^8-fold) upon photoexcitation when compared to ultrafast charge recombination in monomeric TAN (τ_{cr}^{m} < 110 fs). Formation of long-lived charge separated states (τ_{cr}^{a} = 20 μs) could arise from intermolecular electron hopping across naphthalimide units in the stacked antiparallel aggregates of TAN.

4.2. Syntheses and characterization of naphthalimide derivatives AN and TAN

Synthesis of ANBr: To a solution of 4-bromo-N-(2,6-diisopropylaniline)-naphthalene-1,8-dicarboximide (1.1 mmol, Please refer the synthesis of NDI for NBr) in 40 ml THF, 20 ml of 2 M aqueous K_2CO_3 solution was added under nitrogen atmosphere. To this solution, 1.1 mmol of anthracene-9-bromo-10-boronic acid was added followed by Pd(PPh$_3$)$_4$ (14.7 µmol). The reaction mixture was heated at 70 °C for 12 h. The reaction mixture was then cooled after which it was extracted using dichloromethane. The solvent was removed under reduced pressure and the residue purified by column chromatography (silica gel, chloroform: petroleum ether, 4:6) to yield ANBr as yellow powder (60%). m. p. 372 ^{0}C; ^{1}H NMR (500 MHz, CDCl$_3$): δ = 8.79 - 8.78 (d, J = 5 Hz, 1H), 8.63 - 8.62 (d, J = 5 Hz, 2H), 8.58 – 8.59 (d, J = 5 Hz, 1H), 7.79 – 7.77 (d, J = 10 Hz, 1H), 7.55 - 7.53 (t, J = 10 Hz, 2H), 7.43 - 7.41 (t, J = 10 Hz, 3H), 7.30 - 7.26 (m, 6H), 2.83 - 2.78 (m,
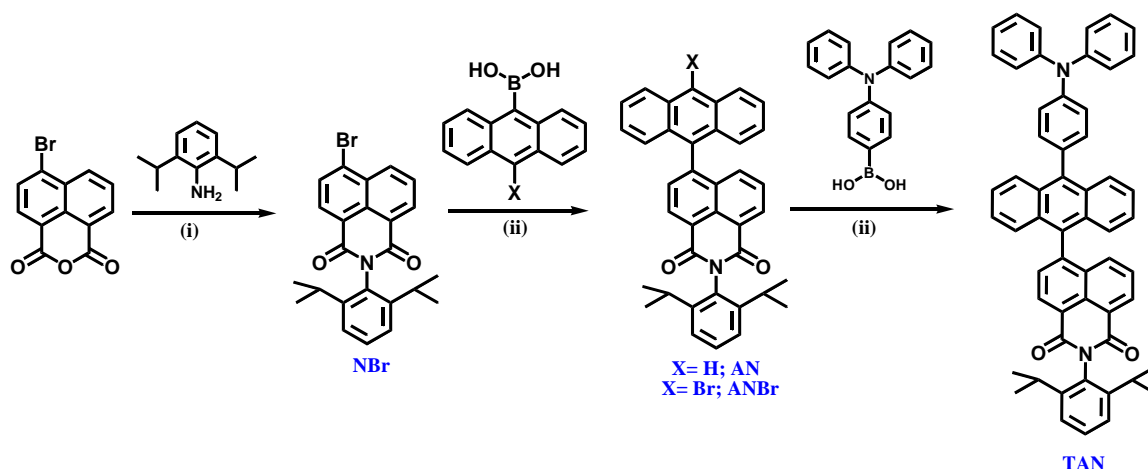
Scheme 4.1. *(i) Acetic acid; 110 ^{o}C; 5 h, (ii) Pd[(PPh$_3$)$_4$]; Anhyd. THF; 2 M K$_2$CO$_3$; 70 ^{o}C; 12 h.*

Chapter 4- Colossal Enhancement in the Lifetime of Charge Separated States in Self-Assembled Twisted Non-Symmetric Donor-Acceptor Triad

143

2H), 1.17 - 1.15 (d, J = 10 Hz, 12H); ^{13}C NMR (125 MHz, CDCl$_3$): δ = 163.23, 163.17, 144.72, 143.43, 132.15, 131.22, 131.12, 130.91, 130.30, 130.27, 129.81, 129.64, 129.38, 128.54, 128.09, 127.67, 127.10, 126.21, 125.29, 125.12, 124.43, 124.16, 123.06, 122.01, 121.50, 28.18, 23.07; IR (KBr): 2960.73, 2868.15, 1705.07, 1666.50, 1587.42, 1438.90, 1361.74, 1336.67, 1236.37, 1190.08, 908.47, 785.02 cm^{-1}; HR-MS (EI)-(m/z): 612.2423. Calcd. for C$_{38}$H$_{30}$BrNO$_2$: 611.5925; Anal. Calcd. for C$_{38}$H$_{30}$BrNO$_2$: C, 74.52; H, 4.95; N, 2.30. Found: C, 73.50; H, 4.99; N, 2.28.

Synthesis of AN: To a solution of 4-bromo-N-(2,6-diisopropylaniline)-naphthalene-1,8-dicarboximide (1.1 mmol) in 40 ml THF, 20 ml of 2 M aqueous K$_2$CO$_3$ solution was added under nitrogen atmosphere. To this solution, 1.1 mmol of corresponding anthracene-9-boronic acid was added followed by Pd(PPh$_3$)$_4$ (14.7 μmol). The reaction mixture was heated at 70 °C for 12 h. The reaction mixture was allowed to cool down, and then it was extracted with dichloromethane. The solvent was removed under reduced pressure and the residue purified by column chromatography (silica gel, EtOAc: petroleum ether) to afford AN as yellow solid (68%). m. p. 370 ^{0}C; ^{1}H NMR (500 MHz, CDCl$_3$): δ = 8.80 - 8.78 (d, J = 10 Hz, 1H), 8.61 - 8.59 (d, J = 10 Hz, 2H), 8.09 - 8.07 (d, J = 10 Hz, 2H), 7.82 - 7.80 (d, J = 10 Hz, 1H), 7.45 - 7.42 (t, J = 6.15 Hz, 5H), 7.31 - 7.29 (d, J = 5.6 Hz, 4H), 7.27 – 7.26 (d, J = 10 Hz, 2H), 2.84 - 2.79 (m, 2H), 1.18 - 1.16 (d, J = 5 Hz, 12H); ^{13}C NMR (125 MHz, CDCl$_3$): δ = 165.01, 164.82, 147.36, 138.68, 133.07, 131.56, 131.21, 129.87, 128.72, 128.60, 127.95, 126.93, 122.50, 121.35, 58.91, 36.83, 31.04; IR (KBr):

3051.39, 2960.73, 2924.09, 2866.22, 1705.07, 1666.50, 1585.49, 1444.68, 1361.74, 1359.82, 1236.37, 1190.08, 900.76, 788.89, 734.88 cm^{-1}; HR-MS (EI)-(m/z): 532.8628. Calcd. for $C_{38}H_{31}NO_2$: 533.3224; Anal. Calcd. for $C_{38}H_{31}NO_2$: C, 85.52; H, 5.87; N, 2.62. Found: C, 85.57; H, 5.83; N, 2.64.

Synthesis of TAN: To a solution of ANBr (1.1 mmol) in 40 ml THF, 20 ml of 2 M aqueous K_2CO_3 solution was added under nitrogen atmosphere. To this solution, 1.1 mmol of 4-(diphenylamino) phenylboronic acid was added followed by Pd(PPh$_3$)$_4$ (14.7 μmol). The reaction mixture was heated at 70 °C for 12 h. The reaction mixture was allowed to cool down and was then extracted using dichloromethane. The solvent was removed under reduced pressure and the residue purified by column chromatography (silica gel, chloroform: petroleum ether, 3:7) to yield TAN as a yellow solid (83%). m. p. 379 °C; ^{1}H NMR (500 MHz, CDCl$_3$): δ = 8.82 - 8.81 (d, J = 5 Hz, 1H), 8.62 - 8.61 (d, J = 5 Hz, 1H), 7.90 - 7.87 (d, J = 15 Hz, 3H), 7.86 - 7.84 (d, J = 10 Hz, 1H), 7.67-7.63 (m, 4H), 7.62-7.59 (d, J = 10 Hz, 2H), 7.58 - 7.57 (d, J = 10 Hz, 2H), 7.49-7.47 (d, J = 10 Hz, 2H), 7.46-7.42 (m, 4H), 7.41-7.37 (m, 2H), 7.37-7.35 (d, J = 10 Hz, 2H), 7.33-7.32 (d, J = 10 Hz, 2H), 7.28 - 7.24 (m, 2H), 7.05 - 7.03 (t, J = 10 Hz, 2H), 2.85 - 2.80 (m, 2H), 1.19 - 1.17 (d, J = 5 Hz, 12H); ^{13}C NMR (125 MHz, CDCl$_3$): δ= 164.28, 147.75, 147.47, 145.76, 144.89, 138.75, 132.28, 132.10, 131.99, 131.92, 131.39, 130.86, 130.56, 130.42, 130.11, 129.58, 129.46, 129.16, 127.52, 127.28, 126.33, 125.98, 125.27, 124.10, 123.29, 122.93, 122.88, 29.22, 24.13, 24.11; IR (KBr): 3062.96, 2962.66, 2927.94, 2868.15, 1710.86, 1670.35, 1589.34, 1489.05, 1354.03,

Chapter 4- Colossal Enhancement in the Lifetime of Charge Separated States in Self-Assembled Twisted Non-Symmetric Donor-Acceptor Triad

145

1274.95, 1234.44, 1190.08, 765.74, 696.30, 511.14 cm^{-1}; HR-MS (EI)-(m/z): 776.1976. Calcd.

for $C_{56}H_{44}N_2O_2$: 776.3403; Anal. Calcd. for $C_{56}H_{44}N_2O_2$: C, 86.57; H, 5.72; N, 3.61. Found:

C, 86.60; H, 5.77; N, 3.59.

4.3. Crystal structure analyses

Palladium (0) catalyzed Suzuki-Miyaura reaction of 4-bromonaphthalimide with

9-anthraceneboronic acid rendered anthracene-naphthalimide (AN) dyad with a

Table 4.1. *Crystal data and structure refinement of ANBr and TAN.*

Unit cell parameters	ANBr	TAN
Empirical formula	$C_{38}H_{31}BrNO_2$	$C_{56}H_{44}N_2O_2$
Formula weight	532.81	776.93
a (Å) :	9.0127(3)	14.5976(7)
b (Å) :	23.8445(9)	9.3958(5)
c (Å) :	14.2725(6)	31.7732(16)
α(alpha):	90°	90°
β(beta):	103.919(2)°	102.659(3)°
γ(gamma):	90°	90°
Volume (Å^3) :	2977.14	4251.96
Crystal system	Monoclinic	Monoclinic
Space group:	$P2_1$/n	$P2_1$/n
Calculated density (mg/m^3):	1.370	1.214
Z:	4	4
Temperature (K) :	296(2)	296(2)
R (F, %):	4.57	8.59
R$_w$ (F^2):	1.050	1.018
CCDC Number	1479113	1479058
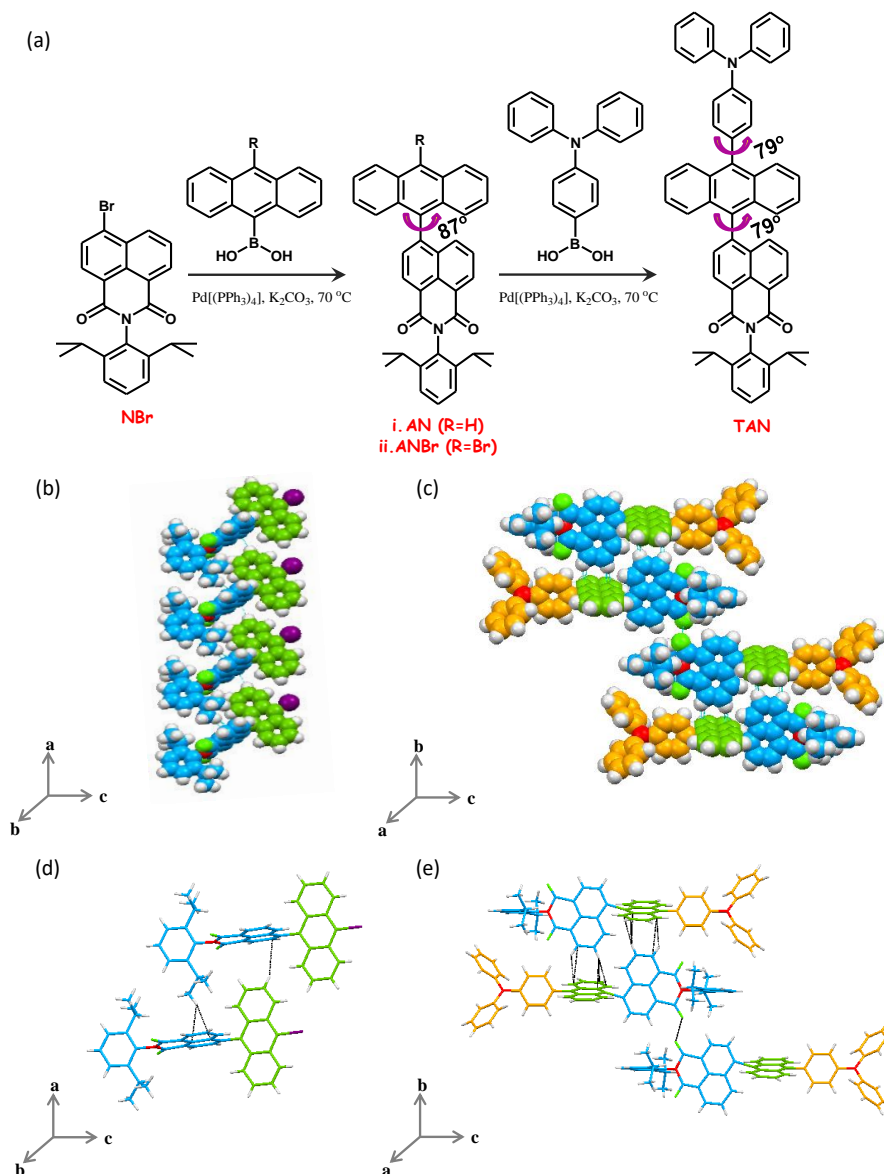
Figure 4.1. *(a) Synthesis scheme for dyad ANBr and the triad TAN with respective chemical structures. Packing arrangements of (b) ANBr (along a-axis) and (c) TAN (along b-axis). Self-assembled structures of (d) ANBr and (e) TAN along a and b-axis, respectively.*

moderate yield (68%). Cross-coupling of ANBr with 4-(diphenylamino)phenylboronic acid offered the triad TAN in 83% yield (Figure 4.1.a, Scheme 4.1.). Slow evaporation of ANBr and TAN from 1:3 dichloromethane:hexane mixture under ambient conditions

Chapter 4- Colossal Enhancement in the Lifetime of Charge Separated States in Self-Assembled Twisted Non-Symmetric Donor-Acceptor Triad

147

furnished yellow crystals of ANBr [180] and TAN. Single crystal X-ray diffraction analyses of ANBr and TAN resulted in solvent free crystals belonging to monoclinic $P2_1/n$ crystal system (Table 4.1). The dihedral angle and C-C bond length between anthracene (A) and naphthalimide (N) units in ANBr is 87° and 1.51 Å respectively suggesting a near-orthogonal arrangement of constituent chromophores in the dyad (Figures 4.1.a,b). X-ray structure and quantum theory of atoms in molecules [181, 182] (QTAIM; Figure 4.2.a-b and Table 4.2) analysis of ANBr indicates presence of C-H••π interaction between i) A and N ($d_{H \cdots C}$ = 2.75 Å) units and ii) N and N ($d_{C \cdots H}$ = 2.68 Å) units along *a*-axis (Figures 4.1.b,d, 4.2.c-d). The unique C-O••Br interaction

Table 4.2. Calculated topological properties of the electron density for the intermolecular interaction in ANBr and TAN.

Description	Interaction	$d,^a$ (Å)	$\rho(r),^b$ eA^{-3}	$\nabla^2 r(r),^c$ eA^{-5}	DE, kJ/mol
	C36•••H78	2.864	0.038735	0.393484	3.3737
ANBr	C104•••H62	2.828	0.043344	0.472095	4.1483
(dimer1)	O70•••H68*	2.733	0.045409	0.603457	5.0934
	O142•••H140*	2.733	0.045342	0.603626	5.0934
	Br72•••O142	3.245	0.046833	0.638376	5.8154
ANBr	Br72••• H102	3.296	0.021817	0.255495	1.8772
(dimer2)	Br72•••H122	3.368	0.020865	0.215298	1.7065
	H140•••O142	2.733	0.045294	0.604421	5.0934
	H68 •••O70	2.733	0.045382	0.603288	5.0934

TAN	C20•••H172	2.701	0.048324	0.540704	4.5683
	C14•••H170	2.602	0.061011	0.686984	5.7367
	C118•••H66	2.601	0.061011	0.687008	5.7367
	C124•••H68	2.703	0.048324	0.540704	4.5683

[a]-distance, [b]-electron density at the BCP and [c]-Laplacian of the electron density at the BCP. *Though the distance is more than the van der Waals radii, QTAIM exhibited density at (3,-1) BCP.

($d_{O•••Br}$ = 3.24 Å) and C-H•••H-C interaction ($d_{H•••H}$ = 2.34 Å) along *a*-axis dictate two
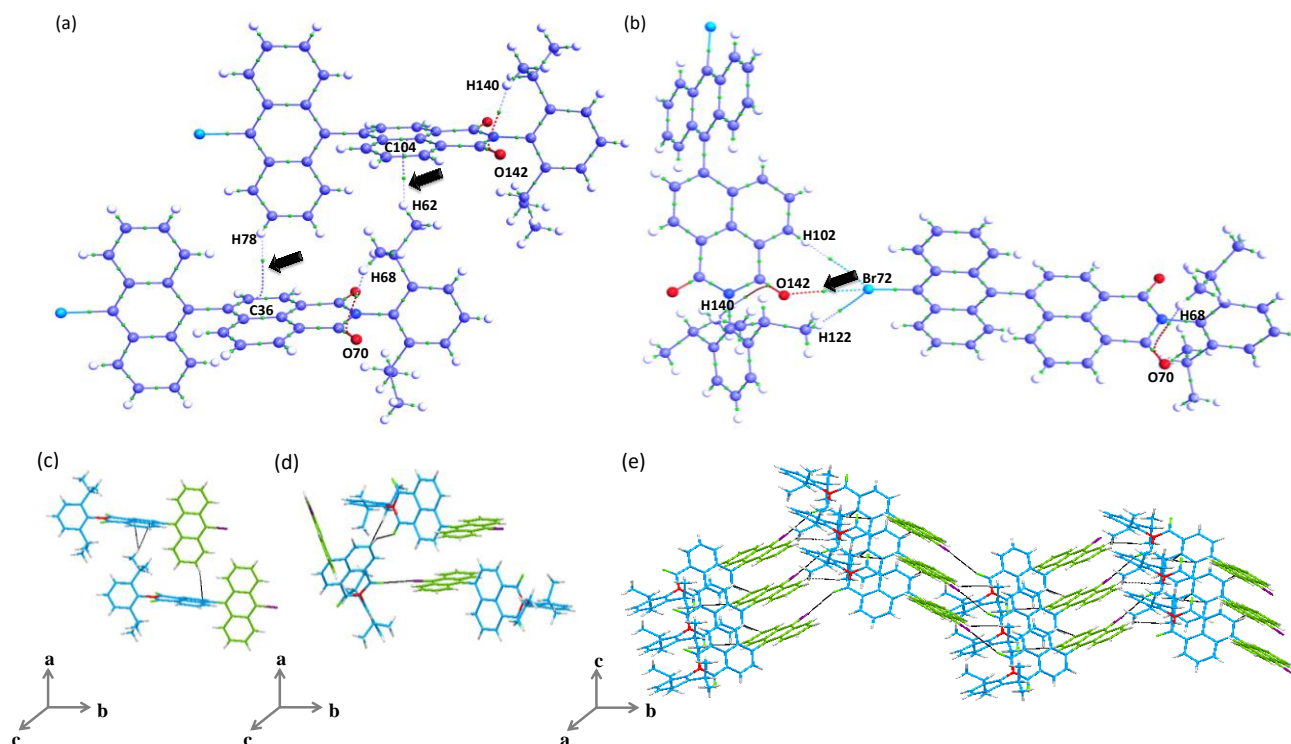
Figure 4.2. QTAIM *topological analyses of ANBr describing* (a) *C-H•••π and* (b) *C-O•••Br interactions. (c), (d) represents self-assembled dimers in ANBr formed as a result of C-H•••π and C-O•••Br interactions respectively. (e) describes wave-like arrangement observed in ANBr.*

Chapter 4- Colossal Enhancement in the Lifetime of Charge Separated States in Self-Assembled Twisted Non-Symmetric Donor-Acceptor Triad

149

dimensional wave-like arrangement in ANBr (Figure 4.2.e). Lack of $\pi-\pi$ stacking interactions between identical units eliminates the possibility of electron donor-on-donor (A-on-A) and/or acceptor-on-acceptor (N-on-N) arrangement in ANBr. In contrast, nonparallel stacks resulting in donor-on-donor and acceptor-on-acceptor arrangement was observed in a related dyad NIN possessing naphthalimide and naphthalene units as reported in our earlier work.

In the triad TAN, the dihedral angle and C-C bond length between i) A and N and ii) (triphenylamine) T and A units are i) 79°and 1.55 Å and ii) 79° and 1.49 Å
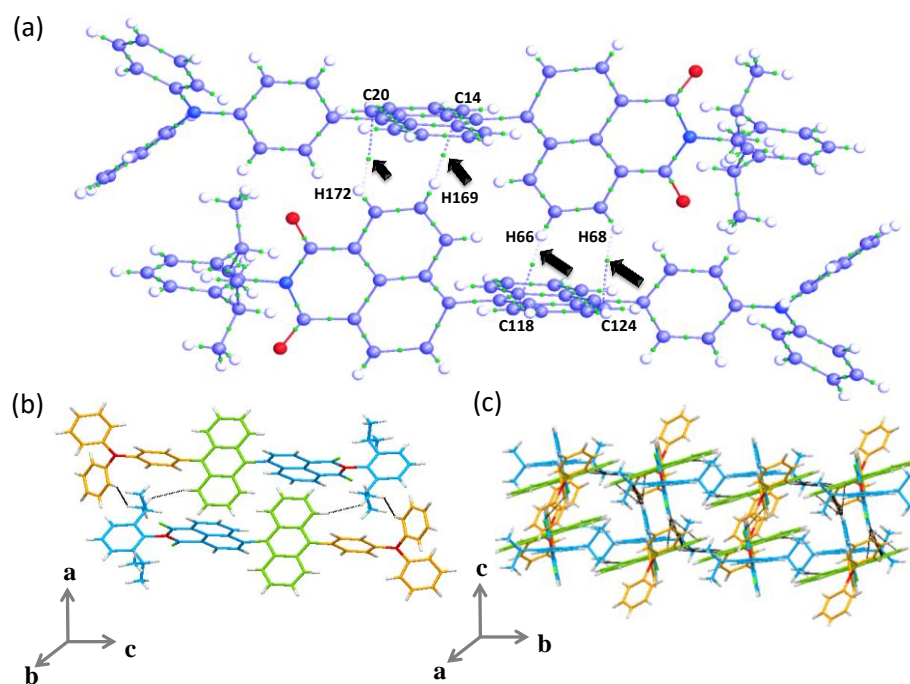
Figure 4.3. QTAIM *topological analyses of TAN representing (a) C-H•••π interaction. (b) describes self-assembled dimers in TAN formed through C-H•••π interaction. (c) perspective view of the packing in TAN along c-axis.*

respectively suggesting a non-parallel arrangement [126] of the adjacent constituent units (Figures 4.1.a,c and e). Dimers in TAN are constituted through co-operative edge-to-face (C-H$\bullet\bullet\pi$, $d_{H\cdots C}$ = 3.62 Å, Figure 4.3.a) interaction between N and A aromatic cores and unique O$\bullet\bullet\bullet$O (imidic oxygen, $d_{O\cdots O}$ = 2.93 Å) interaction [183], as evidenced by QTAIM analysis (Figures 4.1.c,e, 4.3.a, Table 4.2). C-H$\bullet\bullet\pi$ interaction between N and A at a distance of 2.70 Å are also observed between two units of TAN. Dihydrogen (C-H$\bullet\bullet$H-C) interaction between methyl hydrogen of diisopropyl unit and (i) phenyl hydrogens of T ($d_{H\cdots H}$ = 2.37 Å) moiety, and (ii) hydrogen atom of A ($d_{H\cdots H}$ = 2.28 Å) along with C-H$\bullet\bullet\pi$ interactions govern the close- packed arrangement in TAN (Figure 4.3.b).

Table 4.3. Represents percentage of intermolecular interactions and packing motifs in ANBr and TAN obtained from Hirshfeld surface analyses.

	%C$\bullet\bullet$C	%C$\bullet\bullet$H	%H$\bullet\bullet\bullet$H	%O$\bullet\bullet\bullet$H	ρ = [(% C$\bullet\bullet\bullet$H)/(% C$\bullet\bullet\bullet$C)]	Packing motif
ANBr	2.6	27.5	54.4	6.9	10.57	Herringbone
TAN	3.4	23.4	67.7	4.5	6.8	Herringbone

4.4. Hirshfeld surface analyses

Packing motifs responsible for the distinct packing arrangement of ANBr and TAN in the crystalline state are investigated employing Hirshfeld surface (HS) [160]

Chapter 4- Colossal Enhancement in the Lifetime of Charge Separated States in Self-Assembled Twisted Non-Symmetric Donor-Acceptor Triad

151
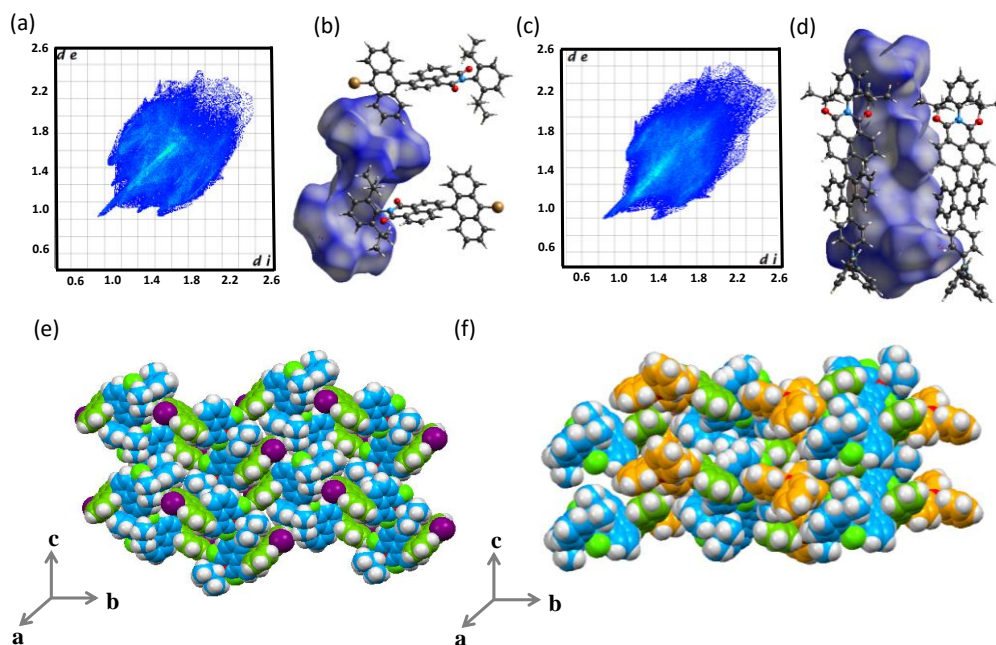
Figure 4.4. *(a), (c) 2D-fingerprint plots for ANBr, TAN respectively and (b), (d) Hirshfeld surface (d_{norm}) for ANBr, TAN respectively obtained from Hirshfeld surface analyses.*

and two- dimensional (2D) fingerprint analyses (Figure 4.4.). Examination of 2D-fingerprint plots (Figures 4a,c) obtained from HS analyses establishes that $\pi-\pi$, C−H•••π, dihydrogen (C−H•••H-C) and C−H•••O interactions dictate packing arrangement in ANBr and TAN. The sharp spikes and a pair of wings observed in the 2D-fingerprint plot of ANBr is attributed to C−H•••π and C−H•••O interactions, whereas in TAN it corresponds to dihydrogen interaction (Table 4.3, Figure 4.5.). A value [184] of $\rho[(\%C\bullet\bullet\bullet H)/(\%C\bullet\bullet\bullet C)] = 10.57$ and 6.8 for ANBr and TAN respectively (Table 4.3), indicates the formation of a herringbone arrangement ($\rho > 4.5$) in the respective crystalline lattice (Table 4.3, Figure 4.4.e-f). The presence of diagnostic intense red and orange hot-spots observed in distinct HS (d_{norm})
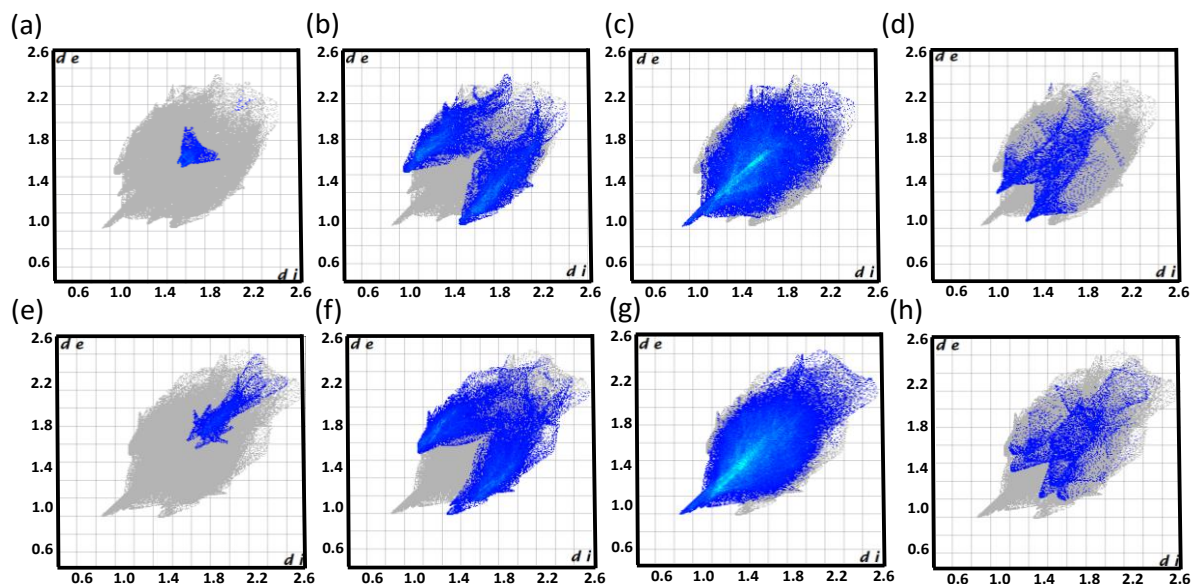
Figure 4.5. *Two-dimensional fingerprint plots of ANBr and TAN determined from Hirshfeld surface (HS) analyses. (a), (e) represents C•••C, (b), (f) depicts C•••H, (c), (g) describes H•••H and (d), (h) represents O•••H interactions observed in ANBr (first row) and TAN (second row) respectively as established from HS analyses.*

maps for ANBr and TAN (Figures 4.4.b,d) indicates the existence of short intermolecular interactions consistent with the crystal structure.

4.5. Morphological analyses

Dynamic light scattering (DLS) experiments were performed to investigate the nature of aggregation in $CHCl_3$ solution of AN and TAN. DLS measurements of 0.8 mM AN in $CHCl_3$ exhibit a bimodal particle size distribution with an average hydrodynamic diameter (D_H) of 560 nm and 4.13 μm respectively (Figure 4.6.a, Table 4.4). DLS measurements of 1 mM TAN in $CHCl_3$ displayed bimodal particle size distribution

Chapter 4- Colossal Enhancement in the Lifetime of Charge Separated States in Self-Assembled Twisted Non-Symmetric Donor-Acceptor Triad

153
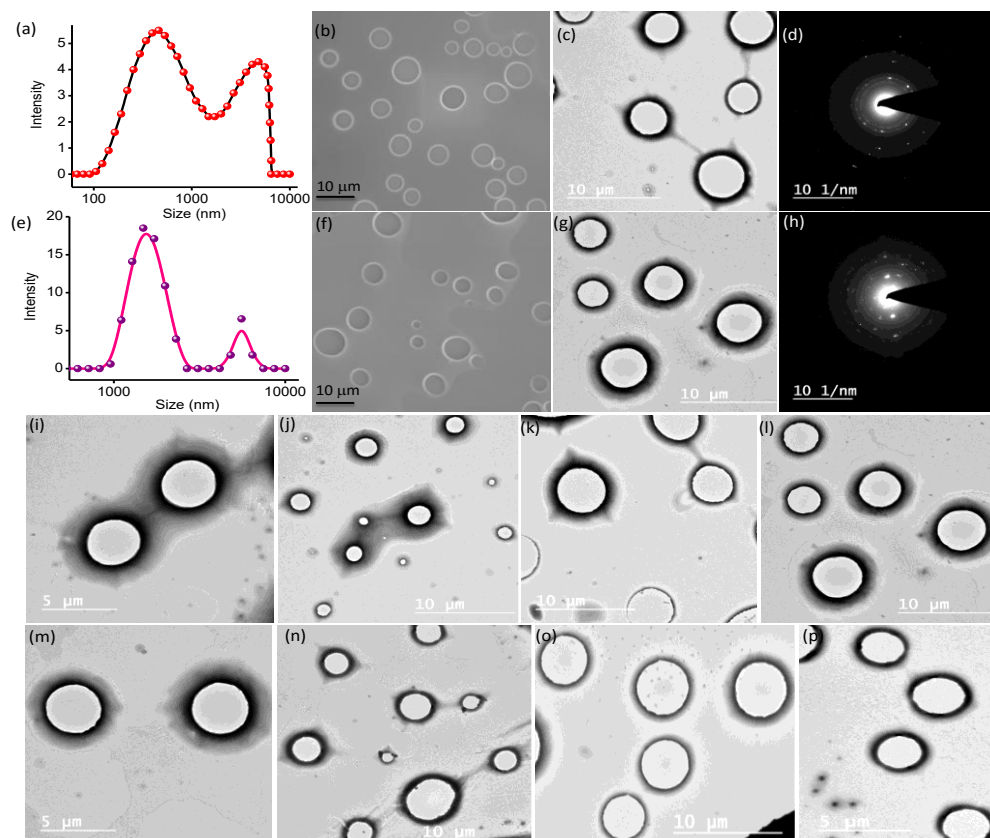
Figure 4.6. *Morphological analyses of AN (first row) and TAN (second row) in CHCl₃. Size distribution obtained from (a), (e) DLS, (b), (f) SEM; (c), (g) TEM and (d), (h) SAED pattern of 0.8 mM AN and 1 mM TAN respectively as dropcasted from CHCl₃. Additional TEM images of (i-l) 0.8 mM AN and (m-p) 1 mM TAN as dropcasted from CHCl₃ respectively.*

possessing D_H of 1.60 μm and 5.56 μm respectively (Figure 4.6.e, Table 4.4).

Morphological analyses of 0.8 mM AN and 1 mM TAN in CHCl₃ using scanning and tunneling electron microscopy further confirmed coexistence of small and large ring-like architectures, consistent with the DLS measurements (Figures 4.6.b-c, 4.6.f-g, 4.6.i-p, A4.1, Table 4.4). Selected area electron diffraction (SAED) measurements of AN and TAN as drop casted from CHCl₃ displayed bright distinct spots validating the crystalline nature of AN and TAN (Figures 4.6.d,h).

Table 4.4. Particle size distribution of AN and TAN obtained from DLS, SEM and TEM measurements.

	Particle size from DLS (μm)	Particle size from SEM (μm)	Particle size from TEM (μm)
AN in CHCl$_3$	0.56, 4.13	1.54 and 11.59	0.64 and 1.294
TAN in CHCl$_3$	1.60, 5.56	0.49 and 2.13	1.74 and 2.89

4.6. Frontier molecular orbital analyses

Having demonstrated the presence of crystalline TAN aggregates in CHCl$_3$ solution, we explored the propensity of the self-assembled TAN triad in regulating the rate of charge recombination. We employed frontier molecular orbital (FMO) analysis, UV-Vis, fluorescence and cyclic voltammetric measurements to examine the amount of perturbations in electronic interactions between donors and acceptor moieties in the aggregated vs. monomeric state of the dyad AN and triad TAN. FMO analyses of ANBr and TAN (Figure 4.7., Table 4.5) establish that the electron density of HOMO is distributed in A and N for ANBr, and A and T units in TAN, whereas electron density of LUMO is solely localized on N unit for both ANBr and TAN. This observation indicates the possibility of charge transfer interactions [162, 185] existing between the constituents of AN and TAN in the ground state. The FMO investigations performed on dimeric ANBr and TAN showed that the difference between LUMO and HOMO energy

Chapter 4- Colossal Enhancement in the Lifetime of Charge Separated States in Self-Assembled Twisted Non-Symmetric Donor-Acceptor Triad

155

levels is reduced. The observed bathochromic shift in the emission maxima could be attributed to the decrease in the energy gap upon aggregation.

Table 4.5. Geometry optimized (B3LYP/6-311G**+ level of theory) calculations and redox properties of AN and TAN using Schrödinger Materials Science Suite using Jaguar DFT engine.

	Energy (eV)				E_g (eV)	Redox Potential (V)	
	HOMO-1	HOMO	LUMO	LUMO+1	(E_{LUMO}-E_{HOMO})	E_{ox}	E_{red}
AN	-6.41	-5.86	-2.74	-2.40	3.12	2.08	-1.30
TAN	-5.64	-5.36	-2.93	-2.10	3.26	1.81	-1.33
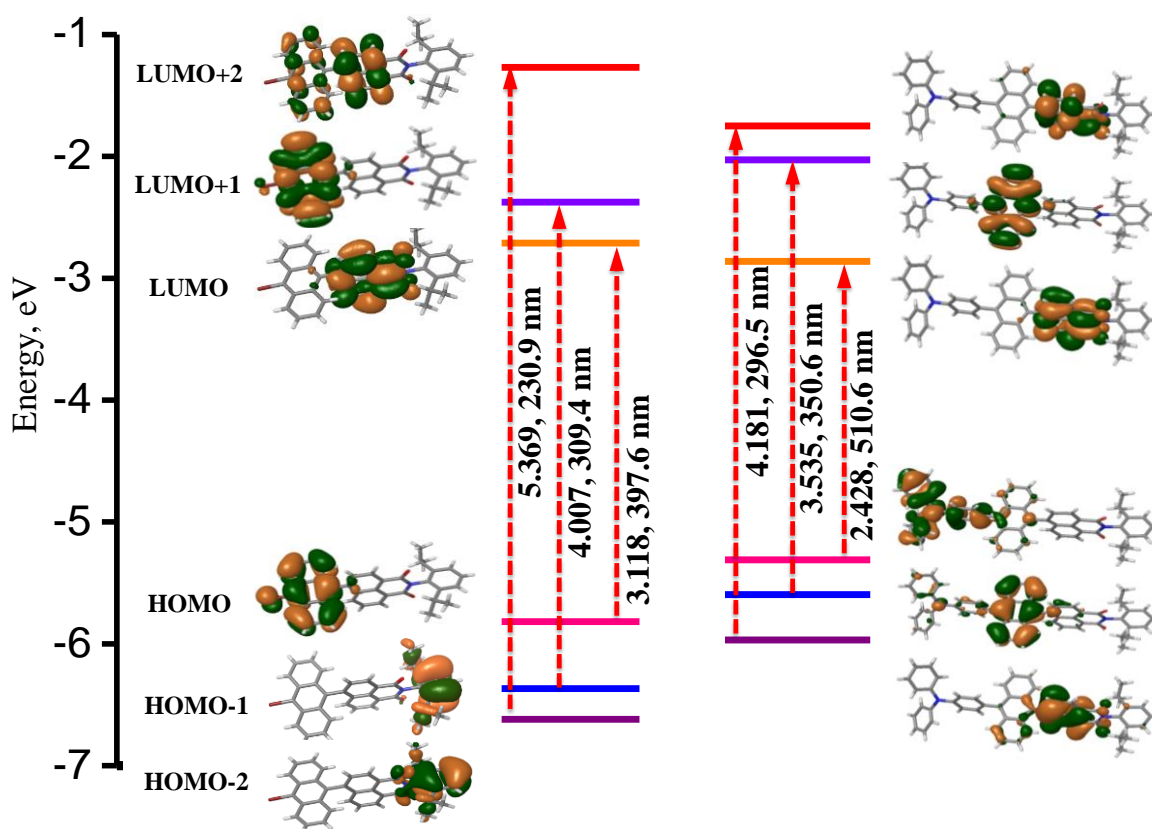
Figure 4.7. *Frontier molecular orbital analyses of ANBr and TAN performed at B3LYP/6-31G+** level of theory.*

4.7. Steady-state absorption and fluorescence measurements

UV-Vis absorption spectrum of AN in ACN (Figure 4.8.a) exhibit bands centered at 260 and 350-395 nm with a shoulder band around 400 nm. The short wavelength absorption band is attributed to $n \rightarrow \pi^*$ (HOMO-1$\rightarrow$LUMO) transition corresponding to N unit, whereas long wavelength band around 350-395 nm is due to $\pi \rightarrow \pi^*$ transition observed in A. The absorption spectrum of TAN (Figure 4.8.a) in ACN comprises of absorption bands centered at 263, 310 and 350 - 395 nm with a shoulder band around 420 nm. The absorption band around 280 - 300 nm is due to $n \rightarrow \pi^*$ (HOMO-1$\rightarrow$LUMO) transition observed in N unit [137], the peak at 310 nm corresponds to the $\pi \rightarrow \pi^*$ transition in T, whereas the band around 350 - 395 nm is due to $\pi \rightarrow \pi^*$ transition in A. Extended shoulder band observed around 400 nm for AN and 420 nm for TAN is attributed to the charge transfer (CT) interactions [29] between the constituent chromophores in the ground state [162]. A red-shift of 20 nm corresponding to the shoulder band in TAN, relative to AN is attributed to the enhancement in the ground state CT interactions in TAN by the incorporation of T (secondary donor) unit.

The emission spectrum of AN in ACN (Figure 4.8.b) consists of a shoulder band around 500 nm and an intense broad band at 620 nm when excited at 440 nm. Remarkable red-shift (ca. 200 nm) in the emission maximum of the peak at 620 nm in AN compared to A and N units indicates the presence of CT interactions between the constituent units, whereas the band around 500 nm arise from localized emission (LE).

Chapter 4- Colossal Enhancement in the Lifetime of Charge Separated States in Self-Assembled Twisted Non-Symmetric Donor-Acceptor Triad

157
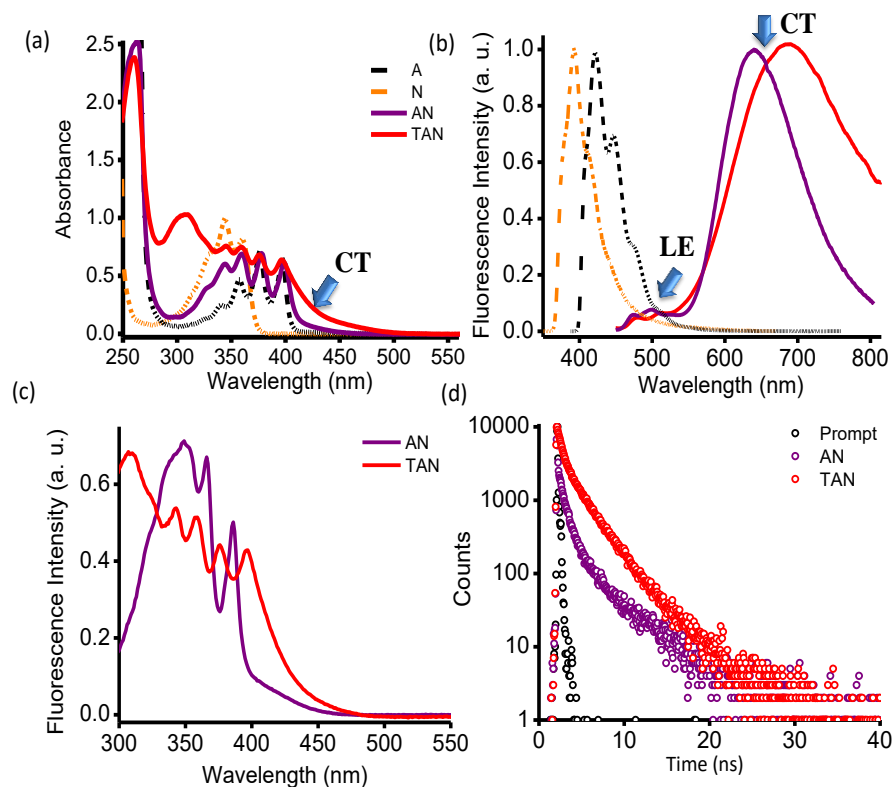
Figure 4.8. *(a) absorption, (b) emission spectra (λ_{ex} = 440 nm), (c) excitation spectra and (d) time correlated single photon counting decay profiles (λ_{ex} = 375 nm) of AN and TAN in ACN.*

The emission spectrum of TAN in ACN (Figure 4.8.b) exhibits LE band around 500 nm and broad CT band centered at 700 nm when excited at 440 nm. Similar to AN, CT band in TAN is red-shifted by ca. 280 nm compared to A and N subunits, confirming the existence of strong CT interactions. Excitation spectra (Figure 4.8.c) of AN and TAN in ACN resembles corresponding absorption spectra establishing emissive nature of charge transfer species formed, when collected at respective emission maxima. Time correlated single photon counting measurements (Figure 4.8.d, Table 4.6) of AN and

TAN in ACN, exhibit bi and tri exponential decay respectively, with an average

fluorescence lifetime of 3.03 and 11.13 ns, when excited at 375 nm.

Table 4.6. Solvent dependent photophysical measurements of AN and TAN.

Solvent	AN						TAN						
	Lifetime (ns)			Φ_f	k_r	k_{nr}	Lifetime (ns)				Φ_f	k_r	k_{nr}
	τ_1 (%)	τ_2 (%)	τ_{avg}		(10^8 s^{-1})	(10^8 s^{-1})	τ_1 (%)	τ_2 (%)	τ_3 (%)	τ_{avg}		(10^8 s^{-1})	(10^8 s^{-1})
Hexane	2.49	-	2.48	0.61	2.46	1.55	2.60	4.40	-	4.13	0.44	1.06	1.36
							(23)	(77)					
Toluene	1.89	-	1.89	0.56	2.96	2.33	2.96	5.17	-	3.94	0.41	1.04	1.49
							(68)	(32)					
CHCl$_3$	1.24	-	1.24	0.23	1.85	6.21	1.12	5.44	-	3.92	0.05	0.13	2.42
							(72)	(28)					
THF	0.08	2.22	2.06	0.20	0.97	3.88	1.32	3.47	-	2.75	0.03	0.11	3.52
	(68)	(32)					(57)	(43)					
ACN	0.07	3.33	3.03	0.09	0.29	3.01	3.10	10.54	4.50	11.13	0.02	0.018	0.88
	(83)	(17)					(22)	(39)	(39)				
MeOH	0.09	1.71	1.62	0.05	0.31	5.86	2.99	11.86	0.68	10.44	0.009	0.0086	0.94
	(51)	(49)					(22)	(43)	(35)				

Chapter 4- Colossal Enhancement in the Lifetime of Charge Separated States in Self-Assembled Twisted Non-Symmetric Donor-Acceptor Triad

159

4.8. Solvent and concentration dependent absorption and fluorescence measurements

Solvent polarity dependent UV-Vis absorption measurements of AN and TAN established negligible changes in the absorption maxima (Figures 4.9.a,c). In contrast,
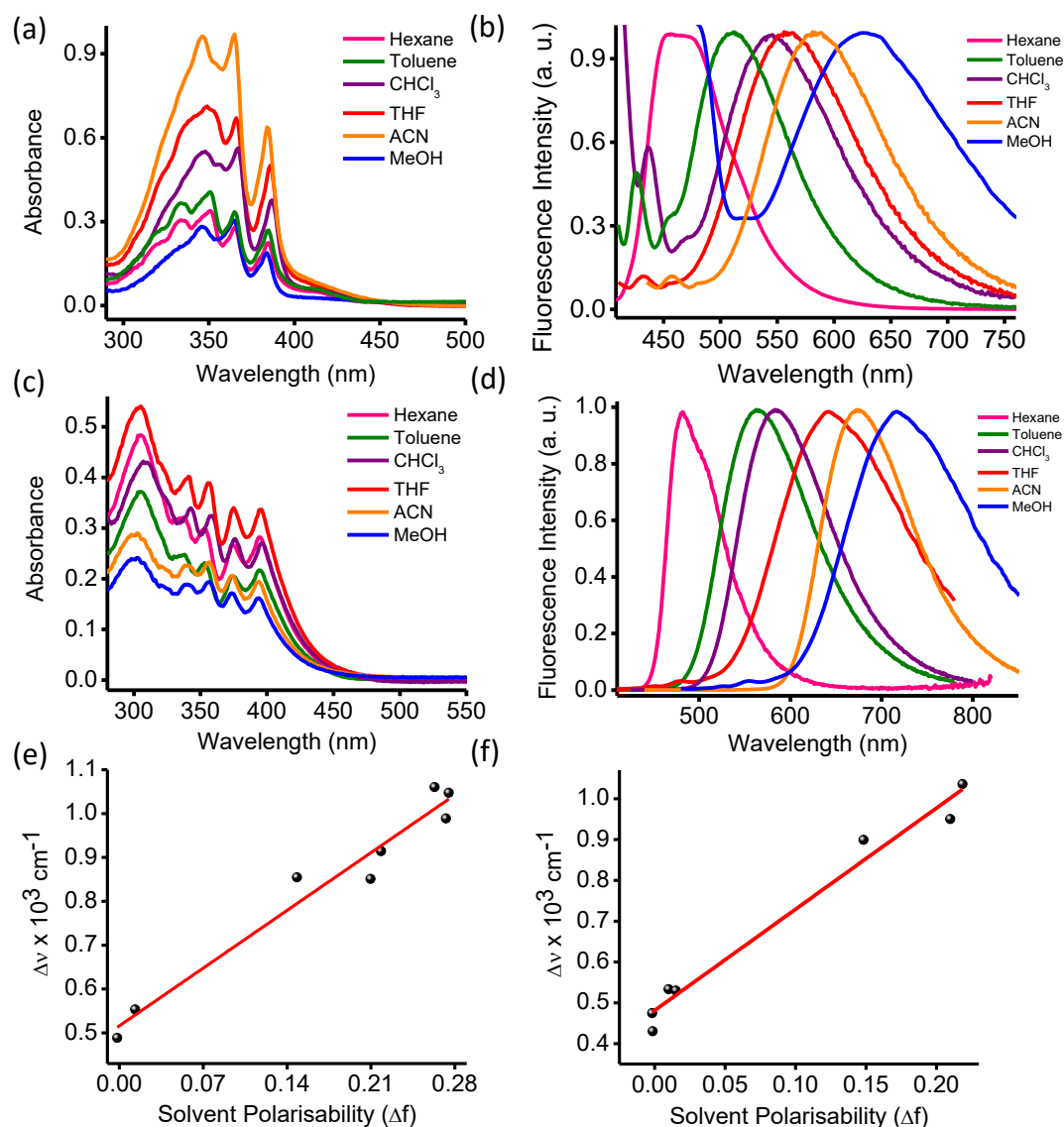
Figure 4.9. *Solvent polarity dependent (a), (c) absorption and (b), (d) emission spectra and (e), (f) Lippert-Mataga plots of AN and TAN respectively.*

AN and TAN indicated a substantial bathochromic shift of 175 and 235 nm respectively, (Figures 4.9.b,d) in the emission maxima with increasing solvent polarity. With increase in the solvent polarity, a 12 and 48-fold decrease in fluorescence quantum yield (Φ_f) of AN and TAN (Table 4.6) respectively, is observed. The reduction in Φ_f of AN and TAN with an increase in solvent polarity establishes the possibility of photoinduced electron transfer [186] in the dyad AN and the triad TAN. The difference between excited and ground state dipole moments ($\Delta\mu$) in AN and TAN (Figures 4.9.e-f) is evaluated to be 4.26 and 5.74 D, respectively, employing Lippert-Mataga [141] equation (Equation 4.1.).

$$\overline{\vartheta_A} - \overline{\vartheta_F} = \frac{2}{hc}\left(\frac{\epsilon-1}{2\epsilon+1} - \frac{n^2-1}{2n^2+1}\right)\frac{(\mu_e-\mu_g)^2}{a^3} + \text{constant} \tag{4.1.}$$

wherein, $\overline{\vartheta_A} - \overline{\vartheta_F}$ is the Stokes shift between absorption and emission intensity in respective solvents expressed in wavenumbers (cm^{-1}), '*h*' the Planck's constant in ergs (6.626x10^{-27} ergs), '*c*' the speed of light in cm/s (3x10^{10} cm/s) and '*a*' the Onsager cavity radius in which the fluorophores resides.

From the centers of spin density distributions and Lippert-Mataga plots charge dependent excitation spectral measurements of AN and TAN in CHCl$_3$ (Figures 4.10.a-d) revealed the probability of aggregation at higher concentrations ($\geq$ 0.5 mM). In CHCl$_3$, as the concentration of AN increases from 0.5 to 0.8 mM, the intensity of separation in AN and TAN is estimated to be 73% and 60% respectively. Concentration absorption band around 300-420 nm decreases, in the excitation spectra. Further increment in the concentration up to 1.3 mM resulted in the appearance of a new red-

Chapter 4- Colossal Enhancement in the Lifetime of Charge Separated States in Self-Assembled Twisted Non-Symmetric Donor-Acceptor Triad

161
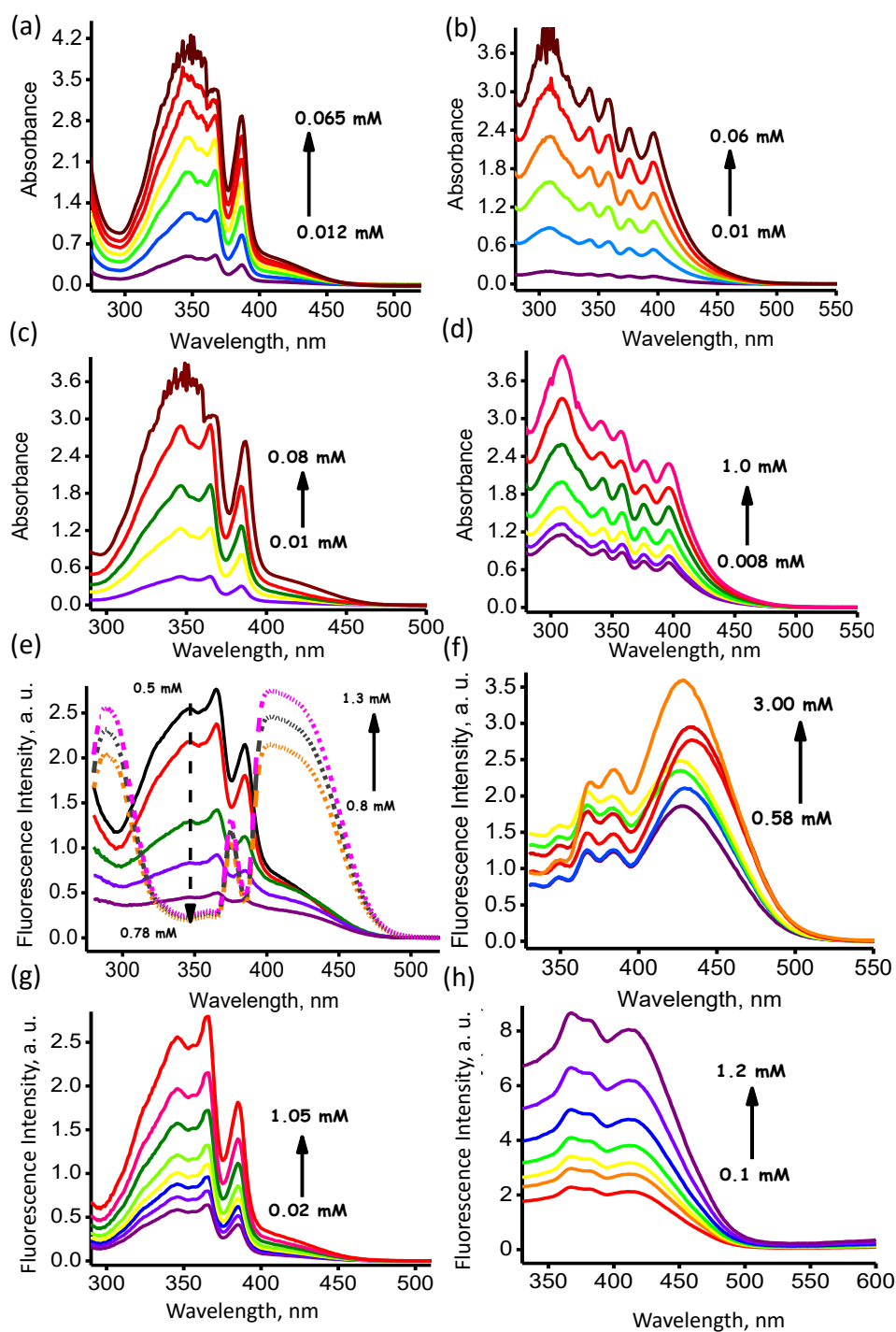
Figure 4.10. *Concentration dependent absorption spectra (a), (c) of AN and (b), (d) of TAN in CHCl₃ and ACN respectively. Concentration dependent excitation spectra of (e) AN, (f) TAN in CHCl₃. Concentration dependent excitation spectra of (g) AN and (h) TAN in ACN.*

shifted broad band around 440 nm confirming the presence of AN aggregate at higher

concentrations. Similar concentration-dependent changes in the excitation spectra for

TAN in CHCl₃ at higher concentrations indicate the possibility of the dimeric

arrangement, similar to that in the crystalline state (Figures 4.10.e-h). In contrast, AN

and TAN in ACN did not show aggregate formation.

The thermodynamic feasibility of photoinduced electron transfer (PET), between

the donor units (A and/or T) and acceptor unit N, in AN and TAN, is evaluated

employing Rehm-Weller analysis [40].

$$\Delta G_{ET} = E_{Ox} - E_{Red} - E_s - \frac{e_0^2}{r_{DA}\varepsilon_s} + S \tag{4.2.}$$

where 'e_o' is the electronic charge, 'r_{DA}' is the centroid to centroid distance between the

donor and the acceptor. From crystal structure of ANBr, 'r_{DA}' between A and N in AN is

estimated to be 5.47 Å (Figure 4.11.). In TAN 'r_{DA}' between A and N is found to be 5.40
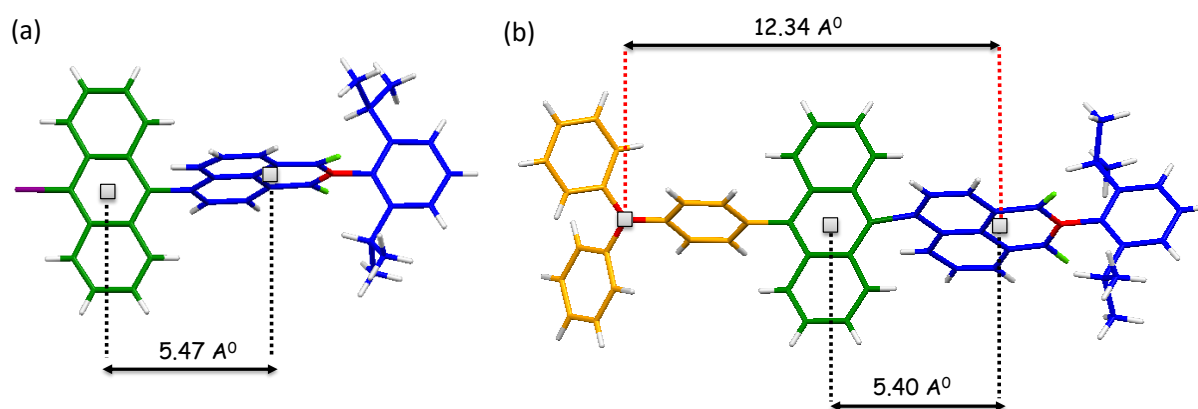
Figure 4.11. *Represents centroid to centroid distance between donor and acceptor units in AnBr and TAN. (▢) shows the centroids of A, N and T units of dyad ANBr and TAN.*

Chapter 4- Colossal Enhancement in the Lifetime of Charge Separated States in Self-Assembled
Twisted Non-Symmetric Donor-Acceptor Triad

163

Å, while 'r_{DA}' between T and N is calculated to be and 12.34 Å from crystal structure

(Figure 4.11.). 'ε' is the static dielectric constant of the solvent in which the redox

potentials are being measured (ACN in this case, ε_s = 38.8), and 'S' is the difference

between the ion pair energy in the polar solvent, in which redox potentials are

measured and other less polar solvents in which the electron-transfer rate constants are

measured and in a polar solvent such as ACN, $\frac{e_0^2}{r_{DA}\varepsilon_s} \cong S \cong 0$ [118].

The oxidation potentials (E_{Ox}) of anthracene (A) and triphenylamine (T) are

found to be 1.31 [187] and 1.05 V [188] respectively, while naphthalimide has a

reduction potential (E_{Red}) of -1.33 V, against saturated calomel electrode (SCE). The

singlet excited state energy (E_s) of the acceptor (NI) is estimated to be 3.17 V. A

favorable Gibb's free energy (ΔG_{ET}) of -0.47 eV for PET from singlet excited state of A

(^{1}A*) to N is observed for AN, upon photoexcitation of A. Furthermore, ΔG_{ET} for PET

from A to N and T to N in TAN are calculated to be -0.48 and -1.09 eV respectively

(Figures A4.2-4.3, appendix).

4.9. Transient absorption experiments

Nanosecond and femtosecond transient absorption (nTA and fTA) spectroscopic

measurements [31, 79, 158] were employed to explore the presence of CTIs in the

monomeric and aggregated state of the dyad AN and triad TAN. Upon photoexcitation
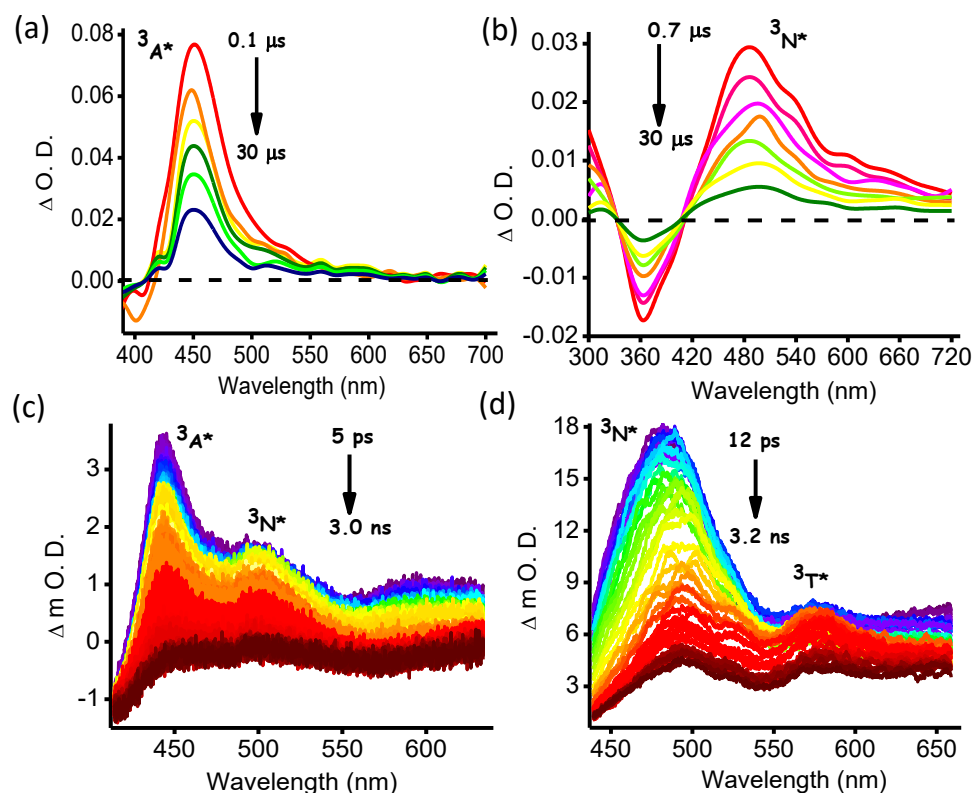
Figure 4.12. *(a), (b) nanosecond (λ_{ex} = 355 nm) and (c), (d) femtosecond (λ_{ex} = 400 nm) transient absorption spectra of 3 μM AN, TAN in ACN respectively.*

of AN at 355 nm, nTA spectra of AN in the monomeric ([AN] = 3 μM in ACN) state exhibited positive absorption centered at 430 nm with a lifetime of 1.08 μs (Figure 4.12.a, A4.4, Table 4.7). nTA spectra of aggregated state ([AN] = 3 mM in CHCl$_3$) displayed a positive absorption centered at 430 nm having a lifetime of 8.98 μs (Figure 4.13.a, Table 4.7, Figure A4.4, appendix). The absorption peak centered at 430 nm in the monomeric and aggregated state of AN could be attributed to the triplet absorption of anthracene (^{3}A*) [189]. nTA spectra of 3 μM TAN in ACN (monomeric) excited at 355 nm, possess a positive absorption at 490 nm, that is characteristic of triplet state absorption of N (^{3}N*)

Chapter 4- Colossal Enhancement in the Lifetime of Charge Separated States in Self-Assembled Twisted Non-Symmetric Donor-Acceptor Triad

165
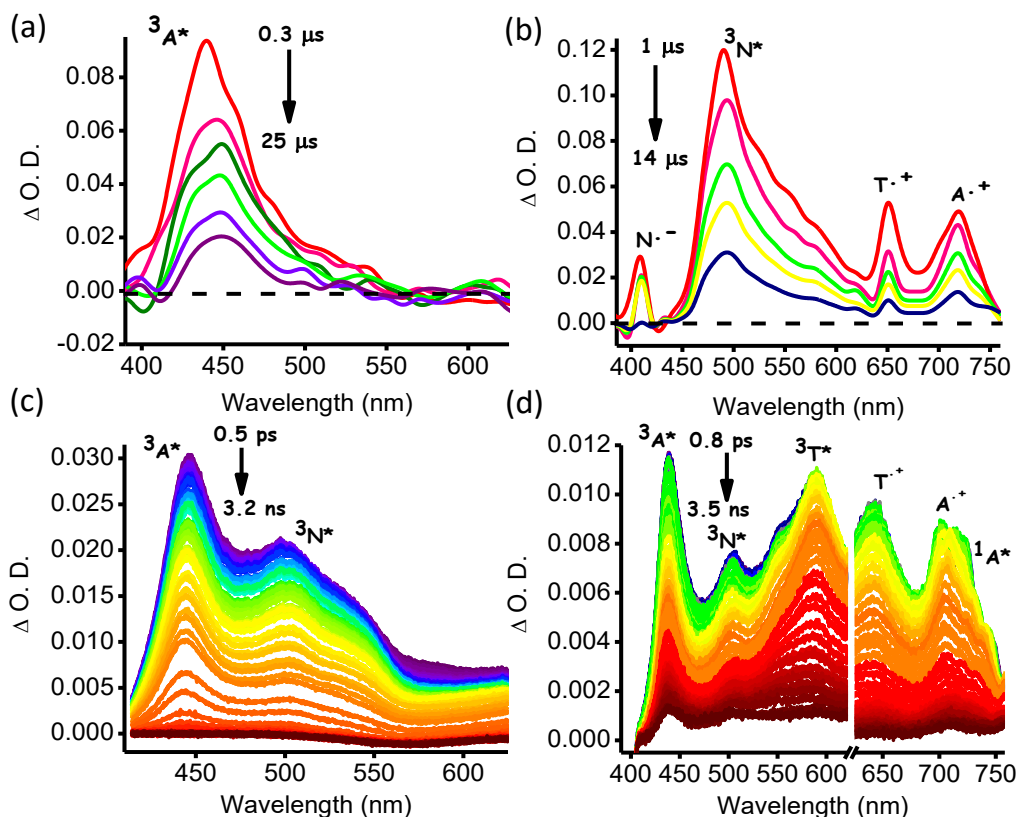
Figure 4.13. *(a), (b) nanosecond (λ_{ex} = 355 nm) and (c), (d) femtosecond (λ_{ex} = 400 nm) transient absorption spectra of 3 mM AN and TAN in CHCl$_3$ respectively.*

[142, 143] with lifetime of 1.57 μs (Figure 4.12.c, Table 4.7). nTA measurement of aggregated TAN (3 mM in CHCl$_3$) has four absorption bands centered at 420, 490, 660 and 710 nm respectively (Figures 4.13.b, Table 4.7). The positive absorption peak centered at 420 nm with a lifetime of 2.51 μs corresponds to the radical anion of N ($N^{.-}$) [142, 158, 165], while a positive absorption band at 490 nm having a lifetime of 1.27 μs corresponds to the triplet absorption of N ($^3N^*$) [123, 142]. The band at 660 nm with a lifetime of 11 μs could be attributed to the radical cation of T ($A^{.+}$) [190], whereas the absorption peak featured at 710 nm that decays with a lifetime of $\cong$ 20 μs could be
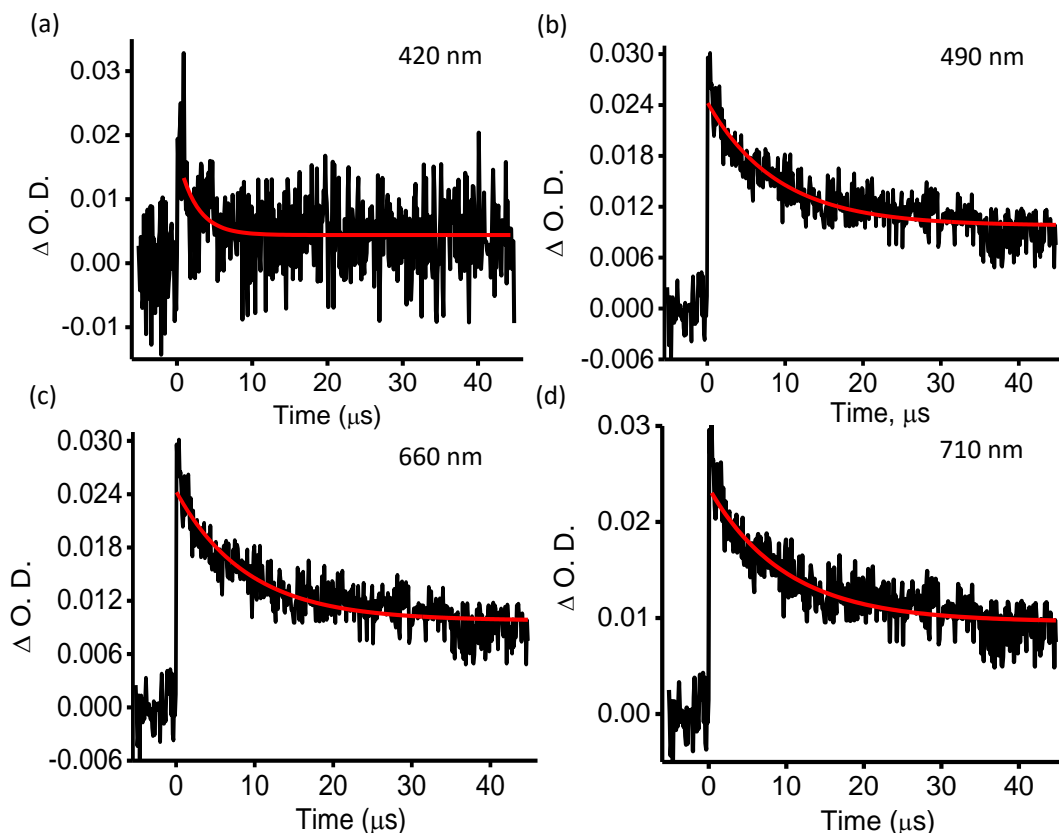
Figure 4.14. *Nanosecond transient decay profiles corresponding to (a) radical anion of $(N^{\cdot-})$, (b) triplet absorption of N $(^3N^*)$, (c) radical cation of T $(T^{\cdot+})$ and (d) radical cation of A $(A^{\cdot+})$ observed in aggregated state of TAN.*

attributed to the radical cation of anthracene ($A^{\cdot+}$, Figure 4.14.) [171]. Observation of triplet absorption of N and A ($^3N^*$ and $^3A^*$) from nTA measurements, upon photoexcitation of N, establishes the possibility of ultrafast charge separation, followed by geminate charge recombination resulting in the population of $^3N^*/^3A^*$ (Figures A4.2-4.3, appendix) [140, 191].

fTA spectra of monomeric AN excited at 400 nm consist of positive absorption bands centered around 446 and 500 nm possessing a lifetime of 1.78 and 2.71 ns respectively (Table 4.7, Figure 4.12.c). The fTA spectra of aggregated AN displays absorption peaks at 443 and 500 nm with a lifetime of 2.35 and 2.99 ns respectively (Table 4.7, Figures 4.13.c). The positive absorption bands at 443 nm correspond to the triplet state absorption of A ($^3A^*$) [189], while the positive absorption at 500 nm is due to the triplet absorption of N ($^3N^*$) [123, 158, 165] respectively. The fTA spectra of monomeric TAN (Table 4.7, Figures 4.12.d, A4.5, appendix) consists of positive absorption bands featured at 481 and 580 nm with lifetimes 0.6 and 0.5 ps respectively. The positive absorption at 481 and 580 nm is ascribed to the triplet absorptions due to N aggregated TAN (Table 4.7, Figure 4.13.d, 15) possesses positive absorption features at ($^3N^*$) [165] and T ($^3T^*$)

Table 4.7. Lifetimes of AN and TAN obtained from kinetic analyses of nTA and fTA spectra (λ_{exc} = 400 nm for fTA and 355 nm for nTA measurements).

	nTA [lifetime, μs (λ, nm)]	fTA [lifetime, ns (λ, nm)]
AN (in ACN)	1.08 (440)	1.78 (443), 2.71 (500)
AN (in CHCl₃)	8.98 (440)	2.35 (443), 2.92 (500)
TAN (in ACN)	1.57 (490)	0.0061 (480), 0.0049 (580)
TAN(in CHCl₃)	2.51 (410), 1.27 (490), 11.01 (660), 20.01 (710)	2.05 (440), 1.31 (500), 1.27 (580), 1.34 (642), 1.19 (700), 2.23 (720)
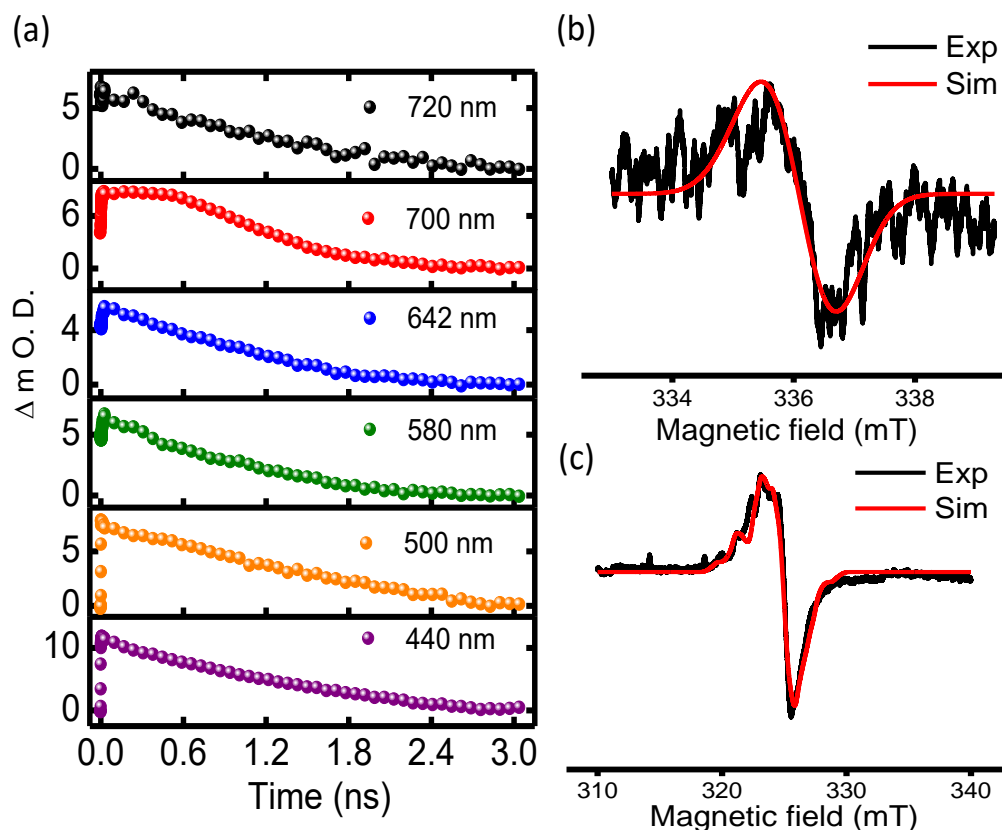
Figure 4.15. *Femtosecond transient decay profiles of (a) TAN in the aggregated state. Experimental (black trace) and simulated (red trace) light induced continuous wave electron paramagnetic resonance spectra of 3 mM of TAN (b) at 298 K and (c) 77 K in CHCl₃.*

[163] units respectively in the triad TAN. The fTA spectra of 440, 500, 580, 642, 700 and 720 nm that are ascribed to the triplet absorption of A ($^3A^*$), N ($^3N^*$), T ($^3T^*$), radical cation of T ($T^{.+}$) [190], radical cation of A ($A^{.+}$) [171] and singlet excited state of A ($^1A^*$) [189] respectively (Figure 4.13.a, Table 4.7). The lifetime of triplet excited states and radical ion-pair intermediates are tabulated in Table 4.7.

The results obtained from fTA measurements are in good agreement with the nTA measurements demonstrating that CTIs exist only in the aggregated state of TAN

in $CHCl_3$ unlike monomeric AN/TAN and aggregated AN. Light-induced continuous wave electron paramagnetic resonance (CW-EPR) measurements were employed to examine the presence of radical ion pair intermediates in TAN (Figures 4.15.b-c). A characteristic steady-state first derivative EPR spectrum is obtained for 3 mM TAN in $CHCl_3$ at 77 K with intense symmetric lines (g ~ 2.0094). Appearance of hyperfine resolved spectrum in the aggregated state at 77 K could be due to the interaction of nuclear spins with the radical ion pair intermediates upon photoexcitation of TAN [87].

4.10. Electrochemical measurements

To examine the redox properties displayed by the twisted dyad AN and triad TAN, cyclic voltammetric (CV) measurements were performed in ACN with n-Bu$_4$NPF$_6$ as the supporting electrolyte. Cyclic voltammograms of 0.8 mM AN in ACN exhibits oxidation peak at 1.42 V, and two reduction peaks at -1.25 and -1.17 V (reversible) respectively. Comparison of cyclic voltammograms of AN with the model compounds A and N in ACN (Figures 4.16.a-b) revealed that oxidation peak at 1.42 V is due to the A unit, while reduction peaks at -1.25 V and -1.17 V are due to the N unit. Cyclic voltammogram of 0.8 mM TAN in ACN exhibit two reversible oxidation potentials at 1.02 V and 1.32 V and reduction potentials at -1.27 V and -1.19 V (reversible). The oxidation peaks 1.02 V and 1.32 V could be attributed to the oxidation of T and A units respectively while the reduction peaks at-1.27 V and -1.19 V could be due to the reduction of N (Figure 4.16.a-b).
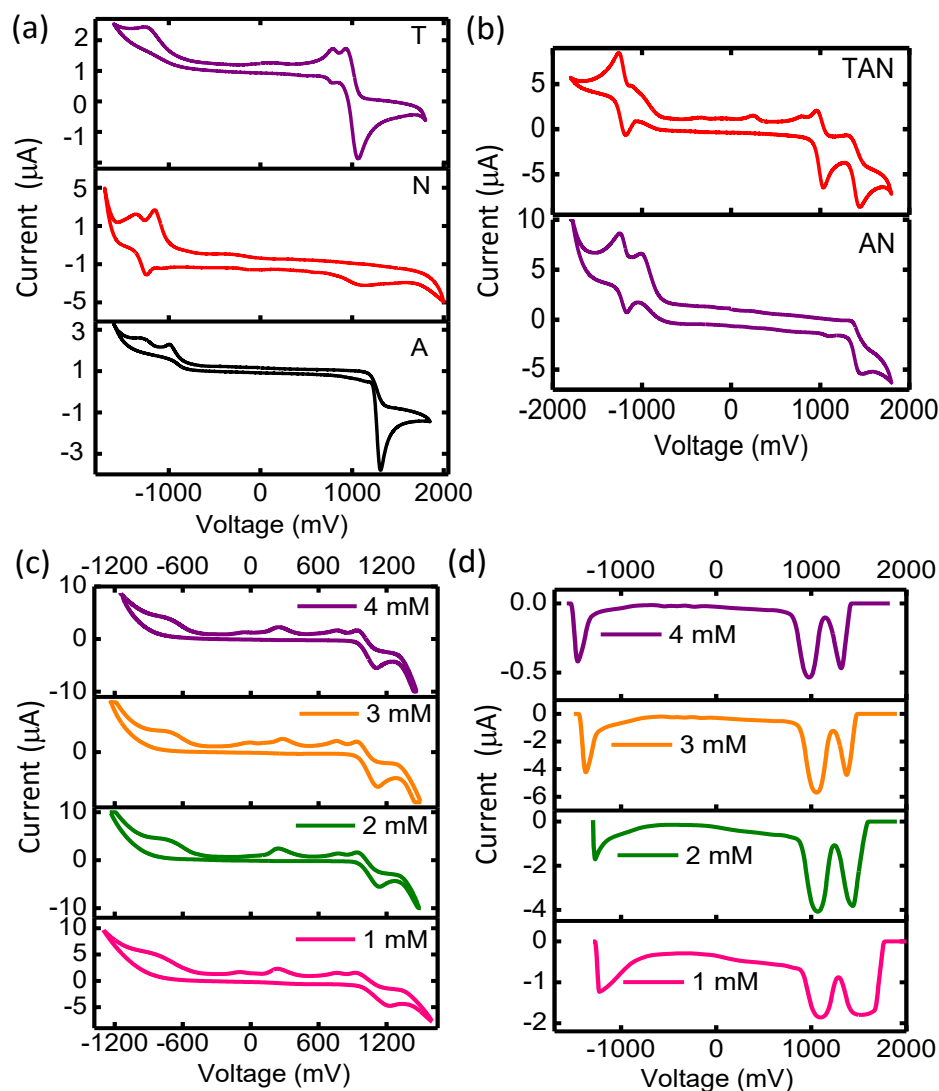
Figure 4.16. *Cyclic voltammetric measurements of (a) model compounds A, N and T and (b) 0.8 mM AN and TAN in ACN. Concentration dependent (c) cyclic and (d) square wave voltammetric measurements of TAN in CHCl₃.*

Concentration dependent cyclic and square wave voltammetric (CDCV and CDSWV respectively) measurements were performed to investigate electrochemical redox properties exhibited by AN and TAN in the aggregated state (CHCl₃). With increase in concentration of TAN from 1 mM to 4 mM, the oxidation corresponding to A unit of

Chapter 4- Colossal Enhancement in the Lifetime of Charge Separated States in Self-Assembled
Twisted Non-Symmetric Donor-Acceptor Triad

171

TAN in CHCl$_3$ becomes more feasible by 210 mV (Figures 4.16.c, Table A4.1, appendix).

CDCV experiments of TAN in CHCl$_3$ demonstrated a difference of 212 mV in the

oxidation potential corresponding to A unit (ΔE_{ox}, Figures 4.16.c, Table A4.1, appendix)

at higher concentration ([TAN] = 4 mM) as compared to the lower concentration ([TAN]

= 1 mM). CDSWV measurements of 4 mM TAN in CHCl$_3$ displayed significant

reduction in the oxidation potential of A unit (ΔE_{ox} = 221 mV, Figures 4.16.d, Table A4.1,

appendix) in TAN compared to the lower concentration ([TAN] = 1 mM) establishes

facile electrochemical oxidation of A in the aggregated state compared to the

monomeric state (Figure 4.17.).
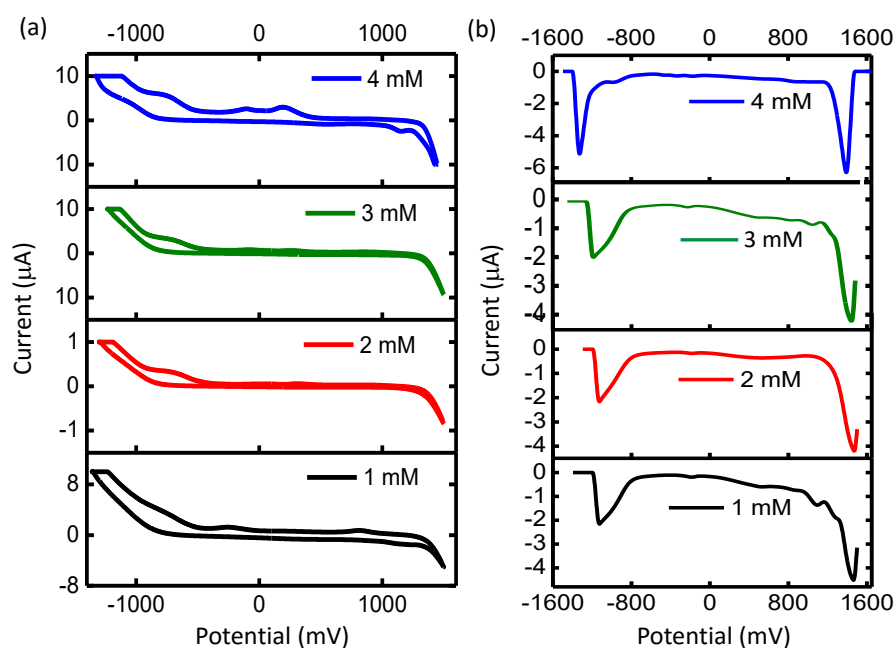
Figure 4.17. *Concentration dependent (a) cyclic and (b) square wave voltammetric measurements of AN in CHCl$_3$.*

The greater ease with which the aggregated TAN could be oxidized relative to the monomeric TAN suggests a favorable alteration in thermodynamic feasibility for photoinduced charge separation/recombination in the monomeric vs. aggregated state. Such perturbations observed in redox behavior of TAN are the direct consequence of delocalization of charge carriers across the aggregated TAN as indicated in Figure 4.18. In contrast, CDCV and CDSWV measurements of AN showed negligible changes in the redox behavior of constituent chromophores upon aggregation (Figure 4.17.). Observation of $^3N^*/^3A^*/^3T^*$ in the monomeric/aggregated AN and TAN, upon photoexcitation of N (λ_{ex} = 355 nm) and A (λ_{ex} = 400 nm) from nTA/fTA measurements
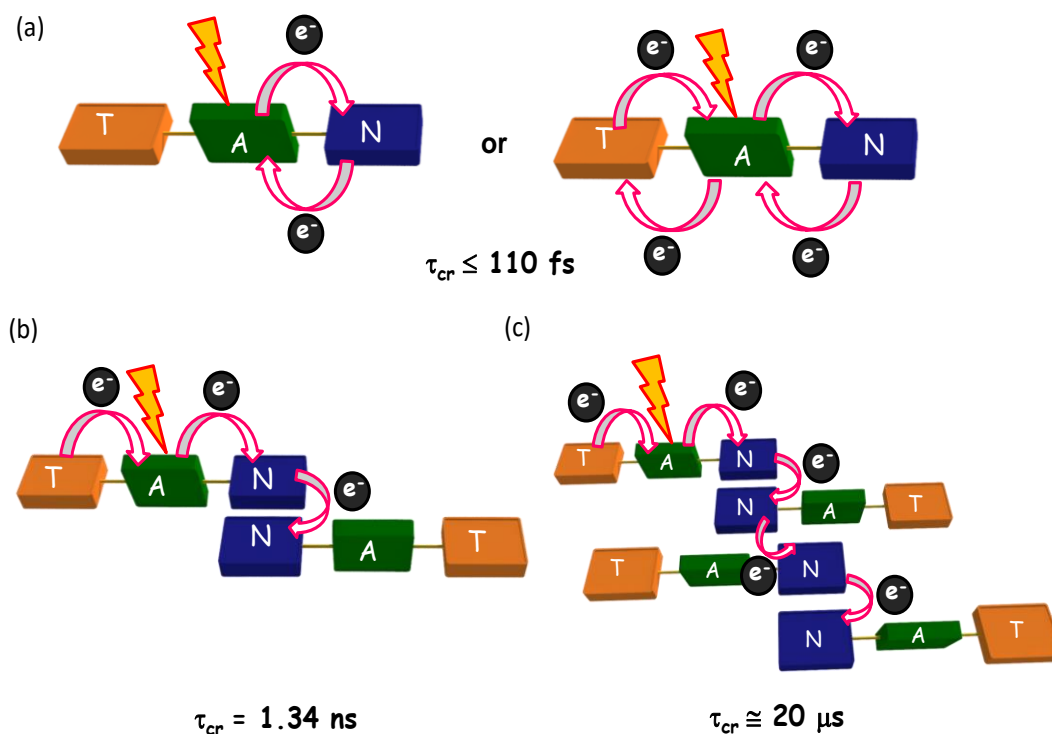
Figure 4.18. *Scheme represents heterogeneity in structure responsible for differences in charge recombination rates observed in TAN.*

Chapter 4- Colossal Enhancement in the Lifetime of Charge Separated States in Self-Assembled Twisted Non-Symmetric Donor-Acceptor Triad

173

indicate the possibility of ultrafast CS followed by geminate charge recombination populating triplet state of N/A/T (Figures A4.2–4.3) [140]. Presence of $^3A^*$ in monomeric and aggregated AN from nTA measurements, upon photoexcitation of N at 355 nm, validates ultrafast CS followed by geminate recombination leading to the formation of $^3A^*$ [192]. This is further confirmed from fTA measurements of monomeric/aggregated AN, wherein photoexcitation of A at 400 nm, generate $^3N^*/^3A^*$. Upon photoexcitation of N at 355 nm, triplet-triplet energy transfer from N to A could also result in population of $^3A^*$. Photoexcitation of N in the monomeric state of TAN generates $^3N^*$ as observed through nTA measurements, whereas photoexcitation of A populates $^3N^*/^3T^*$, as observed using fTA measurements. Upon photoexcitation of A at 400 nm, formation of $^3N^*/^3T^*$ in monomeric TAN observed from fTA measurements further establishes triplet formation via charge recombination of CTIs.

Persistence of charge separated (CS) states, by 10^8-fold in the aggregated TAN in comparison to monomeric/aggregated AN and monomeric TAN could be attributed to the delocalization of photogenerated excitons across aggregates. Upon photoexcitation of A, intramolecular electron transfer from $^1A^*$ to N unit, in monomeric/aggregated AN and monomeric TAN could generate (ΔG_{ET} = -0.48 eV) CTIs, namely $A^{.+}$and $N^{.-}$. The generated CS states, $A^{.+}$ and $N^{.-}$ undergo ultrafast geminate charge recombination ($\leq$ 110 fs, Figure 4.18.a). Subsequently, hole transfer from $A^{.+}$ to T could result in hole residing on T and electron localized on N in monomeric TAN. Enhancement in the

survival time of CTIs from $\tau_{cr}^m \leq 110$ fs in monomeric TAN to $\tau_{cr}^a = 1.34$ ns, 11 μs and $\cong 20$ μs in the aggregated state of TAN could be due to the delocalization via intermolecular charge transfer (Figures 4.18.b-c). The different survival time for CS states could arise from charge recombination occurring in smaller/larger aggregate domains and/or structural heterogeneity[193] in the aggregated TAN (Figures 4.18.). Observation of $^3N^*/^3T^*$ in the aggregated state of TAN from fTA measurements, upon excitation of A further corroborates triplet formation via geminate charge recombination. Presence of $^3A^*$ in aggregated state of TAN could arise via i) direct excitation at 400 nm (fTA) and/or ii) geminate recombination of CS states.

Small increment in the charge separation lifetime (τ_{cs}^a) of ca. 200 and 20-/22-fold were observed in the aggregated An-PDI-An and liquid crystalline BT-PDI-BT respectively relative to the monomeric state. Enhancement (Table 4.8) in the charge recombination lifetime (τ_{cr}^a) of CTIs in the aggregated state relative to the monomeric state is defined by a factor ζ [194]. For J-aggregates of M-NDI-M ($\zeta \approx 500000$), solvent vapor annealed thin films of PDI-DPP-PDI ($\zeta \approx 11765$), helical DPP-PDI-DPP ($\zeta \approx 1000$ and >150), and liquid crystalline BT-PDI-BT ($\zeta \approx 18$) remarkable enhancement in ζ is achieved by various groups. We have demonstrated a colossal enhancement ca. 10^8-fold in ζ through assembling simple modular components via bottom-up approach. Observed long-lived CS states in the aggregated vs. monomeric TAN could be ascribed

Table 4.8. A comparative account of the charge recombination lifetimes of photo-generated radical ion pair intermediates in the monomeric (τ_{cr}^m) and aggregated state. (τ_{cr}^a) reported in various literatures in symmetric donor-acceptor triad.

Charge Recombination lifetime comparison						
	Contributed by	Supramolecular triad architecture	Reference	τ_{cr}^m	τ_{cr}^a	$\zeta=\tau_{cr}^a/\tau_{cr}^m$
1	Our data	**Crystalline Triphenylamine-Anthracene-Naphthalimide**		<110 fs	1.34 ns[b]/ 20 µs[c]	12200[b]/ 181800000[c]
1	Burghardt and coworkers	**J-aggregated Bisthiophene-PDI-Bisthiophene**	*J. Phys. Chem. Lett.* **2016**, *7*, 1327	N.D.	50 ps	
2	Fernandez, Laquai, Ghosh and coworkers	**J-aggregated Melamine-NDI-Melamine**	*Chem. Sci.*, **2016**, *7*, 1115	200 ps	3 ns[b]/ 100 µs[c]	15 [b] / 500000[c]
3	Wasielewski and coworkers	**Slip-stacked PDI-DPP-PDI**	*Chem. Sci.* **2015**, *6*, 402	340 ps	6 ns[d]/ 4 µs[e]	~18[d]/ 11765[e]
4	Scott, Braunshweig and coworkers	**Helical DPP-PDI-DPP**	*J. Phys. Chem. C* **2015**, *119*, 19584	33 ps	32 ns[f]	~1000[f]
5	Braunshweig and coworkers	**Helical DPP-PDI-DPP**	*J. Am. Chem. Soc.* **2014**, *136*, 7809	<200 fs	30 ps	>150
6	Mery and coworkers Haacke and coworkers	**Liquid Crystalline Bisthiophene-PDI-Bisthiophene**	*J. Am. Chem. Soc.* **2014**, *136*, 5981 *Phys. Chem. Chem. Phys.* **2012**, *14*, 273	55 ps	1 ns	18
7	Wasielewski and coworkers	**Columnar DAB-APy-PDI-APy-DAB**	*J. Am. Chem. Soc.* **2009**, *131*, 11919	-	40 ns	-
8	Würthner, Meijer and coworkers	**Chiral OPV-PDI-OPV**	*J. Am. Chem. Soc.* **2002**, *124*, 10252	300 ps	60 ps	0.2

[m]monomeric state; [a]aggregated state; [b]from fTA and [c] nTA measurements; [d]unannealed aggregated thin film; [e]CH_2Cl_2 annealed thin film; [f]polymer thin film

to the intermolecular hopping of electron through acceptor (N) domains (Figure 4.18.) consistent with the long-lived CS states reported in liquid crystalline BT-PDI-BT triad by Burghardt and co-workers (Table 4.8).

4.11. Conclusion

In summary, twisted non-symmetrical triphenylamine-anthracene-naphthalimide (TAN) D-D-A triad for prolonging the charge separated states upon aggregation is reported. TAN triad undergoes self-assembly in CHCl₃ owing to weak co-operative interactions. Solvent polarity dependent absorption and emission measurements demonstrated the presence of ground state CT interactions. Photophysical and electrochemical measurements establish delocalization/hopping of charge carriers through smaller and larger aggregate domains of TAN in the self-

assembled state relative to the monomeric state. Following photoexcitation of A, the triad TAN in the aggregated state exhibit extended charge separated lifetime (τ_{cr}^{a}) of ca. 20 µs compared to the ($\tau_{cr}^{m} \leq 110$ fs) monomer in ACN, as monitored using nTA and fTA spectroscopic techniques. A 10^{8}–fold enhancement in the lifetime of CTIs in the aggregated state when compared to the monomeric TAN could be due to the sequential intra- and inter-molecular electron transfer. Observed long-lived CTIs in the aggregated vs monomeric state of TAN possessing D-D-A components could be attributed to the combined effects of i) nonplanar arrangement of the constituent units and/or ii) the delocalization of excitons across the naphthalimide (electron acceptor) units in the stacked antiparallel dimeric arrangement of TAN. Emergence-upon-assembly approach, thus explored, could be considered as a unique strategy for the construction of ordered and oriented multicomponent architectures to develop organic photovoltaics and photofunctional materials.

Appendix

Materials and Methods

1,8-naphthalic anhydride, 4-bromo-1,8-naphthalic anhydride (95%), 3-amino-1-propanol (≥ 99%), 1-naphthylboronic acid (≥ 95%), phenylboronic acid (95%), Tris-(4-bromophenyl)-amine (94%), 2-isopropoxy-4, 4, 5, 5-tetramethyl-1, 3, 2-dioxaborolane (≥ 96%), R(-)-2-amino-1-butanol, 2,6-diisopropylaniline (97%), 4-(diphenylamino)phenylboronic acid and tetrakis(triphenylphosphine)palladium(0) (99%) were purchased from Sigma Aldrich and used as such without further purification. Melting points (mp) were obtained using a capillary melting point apparatus and are reported without correction. IR spectra were recorded on a Shimadzu IR Prestige-21 FT-IR spectrometer as neat KBr pellets for all the derivatives. ^{1}H and ^{13}C NMR spectra were measured on a 500 MHz and 125 MHz Bruker advanced DPX spectrometer respectively and 1,1,1,1-tetramethylsilane (TMS) is used as the internal standard for ^{1}H and ^{13}C NMR measurements. CHN analyses were carried out on an Elementar vario MICRO cube Elemental Analyzer. All values recorded in elemental analyses are given in percentages. High Resolution Mass Spectra (HRMS) were recorded on Agilent 6538 Ultra High Definition (UHD) Accurate-Mass Q-TOF-LC/MS system using either atmospheric pressure chemical ionization (APCI) or electrospray ionization (ESI) mode. Photophysical measurements of the derivatives were carried out in a cuvette of 3 mm path length unless otherwise mentioned. Absorption and emission spectra were recorded on Shimadzu UV-3600 UV-VIS-NIR and Horiba Jobin Yvon Fluorolog spectrometers respectively. Solution state [123] fluorescence relative quantum yield measurements were performed using a reference dye having considerable emission spectral overlap with the emission spectrum of the sample. Lifetime measurements were carried out in an IBH picosecond time correlated single photon counting (TCSPC) system . Pulse width of the excitation (λ_{exc} = 375 nm) source is determined to be <100 ps. The fluorescence decay profiles were de-convoluted using IBH data station software version 2.1, and fitted with exponential decay, minimizing the χ^2 values.

X-ray crystallography: Single crystals of the synthesized derivatives were grown by slow evaporation of dichloromethane: hexane (1:3). X-ray diffraction experiments were performed choosing high-quality crystals of approximately $0.20 \times 0.15 \times 0.10$ mm^3 dimension. Crystallographic data collected are presented in the supporting information, Table S1. Single crystals were mounted using oil (Infineum V8512) on a glass fiber. All measurements were made on a CCD area detector with graphite monochromatic MoKα radiation. The data were collected using Bruker APEXII detector and processed using APEX2 from Bruker. All structures were solved by direct methods and expanded using Fourier techniques. The non-hydrogen atoms were refined anisotropically. Hydrogen atoms were included in idealized positions, but not refined.

Nanosecond transient absorption (nTA) measurements: Nanosecond laser flash photolysis experiments [195] of the argon purged solutions of the derivatives in ACN (monomeric) and CHCl$_3$, THF (aggregated state) were carried out in an Applied Photophysics Model LKS-60 laser kinetic spectrometer using the third harmonic (355 nm, pulse duration ≈ 10 ns) of a Quanta Ray INDI-40-10 series pulsed Nd:YAG laser as the excitation source .

Femtosecond pump-probe transient absorption (fTA) technique [196]: Spectra-physics Tsunami Oscillator (80 MHz, 800 nm) was used as seed for a Spectra-Physics Spitfire Regenerative amplifier (1 KHz, 4 mJ). A fraction of the amplified output was used to generate 400 nm pump pulse. Residual 800 nm pulse was sent through a delay line inside an Excipro pump-probe spectrometer from CDP Systems. A rotating CaF$_2$ plate (2 mm thickness) was used to generate continuum of white light from the delayed 800 nm pulses. The continuum of white light was split into two and the streams were used as probe and pump pulses. Transient absorption spectra were recorded using a dual diode array detector with a 200 nm detection window with an optical delay of 1.6 fs. Near infrared measurements were performed using a multichannel infrared detector that scans from 900 to 1600 nm. Sample solutions were prepared in a rotating sample cell with 4 mm path length. IRF was determined by solvent (10% benzene in methanol) two photon absorption and was found to be approximately 110 fs at about 530 nm.

Energy per pulse incident on the sample was attenuated employing 80% neutral density filter when required.

fTA measurements of the derivatives presented in the thesis were carried out by exciting the respective sample at 400 nm, 200 nJ, ~110 fs pulses, unless otherwise mentioned. fTA measurements of AN and TAN were performed maintaining the absorbance in the range 0.1-0.2, having satisfactory signal/noise ratio. To evaluate the photo-stability of the samples in the monomeric and aggregated state during the transient measurements steady state absorption spectrum is recorded before and after the laser irradiation. Observed high photo-stability of the samples could be attributed to i) rotating sample cell used during the measurements and/or ii) exceptional stability of the derivatives. Self-assembled solution of the derivatives in $CHCl_3$ and THF were excited with 400 nm, 200 nJ, ~110 fs pulses, to moderate singlet-singlet annihilation [114] that is often observed in multi-chromophoric assemblies. All the features observed in the fTA measurements are laser intensity independent, ruling out the assignment of kinetic components to singlet–singlet annihilation.

Dynamic light scattering (DLS): Dynamic light scattering (DLS) measurement of the derivatives was performed on a Malvern Zeta Sizer Nano Zs equipped with 655 nm laser. The aggregated solutions of the derivatives for DLS analysis were prepared in $CHCl_3$ and THF, and the experiment was carried out in a 3 mL square glass cuvette at 25 ^{0}C at a back scattering angle of 173^0.

Transmission electron microscopy (TEM): TEM measurements were carried out on FEI Tecnai 30 G^2 high resolution transmission electron microscope and JEOL 2010 with an accelerating voltage of 100 kV. The samples were prepared by drop casting $CHCl_3$ or THF solution of the derivatives, on a 400 mesh carbon-coated copper grid (Ted Pella, Inc.) at ambient conditions and allowing the excess solvent to evaporate under air in dust free conditions. TEM images were obtained without staining. The average diameter of the particles was determined from the Lorentzian fit of the histogram of the particle size distribution curves.

Scanning electron microscopy (SEM): FE-SEM measurements of the derivatives $CHCl_3$ and THF was carried out on FEI Nova NanoSEM 450 (FEG type), drop casting the aggregates from $CHCl_3$ and THF on the flat surface of silicon wafer or glass and allowing to evaporate the excess solvent under air in dust free conditions. The sample was further subjected to thin chromium sputtering using JEOL JFC-1100 fine coater to increase the signal/noise ratio. The probing side was inserted into JEOL JSM-5600 LV scanning electron microscope for obtaining the images. The average diameter of the particles was determined from the Lorentzian fit of the size distribution curve.

Cyclic Voltammetry (CV): Electrochemical measurements of the derivatives under investigation were performed on a BASi (Bioanalytical Systems, Inc.) C-3 cell stand controlled by Epsilon electrochemical workstation. A three electrode system is then constructed constituting a glassy carbon as the working electrode, a platinum-wire as the counter electrode, and an $Ag/Ag+$ (3 M NaCl) as the reference electrode. The electrochemical measurements were conducted under nitrogen atmosphere (5 psi, 10 minutes) in a deoxygenated anhydrous acetonitrile of tetra-n-butylammonium hexafluorophosphate (supporting electrolyte, 0.1 M) for monomer, and in $CHCl_3$ or THF for aggregate with a scan rate of 50–100 mV s^{-1}. Calibration of the instrument was performed using the ferrocene/ferrocenium (Fc/Fc^+) redox couple as an external standard and measured under same condition before and after the measurement of samples. The energy level of Fc/Fc+ was assumed to be –4.8 eV with respect to vacuum[197]. The half-wave potential of Fc/Fc^+ was estimated to be 0.5 V with reference to the Ag/Ag^+ electrode.

The HOMO and LUMO energy levels were calculated from the following equations:

$$E_{HOMO} = -(E_{ox}^{onset} + 4.8) \text{ eV and} \tag{A.1.}$$

$$E_{LUMO} = -\left(E_{red}^{onset} + 4.8\right) \text{ eV} \tag{A.2.}$$

respectively, where E_{ox}^{onset} and E_{red}^{onset} are the onset oxidation and reduction potentials relative to the Ag/Ag^+ reference electrode.

The electrochemical energy gap (E_g) is estimated as follows:

$$E_g = (E_{LUMO} - E_{HOMO})\ eV \qquad (A.3.)$$

where E_{LUMO} and E_{HOMO} are the corresponding to HOMO and LUMO energy levels calculated after converting the values in Ag/Ag+ with respect to the standard calomel electrode (SCE) convention.

Determination of fluorescence quantum yield, radiative and non-radiative rate constants:

Solution state fluorescence quantum yields of NI derivatives were calculated by relative quantum yield method as follows [198],

$$\Phi_s = \Phi_{ref}\left(\frac{I_s}{I_{ref}}\right)\left(\frac{OD_{ref}}{OD_s}\right)\left(\frac{n_s}{n_{ref}}\right)^2 \qquad (A.4.)$$

wherein, Φ_s and Φ_{ref} are the quantum yields of sample and reference respectively, I_s and I_{ref} are the area under the emission spectrum for sample and reference respectively. OD_s and OD_{ref} are the absorbances of sample and reference respectively at the excitation wavelength. n_s and n_{ref} are the refractive index of the solvent in which sample and reference are taken.

Radiative (k_r) and non-radiative (k_{nr}) rate constants from the singlet excited states are calculated from the fluorescence quantum yields, Φ_f.

$$\Phi_f = \frac{k_r}{k_r + k_{nr}} \qquad (A.5.)$$

The rate constants k_r and k_{nr} can be evaluated by measuring fluorescence lifetimes (τ_f) from TCSPC measurements. The following equations depict relation between Φ_f, τ_f, k_r and k_{nr}.

$$k_r = \frac{\Phi_f}{\tau_f} \quad \text{and} \qquad (A.6.)$$

$$k_{nr} = \frac{1 - \Phi_f}{\tau_f} \qquad (A.7.)$$

a change in Φ_f could be attributed to the changes in either k_r/k_{nr}. The enhancement in the quantum yield (Φ_f) with increased solvent polarity is due to the stabilization of the excited states by virtue of interaction with the solvent dipoles and decrease in the non-radiative (k_{nr}) rate constant.

Determination of degree of charge separation from Lippert-Mataga plot [198]: The origin of solvent polarity dependent Stokes shifts could be explained using Lippert-Mataga (L-M) plots and Onsager's reaction field model, approximating that a dipole is placed at the center of a vacuum cavity in a homogeneous dielectric medium. The interaction between the solvent and

fluorophores affect the energy difference between the ground and excited states and hence the dipoles associated with them. The difference in excited (μ_e) and ground state (μ_g) dipole moments could be expressed as a function of refractive index (n) and dielectric constant (ϵ) of the medium under consideration and is described as L-M equation as follows,

$$\overline{\vartheta_A} - \overline{\vartheta_F} = \frac{2}{hc}\left(\frac{\epsilon-1}{2\epsilon+1} - \frac{n^2-1}{2n^2+1}\right)\frac{(\mu_e-\mu_g)^2}{a^3} + \text{Constant} \tag{A.8.}$$

wherein, $\overline{\vartheta_A} - \overline{\vartheta_F}$ is the Stokes shift between absorption and emission intensity in respective solvents expressed in wavenumbers (cm⁻¹), '*h*' the Planck's constant in ergs (6.626×10^{-27} ergs), '*c*' the speed of light in cm/s (3×10^{10} cm/s) and '*a*' the Onsager cavity radius in which the fluorophores resides.

A plot of $\Delta \upsilon, (\overline{\vartheta_A} - \overline{\vartheta_F})$ against solvent polarisability parameter, $\Delta f = \left(\frac{\epsilon-1}{2\epsilon+1} - \frac{n^2-1}{2n^2+1}\right)$ yields slope equal to $\frac{2(\mu_e-\mu_g)^2}{hca^3}$, from which difference in excited and ground state dipolemoment (μ_e- μ_g) could be evaluated as, μ_e- $\mu_g = \sqrt{slope \times \frac{hca^3}{2}}$. The Onsager cavity radius is estimated from theoretical calculations using B3LYP/6-3111G**+ level of theory.

L-M equation demonstrates the sensitivity of a molecule to the solvent polarity arising due to the changes in the excited state dipole moment relative to the ground state dipole moment. If the net change in dipole moment is zero (i.e. $\mu_e - \mu_g$ = 0) [199], absorption and emission maxima of the chromophore should not change with solvent polarity. While, if the excited state dipole moment is larger than the ground state (i. e. μ_e > μ_g, positive slope for L-M plot), the absorption and emission maxima are anticipated to red shift with increased solvent polarity. The compounds which display such behavior possess charge transfer (CT) with ($\pi \rightarrow \pi^*$) excited states. Furthermore, if the dipole moment of the excited state decreases with respect to the ground state upon excitation (μ_e < μ_g, negative slope for L-M plot), the absorption and emission maxima are expected to show blue shift with increased solvent polarity. This occurs in molecules with (n$\rightarrow \pi^*$) excited states.

The degree of charge separation is estimated as follows, one Debye (1 D) unit is 1.0×10^{-18} esu cm. 4.8 D is the dipole moment that results from a charge separation of one unit charge (4.8×10^{-10} esu) by 1 Å (10^{-8} cm). Conversion of $\Delta\mu$ expressed in Debye into esu Å units is achieved dividing by a factor of 4.8 esu⁻¹Å⁻¹ which can provide the experimental charge

separation in the molecule. Degree of charge separation (theoretical) in the molecule is obtained from centers of spin density distributions [200].

Rehm–Weller Analysis [198]: The change in free energy for the photoinduced electron transfer (ΔG_{ET}) from D to the singlet excited state of A (exciting either D/A) was estimated employing Rehm–Weller equation, as follows.

$$\Delta G_{ET} = E_{Ox} - E_{Red} - E_s - \frac{e_0^2}{r\varepsilon_s} + S \qquad \text{(A.9.)}$$

where 'e' is the electronic charge, 'r' is the centroid to centroid distance between the donor and the acceptor. 'r' for the derivatives were estimated from the center-to-center distance as obtained from the crystal structure analyses. 'ε_s' is the static dielectric constant of the solvent in which the redox potentials are being measured (ACN in this case, ε_s = 38.8), and 'S' is the difference between the ion pair energy in the solvent, in which redox potentials are measured, and in a polar solvent such as ACN, $S \approx 0$.

Light induced continuous wave- electron paramagnetic resonance (CW-EPR) spectroscopy: Continuous wave EPR (CW-EPR) measurements with X band (8.75-9.65 GHz) were carried using JEOL JES-FA200 ESR spectrometer at room temperature and liquid nitrogen (77 K) temperatures. Samples were prepared by loading the $CHCl_3$ solutions of AN and TAN in quartz cuvettes with inner and outer diameter 4 and 5 mm respectively, followed by subjecting them to nitrogen purging cycles and later sealed using a rubber septum. Samples were photoexcited inside the EPR cavity with a USHIO Optical Modulex-XENON lamp-ES-UXL 500 with an input current of 20 amperes.

Quantum Theory of Atoms and Molecules [201, 202]: The wave functions of the derivatives whose analyses have to be performed were obtained employing the geometries taken from the crystal structure using Gaussian package [203] at B3LYP/6-311G**+ level of theory. Quantum theory of atoms in molecules (QTAIM) analysis helps to understand the description of interatomic interaction in the single crystal X-ray structure. A bond is defined along the bond line between two nuclei, called a bond path, along which electron density is concentrated. In a three dimensional space there are four types of critical points, corresponding to non-degenerate points: termed (3, -3), (3, -1), (3, +1) and (3, +3). The (3, -3) and (3, +3) types represent a

maximum (which corresponds to a nuclear position) and a minimum, respectively. While (3, -1) and (3, +1) types represent saddle points called bond critical points and the ring critical points, respectively. There is also a second set of special gradient paths conjugated to the bond paths which starts at infinity but terminates at the bond critical point instead of being attracted to a nucleus. Therefore, this bundle of paths does not belong to any atom and form a surface called the interatomic surface.

The bond critical point (BCP) is a point along the bond path at the interatomic surface, where the shared electron density reaches a minimum. The physical characteristics of the BCPs [the electron density at BCP, $\rho(rBCP)$, and its Laplacian, $\nabla^2\rho(rBCP)$] reveal the approximate measure of the amount of electron density built up in the bonding region and as such could be taken as characteristic of the bond. When $\nabla^2\rho(rBCP) < 0$ and is large in magnitude, $\rho(rBCP)$ is also large which means that there is a concentration of electronic charge in the internuclear region. This is also an indication of a sharing of electronic charge between both nuclei that defines the covalent (polar) bond. When $\nabla^2\rho(rBCP) < 0$ there is a depletion of electronic charge in the internuclear region. Using the AIM 2000 software package, the electron density was integrated over atomic basins according to QTAIM using PROAIM, and thus the BCP data and the molecular graphs were obtained.

Hirshfeld Analysis [160, 204]: Important intermolecular interactions within the crystal structure of the derivatives were identified through Hirshfeld surface analysis using Crystal Explorer 3.1. The Hirshfeld surface is defined as a set of points in 3D space where the ratio of promolecule and procrystal electron densities is equal to 0.5. The exploration of intermolecular contacts is provided by mapping normalized contact distances (d_{norm}), which is a function of a closest distance from the point to the nuclei interior (di) and exterior (de) to the surface as well as on the van der Waals radii (r_{vdw}). 2D fingerprint which were generated by deriving from the Hirshfeld surface by plotting the fraction of points on the surface as the function of di and de which provide a visual summary of intermolecular contacts within the crystal.

Materials Science Suite: Materials Science Suite 2015-1 provides diverse set of tools for predicting and computing reactivity and properties of chemical systems. It encompasses tools to

facilitate in generating all the steps in a chemical simulation, including structure generation, property prediction followed by data analyses. The core simulation engine, Jaguar[205] is a high performance *ab intio* quantum mechanical package commercially produced and maintained by Schrodinger Inc. Employing pseudospectral approach, Jaguar estimates the Coulomb and exchange terms, providing significant advantages of exact exchange terms.

Geometry optimization and single point energy calculations for monomer, dimer and tetramer were performed at B3LYP/6-311G**+ level of theory using the crystal structure data, for Frontier molecular orbital (FMO) analyses. Energy gap is determined as the difference between energies of LUMO and HOMO as described in equation3. Energy level diagram is plotted using the energies obtained from FMO analyses.

Additional figures from chapter-2
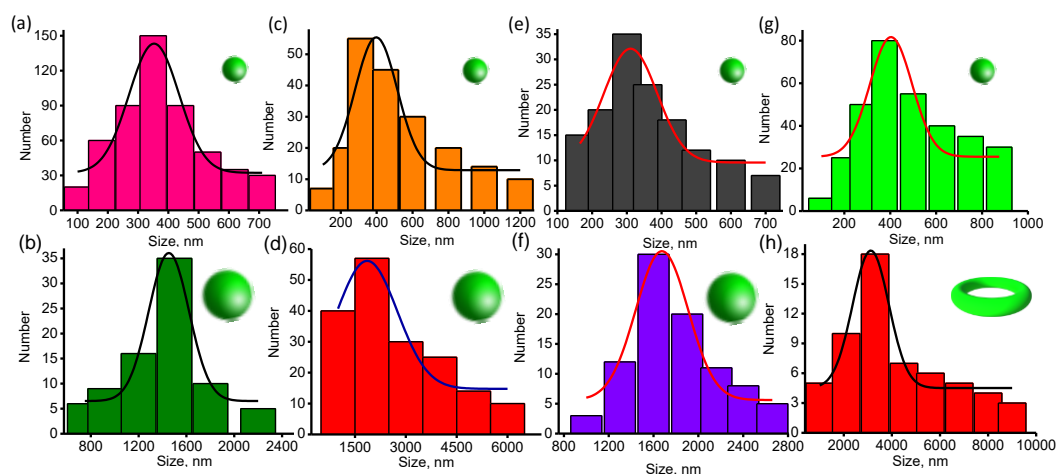
Figure A2.1. *Particle size distribution of NIN obtained from (a-b) AFM, (c-d) confocal, (e-f) SEM and (g-h) TEM measurements.*
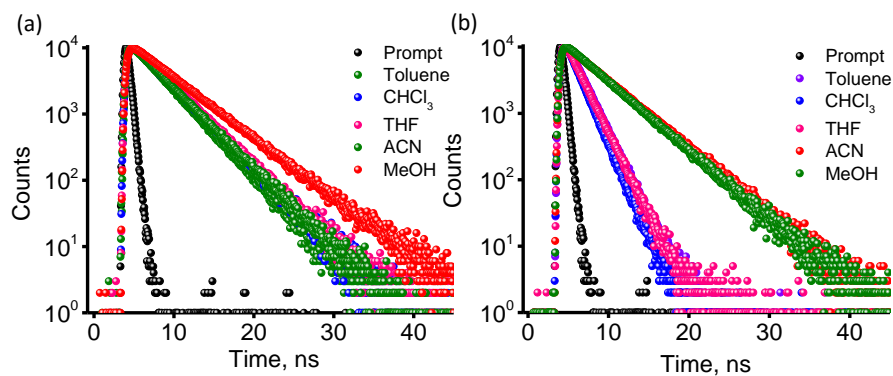
Figure A2.2. *Solvent polarity dependent fluorescence lifetime decay profiles of (a) NIPh and (b) NIN (λ_{exc} = 340 nm) and collected at respective emission maxima.*
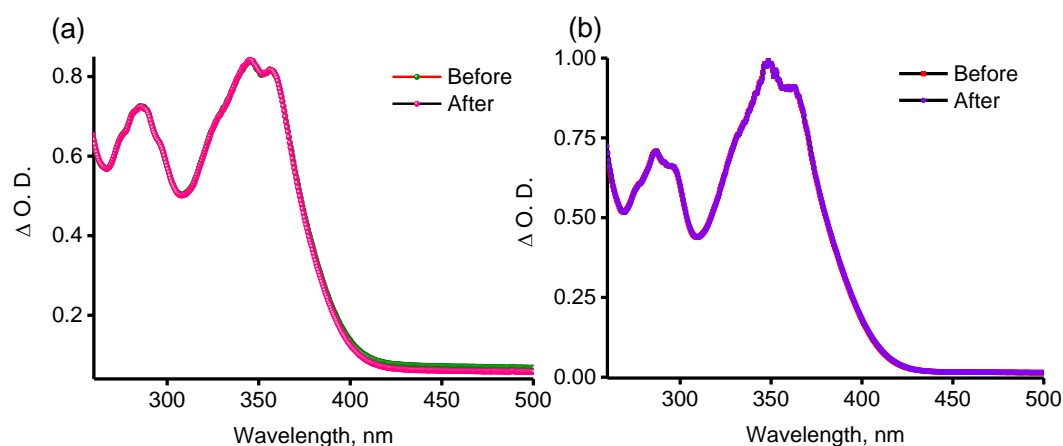
Figure A2.3. *Steady state UV-Vis absorption spectra of NIN in (a) ACN and (b) CHCl₃ before and after fTA measurements.*

Additional figures from chapter-3

Table A3.1. Crystal data and structure refinement of TNDI.

Unit cell parameters	TNDI
Empirical formula	$C_{42}H_{36}N_2O_2$
Formula weight	600.73
a (Å) :	23.1475(13)

b (Å) :	23.1475(13)
c (Å) :	12.6145(9)
	A
α(alpha):	90⁰
β(beta):	90⁰
γ(gamma):	90⁰
Volume (Å³) :	6758.9(7)
Crystal system	Tetragonal
Space group:	*P*4(2)/n
Calculated density (mg/m³):	1.181
Z:	8
Temperature (K) :	296(2)
R (F, %):	9.58
R_w (F²):	1.066
CCDC Number	1490062
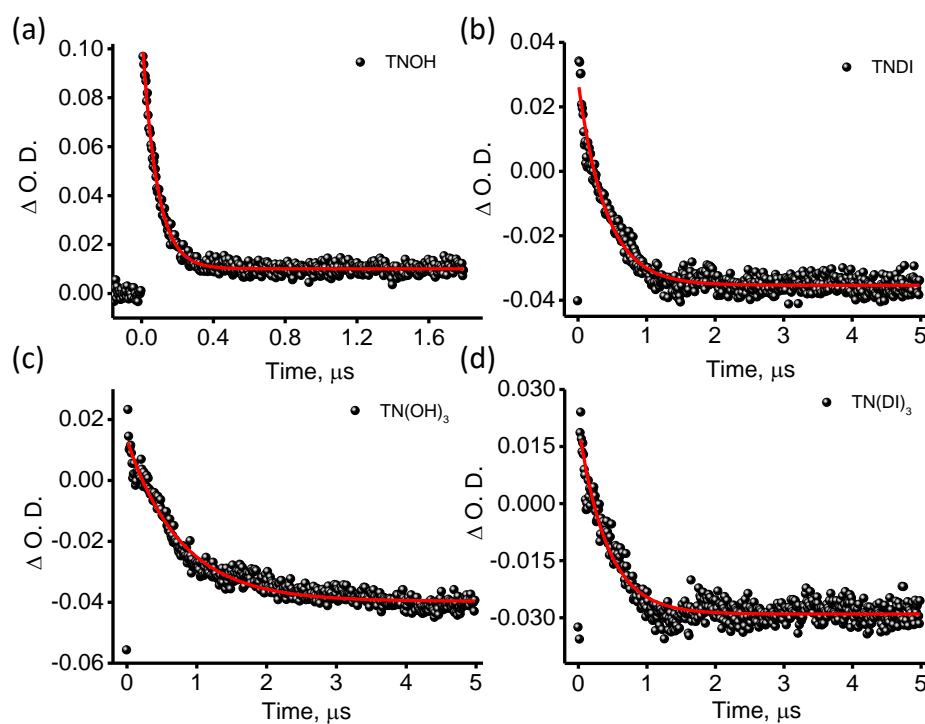
Figure A3.1. *Kinetic decay profiles of TNOH, TNDI, TN(OH)₃ and TN(DI)₃ in the monomeric state (ACN) obtained from* nTA *measurements.*
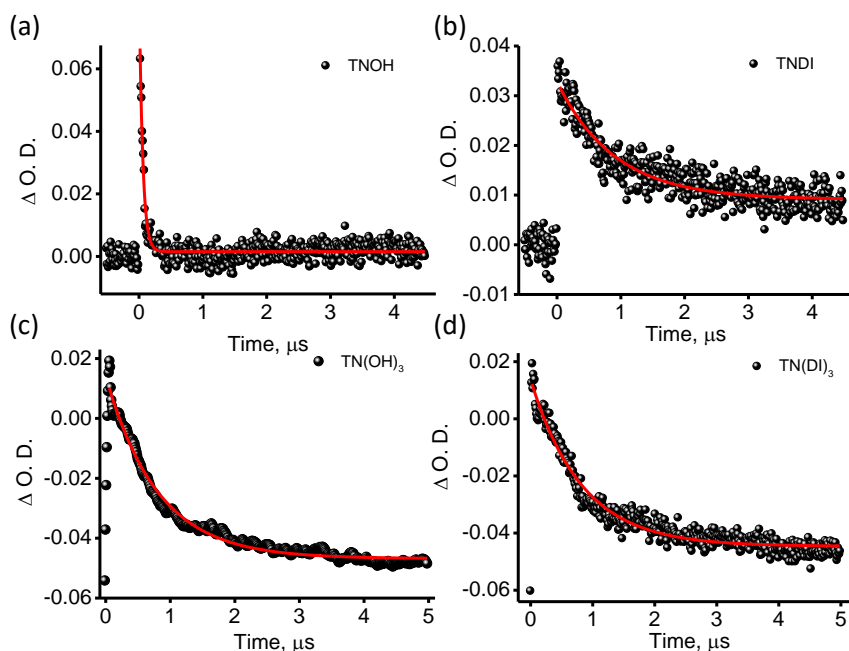
Figure A3.2. *Kinetic decay profiles of TNOH, TNDI, TN(OH)₃ and TN(DI)₃ in the aggregated state (THF) obtained from* nTA *measurements.*
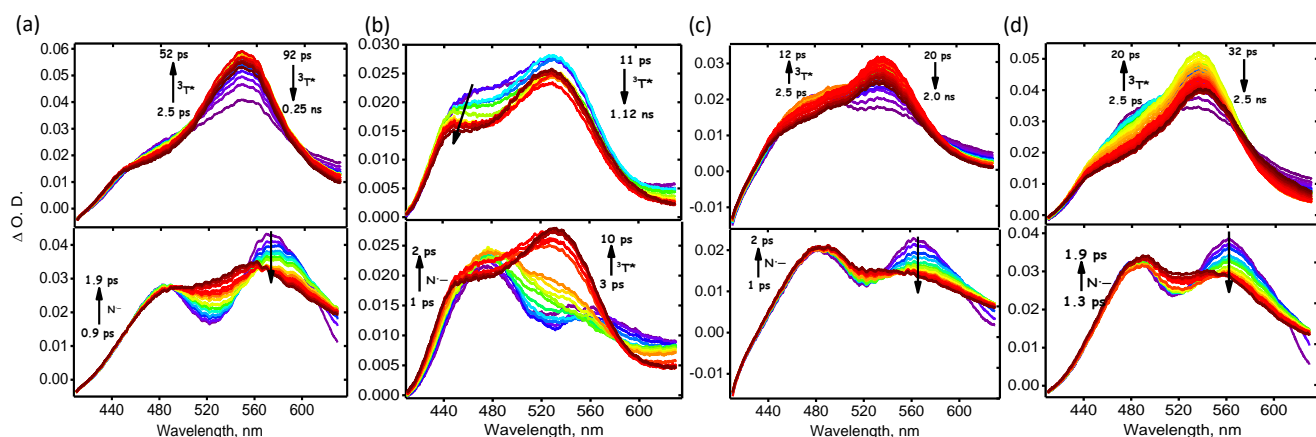
Figure A3.3. *fTA measurements of (a) TNOH, (b) TNDI, (c) TN(OH)₃ and (d) TN(DI)₃ respectively in THF.*
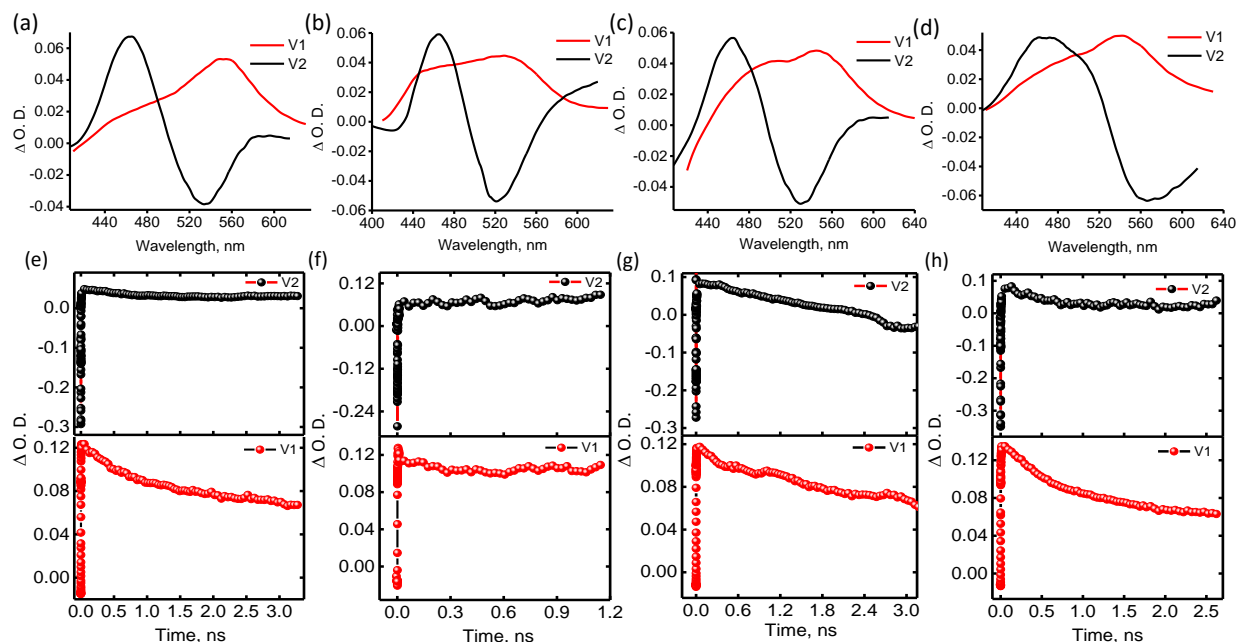
Figure A3.4. *Species associated decay spectra obtained for (a) TNOH, (b) TNDI, (c) TN(OH)₃ and (d) TN(OH)₃ respectively after SVD and global analysis of fTA spectra in THF. (e-h) represents corresponding left singular vectors.*
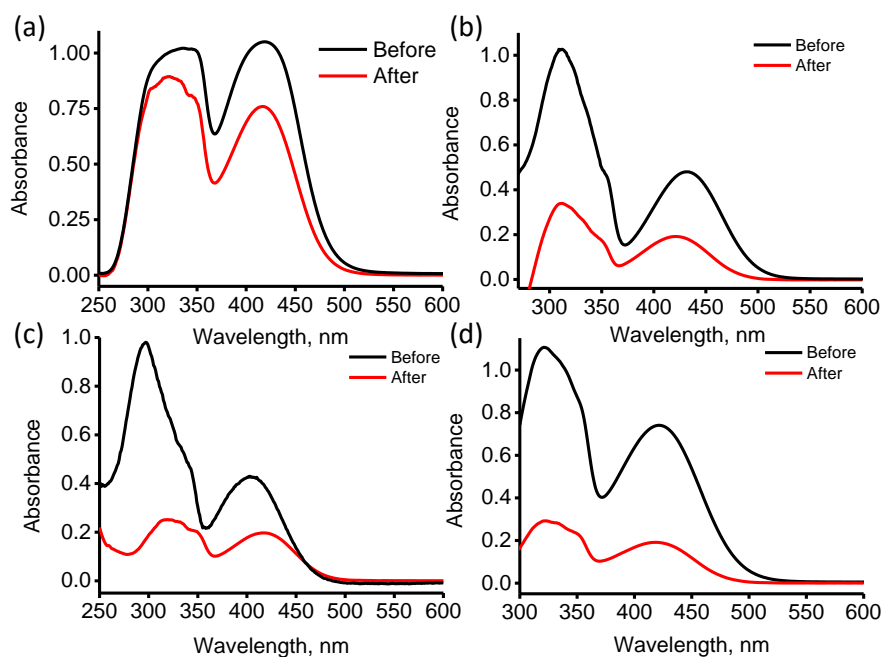
Figure A3.5. *Steady-state UV-Vis absorption spectra of (a) TNOH, (b) TNDI, (c) TN(OH)₃ and (d) TN(DI)₃ in THF recorded before and after laser irradiation.*

Additional figures from Chapter-4

Table A4.1. Concentration dependent cyclic (CDCV) and square wave (CDSWV) voltammetric measurements of TAN in CHCl$_3$.

	CV of TAN (Potential, V)			SW of TAN (Potential, V)		
1 mM	1.323	0.936	-0.833	1.533	1.094	-1.218
2 mM	1.138	0.949	-0.720	1.427	1.069	-1.279
3 mM	1.116	0.939	-0.719	1.376	1.044	-1.373
4 mM	1.111	0.940	-0.729	1.312	0.976	-1.446
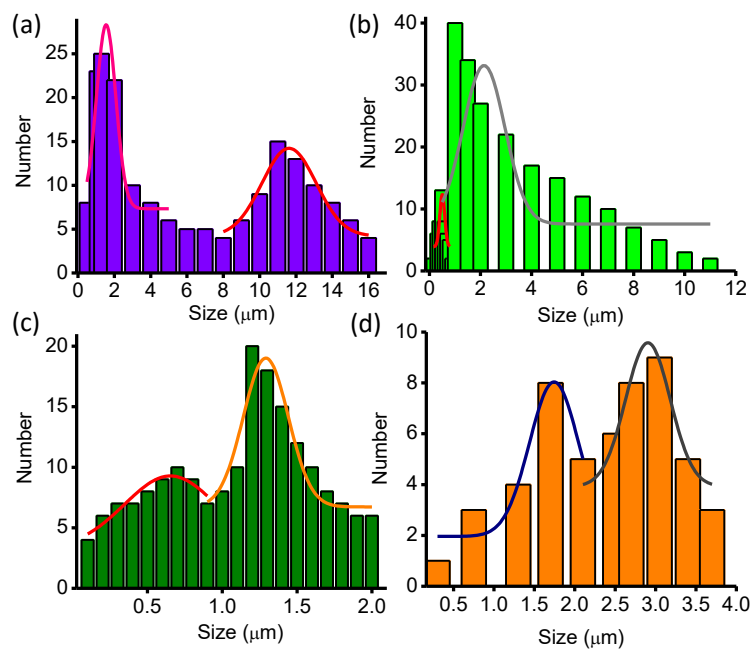
Figure A4.1. *Size distribution of (a), (c) AN and (b), (d) TAN obtained from SEM (first row) and TEM (second row) analyses.*
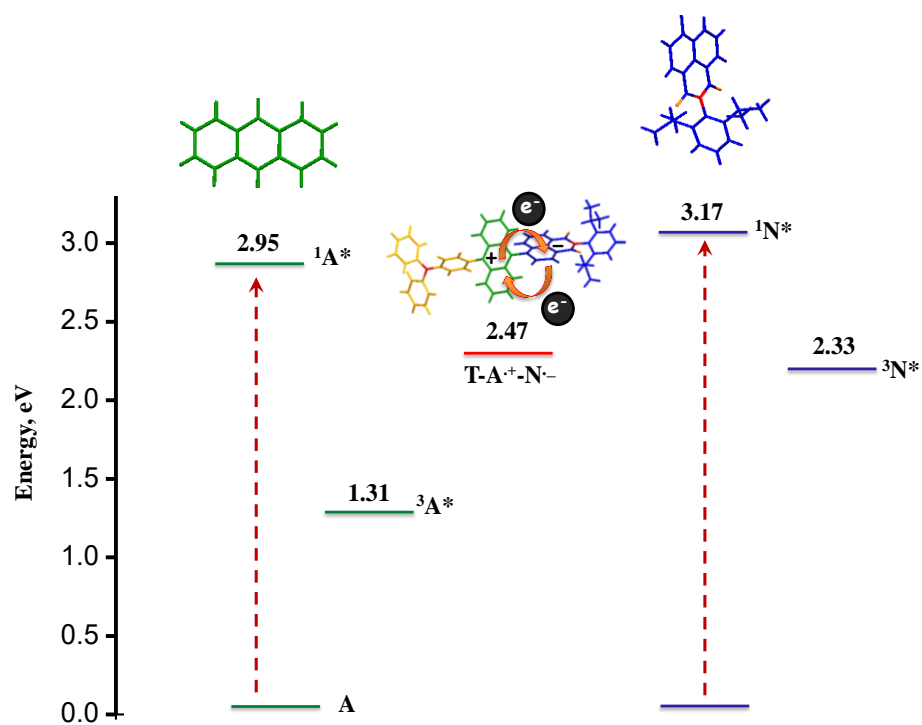
Figure 4.2. *Jablonski diagram of dyad and triad representing various photoprocesses upon photoexcitation at 355 and 400 nm.*
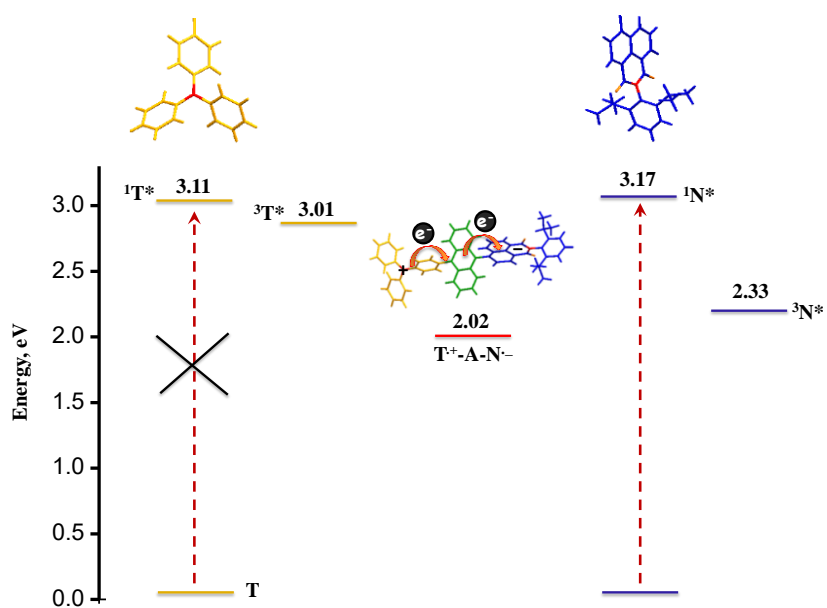
Figure A4.3. *Jablonski diagram of triad TAN representing various photoprocesses upon photoexcitation at 355 nm.*
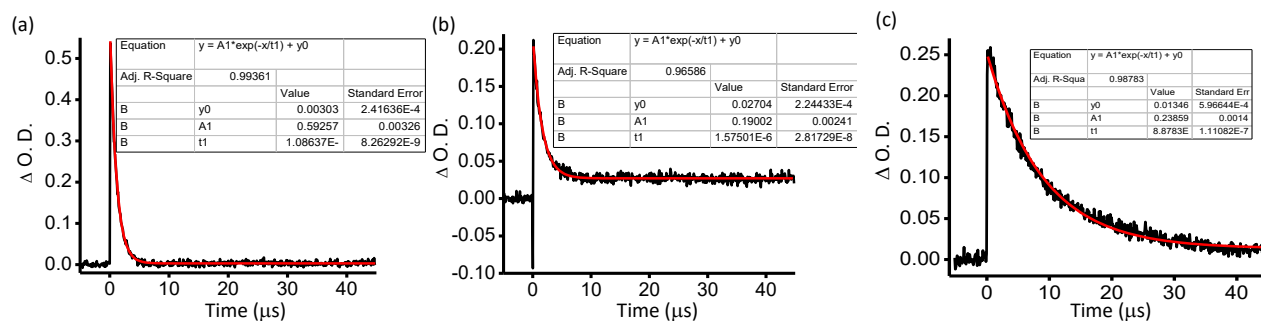
Figure A4.4. *Nanosecond transient decay profiles corresponding to (a) monomeric AN, (b) aggregated AN and (c) monomeric TAN.*
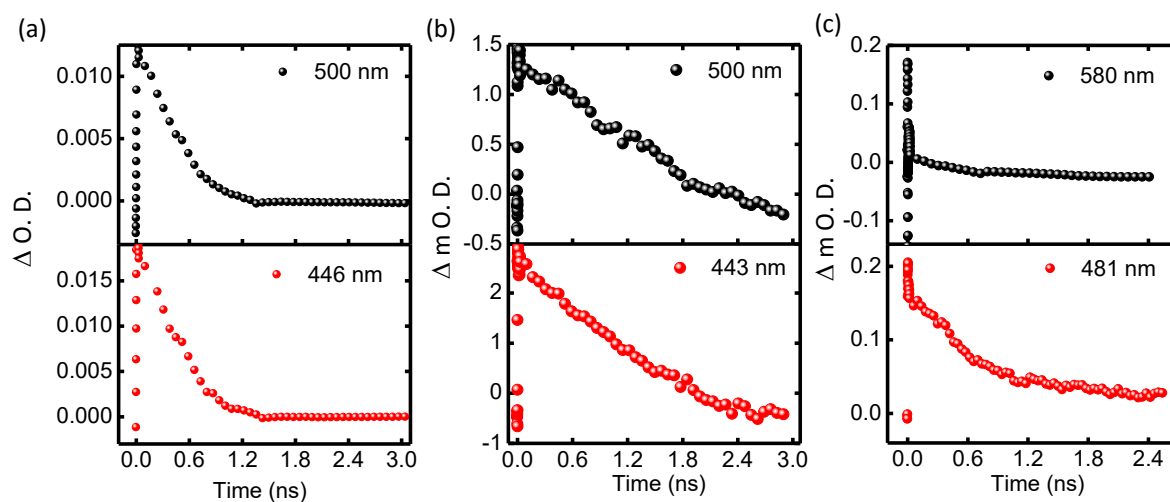
Figure A4.5. *Femtosecond transient decay profiles of monomeric (a) AN, (c) TAN in ACN and (b) aggregated AN in CHCl₃.*

5. Bibliography

[1] Gust D, Moore TA. Mimicking Photosynthesis. Science. **244**, 35-41, (1989).

[2] Gust D, Moore TA, Moore AL. Solar Fuels via Artificial Photosynthesis. Acc. Chem. Res. **42**, 1890-1898, (2009).

[3] Blankenship RE. *Molecular Mechanisms of Photosynthesis*. Oxford/Malden: Blackwell Science; (2002).

[4] Rabinowitch E. Photosynthesis and Energy Transfer. J. Phys. Chem. **61**, 870-878, (1957).

[5] Ruban AV, Johnson MP, Duffy CDP. Natural light harvesting: principles and environmental trends. Energy. Environ. Sci. **4**, 1643-1650, (2011).

[6] Chandler DE, Strümpfer J, Sener M, Scheuring S, Schulten K. Light Harvesting by Lamellar Chromatophores in Rhodospirillum photometricum. Biophys. J. **106**, 2503-2510, (2014).

[7] Wasielewski MR. Photoinduced electron transfer in supramolecular systems for artificial photosynthesis. Chem. Rev. **92**, 435-461, (1992).

[8] Scholes GD, Mirkovic T, Turner DB, Fassioli F, Buchleitner A. Solar light harvesting by energy transfer: from ecology to coherence. Energy. Environ. Sci. **5**, 9374-9393, (2012).

[9] Tran PD, Wong LH, Barber J, Loo JSC. Recent advances in hybrid photocatalysts for solar fuel production. Energy. Environ. Sci. **5**, 5902-5918, (2012).

[10] Nelson CA, Monahan NR, Zhu XY. Exceeding the Shockley-Queisser limit in solar energy conversion. Energy. Environ. Sci. **6**, 3508-3519, (2013).

[11] Tune DD, Shapter JG. The potential sunlight harvesting efficiency of carbon nanotube solar cells. Energy. Environ. Sci. **6**, 2572-2577, (2013).

[12] Tetreault N, Gratzel M. Novel nanostructures for next generation dye-sensitized solar cells. Energy Environ. Sci. **5**, 8506-8516, (2012).

[13] Siddiki MK, Li J, Galipeau D, Qiao Q. A review of polymer multijunction solar cells. Energy Environ. Sci. **3**, 867-883, (2010).

[14] Hamann TW, Jensen RA, Martinson ABF, Van Ryswyk H, Hupp JT. Advancing beyond current generation dye-sensitized solar cells. Energy. Environ. Sci. **1**, 66-78, (2008).

[15] Yu G, Gao J, Hummelen JC, Wudl F, Heeger AJ. Polymer Photovoltaic Cells: Enhanced Efficiencies via a Network of Internal Donor-Acceptor Heterojunctions. Science. **270**, 1789-1791, (1995).

[16] Tang CW. Two-layer organic photovoltaic cell. Appl Phys Lett. **48**, 183-185, (1986).

[17] Park SH, Roy A, Beaupre S, Cho S, Coates N, Moon JS, et al. Bulk heterojunction solar cells with internal quantum efficiency approaching 100%. Nat. Photon. **3**, 297-302, (2009).

[18] Hide F, Díaz-García MA, Schwartz BJ, Andersson MR, Pei Q, Heeger AJ. Semiconducting Polymers: A New Class of Solid-State Laser Materials. Science. **273**, 1833-1836, (1996).

[19] Chen H-Y, Hou J, Zhang S, Liang Y, Yang G, Yang Y, et al. Polymer solar cells with enhanced open-circuit voltage and efficiency. Nat. Photon. **3**, 649-653, (2009).

[20] Sonar P, Fong Lim JP, Chan KL. Organic non-fullerene acceptors for organic photovoltaics. Energy. Environ. Sci. **4**, 1558-1574, (2011).

[21] Zhan C, Yao J. More than Conformational "Twisting" or "Coplanarity": Molecular Strategies for Designing High-Efficiency Nonfullerene Organic Solar Cells. Chem. Mater. **28**, 1948-1964, (2016).

[22] Heeger AJ. 25th Anniversary Article: Bulk Heterojunction Solar Cells: Understanding the Mechanism of Operation. Adv. Mater. **26**, 10-28, (2014).

[23] Lu L, Zheng T, Wu Q, Schneider AM, Zhao D, Yu L. Recent Advances in Bulk Heterojunction Polymer Solar Cells. Chem. Rev. **115**, 12666-12731, (2015).

[24] Bhosale R, Misek J, Sakai N, Matile S. Supramolecular n/p-heterojunction photosystems with oriented multicolored antiparallel redox gradients (OMARG-SHJs). Chem. Soc. Rev. **39**, 138-149, (2010).

[25] Goetz KP, Vermeulen D, Payne ME, Kloc C, McNeil LE, Jurchescu OD. Charge-transfer complexes: new perspectives on an old class of compounds. J Mater Chem C. **2**, 3065-3076, (2014).

[26] Wang M, Wudl F. Top-down meets bottom-up: organized donor-acceptor heterojunctions for organic solar cells. J. Mater. Chem. **22**, 24297-24314, (2012).

[27] Bolag A, Sakai N, Matile S. Dipolar Photosystems: Engineering Oriented Push–Pull Components into Double- and Triple-Channel Surface Architectures. Chem. Eur. J. **22**, 9006-9014, (2016).

[28] Würthner F. Generating a Photocurrent on the Nanometer Scale. Science. **314**, 1693-1694, (2006).

[29] Patwardhan S, Sengupta S, Siebbeles LDA, Würthner F, Grozema FC. Efficient Charge Transport in Semisynthetic Zinc Chlorin Dye Assemblies. J. Am. Chem. Soc. **134**, 16147-16150, (2012).

[30] Hayashi H, Sobczuk A, Bolag A, Sakai N, Matile S. Antiparallel three-component gradients in double-channel surface architectures. Chem. Sci. **5**, 4610-4614, (2014).

[31] Cheriya RT, Mallia AR, Hariharan M. Light harvesting vesicular donor-acceptor scaffold limits the rate of charge recombination in the presence of an electron donor. Energy. Environ. Sci. **7**, 1661-1669, (2014).

[32] Benesi HA, Hildebrand JH. A Spectrophotometric Investigation of the Interaction of Iodine with Aromatic Hydrocarbons. J. Am. Chem. Soc. **71**, 2703-2707, (1949).

[33] Keefer RM, Andrews LJ. Equilibrium Constants for the Interaction of Halogens with Alcohols and Ethers. J. Am. Chem. Soc. **75**, 3561-3564, (1953).

[34] Fukuzumi S, Wong CL, Kochi JK. Unified view of Marcus electron transfer and Mulliken charge transfer theories in organometallic chemistry. Steric effects in alkylmetals as quantitative probes for outer-sphere and inner-sphere mechanisms. J. Am. Chem. Soc. **102**, 2928-2939, (1980).

[35] Mulliken RS. Molecular Compounds and their Spectra. II. J. Am. Chem. Soc. **74**, 811-824, (1952).

[36] Mulliken RS. Electronic Population Analysis on LCAO-MO Molecular Wave Functions. IV. Bonding and Antibonding in LCAO and Valence-Bond Theories. J. Chem. Phys. **23**, 2343-2346, (1955).

[37] Staemmler V. *The Donor-Acceptor Approach to Molecular Interactions*. Von V. Gutmann. Plenum Press, New York 1978. Angew. Chem. **91**, 595-595, (1979).

[38] Okada T, Fujita T, Kubota M, Masaki S, Mataga N, Ide R, et al. Intramolecular electron donor-acceptor interactions in the excited state of (anthracene)-(CH2)n-(N,N-dimethylaniline) systems. Chem. Phys. Lett. **14**, 563-568, (1972).

[39] Turro NJ, Ramamurthy V, Scaiano JC. *Energy and Electron Transfer. Modern Molecular Photochemistry of Organic Molecules*. USA: University Science Books; 2010. p. 383-481.

[40] Weller A. Photoinduced Electron Transfer in Solution: Exciplex and Radical Ion Pair Formation Free Enthalpies and their Solvent Dependence. z Astro. Phys. chem. **133**, 93, (1982).

[41] Prasad E, Gopidas KR. Photoinduced Electron Transfer in Hydrogen Bonded Donor−Acceptor Systems. Study of the Dependence of Rate on Free Energy and

Simultaneous Observation of the Marcus and Rehm−Weller Behaviors†. J. Am. Chem. Soc. **122**, 3191-3196, (2000).

[42] Alves H, Molinari AS, Xie H, Morpurgo AF. Metallic conduction at organic charge-transfer interfaces. Nat. Mater. **7**, 574-580, (2008).

[43] Chiang CK, Fincher CR, Park YW, Heeger AJ, Shirakawa H, Louis EJ, et al. Electrical Conductivity in Doped Polyacetylene. Phys Rev Lett. **39**, 1098-1101, (1977).

[44] Fu H. *Organic Photonic Devices. Organic Optoelectronics*: Wiley-VCH Verlag GmbH & Co. KGaA; 2013. p. 351-374.

[45] Kamran M, Friebe VM, Delgado JD, Aartsma TJ, Frese RN, Jones MR. Demonstration of asymmetric electron conduction in pseudosymmetrical photosynthetic reaction centre proteins in an electrical circuit. Nat. Commun.; 2015.

[46] Haddon RC, Hebard AF, Rosseinsky MJ, Murphy DW, Duclos SJ, Lyons KB, et al. Conducting films of C_{60} and C_{70} by alkali-metal doping. Nature. **350**, 320-322, (1991).

[47] Hebard AF, Rosseinsky MJ, Haddon RC, Murphy DW, Glarum SH, Palstra TTM, et al. Superconductivity at 18 K in potassium-doped C_{60}. Nature. **350**, 600-601, (1991).

[48] Reyren N, Thiel S, Caviglia AD, Kourkoutis LF, Hammerl G, Richter C, et al. Superconducting Interfaces Between Insulating Oxides. Science. **317**, 1196-1199, (2007).

[49] de Boer RWI, Klapwijk TM, Morpurgo AF. Field-effect transistors on tetracene single crystals. Appl. Phys. Lett. **83**, 4345-4347, (2003).

[50] Calhoun MF, Sanchez J, Olaya D, Gershenson ME, Podzorov V. Electronic functionalization of the surface of organic semiconductors with self-assembled monolayers. Nat. Mater. **7**, 84-89, (2008).

[51] Ohtomo A, Hwang HY. A high-mobility electron gas at the $LaAlO_3/SrTiO_3$ heterointerface. Nature. **427**, 423-426, (2004).

[52] Jérome D. Organic Conductors: From Charge Density Wave TTF−TCNQ to Superconducting (TMTSF)2PF6. Chem. Rev. **104**, 5565-5592, (2004).

[53] Hunter CA, Sanders JKM. The nature of π-π interactions. J. Am. Chem. Soc. **112**, 5525-5534, (1990).

[54] Cozzi F, Ponzini F, Annunziata R, Cinquini M, Siegel JS. Polar Interactions between Stacked π Systems in Fluorinated 1,8-Diarylnaphthalenes: Importance of

Quadrupole Moments in Molecular Recognition. Angew. Chem. Int. Ed. **34**, 1019-1020, (1995).

[55] Williams JH, Cockcroft JK, Fitch AN. Structure of the Lowest Temperature Phase of the Solid Benzene–Hexafluorobenzene Adduct. Angew. Chem. Int. Ed. **31**, 1655-1657, (1992).

[56] Rashkin MJ, Waters ML. Unexpected Substituent Effects in Offset $\pi-\pi$ Stacked Interactions in Water. J. Am. Chem. Soc. **124**, 1860-1861, (2002).

[57] Wheeler SE, McNeil AJ, Müller P, Swager TM, Houk KN. Probing Substituent Effects in Aryl–Aryl Interactions Using Stereoselective Diels–Alder Cycloadditions. J. Am. Chem. Soc. **132**, 3304-3311, (2010).

[58] Scott Lokey R, Iverson BL. Synthetic molecules that fold into a pleated secondary structure in solution. Nature. **375**, 303-305, (1995).

[59] Martinez CR, Iverson BL. Rethinking the term "π-stacking". Chem Sci. **3**, 2191-2201, (2012).

[60] Hobza PM-D, K. *Non-covalent Interactions: Theory and Experiment*: RSC Publishing (2009).

[61] Gale PA, Sessler JL, Steed JW. Supramolecular Chemistry-Introducing the latest web themed issue. Chem. Commun. **47**, 5931-5932, (2011).

[62] Müller-Dethlefs K, Hobza P. Noncovalent Interactions: A Challenge for Experiment and Theory. Chem. Rev. **100**, 143-168, (2000).

[63] Mahadevi AS, Sastry GN. Cooperativity in Noncovalent Interactions. Chem. Rev. **116**, 2775-2825, (2016).

[64] Gélinas S, Rao A, Kumar A, Smith SL, Chin AW, Clark J, et al. Ultrafast Long-Range Charge Separation in Organic Semiconductor Photovoltaic Diodes. Science. **343**, 512-516, (2014).

[65] Yamamoto Y, Fukushima T, Suna Y, Ishii N, Saeki A, Seki S, et al. Photoconductive Coaxial Nanotubes of Molecularly Connected Electron Donor and Acceptor Layers. Science. **314**, 1761-1764, (2006).

[66] Zhang W, Jin W, Fukushima T, Saeki A, Seki S, Aida T. Supramolecular Linear Heterojunction Composed of Graphite-Like Semiconducting Nanotubular Segments. Science. **334**, 340-343, (2011).

[67] Wu Y-L, Brown KE, Wasielewski MR. Extending Photoinduced Charge Separation Lifetimes by Using Supramolecular Design: Guanine–Perylenediimide G-Quadruplex. J. Am. Chem. Soc. **135**, 13322-13325, (2013).

[68] Tauber MJ, Kelley RF, Giaimo JM, Rybtchinski B, Wasielewski MR. Electron Hopping in π-Stacked Covalent and Self-Assembled Perylene Diimides Observed by ENDOR Spectroscopy. J. Am. Chem. Soc. **128**, 1782-1783, (2006).

[69] Kelley RF, Tauber MJ, Wasielewski MR. Linker-Controlled Energy and Charge Transfer within Chlorophyll Trefoils. Angew. Chem. Int. Ed. **45**, 7979-7982, (2006).

[70] Gunderson VL, Mickley Conron SM, Wasielewski MR. Self-assembly of a hexagonal supramolecular light-harvesting array from chlorophyll a trefoil building blocks. Chem. Commun. **46**, 401-403, (2010).

[71] Lefler KM, Co DT, Wasielewski MR. Self-Assembly-Induced Ultrafast Photodriven Charge Separation in Perylene-3,4-dicarboximide-Based Hydrogen-Bonded Foldamers. J. Phys. Chem. Lett. **3**, 3798-3805, (2012).

[72] Pho TV, Toma FM, Chabinyc ML, Wudl F. Self-Assembling Decacyclene Triimides Prepared through a Regioselective Hextuple Friedel–Crafts Carbamylation. Angew. Chem. Int. Ed. **52**, 1446-1451, (2013).

[73] Toma FM, Puntoriero F, Pho TV, La Rosa M, Jun Y-S, Tremolet de Villers BJ, et al. Polyimide Dendrimers Containing Multiple Electron Donor–Acceptor Units and Their Unique Photophysical Properties. Angew. Chem. Int. Ed. **54**, 6775-6779, (2015).

[74] Dössel LF, Kamm V, Howard IA, Laquai F, Pisula W, Feng X, et al. Synthesis and Controlled Self-Assembly of Covalently Linked Hexa-peri-hexabenzocoronene/Perylene Diimide Dyads as Models To Study Fundamental Energy and Electron Transfer Processes. J. Am. Chem. Soc. **134**, 5876-5886, (2012).

[75] Schenning APHJ, v. Herrikhuyzen J, Jonkheijm P, Chen Z, Würthner F, Meijer EW. Photoinduced Electron Transfer in Hydrogen-Bonded Oligo(p-phenylene vinylene)–Perylene Bisimide Chiral Assemblies. J. Am. Chem. Soc. **124**, 10252-10253, (2002).

[76] Hartnett PE, Dyar SM, Margulies EA, Shoer LE, Cook AW, Eaton SW, et al. Long-lived charge carrier generation in ordered films of a covalent perylenediimide-diketopyrrolopyrrole-perylenediimide molecule. Chem. Sci. **6**, 402-411, (2015).

[77] Ley D, Guzman CX, Adolfsson KH, Scott AM, Braunschweig AB. Cooperatively Assembling Donor–Acceptor Superstructures Direct Energy Into an Emergent Charge Separated State. J. Am. Chem. Soc. **136**, 7809-7812, (2014).

[78] Guzman CX, Calderon RMK, Li Z, Yamazaki S, Peurifoy SR, Guo C, et al. Extended Charge Carrier Lifetimes in Hierarchical Donor–Acceptor Supramolecular Polymer Films. J. Phys. Chem. C. **119**, 19584-19589, (2015).

[79] Sakai N, Lista M, Kel O, Sakurai S-i, Emery D, Mareda J, et al. Self-Organizing Surface-Initiated Polymerization: Facile Access to Complex Functional Systems. J. Am. Chem. Soc. **133**, 15224-15227, (2011).

[80] Sforazzini G, Orentas E, Bolag A, Sakai N, Matile S. Toward Oriented Surface Architectures with Three Coaxial Charge-Transporting Pathways. J. Am. Chem. Soc. **135**, 12082-12090, (2013).

[81] Lista M, Orentas E, Areephong J, Charbonnaz P, Wilson A, Zhao Y, et al. Self-organizing surface-initiated polymerization, templated self-sorting and templated stack exchange: synthetic methods to build complex systems. Org. Biomol. Chem. **11**, 1754-1765, (2013).

[82] Sforazzini G, Turdean R, Sakai N, Matile S. Double-channel photosystems with antiparallel redox gradients: templated stack exchange with porphyrins and phthalocyanines. Chem. Sci. **4**, 1847-1851, (2013).

[83] Sinks LE, Rybtchinski B, Iimura M, Jones BA, Goshe AJ, Zuo X, et al. Self-Assembly of Photofunctional Cylindrical Nanostructures Based on Perylene-3,4:9,10-bis(dicarboximide). Chem. Mater. **17**, 6295-6303, (2005).

[84] Polkehn M, Tamura H, Eisenbrandt P, Haacke S, Méry S, Burghardt I. Molecular Packing Determines Charge Separation in a Liquid Crystalline Bisthiophene–Perylene Diimide Donor–Acceptor Material. J. Phys. Chem. Lett. **7**, 1327-1334, (2016).

[85] Roland T, Leonard J, Hernandez Ramirez G, Mery S, Yurchenko O, Ludwigs S, et al. Sub-100 fs charge transfer in a novel donor-acceptor-donor triad organized in a smectic film. Phys. Chem. Chem. Phys. **14**, 273-279, (2012).

[86] Schwartz P-O, Biniek L, Zaborova E, Heinrich B, Brinkmann M, Leclerc N, et al. Perylenediimide-Based Donor–Acceptor Dyads and Triads: Impact of Molecular Architecture on Self-Assembling Properties. J. Am. Chem. Soc. **136**, 5981-5992, (2014).

[87] Kar H, Gehrig DW, Allampally NK, Fernandez G, Laquai F, Ghosh S. Cooperative supramolecular polymerization of an amine-substituted naphthalene-diimide and its impact on excited state photophysical properties. Chem. Sci. **7**, 1115-1120, (2016).

[88] Amerongen HV, Valkunas L, Grondelle RV. *Photosynthetic Excitons*. London: World Scientific; (2000).

[89] Scarongella M, Paraecattil AA, Buchaca-Domingo E, Douglas JD, Beaupre S, McCarthy-Ward T, et al. The influence of microstructure on charge separation dynamics in organic bulk heterojunction materials for solar cell applications. J. Mater. Chem. A. **2**, 6218-6230, (2014).

[90] Siebbeles LDA, Grozema FC. *Charge and Exciton Transport Through Molecular Wires*. Germany: Wiley-VCH; (2011).

[91] Vura-Weis J, Abdelwahed SH, Shukla R, Rathore R, Ratner MA, Wasielewski MR. Crossover from Single-Step Tunneling to Multistep Hopping for Molecular Triplet Energy Transfer. Science. **328**, 1547-1550, (2010).

[92] Zhang Y, Dood J, Beckstead AA, Li X-B, Nguyen KV, Burrows CJ, et al. Efficient UV-induced charge separation and recombination in an 8-oxoguanine-containing dinucleotide. Proc. Natl. Acad. Sci. **111**, 11612-11617, (2014).

[93] Sukegawa J, Schubert C, Zhu X, Tsuji H, Guldi DM, Nakamura E. Electron transfer through rigid organic molecular wires enhanced by electronic and electron–vibration coupling. Nat. Chem. **6**, 899-905, (2014).

[94] Lazarides T, McCormick TM, Wilson KC, Lee S, McCamant DW, Eisenberg R. Sensitizing the Sensitizer: The Synthesis and Photophysical Study of Bodipy−Pt(II)(diimine)(dithiolate) Conjugates. J. Am. Chem. Soc. **133**, 350-364, (2011).

[95] Fukuzumi S, Ohkubo K, E W, Ou Z, Shao J, Kadish KM, et al. Metal-Centered Photoinduced Electron Transfer Reduction of a Gold(III) Porphyrin Cation Linked with a Zinc Porphyrin to Produce a Long-Lived Charge-Separated State in Nonpolar Solvents. J. Am. Chem. Soc. **125**, 14984-14985, (2003).

[96] Koch M, Letrun R, Vauthey E. Exciplex Formation in Bimolecular Photoinduced Electron-Transfer Investigated by Ultrafast Time-Resolved Infrared Spectroscopy. J. Am. Chem. Soc. **136**, 4066-4074, (2014).

[97] Winters MU, Dahlstedt E, Blades HE, Wilson CJ, Frampton MJ, Anderson HL, et al. Probing the Efficiency of Electron Transfer through Porphyrin-Based Molecular Wires. J. Am. Chem. Soc. **129**, 4291-4297, (2007).

[98] Bartynski AN, Gruber M, Das S, Rangan S, Mollinger S, Trinh C, et al. Symmetry-Breaking Charge Transfer in a Zinc Chlorodipyrrin Acceptor for High Open Circuit Voltage Organic Photovoltaics. J. Am. Chem. Soc. **137**, 5397-5405, (2015).

[99] Rubtsov IV, Kang YK, Redmore NP, Allen RM, Zheng J, Beratan DN, et al. The Degree of Charge Transfer in Ground and Charge-Separated States Revealed by Ultrafast Visible Pump/Mid-IR Probe Spectroscopy. J. Am. Chem. Soc. **126**, 5022-5023, (2004).

[100] Campagna SS, S.; Puntoriero, F.; Di Pietro, C.; Ricevuto, V. *Electron Transfer in Chemistry*. Weinheim: Wiley-VCH Verlag GmbH; (2001).

[101] Hammarström L. Accumulative Charge Separation for Solar Fuels Production: Coupling Light-Induced Single Electron Transfer to Multielectron Catalysis. Acc. Chem. Res. **48**, 840-850, (2015).

[102] Bell TDM, Stefan A, Masuo S, Vosch T, Lor M, Cotlet M, et al. Electron Transfer at the Single-Molecule Level in a Triphenylamine–Perylene Imide Molecule. Chem. Phys. Chem. **6**, 942-948, (2005).

[103] Difley S, Wang L-P, Yeganeh S, Yost SR, Voorhis TV. Electronic Properties of Disordered Organic Semiconductors via QM/MM Simulations. Acc. Chem. Res. **43**, 995-1004, (2010).

[104] Beckers EHA, Meskers SCJ, Schenning APHJ, Chen Z, Würthner F, Marsal P, et al. Influence of Intermolecular Orientation on the Photoinduced Charge Transfer Kinetics in Self-Assembled Aggregates of Donor–Acceptor Arrays. J. Am. Chem. Soc. **128**, 649-657, (2005).

[105] Savoie BM, Jackson NE, Chen LX, Marks TJ, Ratner MA. Mesoscopic Features of Charge Generation in Organic Semiconductors. Acc. Chem. Res. **47**, 3385-3394, (2014).

[106] Gust D, Moore TA, Moore AL. Molecular mimicry of photosynthetic energy and electron transfer. Acc. Chem. Res. **26**, 198-205, (1993).

[107] Gust D, Moore TA, Moore AL. Mimicking Photosynthetic Solar Energy Transduction. Acc. Chem. Res. **34**, 40-48, (2001).

[108] Gust D, Moore TA, Moore AL, Macpherson AN, Lopez A, DeGraziano JM, et al. Photoinduced electron and energy transfer in molecular pentads. J. Am. Chem. Soc. **115**, 11141-11152, (1993).

[109] Liddell PA, Kuciauskas D, Sumida JP, Nash B, Nguyen D, Moore AL, et al. Photoinduced Charge Separation and Charge Recombination to a Triplet State in a Carotene–Porphyrin–Fullerene Triad. J. Am. Chem. Soc. **119**, 1400-1405, (1997).

[110] Dimitrov SD, Wheeler S, Niedzialek D, Schroeder BC, Utzat H, Frost JM, et al. Polaron pair mediated triplet generation in polymer/fullerene blends. Nat. Commun. **6**, 1-8, (2015).

[111] Barter LMC, Durrant JR, Klug DR. A quantitative structure–function relationship for the Photosystem II reaction center: Supermolecular behavior in natural photosynthesis. Proc. Natl. Acad. Sci. **100**, 946-951, (2003).

[112] Dössel LF, Kamm V, Howard IA, Laquai F, Pisula W, Feng X, et al. Synthesis and Controlled Self-Assembly of Covalently Linked Hexa-peri-hexabenzocoronene/Perylene Diimide Dyads as Models To Study Fundamental Energy and Electron Transfer Processes. J. Am. Chem. Soc. **134**, 5876-5886, (2012).

[113] Chu C-C, Raffy G, Ray D, Guerzo AD, Kauffmann B, Wantz G, et al. Self-Assembly of Supramolecular Fullerene Ribbons via Hydrogen-Bonding Interactions and Their Impact on Fullerene Electronic Interactions and Charge Carrier Mobility. J. Am. Chem. Soc. **132**, 12717-12723, (2010).

[114] Wu Y-L, Brown KE, Wasielewski MR. Extending Photoinduced Charge Separation Lifetimes by Using Supramolecular Design: Guanine–Perylenediimide G-Quadruplex. J. Am. Chem. Soc. **135**, 13322-13325, (2013).

[115] García-Iglesias M, Peuntinger K, Kahnt A, Krausmann J, Vázquez P, González-Rodríguez D, et al. Supramolecular Assembly of Multicomponent Photoactive Systems via Cooperatively Coupled Equilibria. J. Am. Chem. Soc. **135**, 19311-19318, (2013).

[116] Hizume Y, Tashiro K, Charvet R, Yamamoto Y, Saeki A, Seki S, et al. Chiroselective Assembly of a Chiral Porphyrin–Fullerene Dyad: Photoconductive Nanofiber with a Top-Class Ambipolar Charge-Carrier Mobility. J. Am. Chem. Soc. **132**, 6628-6629, (2010).

[117] Pisula W, Kastler M, Wasserfallen D, Robertson JWF, Nolde F, Kohl C, et al. Pronounced Supramolecular Order in Discotic Donor–Acceptor Mixtures. Angew. Chem. Int. Ed. **45**, 819-823, (2006).

[118] Sinks LE, Rybtchinski B, Iimura M, Jones BA, Goshe AJ, Zuo X, et al. Self-Assembly of Photofunctional Cylindrical Nanostructures Based on Perylene-3,4:9,10-bis(dicarboximide). Chem. Mater. **17**, 6295-6303, (2005).

[119] Bill NL, Ishida M, Kawashima Y, Ohkubo K, Sung YM, Lynch VM, et al. Long-lived charge-separated states produced in supramolecular complexes between anionic and cationic porphyrins. Chem. Sci. **5**, 3888-3896, (2014).

[120] Schenning APHJ, v. Herrikhuyzen J, Jonkheijm P, Chen Z, Würthner F, Meijer EW. Photoinduced Electron Transfer in Hydrogen-Bonded Oligo(p-phenylene vinylene)–Perylene Bisimide Chiral Assemblies. J. Am. Chem. Soc. **124**, 10252-10253, (2002).

[121] Hayashi H, Nihashi W, Umeyama T, Matano Y, Seki S, Shimizu Y, et al. Segregated Donor–Acceptor Columns in Liquid Crystals That Exhibit Highly Efficient Ambipolar Charge Transport. J. Am. Chem. Soc. **133**, 10736-10739, (2011).

[122] Markovitsi D, Germain A, Millie P, Lecuyer P, Gallos L, Argyrakis P, et al. Triphenylene Columnar Liquid Crystals: Excited States and Energy Transfer. J. Phys. Chem. **99**, 1005-1017, (1995).

[123] Cheriya RT, Joy J, Alex AP, Shaji A, Hariharan M. Energy Transfer in Near-Orthogonally Arranged Chromophores Separated through a Single Bond. J. Phys. Chem. C. **116**, 12489-12498, (2012).

[124] Khandelwal H, Mallia AR, Cheriya RT, Hariharan M. Effect of temperature on symmetry breaking excited state charge separation: restoration of symmetry at elevated temperature. Phys. Chem. Chem Phys. **14**, 15282-15285, (2012).

[125] Joy J, Cheriya RT, Nagarajan K, Shaji A, Hariharan M. Breakdown of Exciton Splitting through Electron Donor–Acceptor Interaction: A Caveat for the Application of Exciton Chirality Method in Macromolecules. J. Phys. Chem C. **117**, 17927-17939, (2013).

[126] Rajaram S, Shivanna R, Kandappa SK, Narayan KS. Nonplanar Perylene Diimides as Potential Alternatives to Fullerenes in Organic Solar Cells. J. Phys. Chem. Lett. **3**, 2405-2408, (2012).

[127] Bakulin AA, Dimitrov SD, Rao A, Chow PCY, Nielsen CB, Schroeder BC, et al. Charge-Transfer State Dynamics Following Hole and Electron Transfer in Organic Photovoltaic Devices. J. Phys. Chem. Lett. **4**, 209-215, (2012).

[128] Bader RFW. *Atoms in Molecules: A Quantum Theory*. Oxford, U.K.: Oxford University Press; (1990).

[129] Rajagopal SK, Philip AM, Nagarajan K, Hariharan M. Progressive acylation of pyrene engineers solid state packing and colour via C-H•••H-C, C-H•••O and π-π interactions. Chem. Commun. **50**, 8644-8647, (2014).

[130] Nagarajan K, Rajagopal SK, Hariharan M. C-H•••H-C and C-H•••π contacts aid transformation of dimeric to monomeric anthracene in the solid state. CrystEngComm. **16**, 8946-8949, (2014).

[131] Observed aberration in the crystalline (triclinic) vs. aggregated (hexagonal/cubic) state of NIN could arise from the reorganization of NIN spherical assembly in $CHCl_3$.

[132] Kim J-K, Lee E, Huang Z, Lee M. Nanorings from the Self-Assembly of Amphiphilic Molecular Dumbbells. J. Am. Chem. Soc. **128**, 14022-14023, (2006).

[133] Jia H, Schmid B, Liu S-X, Jaggi M, Monbaron P, Bhosale SV, et al. Tetrathiafulvalene-Fused Porphyrins via Quinoxaline Linkers: Symmetric and Asymmetric Donor–Acceptor Systems. Chem. Phys. Chem. **13**, 3370-3382, (2012).

[134] Lee J, Baek K, Kim M, Yun G, Ko YH, Lee N-S, et al. Hollow nanotubular toroidal polymer microrings. Nat. Chem. **6**, 97-103, (2014).

[135] Kucheryavy P, Li G, Vyas S, Hadad C, Glusac KD. Electronic Properties of 4-Substituted Naphthalimides. J. Phys. Chem. A. **113**, 6453-6461, (2009).

[136] Kucheryavy P, Khatmullin R, Mirzakulova E, Zhou D, Glusac KD. Photoinduced Electron Transfer in Naphthalimide-Pyridine Systems: Effect of Proton Transfer on Charge Recombination Efficiencies. J. Phys. Chem. A. **115**, 11606-11614, (2011).

[137] Inari T, Yamano M, Hirano A, Sugawa K, Otsuki J. Photophysical and Electrochemical Properties of Thienylnaphthalimide Dyes with Excellent Photostability. J. Phys. Chem. A. **118**, 5178-5188, (2014).

[138] Lemaur V, Steel M, Beljonne D, Brédas J-L, Cornil J. Photoinduced Charge Generation and Recombination Dynamics in Model Donor/Acceptor Pairs for Organic Solar Cell Applications: A Full Quantum-Chemical Treatment. J. Am. Chem. Soc. **127**, 6077-6086, (2005).

[139] Coropceanu V, Cornil J, da Silva Filho DA, Olivier Y, Silbey R, Brédas J-L. Charge Transport in Organic Semiconductors. Chem. Rev. **107**, 926-952, (2007).

[140] Dance ZEX, Mickley SM, Wilson TM, Ricks AB, Scott AM, Ratner MA, et al. Intersystem Crossing Mediated by Photoinduced Intramolecular Charge Transfer: Julolidine−Anthracene Molecules with Perpendicular π Systems. J. Phys. Chem. A. **112**, 4194-4201, (2008).

[141] Lippert E, Naturforsch Z. Astrophys Phys. Phys. Chem. **10**, 541-545, (1955).

[142] Cho DW, Fujitsuka M, Sugimoto A, Yoon UC, Mariano PS, Majima T. Photoinduced Electron Transfer Processes in 1,8-Naphthalimide-Linker-Phenothiazine Dyads. J. Phys. Chem. B. **110**, 11062-11068, (2006).

[143] Kawai K, Hayashi M, Majima T. HOMO Energy Gap Dependence of Hole-Transfer Kinetics in DNA. J. Am. Chem. Soc. **134**, 4806-4811, (2012).

[144] Vogt RA, Gray TG, Crespo-Hernández CE. Subpicosecond Intersystem Crossing in Mono- and Di(organophosphine)gold(I) Naphthalene Derivatives in Solution. J. Am. Chem. Soc. **134**, 14808-14817, (2012).

[145] Vogt RA, Reichardt C, Crespo-Hernández CE. Excited-State Dynamics in Nitro-Naphthalene Derivatives: Intersystem Crossing to the Triplet Manifold in Hundreds of Femtoseconds. J. Phys. Chem. A. **117**, 6580-6588, (2013).

[146] Kotani H, Ohkubo K, Fukuzumi S. Formation of a long-lived electron-transfer state of a naphthalene-quinolinium ion dyad and the p-dimer radical cation. Farad. Discuss. **155**, 89-102, (2012).

[147] Lifetime of N_2^+ could not be measured due to the lack of NIR detector coupled to our nTA spectrometer.

[148] Remón P, Parente Carvalho C, Baleizão C, Berberan-Santos MN, Pischel U. Highly Efficient Singlet–Singlet Energy Transfer in Light-Harvesting [60,70]Fullerene–4-Amino-1,8-naphthalimide Dyads. Chem. Phys. Chem. **14**, 2717-2724, (2013).

[149] Yin H, Li H, Xia G, Ruan C, Shi Y, Wang H, et al. A novel non-fluorescent excited state intramolecular proton transfer phenomenon induced by intramolecular hydrogen bonds: an experimental and theoretical investigation. Sci. Rep. **6**, 19774, (2016).

[150] Suneesh CV, Gopidas KR. Long-Lived Photoinduced Charge Separation in Flexible 9,10-Bis(phenylethynyl)anthracene–Phenothiazine Dyads. J. Phys. Chem. C. **113**, 1606-1614, (2009).

[151] Gunderson VL, Smeigh AL, Kim CH, Co DT, Wasielewski MR. Electron Transfer within Self-Assembling Cyclic Tetramers Using Chlorophyll-Based Donor–Acceptor Building Blocks. J. Am. Chem. Soc. **134**, 4363-4372, (2012).

[152] Rieth S, Li Z, Hinkle CE, Guzman CX, Lee JJ, Nehme SI, et al. Superstructures of Diketopyrrolopyrrole Donors and Perylenediimide Acceptors Formed by Hydrogen-Bonding and π···π Stacking. J. Phys. Chem. C. **117**, 11347-11356, (2013).

[153] Chang W, Congreve DN, Hontz E, Bahlke ME, McMahon DP, Reineke S, et al. Spin-dependent charge transfer state design rules in organic photovoltaics. Nat. Commun. **6**, 1-6, (2015).

[154] Liu K, Song C-L, Zhou Y-C, Zhou X-Y, Pan X-J, Cao L-Y, et al. Tuning the ambipolar charge transport properties of N-heteropentacenes by their frontier molecular orbital energy levels. J. Mater. Chem. C. **3**, 4188-4196, (2015).

[155] Rao KV, Haldar R, Kulkarni C, Maji TK, George SJ. Perylene Based Porous Polyimides: Tunable, High Surface Area with Tetrahedral and Pyramidal Monomers. Chem. Mater. **24**, 969-971, (2012).

[156] Kushida T, Shuto A, Yoshio M, Kato T, Yamaguchi S. A Planarized Triphenylborane Mesogen: Discotic Liquid Crystals with Ambipolar Charge-Carrier Transport Properties. Angew. Chem. Int. Ed. **54**, 6922-6925, (2015).

[157] Eaton SW, Shoer LE, Karlen SD, Dyar SM, Margulies EA, Veldkamp BS, et al. Singlet Exciton Fission in Polycrystalline Thin Films of a Slip-Stacked Perylenediimide. J. Am. Chem. Soc. **135**, 14701–14712, (2013).

[158] Mallia AR, Salini PS, Hariharan M. Nonparallel Stacks of Donor and Acceptor Chromophores Evade Geminate Charge Recombination. J. Am. Chem. Soc. **137**, 15604-15607, (2015).

[159] Nagarajan K, Mallia AR, Reddy VS, Hariharan M. Access to Triplet Excited State in Core-Twisted Perylenediimide. J. Phys. Chem. C. **120**, 8443-8450, (2016).

[160] Spackman MA, Jayatilaka D. Hirshfeld surface analysis. CrystEngComm. **11**, 19-32, (2009).

[161] Wang H, Wang W, Jin WJ. σ-Hole Bond vs π-Hole Bond: A Comparison Based on Halogen Bond. Chem. Rev. **116**, 5072-5104, (2016).

[162] Kucheryavy P, Li G, Vyas S, Hadad C, Glusac KD. Electronic Properties of 4-Substituted Naphthalimides. J. Phys. Chem. A. **113**, 6453-6461, (2009).

[163] Terry GC, Uffindell VE, Willets FW. Triplet State of Triphenylamine. Nature. **223**, 1050-1051, (1969).

[164] Ricks AB, Solomon GC, Colvin MT, Scott AM, Chen K, Ratner MA, et al. Controlling Electron Transfer in Donor−Bridge−Acceptor Molecules Using Cross-Conjugated Bridges. J. Am. Chem. Soc. **132**, 15427-15434, (2010).

[165] Cho DW, Fujitsuka M, Sugimoto A, Yoon UC, Majima T. Regulation of photodynamic interactions in 1,8-naphthalimide-linker-phenothiazine dyads by cyclodextrins. Phys Chem Chem Phys. **16**, 5779-5784, (2014).

[166] Safont-Sempere MM, Fernández G, Würthner F. Self-Sorting Phenomena in Complex Supramolecular Systems. Chem. Rev. **111**, 5784-5814, (2011).

[167] Burrezo PM, Zhu X, Zhu S-F, Yan Q, López Navarrete JT, Tsuji H, et al. Planarization, Fusion, and Strain of Carbon-Bridged Phenylenevinylene Oligomers Enhance π-Electron and Charge Conjugation: A Dissectional Vibrational Raman Study. J. Am. Chem. Soc. **137**, 3834-3843, (2015).

[168] Tachibana Y, Vayssieres L, Durrant JR. Artificial photosynthesis for solar water-splitting. Nature Photon. **6**, 511-518, (2012).

[169] McConnell I, Li G, Brudvig GW. Energy Conversion in Natural and Artificial Photosynthesis. Chemistry & Biology. **17**, 434-447, (2010).

[170] Meyer GJ. *Molecular Level Artificial Photosynthetic Materials*. New York: Ed.; Wiley; (1997).

[171] Fukuzumi S, Kotani H, Ohkubo K, Ogo S, Tkachenko NV, Lemmetyinen H. Electron-Transfer State of 9-Mesityl-10-methylacridinium Ion with a Much Longer Lifetime and Higher Energy Than That of the Natural Photosynthetic Reaction Center. J. Am. Chem. Soc. **126**, 1600-1601, (2004).

[172] Shubina TE, Sharapa DI, Schubert C, Zahn D, Halik M, Keller PA, et al. Fullerene Van der Waals Oligomers as Electron Traps. J. Am. Chem. Soc. **136**, 10890-10893, (2014).

[173] D'Souza F, Gadde S, Schumacher AL, Zandler ME, Sandanayaka ASD, Araki Y, et al. Supramolecular Triads of Free-Base Porphyrin, Fullerene, and Ferric Porphyrins via the "Covalent-Coordinate" Binding Approach: Formation, Sequential Electron Transfer, and Charge Stabilization. J. Phys. Chem. C. **111**, 11123-11130, (2007).

[174] Sandroni M, Maufroy A, Rebarz M, Pellegrin Y, Blart E, Ruckebusch C, et al. Design of Efficient Photoinduced Charge Separation in Donor–Copper(I)–Acceptor Triad. J. Phys. Chem. C. **118**, 28388-28400, (2014).

[175] Kahnt A, Kärnbratt J, Esdaile LJ, Hutin M, Sawada K, Anderson HL, et al. Temperature Dependence of Charge Separation and Recombination in Porphyrin Oligomer–Fullerene Donor–Acceptor Systems. J. Am. Chem. Soc. **133**, 9863-9871, (2011).

[176] Diesenhofer J, Norris JR. *The Photosynthetic Reaction Centre*. San Diego: Eds.; Academic Press; (1993).

[177] Nocera DG. The Artificial Leaf. Acc Chem Res. **45**, 767-776, (2012).

[178] Würthner F, Chen Z, Hoeben FJM, Osswald P, You C-C, Jonkheijm P, et al. Supramolecular p–n-Heterojunctions by Co-Self-Organization of Oligo(p-phenylene Vinylene) and Perylene Bisimide Dyes. J. Am. Chem. Soc. **126**, 10611-10618, (2004).

[179] Supur M, Sung YM, Kim D, Fukuzumi S. Enhancement of Photodriven Charge Separation by Conformational and Intermolecular Adaptations of an Anthracene–

Perylenediimide–Anthracene Triad to an Aqueous Environment. J. Phys. Chem. C. **117**, 12438-12445, (2013).

[180] Attempts to crystallise the dyad (AN) without bromine atom was unsuccessful.

[181] Rajagopal SK, Philip AM, Nagarajan K, Hariharan M. Progressive acylation of pyrene engineers solid state packing and colour via C-H•••H-C, C-H•••O and π-π interactions. Chem. Commun. **50**, 8644-8647, (2014).

[182] Nagarajan K, Rajagopal SK, Hariharan M. C-H•••H-C and C-H•••π contacts aid transformation of dimeric to monomeric anthracene in the solid state. CrystEngComm. **16**, 8946-8949, (2014).

[183] Das M, Ghosh BN, Bauza A, Rissanen K, Frontera A, Chattopadhyay S. Observation of novel oxygen•••oxygen interaction in supramolecular assembly of cobalt(III) Schiff base complexes: a combined experimental and computational study. RSC Advances. **5**, 73028-73039, (2015).

[184] Loots L, Barbour LJ. A simple and robust method for the identification of π-π packing motifs of aromatic compounds. CrystEngComm. **14**, 300-304, (2012).

[185] Kucheryavy P, Khatmullin R, Mirzakulova E, Zhou D, Glusac KD. Photoinduced Electron Transfer in Naphthalimide-Pyridine Systems: Effect of Proton Transfer on Charge Recombination Efficiencies. J. Phys. Chem. A. **115**, 11606-11614, (2011).

[186] Imahori H, Hagiwara K, Aoki M, Akiyama T, Taniguchi S, Okada T, et al. Linkage and Solvent Dependence of Photoinduced Electron Transfer in Zincporphyrin-C60 Dyads. J. Am. Chem. Soc. **118**, 11771-11782, (1996).

[187] Majeski EJ, Stuart JD, Ohnesorge WE. Controlled potential oxidation of anthracene in acetonitrile. II. J. Am. Chem. Soc. **90**, 633-636, (1968).

[188] Su C, Yang F, Ji L, Xu L, Zhang C. Polytriphenylamine derivative with high free radical density as the novel organic cathode for lithium ion batteries. J. Mater. Chem. A. **2**, 20083-20088, (2014).

[189] Lauer A, Dobryakov AL, Kovalenko SA, Fidder H, Heyne K. Dual photochemistry of anthracene-9,10-endoperoxide studied by femtosecond spectroscopy. Phys. Chem. Chem. Phys. **13**, 8723-8732, (2011).

[190] Voloshchuk R, Gryko DT, Chotkowski M, Ciuciu AI, Flamigni L. Photoinduced Electron Transfer in an Amine–Corrole–Perylene Bisimide Assembly: Charge Separation over Terminal Components Favoured by Solvent Polarity. Chem Eur J. **18**, 14845-14859, (2012).

[191] Dimitrov SD, Wheeler S, Niedzialek D, Schroeder BC, Utzat H, Frost JM, et al. Polaron pair mediated triplet generation in polymer/fullerene blends. Nat. Commun. **6**, 1-8, (2015).

[192] Filatov MA, Etzold F, Gehrig D, Laquai F, Busko D, Landfester K, et al. Interplay between singlet and triplet excited states in a conformationally locked donor-acceptor dyad. Dalton Trans. **44**, 19207-19217, (2015).

[193] Gera R, Das A, Jha A, Dasgupta J. Light-Induced Proton-Coupled Electron Transfer Inside a Nanocage. J. Am. Chem. Soc. **136**, 15909-15912, (2014).

[194] Ratio of rate of charge recombination in the aggregated to the monomeric state is defined as, $\zeta=[\tau_{cr}^{a}/\tau_{cr}^{m}]$.

[195] Harriman A, Rostron JP, Cesario M, Ulrich G, Ziessel R. Electron Transfer in Self-Assembled Orthogonal Structures. J. Phys. Chem. A. **110**, 7994-8002, (2006).

[196] Mallia AR, Salini PS, Hariharan M. Nonparallel Stacks of Donor and Acceptor Chromophores Evade Geminate Charge Recombination. J Am Chem Soc. **137**, 15604-15607, (2015).

[197] Deng P, Liu L, Ren S, Li H, Zhang Q. N-acylation: an effective method for reducing the LUMO energy levels of conjugated polymers containing five-membered lactam units. Chem. Commun. **48**, 6960-6962, (2012).

[198] Lakowicz JR. *Principles of Fluorescence Spectroscopy*. New York: Springer; (2006).

[199] Kucheryavy P, Li G, Vyas S, Hadad C, Glusac KD. Electronic Properties of 4-Substituted Naphthalimides. J. Phys. Chem. A. **113**, 6453-6461, (2009).

[200] Dance ZEX, Mickley SM, Wilson TM, Ricks AB, Scott AM, Ratner MA, et al. Intersystem Crossing Mediated by Photoinduced Intramolecular Charge Transfer: Julolidine−Anthracene Molecules with Perpendicular π Systems. J. Phys. Chem. A. **112**, 4194-4201, (2008).

[201] Rajagopal SK, Philip AM, Nagarajan K, Hariharan M. Progressive acylation of pyrene engineers solid state packing and colour via C-H•••H-C, C-H•••O and π- π interactions. Chem. Commun. **50**, 8644-8647, (2014).

[202] Nagarajan K, Rajagopal SK, Hariharan M. C-H•••H-C and C-H•••π contacts aid transformation of dimeric to monomeric anthracene in the solid state. CrystEngComm. **16**, 8946-8949, (2014).

[203] Frisch MJ, Trucks GW, Schlegel HB, Scuseria GE, Robb MA, Cheeseman JR, et al. Gaussian 09. Wallingford, CT, USA: Gaussian, Inc.; 2009.

[204] Mallia AR, Sethy R, Bhat V, Hariharan M. Crystallization induced enhanced emission in conformational polymorphs of a rotationally flexible molecule. J. Mater. Chem. C. **4**, 2931-2935, (2016).

[205] Bochevarov AD, Harder E, Hughes TF, Greenwood JR, Braden DA, Philipp DM, et al. Jaguar: A high-performance quantum chemistry software program with strengths in life and materials sciences. Int. J. Quant. Chem. **113**, 2110-2142, (2013).

List of publications

1. Nonparallel Stacks of Donor and Acceptor Chromophores Evade Geminate Charge Recombination

   A. R. Mallia, P. S. Salini and M. Hariharan*

   J. Am. Chem. Soc. **2015**, *137*, 15604–15607 (**Front Cover and JACS Spotlights**).

2. Crystallization induced enhanced emission in conformational polymorphs of a rotationally flexible molecule

   A. R. Mallia,$^{\perp}$ R. Sethy,$^{\perp}$ V. Bhat and M. Hariharan*

   J. Mater. Chem. C **2016**, *4*, 2931-2935.

3. Access to Triplet Excited State in Core-Twisted Perylenediimide

   K. Nagarajan, **A. R. Mallia**, V. S. Reddy and M. Hariharan*

   J. Phys. Chem. C **2016**, *120* , 8443–8450.

4. Light Harvesting Vesicular Donor-Acceptor Scaffold Limits the Rate of Charge Recombination in the Presence of an Electron Donor

   R. T. Cheriya, **A. R. Mallia** and M. Hariharan*

   Energy Environ. Sci. **2014**, *7*, 1661-1669 (**Front Cover; Hot Article**).

5. Effect of Temperature on Symmetry Breaking Excited State Charge Separation: Restoration of Symmetry at Elevated Temperature

   H. Khandelwal, **A. R. Mallia**, R. T. Cheriya and M. Hariharan*

   Phys. Chem. Chem. Phys., **2012**, *14*, 15282-15285.

6. Columnar/Lamellar Packing in Cocrystals of Arylbipyridines with Diiodoperfluorobenzene: Role of Weak Interactions

   R. Ramakrishnan,$^{\perp}$ **A. R. Mallia**,$^{\perp}$ Niyas. M. A., R. Sethy and M. Hariharan* (Under revision)

7. Colossal Enhancement in the Lifetime of Charge Separated States in Self-Assembled Twisted Non-Symmetric Donor-Acceptor Triad

   A. R. Mallia, A. M. Phillip, V. Bhat and M. Hariharan*

   (Submitted)

   ($^{\perp}$ Both the authors contributed equally)

Presentations at Conferences

- Received "Malhotra Weikfield Foundation Nanoscience Award" from Malhotra Weikfield Foundation for Advanced Studies in Nano Science Technology for the Academic Year 2016-2017, during 8th Bangalore India Nano conference held at Hotel Lalit Ashok, Bangalore, March 03-05, 2016.
- Oral Presentation: "Non-parallel Stacks of Donor and Acceptor Chromophores Evade Geminate Charge Recombination" during Annual Technical Meeting of MRSI, Trivandrum Chapter, held at IIST-Trivandrum on 02-04-2016.
- Poster Presentation: "Non-parallel Stacks of Donor and Acceptor Chromophores Evade Geminate Charge Recombination" during 8th Bangalore India Nano conference held at Hotel Lalit Ashok, Bangalore, March 03-05, 2016.
- Poster Presentation: "Non-parallel Stacks of Donor and Acceptor Chromophores Evade Geminate Charge Recombination" during Inter-IISER Chemistry Meet-2015 to be held at IISER-Thiruvananthapuram, India, December 11-13, 2015.
- Poster Presentation: "Light harvesting vesicular donor–acceptor scaffold limits the rate of charge recombination in the presence of an electron donor" during 'Challenges in Organic Materials and Supramolecular Chemistry, ISACS18' held at Indian Institute of Science, Bangalore, India, November 19-21, 2015. [Received Chemical Science Best Poster Award from Royal Society of Chemistry, UK].
- Poster Presentation: "Light harvesting vesicular donor–acceptor scaffold limits the rate of charge recombination in the presence of an electron donor" during 'Temporally and Spatially Resolved Molecular Science Faraday Discussion 177' held at Indian Institute of Science, Bangalore, India, January 12-14, 2015.
- Poster Presentation: "Light harvesting vesicular donor–acceptor scaffold limits the rate of charge recombination in the presence of an electron donor" during '8th Asian Photochemistry Conference-APC2014' held at Taj Vivanta, Thiruvananthapuram, India, November 10-13, 2014.
- Poster Presentation: "Light harvesting vesicular donor–acceptor scaffold limits the rate of charge recombination in the presence of an electron donor" at Organic Devices: the Future Ahead (ODeFA) held at Bhabha Atomic Research Centre, Mumbai, India, March 3-6, 2014.
- Attended one day conference "ACS on Campus" an initiative from American Chemical Society held at NIIST-Thiruvananthapuram, India, November 23, 2013.
- Attended Inter-IISER Chemistry Meet-2011 held at IISER-Thiruvananthapuram, India, December, 2011.

Copyright Clearance Center

RightsLink®

Home | Account Info | Help | Live Cha

Science

AAAS

Title:	Photoconductive Coaxial Nanotubes of Molecularly Connected Electron Donor and Acceptor Layers
Author:	Yohei Yamamoto,Takanori Fukushima,Yuki Suna,Noriyuki Ishii,Akinori Saeki,Shu Seki,Seiichi Tagawa,Masateru Taniguchi,Tomoji Kawai,Takuzo Aida
Publication:	Science
Publisher:	The American Association for the Advancement of Science
Date:	Dec 15, 2006

Copyright © 2006, American Association for the Advancement of Science

Review Order

Please review the order details and the associated terms and conditions.

No royalties will be charged for this reuse request although you are required to obtain a license and comply with the license terms and conditions. To obtain the license, click the Accept button below.

Licensed Content Publisher	The American Association for the Advancement of Science
Licensed Content Publication	Science
Licensed Content Title	Photoconductive Coaxial Nanotubes of Molecularly Connected Electron Donor and Acceptor Layers
Licensed Content Author	Yohei Yamamoto,Takanori Fukushima,Yuki Suna,Noriyuki Ishii,Akinori Saeki,Shu Seki,Seiichi Tagawa,Masateru Taniguchi,Tomoji Kawai,Takuzo Aida
Licensed Content Date	Dec 15, 2006
Licensed Content Volume	314
Licensed Content Issue	5806
Volume number	314
Issue number	5806
Type of Use	Thesis / Dissertation
Requestor type	Scientist/individual at a research institution
Format	Print and electronic
Portion	Figure
Number of figures/tables	1
Order reference number	
Title of your thesis / dissertation	Strategies to Reduce Rate of Charge Recombination: Long-Lived Charge Separated States Through Self-Assembly
Expected completion date	Jul 2016
Estimated size(pages)	160
Requestor Location	Ajith Ravi Mallia School of Chemistry IISER-Thiruvananthapuram, CET Campus Computer Science Building Thiruvananthapuram, Kerala 695016 India Attn: Ajith Ravi Mallia
Total	0.00 USD

Copyright Clearance Center RightsLink®

Science / AAAS

Title:	Supramolecular Linear Heterojunction Composed of Graphite-Like Semiconducting Nanotubular Segments
Author:	Wei Zhang,Wusong Jin,Takanori Fukushima,Akinori Saeki,Shu Seki,Takuzo Aida
Publication:	Science
Publisher:	The American Association for the Advancement of Science
Date:	Oct 21, 2011

Copyright © 2011, Copyright © 2011, American Association for the Advancement of Science

Review Order

Please review the order details and the associated terms and conditions.

No royalties will be charged for this reuse request although you are required to obtain a license and comply with the license terms and conditions. To obtain the license, click the Accept button below.

Licensed Content Publisher	The American Association for the Advancement of Science
Licensed Content Publication	Science
Licensed Content Title	Supramolecular Linear Heterojunction Composed of Graphite-Like Semiconducting Nanotubular Segments
Licensed Content Author	Wei Zhang,Wusong Jin,Takanori Fukushima,Akinori Saeki,Shu Seki,Takuzo Aida
Licensed Content Date	Oct 21, 2011
Licensed Content Volume	334
Licensed Content Issue	6054
Volume number	334
Issue number	6054
Type of Use	Thesis / Dissertation
Requestor type	Scientist/individual at a research institution
Format	Print and electronic
Portion	Figure
Number of figures/tables	1
Order reference number	
Title of your thesis / dissertation	Strategies to Reduce Rate of Charge Recombination: Long-Lived Charge Separated States Through Self-Assembly
Expected completion date	Jul 2016
Estimated size(pages)	160
Requestor Location	Ajith Ravi Mallia School of Chemistry IISER-Thiruvananthapuram, CET Campus Computer Science Building Thiruvananthapuram, Kerala 695016 India Attn: Ajith Ravi Mallia
Total	0.00 USD

Copyright Clearance Center RightsLink®

Home | Account Info | Help | Live Ch

ACS Publications
Most Trusted. Most Cited. Most Read.

Title:	Extended Charge Carrier Lifetimes in Hierarchical Donor–Acceptor Supramolecular Polymer Films
Author:	Carmen X. Guzman, Rafael M. Krick Calderon, Zhong Li, et al
Publication:	The Journal of Physical Chemistry C
Publisher:	American Chemical Society
Date:	Aug 1, 2015

Copyright © 2015, American Chemical Society

PERMISSION/LICENSE IS GRANTED FOR YOUR ORDER AT NO CHARGE

This type of permission/license, instead of the standard Terms & Conditions, is sent to you because no fee is being charged for your order. Please note the following:

- Permission is granted for your request in both print and electronic formats, and translations.
- If figures and/or tables were requested, they may be adapted or used in part.
- Please print this page for your records and send a copy of it to your publisher/graduate school.
- Appropriate credit for the requested material should be given as follows: "Reprinted (adapted) with permission from (COMPLETE REFERENCE CITATION). Copyright (YEAR) American Chemical Society." Insert appropriate information in place of the capitalized words.
- One-time permission is granted only for the use specified in your request. No additional uses are granted (such as derivative works or other editions). For any other uses, please submit a new request.

If credit is given to another source for the material you requested, permission must be obtained from that source.

BACK | CLOSE WINDOW

Copyright Clearance Center

RightsLink®

ACS Publications
Most Trusted. Most Cited. Most Read.

Title: Electron Hopping in π-Stacked Covalent and Self-Assembled Perylene Diimides Observed by ENDOR Spectroscopy

Author: Michael J. Tauber, Richard F. Kelley, Jovan M. Giaimo, et al

Publication: Journal of the American Chemical Society

Publisher: American Chemical Society

Date: Feb 1, 2006

Copyright © 2006, American Chemical Society

Logged in as:
Ajith Ravi Mallia

LOGOUT

PERMISSION/LICENSE IS GRANTED FOR YOUR ORDER AT NO CHARGE

This type of permission/license, instead of the standard Terms & Conditions, is sent to you because no fee is being charged for your order. Please note the following:

- Permission is granted for your request in both print and electronic formats, and translations.
- If figures and/or tables were requested, they may be adapted or used in part.
- Please print this page for your records and send a copy of it to your publisher/graduate school.
- Appropriate credit for the requested material should be given as follows: "Reprinted (adapted) with permission from (COMPLETE REFERENCE CITATION). Copyright (YEAR) American Chemical Society." Insert appropriate information in place of the capitalized words.
- One-time permission is granted only for the use specified in your request. No additional uses are granted (such as derivative works or other editions). For any other uses, please submit a new request.

If credit is given to another source for the material you requested, permission must be obtained from that source.

BACK   CLOSE WINDOW

Copyright Clearance Center | RightsLink®

Home | Account Info | He

ACS Publications
Most Trusted. Most Cited. Most Read.

Title: Segregated Donor–Acceptor Columns in Liquid Crystals That Exhibit Highly Efficient Ambipolar Charge Transport

Author: Hironobu Hayashi, Wataru Nihashi, Tomokazu Umeyama, et al

Publication: Journal of the American Chemical Society

Publisher: American Chemical Society

Date: Jul 1, 2011

Copyright © 2011, American Chemical Society

Logged in as:
Ajith Ravi Mallia
Account #:
3001046277

LOGOUT

PERMISSION/LICENSE IS GRANTED FOR YOUR ORDER AT NO CHARGE

This type of permission/license, instead of the standard Terms & Conditions, is sent to you because no fee is being charged for your order. Please note the following:

- Permission is granted for your request in both print and electronic formats, and translations.
- If figures and/or tables were requested, they may be adapted or used in part.
- Please print this page for your records and send a copy of it to your publisher/graduate school.
- Appropriate credit for the requested material should be given as follows: "Reprinted (adapted) with permission from (COMPLETE REFERENCE CITATION). Copyright (YEAR) American Chemical Society." Insert appropriate information in place of the capitalized words.
- One-time permission is granted only for the use specified in your request. No additional uses are granted (such as derivative works or other editions). For any other uses, please submit a new request.

If credit is given to another source for the material you requested, permission must be obtained from that source.

BACK | CLOSE WINDOW

Copyright Clearance Center **RightsLink®**

ANGEWANDTE CHEMIE
1995 34/11

Title: Linker-Controlled Energy and Charge Transfer within Chlorophyll Trefoils

Author: Richard F. Kelley,Michael J. Tauber,Michael R. Wasielewski

Publication: Angewandte Chemie International Edition

Publisher: John Wiley and Sons

Date: Nov 3, 2006

Copyright © 2006 WILEY-VCH Verlag GmbH & Co. KGaA, Weinheim

Logged in as:
Ajith Ravi Mallia
Account #:
3001046277

LOGOUT

Review Order

Please review the order details and the associated <u>terms and conditions</u>.

No royalties will be charged for this reuse request although you are required to obtain a license and comply with the license terms and conditions. To obtain the license, click the Accept button below.

Licensed Content Publisher	John Wiley and Sons
Licensed Content Publication	Angewandte Chemie International Edition
Licensed Content Title	Linker-Controlled Energy and Charge Transfer within Chlorophyll Trefoils
Licensed Content Author	Richard F. Kelley,Michael J. Tauber,Michael R. Wasielewski
Licensed Content Date	Nov 3, 2006
Licensed Content Pages	4
Type of use	Dissertation/Thesis
Requestor type	University/Academic
Format	Print and electronic
Portion	Figure/table
Number of figures/tables	1
Original Wiley figure/table number(s)	Figure 1
Will you be translating?	No
Title of your thesis / dissertation	Strategies to Reduce Rate of Charge Recombination: Long-Lived Charge Separated States Through Self-Assembly
Expected completion date	Aug 2016
Expected size (number of pages)	150
Requestor Location	Ajith Ravi Mallia School of Chemistry IISER-Thiruvananthapuram, CET Campus Computer Science Building Thiruvananthapuram, Kerala 695016 India Attn: Ajith Ravi Mallia
Publisher Tax ID	EU826007151
Total	0.00 USD

Copyright Clearance Center

RightsLink®

Home | Account Info | Help | Live Chat

nature publishing group

Title:	Metallic conduction at organic charge-transfer interfaces
Author:	Helena Alves, Anna S. Molinari, Hangxing Xie and Alberto F. Morpurgo
Publication:	Nature Materials
Publisher:	Nature Publishing Group
Date:	Jun 15, 2008

Copyright © 2008, Rights Managed by Nature Publishing Group

Logged in as:
Ajith Ravi Mallia
Account #:
3001046277

LOGOUT

Review Order

Please review the order details and the associated terms and conditions.

Licensed Content Publisher	Nature Publishing Group
Licensed Content Publication	Nature Materials
Licensed Content Title	Metallic conduction at organic charge-transfer interfaces
Licensed Content Author	Helena Alves, Anna S. Molinari, Hangxing Xie and Alberto F. Morpurgo
Licensed Content Date	Jun 15, 2008
Licensed Content Volume	7
Licensed Content Issue	7
Type of Use	reuse in a dissertation / thesis
Requestor type	academic/educational
Format	print and electronic
Portion	figures/tables/illustrations
Number of figures/tables/illustrations	1
High-res required	yes
Figures	Figure 1
Author of this NPG article	no
Your reference number	
Title of your thesis / dissertation	Strategies to Reduce Rate of Charge Recombination: Long-Lived Charge Separated States Through Self-Assembly
Expected completion date	Aug 2016
Estimated size (number of pages)	150
Requestor Location	Ajith Ravi Mallia School of Chemistry IISER-Thiruvananthapuram, CET Campus Computer Science Building Thiruvananthapuram, Kerala 695016 India Attn: Ajith Ravi Mallia
Total	158.70 USD

Copyright Clearance Center

RightsLink®

Home | Account Info | Help | Live

ACS Publications
Most Trusted. Most Cited. Most Read.

Title:	Synthesis and Controlled Self-Assembly of Covalently Linked Hexa-peri-hexabenzocoronene/Perylene Diimide Dyads as Models To Study Fundamental Energy and Electron Transfer Processes
Author:	Lukas F. Dössel, Valentin Kamm, Ian A. Howard, et al
Publication:	Journal of the American Chemical Society
Publisher:	American Chemical Society
Date:	Apr 1, 2012

Copyright © 2012, American Chemical Society

PERMISSION/LICENSE IS GRANTED FOR YOUR ORDER AT NO CHARGE

This type of permission/license, instead of the standard Terms & Conditions, is sent to you because no fee is being charged for your order. Please note the following:

- Permission is granted for your request in both print and electronic formats, and translations.
- If figures and/or tables were requested, they may be adapted or used in part.
- Please print this page for your records and send a copy of it to your publisher/graduate school.
- Appropriate credit for the requested material should be given as follows: "Reprinted (adapted) with permission from (COMPLETE REFERENCE CITATION). Copyright (YEAR) American Chemical Society." Insert appropriate information in place of the capitalized words.
- One-time permission is granted only for the use specified in your request. No additional uses are granted (such as derivative works or other editions). For any other uses, please submit a new request.

If credit is given to another source for the material you requested, permission must be obtained from that source.

BACK | CLOSE WINDOW

Copyright Clearance Center

RightsLink®

Home | Account Info | Help | Live Chat

nature publishing group

Title: Structural diversity in binary superlattices self-assembled from polymer-grafted nanocrystals

Author: Xingchen Ye, Chenhui Zhu, Peter Ercius, Shilpa N. Raja, Bo He, Matthew R. Jones

Publication: Nature Communications

Publisher: Nature Publishing Group

Date: Dec 2, 2015

Copyright © 2015, Rights Managed by Nature Publishing Group

Logged in as:
Ajith Ravi Mallia
Account #:
3001046277

LOGOUT

Creative Commons

CLOSE WINDOW

Are you the author of this NPG article?

To order reprints of this content, please contact the Nature Publishing Group reprint office by e-mail: reprints@nature.com.

Copyright Clearance Center

RightsLink®

Home | Account Info | Help | Live Chat

Science

AAAS

Title:	Ultrafast Long-Range Charge Separation in Organic Semiconductor Photovoltaic Diodes
Author:	Simon Gélinas,Akshay Rao,Abhishek Kumar,Samuel L. Smith,Alex W. Chin,Jenny Clark,Tom S. van der Poll,Guillermo C. Bazan,Richard H. Friend
Publication:	Science
Publisher:	The American Association for the Advancement of Science
Date:	Jan 31, 2014

Copyright © 2014, Copyright © 2014, American Association for the Advancement of Science

Logged in as:
Ajith Ravi Mallia
Account #:
3001046277

LOGOUT

Review Order

Please review the order details and the associated terms and conditions.

No royalties will be charged for this reuse request although you are required to obtain a license and comply with the license terms and conditions. To obtain the license, click the Accept button below.

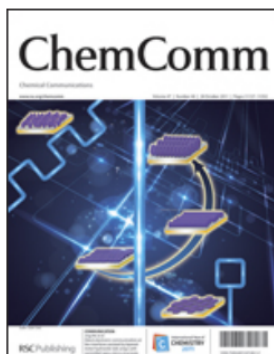|	
Licensed Content Publisher	The American Association for the Advancement of Science
Licensed Content Publication	Science
Licensed Content Title	Ultrafast Long-Range Charge Separation in Organic Semiconductor Photovoltaic Diodes
Licensed Content Author	Simon Gélinas,Akshay Rao,Abhishek Kumar,Samuel L. Smith,Alex W. Chin,Jenny Clark,Tom S. van der Poll,Guillermo C. Bazan,Richard H. Friend
Licensed Content Date	Jan 31, 2014
Licensed Content Volume	343
Licensed Content Issue	6170
Volume number	343
Issue number	6170
Type of Use	Thesis / Dissertation
Requestor type	Scientist/individual at a research institution
Format	Print and electronic
Portion	Figure
Number of figures/tables	1
Order reference number	
Title of your thesis / dissertation	Strategies to Reduce Rate of Charge Recombination: Long-Lived Charge Separated States Through Self-Assembly
Expected completion date	Jul 2016
Estimated size(pages)	160
Requestor Location	Ajith Ravi Mallia School of Chemistry IISER-Thiruvananthapuram, CET Campus Computer Science Building Thiruvananthapuram, Kerala 695016 India Attn: Ajith Ravi Mallia
Total	0.00 USD

Copyright Clearance Center

RightsLink®

Home   Account Info   Help   Live

ChemComm

Chemical Communications

RSC Publishing

Title: Self-assembly of a hexagonal supramolecular light-harvesting array from chlorophyll a trefoil building blocks

Author: Victoria L. Gunderson,Sarah M. Mickley Conron,Michael R. Wasielewski

Publication: Chemical Communications (Cambridge)

Publisher: Royal Society of Chemistry

Date: Dec 1, 2009

Copyright © 2009, Royal Society of Chemistry

Logged in as:
Ajith Ravi Mallia
Account #:
3001046277

LOGOUT

Review Order

Please review the order details and the associated terms and conditions.

No royalties will be charged for this reuse request although you are required to obtain a license and comply with the license terms and conditions. To obtain the license, click the Accept button below.

Licensed Content Publisher	Royal Society of Chemistry
Licensed Content Publication	Chemical Communications (Cambridge)
Licensed Content Title	Self-assembly of a hexagonal supramolecular light-harvesting array from chlorophyll a trefoil building blocks
Licensed Content Author	Victoria L. Gunderson,Sarah M. Mickley Conron,Michael R. Wasielewski
Licensed Content Date	Dec 1, 2009
Licensed Content Volume	46
Licensed Content Issue	3
Type of Use	Thesis/Dissertation
Requestor type	non-commercial (non-profit)
Portion	figures/tables/images
Number of figures/tables/images	1
Distribution quantity	1
Format	print and electronic
Will you be translating?	no
Order reference number	
Title of the thesis/dissertation	Strategies ti reduce rate of charge recombination through Self-assembly
Expected completion date	Aug 2016
Estimated size	150
Requestor Location	Ajith Ravi Mallia School of Chemistry IISER-Thiruvananthapuram, CET Campus Computer Science Building Thiruvananthapuram, Kerala 695016 India Attn: Ajith Ravi Mallia
Total	0.00 USD

Copyright Clearance Center — **RightsLink**®

ACS Publications
Most Trusted. Most Cited. Most Read.

Title: Extending Photoinduced Charge Separation Lifetimes by Using Supramolecular Design: Guanine–Perylenediimide G-Quadruplex

Author: Yi-Lin Wu, Kristen E. Brown, Michael R. Wasielewski

Publication: Journal of the American Chemical Society

Publisher: American Chemical Society

Date: Sep 1, 2013

Copyright © 2013, American Chemical Society

Logged in as:
Ajith Ravi Mallia
Account #:
3001046277

LOGOUT

PERMISSION/LICENSE IS GRANTED FOR YOUR ORDER AT NO CHARGE

This type of permission/license, instead of the standard Terms & Conditions, is sent to you because no fee is being charged for your order. Please note the following:

- Permission is granted for your request in both print and electronic formats, and translations.
- If figures and/or tables were requested, they may be adapted or used in part.
- Please print this page for your records and send a copy of it to your publisher/graduate school.
- Appropriate credit for the requested material should be given as follows: "Reprinted (adapted) with permission from (COMPLETE REFERENCE CITATION). Copyright (YEAR) American Chemical Society." Insert appropriate information in place of the capitalized words.
- One-time permission is granted only for the use specified in your request. No additional uses are granted (such as derivative works or other editions). For any other uses, please submit a new request.

If credit is given to another source for the material you requested, permission must be obtained from that source.

BACK | **CLOSE WINDOW**